

**SYNTHESIS AND CHARACTERIZATION OF ZINC OXIDE AND  
TIN OXIDE BASED NANOSTRUCTURES FOR GAS SENSING  
APPLICATIONS**

**THARSIKA THABOTHANAYAKAM**

**THESIS SUBMITTED IN FULFILMENT OF THE  
REQUIREMENTS FOR THE DEGREE OF DOCTOR OF  
PHILOSOPHY**

**FACULTY OF ENGINEERING  
UNIVERSITY OF MALAYA  
KUALA LUMPUR**

**2015**

UNIVERSITY OF MALAYA

**ORIGINAL LITERARY WORK DECLARATION**

Name of Candidate: Tharsika Thabothanayakam

(Passport No: N2563261)

Registration/Matric No: KHA110101

Name of Degree: Doctor of Philosophy

Title of Dissertation (“this Work”):

**SYNTHESIS AND CHARACTERIZATION OF ZINC OXIDE AND TIN OXIDE  
BASED NANOSTRUCTURES FOR GAS SENSING APPLICATIONS**

Field of Study: Advanced Material / Nanomaterials

I do solemnly and sincerely declare that:

- (1) I am the sole author/writer of this Work;
- (2) This Work is original;
- (3) Any use of any work in which copyright exists was done by way of fair dealing and for permitted purposes and any excerpt or extract from, or reference to or reproduction of any copyright work has been disclosed expressly and sufficiently and the title of the Work and its authorship have been acknowledged in this Work;
- (4) I do not have any actual knowledge nor do I ought reasonably to know that the making of this work constitutes an infringement of any copyright work;
- (5) I hereby assign all and every rights in the copyright to this Work to the University of Malaya (“UM”), who henceforth shall be owner of the copyright in this Work and that any reproduction or use in any form or by any means whatsoever is prohibited without the written consent of UM having been first had and obtained;
- (6) I am fully aware that if in the course of making this Work I have infringed any copyright whether intentionally or otherwise, I may be subject to legal action or any other action as may be determined by UM.

Candidate’s Signature

Date:

Subscribed and solemnly declared before,

Witness’s Signature

Date:

Name:

Designation:

## ABSTRACT

This thesis focuses on the fabrication of one-dimensional ZnO and SnO<sub>2</sub> based nanostructures with various morphologies by a single-step carbon-assisted thermal evaporation process and investigates their gas sensing properties. A mixture of zinc oxide, tin oxide and carbon powders was used as a source material which was loaded in a quartz boat and placed at the center of a tube furnace. A gold coated alumina substrate was placed next to quartz boat at downstream of gas flow direction. The furnace was heated to a particular growth temperature for a certain time while maintaining a constant flow of purified Ar gas. Grey and white fluffy deposits formed on Au coated alumina substrate and at the side and top of the quartz boat, respectively. The deposits collected from alumina substrate and the quartz boat were examined and found to be nanostructured in nature. The effects of different parameters such as growth temperature (800 - 950 °C), growth time (15 min - 120 min) and distance between the source and alumina substrate (3 cm - 12 cm) on the structure of the deposits were studied. Crystallographic phase, microstructure and elemental composition of nanostructures were investigated by X-ray diffractometer (XRD), field-emission scanning electron microscopy (FESEM) and transmission electron microscopy (TEM) equipped with an energy dispersive X-ray spectroscopy (EDS). The crystalline quality of samples was analysed by photoluminescence spectroscopy (PL). The nanostructures were used to fabricate resistor-type sensors on a gold interdigitated alumina substrate. The gas sensing properties of these nanostructures based sensors were studied by measuring their sensitivity towards methane, hydrogen, ethanol and carbon monoxide over different gas concentrations and operating temperatures. Results show that single-crystalline Zn<sub>2</sub>SnO<sub>4</sub> nanowires grew at 834 °C on the Au coated alumina substrate. Nanowires have an average diameter of about 15 to 80 nm and length ranging from two

to several tens of micrometers. The white fluffy mass found on a quartz boat exhibited SnO<sub>2</sub>-core/ZnO-shell nanowires as well as hierarchical nanostructures. Nanostructures deposited on the quartz boat consisted of pristine SnO<sub>2</sub> nanowires with a rectangular cross-section, SnO<sub>2</sub>-core/ZnO-shell nanowires and SnO<sub>2</sub>-core/ZnO-shell hierarchical nanostructures at a growth time of 15 min, 30 min, and exceeding 60 min, respectively. The hexagonal shape of ZnO branches grew on the ZnO shell layer in the hierarchical nanostructures. Growth mechanisms of Zn<sub>2</sub>SnO<sub>4</sub> nanowires and SnO<sub>2</sub>-core/ZnO-shell nanostructures are suggested. Zn<sub>2</sub>SnO<sub>4</sub> nanowires based sensors showed excellent sensitivity and selectivity towards ethanol with quick response and recovery times. SnO<sub>2</sub>-core/ZnO-shell hierarchical nanostructures deposited at 90 min exhibited 5 folds enhanced sensitivity than that of pristine SnO<sub>2</sub> nanowires towards 20 ppm ethanol at 400 °C. This improvement in ethanol sensitivity was attributed to highly active sensing sites and the synergistic effect of the encapsulation of SnO<sub>2</sub> by ZnO nanostructures. SnO<sub>2</sub>-core/ZnO-shell hierarchical nanostructures grown for 90 min showed higher sensitivity of 76 compared with Zn<sub>2</sub>SnO<sub>4</sub> nanowires based sensor of 60.8 for 100 ppm ethanol. Specifically, SnO<sub>2</sub>-core/ZnO-shell hierarchical nanostructures prepared by the single carbon assisted thermal evaporation method are promising candidates for the detection of ethanol with high sensitivity and selectivity against other gases.



## ABSTRAK

Tesis ini memberi tumpuan kepada penghasilan nanostruktur satu-dimensi berasaskan ZnO dan SnO<sub>2</sub> dengan pelbagai morfologi melalui proses penyejatan haba satu-langkah dengan bantuan karbon dan menyiasat ciri-ciri pengesanan gas mereka. Campuran zink oksida, timah oksida dan serbuk karbon telah digunakan sebagai bahan sumber yang telah dimuatkan di dalam bot kuarza dan diletakkan di tengah-tengah sebuah relau tiub. Sebuah substrat alumina bersalut emas diletakkan di sebelah bot kuarza di hilir arah aliran gas. Relau dipanaskan pada suhu pertumbuhan untuk masa yang tertentu di samping mengekalkan kadar aliran gas Ar tulen. Deposit berwarna kelabu dan putih bergebu terbentuk di substrat alumina bersalut Au serta di sisi dan atas bot kuarza, masing-masing. Deposit yang dikumpul daripada substrat alumina dan bot kuarza telah diperiksa dan didapati bernanostruktur. Kesan-kesan parameter seperti suhu pertumbuhan (800-950 °C), masa pertumbuhan (15 min - 120 min) dan jarak di antara sumber dan alumina substrat (3 cm - 12 cm) pada struktur deposit telah dikaji. Fasa kristalografi, mikrostruktur dan komposisi unsur struktur-struktur nano telah disiasat oleh X-ray diffractometer (XRD), field-emission scanning electron mikroskopi (FESEM) dan transmission electron mikroskopi (TEM) dilengkapi dengan energy dispersive X-ray spektroskopi (EDS). Kualiti kristal sampel dianalisis dengan photoluminescence spektroskopi (PL). Struktur-struktur nano tersebut digunakan untuk menghasilkan sensor jenis-perintang pada substrat alumina interdigitated emas. Sifat-sifat pengesanan gas sensor berasaskan struktur-struktur nano ini dikaji dengan mengukur kepekaan mereka terhadap metana, hidrogen, etanol dan karbon monoksida dengan kepekatan gas dan suhu operasi yang berbeza. Keputusan menunjukkan nanowayar Zn<sub>2</sub>SnO<sub>4</sub> kristal-tunggal ditumbuhkan pada 834 °C atas substrat alumina bersalut Au. Nanowayar tersebut mempunyai diameter purata kira-kira 15-80 nm dan

panjang di antara dua hingga beberapa puluh mikrometer. Jisim gebu berwarna putih ditemui pada bot kuarza menunjukkan struktur nanowayar  $\text{SnO}_2$ -teras/ $\text{ZnO}$ -shell serta struktur-struktur nano hierarki. Nanostruktur yang didepositkan pada bot kuarza terdiri daripada nanowayar  $\text{SnO}_2$  dengan keratan rentas segi empat tepat, nanowayar  $\text{SnO}_2$ -teras/ $\text{ZnO}$ -shell dan  $\text{SnO}_2$ -teras/ $\text{ZnO}$ -shell nanostruktur hierarki pada masa pertumbuhan 15 min, 30 min, dan melebihi 60 min, masing-masing. Cawangan  $\text{ZnO}$  berbentuk heksagon tumbuh pada lapisan shell  $\text{ZnO}$  dalam struktur-struktur nano hierarki. Mekanisme pertumbuhan nanowayar  $\text{Zn}_2\text{SnO}_4$  dan struktur-struktur nano  $\text{SnO}_2$ -teras/ $\text{ZnO}$ -shell adalah disyorkan. Sensor berasaskan nanowayar  $\text{Zn}_2\text{SnO}_4$  menunjukkan sensitiviti dan pemilihan yang sangat baik terhadap etanol dengan tindak balas dan masa pemulihan yang cepat.  $\text{SnO}_2$ -teras/ $\text{ZnO}$ -shell nanostruktur hierarki didepositkan untuk 90 min menunjukkan peningkatan sensitiviti 5 kali ganda berbanding dengan nanowayar  $\text{SnO}_2$  terhadap 20 ppm etanol pada  $400^\circ\text{C}$ . Peningkatan dalam sensitiviti etanol adalah disebabkan oleh laman sensing yang sangat aktif dan kesan sinergi daripada pengkapsulan  $\text{SnO}_2$  dengan nano  $\text{ZnO}$ .  $\text{SnO}_2$ -teras/ $\text{ZnO}$ -shell nanostruktur hierarki yang ditumbuh selama 90 min menunjukkan kepekaan yang lebih tinggi, 76 berbanding dengan nanowayar berasaskan  $\text{Zn}_2\text{SnO}_4$ , 60.8 bagi 100 ppm etanol. Secara khusus,  $\text{SnO}_2$ -teras/ $\text{ZnO}$ -shell nanostruktur hierarki yang disediakan melalui kaedah penyejatan haba satu-langkah dengan bantuan karbon merupakan calon yang menjanjikan untuk mengesan etanol dengan sensitiviti yang tinggi serta mempunyai pemilihan keutamaan terhadap etanol berbanding gas-gas lain.

## ACKNOWLEDGMENTS

First and foremost, I would like to express my most sincere and respectful gratitude to my main supervisor, Professor A.S.M.A. Haseeb, Department of Mechanical Engineering, University of Malaya. He offers me a great opportunity to work under his guidance and for making this project such a pleasant experience. I deeply appreciate the constant support which I have received during the past three years.

Together with him, I would like to express my sincere gratitude to my external advisor Professor Sheikh A. Akbar, Department of Materials Science and Engineering, Ohio State University, Columbus, USA. I appreciate his consideration and invaluable assistance that enabled me to experience a great deal of success throughout my PhD research program. Moreover, I would like to thank my co-supervisors, Dr. Mohd Faizul Bin Mohd Sabri, and Dr. Wong Yew Hoong, for offering me valuable suggestions, providing ever positive attitude and precious help during the discussion, and their effort spent in reviewing manuscript for all the time.

Special thanks go to the Bright Spark Unit, University of Malaya for providing financial support through their Bright Spark Scholarship program in my entire study period. My appreciation extends to Mr. Nazarul Zaman, technical staff of UM and Ms. Siti Rahmah Esa, technical staff of MIMOS. Sdn. Bhd for their valuable support in FESEM and TEM analysis. I wish to thank my close university colleagues for providing a friendly and relaxed atmosphere for conducting research. In addition, words are lacking to express my heartiest gratitude to my fiancé Mr. M. Thanihaichelvan and my family members for their support for completing my PhD studies over here. Again, I would like to thank everyone who has contributed to the successful completion of this research work direct or indirectly.

## TABLE OF CONTENTS

<b>ORIGINAL LITERARY WORK DECLARATION</b>	Ii
<b>ABSTRACT</b>	Iii
<b>ABSTRAK</b>	V
<b>ACKNOWLEDGEMENTS</b>	Vii
<b>TABLE OF CONTENTS</b>	Viii
<b>LIST OF FIGURES</b>	Xi
<b>LIST OF TABLES</b>	Xiii
<b>LIST OF ABBREVIATIONS</b>	Xix
<b>CHAPTER 1 INTRODUCTION</b>	1
1.1 Background	1
1.2 Research Objectives	3
1.3 Scope of Research	4
1.4 Organization of Thesis	5
<b>CHAPTER 2 LITERATURE REVIEW</b>	6
2.1 Metal Oxide Nanostructures and Its Application	6
2.2 Nanostructures based on Zinc Oxide and Tin Oxide	6
2.2.1 Zinc Oxide (ZnO)	7
2.2.2 Tin Oxide (SnO <sub>2</sub> )	9
2.2.3 Zinc Stannate (Zn <sub>2</sub> SnO <sub>4</sub> )	10
2.3 Overview of Gas Sensors	11
2.3.1 Solid State Gas Sensors	11
2.3.1.1 Solid Electrolyte Gas Sensors	12
2.3.1.2 Catalytic Combustion Gas Sensors	13
2.3.1.3 Semiconductor Gas Sensors	13
2.3.2 Gas Sensor Performance Characteristics	15
2.3.2.1 Sensitivity	15
2.3.2.2 Selectivity	15
2.3.2.3 Optimum Working Temperature	16
2.3.2.4 Response and Recovery Times	16
2.3.2.5 Lower Limit of Detection	17
2.3.3 Fabrication of Gas Sensor	17

2.4	Metal Oxide Semiconductor Material for Gas Sensing	19
2.4.1	Gas Sensing Mechanism	21
2.4.2	Factors Influencing the Enhanced Sensitivity and Selectivity	22
2.4.2.1	Development of Nanostructures with Different Morphologies	23
2.4.2.2	Doping of Metal Oxide Catalyst	24
2.4.2.3	Surface Modification by Noble Metal Particles	25
2.4.2.4	Mixed Metal Oxide Nanostructures	26
2.5	Gas Sensors based on ZnO/SnO <sub>2</sub> Nanostructures	28
2.5.1	Growth and Characterization	28
2.5.1.1	Nanostructures by Single-Step Process	29
2.5.1.2	Nanostructures by Two-Step Process	34
2.5.2	Sensing Performance of ZnO/SnO <sub>2</sub> Nanostructures	41
2.6	Gas Sensors based on Zn <sub>2</sub> SnO <sub>4</sub> Nanostructures	48
2.6.1	Growth and Characterization	48
2.6.2	Sensing Performance of Zn <sub>2</sub> SnO <sub>4</sub> Nanostructures	54
2.7	Summary of Literature	59
<b>CHAPTER 3</b>	<b>METHODOLOGY</b>	60
3.1	Experimental Flow Chart	60
3.2	Materials and Chemicals	61
3.3	Preparation of Precursor Mixture	61
3.4	Substrate Preparation	62
3.5	Synthesis of Zinc Oxide and Tin Oxide based Nanostructures	63
3.6	Sensor Fabrication	65
3.7	Characterization Techniques	66
3.7.1	X-ray Diffraction (XRD)	66
3.7.2	Field Emission Scanning Electron Microscopy Analysis (FESEM)	66
3.7.3	Transmission Electron Microscopy Analysis (TEM)	66
3.7.4	Photoluminescence Spectroscopy (PL)	67
3.7.5	Sensor Measurements	67
<b>CHAPTER 4</b>	<b>RESULTS AND DISCUSSION</b>	70
4.1	Microstructure of Mixed Powder after Ball Mill	70
4.2	Growth of Nanostructures based on Zinc Oxide and Tin Oxide	71
4.3	Characterization of Zn <sub>2</sub> SnO <sub>4</sub> Nanowires	72

4.3.1	X-ray Diffraction Analysis	72
4.3.2	Effect of Au Catalyst and Activated Carbon	73
4.3.3	Effect of Source Mixture	76
4.3.4	Effect of Substrate Position and Various Growth Temperature	78
4.3.5	Effect of Growth Time	81
4.3.6	Transmission Electron Microscopy Analysis	82
4.3.7	Photoluminescence Studies	86
4.3.8	Growth Mechanism of $\text{Zn}_2\text{SnO}_4$ Nanowires	88
4.4	Characterization of $\text{SnO}_2$ -Core/ $\text{ZnO}$ -Shell Nanostructures	90
4.4.1	X-ray Diffraction Analysis	92
4.4.2	Effect of Growth Time	93
4.4.3	Transmission Electron Microscopy Analysis	97
4.4.3.1	Nanowires obtained at 15 minutes	98
4.4.3.2	Nanostructures synthesized at 30 minutes	100
4.4.3.3	Nanostructures obtained at 120 minutes	103
4.4.4	Photoluminescence Studies	109
4.4.5	Growth Mechanism of $\text{SnO}_2$ -Core/ $\text{ZnO}$ -Shell Nanostructures	113
4.5	Gas Sensing Properties of $\text{Zn}_2\text{SnO}_4$ Nanowires	116
4.5.1	Variation of Operating Temperature	117
4.5.2	Dynamic Gas Response	118
4.5.3	Variation of Gas Sensitivity with Concentration	120
4.5.4	Selectivity of $\text{Zn}_2\text{SnO}_4$ Nanowires based Sensor	122
4.5.5	Sensing Mechanism for $\text{Zn}_2\text{SnO}_4$ Nanowires	124
4.6	Sensing Performance of $\text{SnO}_2$ -Core/ $\text{ZnO}$ -Shell Nanostructures	126
4.6.1	Variation of Operating Temperature	127
4.6.2	Dynamic Gas Response	128
4.6.3	Selectivity of $\text{SnO}_2$ -Core/ $\text{ZnO}$ -Shell Nanostructures based Sensor	130
4.6.4	Sensing Mechanism for $\text{SnO}_2$ -Core/ $\text{ZnO}$ -Shell Nanostructures	132
<b>CHAPTER 5 CONCLUSIONS AND RECOMMENDATIONS</b>		138
5.1	Conclusions	138
5.2	Recommendations for Future Work	140
<b>REFERENCES</b>		142
<b>LIST OF PUBLICATIONS AND PAPERS PRESENTED</b>		165

## LIST OF FIGURES

FIGURES		PAGE
Figure 2.1	Explanation of the response time and recovery time in sensors.	17
Figure 2.2	Schematic illustration of fabricated sensor device: (a) bulk sensor (Yu & Choi, 2001), (b) interdigitated substrate based sensor (Jiménez-Cadena <i>et al.</i> , 2007), (c) tube-type sensor (Wan <i>et al.</i> , 2008b), and (d) FET type sensor (Huang & Wan, 2009).	19
Figure 2.3	Pristine nanostructures for gas sensing: (a) In <sub>2</sub> O <sub>3</sub> nanowires for N <sub>2</sub> O detection (Rout <i>et al.</i> , 2006), (b) WO <sub>3</sub> nanowires for NO <sub>2</sub> detection (Cao <i>et al.</i> , 2009), and (c) ZnO nanowires for ethanol sensing (Wan <i>et al.</i> , 2004).	20
Figure 2.4	Sensing mechanism of reducing gas towards n-type sensing materials: (a) before adsorption of oxygen, (b) adsorption of oxygen in air environment and (c) adsorption of oxygen in reducing gas environment (Arafat <i>et al.</i> , 2014).	21
Figure 2.5	Various morphologies nanostructures for gas sensing: (a) hierarchical In <sub>2</sub> O <sub>3</sub> nanostructure (Jiang <i>et al.</i> , 2013), (b) ZnO dendrite nanostructure (Zhang <i>et al.</i> , 2008), and (c) $\alpha$ -Fe <sub>2</sub> O <sub>3</sub> flower-like nanostructure (Agarwala <i>et al.</i> , 2012).	24
Figure 2.6	Doping of metal oxide catalyst for gas sensing: (a) PbO nanoparticle decorated on ZnO flower-like nanostructure (Lou <i>et al.</i> , 2013), (b) Co <sub>3</sub> O <sub>4</sub> nanoisland decorated on ZnO nanowires (Na <i>et al.</i> , 2011), and (c) Cr <sub>2</sub> O <sub>3</sub> nanoparticle decorated on ZnO nanowire (Woo <i>et al.</i> , 2012).	25
Figure 2.7	Surface modification using noble metal nanoparticles for gas sensing: (a) Au nanoparticle decorated on ZnO nanowires (Rai <i>et al.</i> , 2012), (b) Pt nanoparticle decorated on WO <sub>3</sub> nanowires (Zhu <i>et al.</i> , 2010), and (c) Pd nanoparticle decorated on SnO <sub>2</sub> nanowires (Kolmakov <i>et al.</i> , 2005).	26
Figure 2.8	Mixed nanostructures for gas sensing application: (a) ZnO/TiO <sub>2</sub> hierarchical nanostructure (Deng <i>et al.</i> , 2013), (b) W <sub>18</sub> O <sub>49</sub> /SnO <sub>2</sub> nanowires (Sen <i>et al.</i> , 2010), and (c) SnO <sub>2</sub> /In <sub>2</sub> O <sub>3</sub> hierarchical nanostructure (Her <i>et al.</i> , 2012).	28
Figure 2.9	Different morphologies of ZnO/SnO <sub>2</sub> nanostructures obtained	

	by single-step process: (a) mesoporous nanofibers (Song <i>et al.</i> , 2009), (b) hollow nanofibers (Wei <i>et al.</i> , 2011), (c) ZnO nanonodules on the SnO <sub>2</sub> nanofiber (Lee <i>et al.</i> , 2012b), (d) triangular SnO <sub>2</sub> nanoparticles on ZnO nanobelts (Wang <i>et al.</i> , 2007), (e) SnO <sub>2</sub> /ZnO/SnO <sub>2</sub> triaxial nanobelt (Zhao <i>et al.</i> , 2006), and (f) flower-like nanostructure (Li <i>et al.</i> , 2011).	32
Figure 2.10	Different morphologies of ZnO/SnO <sub>2</sub> nanostructures obtained by two-step process: (a) SnO <sub>2</sub> -core/ZnO-shell nanowires (Park <i>et al.</i> , 2013a), (b, c, d and e) SnO <sub>2</sub> -ZnO hierarchical nanostructures (Sun <i>et al.</i> , 2007; Cheng <i>et al.</i> , 2009; Dai <i>et al.</i> , 2013; Lan <i>et al.</i> , 2012), and (f) SnO <sub>2</sub> capped ZnO nanowire (Liu <i>et al.</i> , 2008b).	36
Figure 2.11	Schematic diagram showing the formation of the SnO <sub>2</sub> /ZnO hierarchical nanostructures (Lan <i>et al.</i> , 2012).	37
Figure 2.12	Various morphologies of Zn <sub>2</sub> SnO <sub>4</sub> nanostructures: (a) hierarchical nanostructure (Chen <i>et al.</i> , 2011), (b) nanoflower (Mary Jaculine <i>et al.</i> , 2013), (c) cube-like nanoparticles (Jiang <i>et al.</i> , 2012), (d) nanofibers (Choi <i>et al.</i> , 2011), (e) zig-zag nanowire (Wang <i>et al.</i> , 2007), (f) nanobelts and nanoring (Wang <i>et al.</i> , 2004), and (g) dendritic structure (Jun <i>et al.</i> , 2008).	51
Figure 3.1	Flow chart of the experimental procedure adopted in this work.	60
Figure 3.2	(a) Experimental setup for the growth of SnO <sub>2</sub> -core/ZnO-shell nanostructures (location B) and Zn <sub>2</sub> SnO <sub>4</sub> nanowires (location A), (b) measured temperature as a function of distance from the center of the furnace at 25 sccm Ar flow for various furnace center temperatures.	64
Figure 3.3	Schematic illustration for sensor fabrication process using SnO <sub>2</sub> -core/ZnO-shell nanostructures: (a) drop coating SnO <sub>2</sub> /ZnO nanostructure suspension on printed Au interdigitated electrode, (b) nanostructures arrangement on sensor device, (c) Heat treatment of sensor device.	65
Figure 3.4	Schematic representation of setup for gas sensor characterization.	68
Figure 4.1	(a) Morphology and (b) XRD of source powder mixture after milling of 8 hours.	70



Figure 4.2	Schematic representation of formation of nanostructures at different places.	71
Figure 4.3	XRD patterns of nanowires obtained on Au coated alumina substrate at a furnace temperature of 900 °C with the deposition time of 120 min with molar ratio of ZnO to SnO <sub>2</sub> in the source mixture of 9:1 [ZTO represents Zn <sub>2</sub> SnO <sub>4</sub> phase].	73
Figure 4.4	FESEM micrographs of the nanostructures prepared with molar ratio of ZnO to SnO <sub>2</sub> in the source mixture of 9:1 at a furnace temperature of 900 °C for 120 min grown on (a) alumina substrate in the presence of activated carbon, (b) Au/alumina substrate in the absence of activated carbon, (c) EDS analysis of spheroidal shaped particles on alumina substrate, (d) alumina substrate in the presence of both Au layer and activated carbon, (e) enlarged view of tip of the nanowire and (f) EDS analysis of tip of the nanowire.	75
Figure 4.5	FESEM micrographs for nanostructures obtained at a furnace temperature of 900 °C with the deposition time of 120 min for different molar ratio of ZnO to SnO <sub>2</sub> in the source mixture (a) 1:9, (b) 2:8, (c) 3:7, (d) 4:6, (e) 5:5, (f) 6:4, (g) 7:3, (h) 8:2 and (d) 9:1.	77
Figure 4.6	Top image: FESEM images of the nanostructures fabricated at different furnace temperature with various deposition positions of substrate from the center of the furnace. Bottom image: zoom in the FESEM images of nanostructures fabricated at 850 °C and 900 °C with the deposition positions of substrate at 6 cm and 9 cm.	80
Figure 4.7	FESEM micrographs of the nanostructures synthesized at different growth time on Au/alumina substrate at a furnace center temperature of 900 °C: (a) 15 min, (b) 30 min, (c) 60 min, (d) 90 min and (e) 120 min. Inset are images of a single nanowire corresponding to the growth time.	82
Figure 4.8	(a) Low magnification TEM images of a single Zn <sub>2</sub> SnO <sub>4</sub> nanowire deposited at 120 min, (b) nanowire with a gold catalyst at its tip, (c) High-resolution TEM image of the nanowire showing the lattice fringes and corresponding (d) SAED pattern over this single Zn <sub>2</sub> SnO <sub>4</sub> nanowire.	83
Figure 4.9	(a) STEM image of an Zn <sub>2</sub> SnO <sub>4</sub> nanowire showing the line scan trajectory, (b) Integrated EDX spectrum of the nanowire,	

	and (c) Integrated peak counts as a function of spot position for Zn, Sn and O.	84
Figure 4.10	(a) STEM image of an $\text{Zn}_2\text{SnO}_4$ nanowire, (b) Integrated EDX spectrum of the nanowire, (c) Magnified image of the mapping area indicated by box in (a), The colour maps demonstrating the spatial distribution of different elements, (d) Zn, (e) O, and (f) Sn, which are labelled in blue, red, green, respectively.	85
Figure 4.11	Photoluminescence spectrum of $\text{Zn}_2\text{SnO}_4$ nanowires measured at room temperature with a power source of 2 mW, and inset shows the enlarged view of photoluminescence spectrum of $\text{Zn}_2\text{SnO}_4$ nanowires recorded by increased power source of 10 mW within the wavelength range of 360-400 nm.	87
Figure 4.12	Schematic diagram of growth of $\text{Zn}_2\text{SnO}_4$ nanowires on Au/alumina substrate [adapted from Jie <i>et al.</i> , 2004].	89
Figure 4.13	Phase diagram for the $\text{GaO}_{1.5}$ - $\text{SnO}_2$ - $\text{ZnO}$ system at 1250 °C (Palmer & Poeppelmeier, 2002).	90
Figure 4.14	Photograph of nanostructures visible as white fluffy mass with naked eyes formed at the edges and the top of the quartz boat at various growth times (a) 15 min, (b) 30 min, (c) 60 min, (d) 90 min and (e) 120 min. Arrow shows the direction of Ar flow.	92
Figure 4.15	XRD patterns of $\text{SnO}_2/\text{ZnO}$ nanostructures obtained at different growth time at a furnace temperature of 900 °C: (a) 15 min, (b) 30 min, (c) 60 min, (d) 90 min, and (e) 120 min.	93
Figure 4.16	FESEM images of $\text{SnO}_2$ - $\text{ZnO}$ nanostructures obtained at different growth time at a furnace temperature of 900 °C: (a) 15 min, (b) 30 min, (c) 60 min, (d) 90 min, and (e) 120 min.	95
Figure 4.17	FESEM micrographs of a single $\text{SnO}_2/\text{ZnO}$ nanostructure obtained at different growth time at a furnace temperature of 900 °C: (a) 15 min, (b) 30 min, (c) 60 min, (d) 90 min, and (e and f) 120 min.	97
Figure 4.18	(a) STEM image of $\text{SnO}_2/\text{ZnO}$ nanowire grown at 15 min showing the linescan trajectory, (b) Integrated EDX spectrum of the nanowire, and (c) Integrated peak intensities as a function of spot position for Zn, Sn and O peaks.	98
Figure 4.19	(a) STEM image of $\text{SnO}_2/\text{ZnO}$ nanowire grown at 15 min, (b)	

	Integrated EDX spectrum of the nanowire, (c) Magnified image of the mapping area indicated by box in (a), The colour maps demonstrating the spatial distribution of different elements, (d) Sn, and (e) O which are labelled in green, red, respectively.	99
Figure 4.20	(a) Low magnification TEM images of a single SnO <sub>2</sub> nanowire deposited at 15 min, and (b) HRTEM image of SnO <sub>2</sub> nanowire.	100
Figure 4.21	(a) STEM image of SnO <sub>2</sub> /ZnO nanowire grown at 30 min showing the linescan trajectory, (b) Integrated EDX spectrum of the nanowire, and (c) Integrated peak intensities as a function of spot position for Zn, Sn and O peaks.	101
Figure 4.22	(a) STEM image of SnO <sub>2</sub> /ZnO nanowire grown at 30 min, (b) Integrated EDX spectrum of the nanowire, (c) Magnified image of the mapping area indicated by box in (a), The colour maps demonstrating the spatial distribution of different elements, (d) Zn, (e) O, and (f) Sn which are labelled in blue, red, green, respectively.	102
Figure 4.23	(a) Typical low magnification TEM images of a single SnO <sub>2</sub> -core/ZnO-shell nanowire deposited at 30 min, (b) HRTEM image of SnO <sub>2</sub> -core/ZnO-shell nanowire.	103
Figure 4.24	(a) STEM image of hierarchical SnO <sub>2</sub> /ZnO nanostructure grown at 120 min showing the linescan trajectory of backbone nanowire, (b) Integrated EDX spectrum of the backbone nanowire, and (c) Integrated peak intensities as a function of spot position for Zn, Sn and O peaks.	104
Figure 4.25	(a) STEM image of hierarchical SnO <sub>2</sub> /ZnO nanostructure grown at 120 min, (b) Integrated EDX spectrum of the backbone nanowire, (c) Magnified image of the mapping area indicated by box in (a), The colour maps demonstrating the spatial distribution of different elements, (d) Zn, (e) O, and (f) Sn which are labelled in blue, red, green, respectively.	105
Figure 4.26	(a) STEM image of hierarchical SnO <sub>2</sub> /ZnO nanostructure grown at 120 min showing the linescan trajectory of branch, (b) Integrated EDX spectrum of the branch, and (c) Integrated peak intensities as a function of spot position for Zn, Sn and O peaks.	106
Figure 4.27	(a) STEM image of branch of hierarchical nanostructure grown	

	at 120 min, (b) Integrated EDX spectrum of the branch nanowire, (c) Magnified image of the mapping area indicated by box in (a), The colour maps demonstrating the spatial distribution of different elements,(d) O, (e) Zn, and (f) Sn which are labelled in red, blue, green, respectively.	107
Figure 4.28	(a) Low magnification TEM images of hierarchical core-shell nanostructure deposited at 120 min, HRTEM images of (b) hierarchical nanostructure, (c) interface between core-shell structure of backbone nanowire and (d) branch nanostructure.	108
Figure 4.29	(a) Photoluminescence (PL) spectra of SnO <sub>2</sub> /ZnO nanostructures obtained at different growth times, and (b) enlarged view of PL spectra of SnO <sub>2</sub> /ZnO nanostructures within a wavelength of 360-420 nm.	110
Figure 4.30	Ellingham diagram for several metal oxides as a function of temperature showing the stability of the compounds (Ellingham <i>et al.</i> 1944).	114
Figure 4.31	Vapour pressure detail of (a) SnO <sub>2</sub> and (b) ZnO nanostructure as a function of temperature (Lamoreaux <i>et al.</i> , 1987b).	115
Figure 4.32	Sensitivity of Zn <sub>2</sub> SnO <sub>4</sub> sensor investigated at various operating temperatures for different gases at concentration of 50 ppm: (a) ethanol, (b) hydrogen, (c) carbon monoxide, and (d) methane.	118
Figure 4.33	Five cycles of response-recovery characteristics of Zn <sub>2</sub> SnO <sub>4</sub> nanowires sensor exposed to different gas concentrations at an optimum operating temperature of 500 °C: (a) ethanol, (b) hydrogen, (c) carbon monoxide, and (d) methane.	120
Figure 4.34	Sensitivity of Zn <sub>2</sub> SnO <sub>4</sub> nanowires sensor as a function of various gas concentrations: (a) ethanol, (b) hydrogen, (c) carbon monoxide, and (d) methane.	122
Figure 4.35	Variation of sensitivity as a function of operating temperature of Zn <sub>2</sub> SnO <sub>4</sub> nanowires gas sensors to 50 ppm of methane, hydrogen, ethanol, and carbon monoxide.	123
Figure 4.36	Sensitivity of SnO <sub>2</sub> -core/ZnO-shell nanostructure grown for 90 min sensor investigated at various operating temperatures for different gases: (a) ethanol, (b) hydrogen, (c) carbon monoxide, and (d) methane.	128

Figure 4.37	Time-dependent sensitivity of various growth times of SnO <sub>2</sub> -core/ZnO-shell nanostructure sensors with different gas concentrations at an optimum operating temperature of 400 °C: (a) ethanol, (b) hydrogen, (c) carbon monoxide, and (d) methane.	130
Figure 4.38	Sensitivity bar chart of sensors towards 20 ppm of methane, hydrogen, carbon monoxide and ethanol.	131
Figure 4.39	Energy band diagram of (a) SnO <sub>2</sub> and ZnO, and (b) SnO <sub>2</sub> -core/ZnO-shell nanostructures (adapted from Zhang <i>et al.</i> , 2011; Zhang <i>et al.</i> , 2010; Zheng <i>et al.</i> , 2009).	134

## LIST OF TABLES

TABLE		PAGE
Table 2.1	Overview of the physical properties of the zinc and tin based oxides (Batzill & Diebold, 2005; Ellmer, 2001).	7
Table 2.2	Summary of various processing routes for the production of ZnO/SnO <sub>2</sub> nanostructures.	39
Table 2.3	Summary of gas sensing properties of ZnO/SnO <sub>2</sub> nanostructures.	46
Table 2.4	Summary of gas sensing properties of Zn <sub>2</sub> SnO <sub>4</sub> (ZTO) nanostructures.	58
Table 4.1	Growth temperatures of nanostructures obtained at different furnace temperatures and various substrate positions.	80
Table 4.2	Brief summary of Zn <sub>2</sub> SnO <sub>4</sub> gas sensor upon exposure to 100 ppm ethanol.	125
Table 4.3	Brief summary of ZnO/SnO <sub>2</sub> gas sensor upon exposure to 100 ppm ethanol.	133
Table 4.4	The value of electronic properties of ZnO and SnO <sub>2</sub> nanostructures (Robertson <i>et al.</i> , 2006; Zhang <i>et al.</i> , 2010; Zheng <i>et al.</i> , 2009).	134

## LIST OF ABBREVIATIONS

1-D	One dimensional
Ag	Silver
Al	Aluminum
Al <sub>2</sub> O <sub>3</sub>	Alumina
ALD	Atomic Layer Deposition
Ar	Argon
Au	Gold
C	Carbon
C <sub>2</sub> H <sub>5</sub> OH	Ethanol
C <sub>3</sub> H <sub>6</sub> O	Acetone
C <sub>3</sub> H <sub>9</sub> N	Trimethylamine
C <sub>4</sub> H <sub>10</sub>	Butane
C <sub>4</sub> H <sub>9</sub> NH <sub>2</sub>	n-butylamine
C <sub>6</sub> H <sub>12</sub> N <sub>4</sub>	Hexamethylenetetramine
CdO	Cadmium oxide
CeO <sub>2</sub>	Cerium oxide
CH <sub>3</sub> CHO	Acetaldehyde
CH <sub>3</sub> CN	Acetonitrile
CH <sub>3</sub> OH	Methanol
CH <sub>4</sub>	Methane
CHCl <sub>3</sub>	Chloroform
(CH <sub>3</sub> ) <sub>4</sub> Sn	Tetramethyltin
CNT	Carbon nanotube
CO	Carbon monoxide
CO <sub>2</sub>	Carbon dioxide
Co <sub>3</sub> O <sub>4</sub>	Cobalt(II,III) oxide
Cr <sub>2</sub> O <sub>3</sub>	Chromium(III) oxide
CTAB	Cetyltrimethylammonium bromide
Cu	Copper
CuO	Copper(II) oxide
DBTD	Dibutyltin diacetate
DEZn	Diethylzinc
DGDE	Diethylene Glycol Dibutyl Ether

DL	Deep Level
DMF	<i>N,N</i> dimethylformamide
EDA	Ethylenediamine
EDS	Energy Dispersive X-ray Spectroscopy
Fe <sub>2</sub> O <sub>3</sub>	Iron(III) oxide
FESEM	Field Emission Scanning Electron Microscopy
FET	Field Effect Transistor
GL	Green Luminescence
H <sub>2</sub>	Hydrogen
H <sub>2</sub> O <sub>2</sub>	Hydrogen peroxide
H <sub>2</sub> S	Hydrogen sulphide
HCHO	Formaldehyde
HMT	Hexamethylenetetramine
HRTEM	High Resolution Transmission Electron Microscopy
In <sub>2</sub> O <sub>3</sub>	Indium(III) oxide
JCPDS	Joint Committee on Powder Diffraction Standards
KBH <sub>4</sub>	Potassium borohydride
Li	Lithium
LPG	Liquefied Petroleum Gas
MFC	Mass flow controller
MoO <sub>3</sub>	Molybdenum trioxide
MOSFET	Metal Oxide-Semiconductor Field Effect Transistors
N <sub>2</sub> O	Nitrous oxide
Na <sub>2</sub> SnO <sub>3</sub> .4H <sub>2</sub> O	Sodium stannate tetrahydrate
NH <sub>3</sub>	Ammonia
NH <sub>4</sub> Ac	Ammonium acetate
(NH <sub>4</sub> ) <sub>2</sub> SnF <sub>6</sub>	Ammonium hexafluorostannate
NiO	Nickel oxide
NNH	Nanofiber-Nanowire Heterostructure
NO	Nitric oxide
NO <sub>2</sub>	Nitrogen dioxide
O <sub>2</sub>	Oxygen
PAN	Polyacrylonitrile
Pd	Palladium
PdO	Palladium(II) oxide



PL	Photoluminescence
PLD	Pulsed Laser Deposition
ppb	Part per billion
ppm	Part per million
Pt	Platinum
PVA	Polyvinyl alcohol
PVAc	Polyvinyl acetate
PVD	Physical Vapour Deposition
PVP	Polyvinylpyrrolidone
R <sub>a</sub>	Resistance in ambient air or nitrogen environment
RF	Radiofrequency
R <sub>g</sub>	Resistance in test gas environment
Rh	Rhodium
RT	Room Temperature
SAED	Selected Area Electron Diffraction
sccm	Standard Cubic Centimeters per Minute
SiO <sub>2</sub>	Silicon dioxide
SMOGS	Single Metal Oxide Gas Sensors
Sn	Tin
SnCl <sub>2</sub> .2H <sub>2</sub> O	Tin(II) chloride dihydrate
SnO	Tin(II) oxide
SnO <sub>2</sub>	Tin oxide
SO <sub>x</sub>	Sulphur oxides
STEM	Scanning Transmission Electron Microscopy
TCO	Transparent Conducting Oxide
TEM	Transmission Electron Microscopy
TeO <sub>2</sub>	Tellurium dioxide
TiO <sub>2</sub>	Titanium dioxide
TMA	Trimethylamine
UV	Ultra-Violet
VLS	Vapor-Liquid-Solid
VS	Vapor-Solid
WO <sub>3</sub>	Tungsten trioxide
XRD	X-ray Diffraction
Zn	Zinc

$\text{Zn}(\text{Ac})_2$	Zinc acetate
$\text{Zn}(\text{CH}_3\text{CO}_2)_2$ ,	Zinc acetate
$\text{Zn}_2\text{SnO}_4$	Zinc stannate
$\text{ZnCl}_2$	Zinc chloride
$\text{ZnCO}_3$	Zinc carbonate
$\text{ZnNO}_3$	Zinc nitrate
$\text{ZnO}$	Zinc oxide
$(\text{Zn}(\text{C}_2\text{H}_5)_2$	Diethylzinc
ZTO	Zinc stannate

# CHAPTER 1

## INTRODUCTION

### 1.1 Background

Solid-state resistive-type single metal oxide gas sensors (SMOGS) have been widely used in applications ranging from health and safety (Barreca *et al.*, 2007; Comini *et al.*, 2002; Kim *et al.*, 2007b; Zampiceni *et al.*, 2003; Zhang & Zhang, 2008a) to energy efficiency and emission control in combustion processes (Comini *et al.*, 2001; Zhu *et al.*, 1996). These sensors are attractive because of their high sensitivity, low cost, compatibility and simplicity with modern electronic devices. SMOGS are typically designed to be compact in size, portable and able to integrate easily with the environment in gas sensing applications (Miller *et al.*, 2014). Until now, several metal oxides including  $\text{TiO}_2$ ,  $\text{In}_2\text{O}_3$ ,  $\text{WO}_3$ ,  $\text{ZnO}$ ,  $\text{TeO}_2$ ,  $\text{CuO}$ ,  $\text{SnO}_2$  and  $\text{NiO}$  are used in resistive-type SMOGS (Arafat *et al.*, 2012). However, resistive-type SMOGS generally have the disadvantage of poor selectivity between gases, low sensitivity and high operating temperature (Arafat *et al.*, 2014).

Several approaches have been used to improve the sensitivity and selectivity of these single metal oxides (Yamazoe, 2005). These include addition of noble metals (Kim *et al.*, 2011; Penza *et al.*, 2009; Shen *et al.*, 2014; Yang *et al.*, 2010), doping of metal oxide catalyst (Nanto *et al.*, 1996; Qi *et al.*, 2008), developing composite metal oxides consisting of binary or ternary phase metal oxide systems (Tang *et al.*, 2006b; Yu & Choi, 2001), and development of nanostructures with different morphologies (Khoang *et al.*, 2012a; Xu *et al.*, 2013; Zhang *et al.*, 2012; Zhang *et al.*, 2009). Among the approaches used, tailoring of composite metal oxides with different morphologies presents a good potential for tuning the sensitivity and selectivity during gas sensing.

Many recent studies have shown that the selectivity and operating temperature of resistive-type metal oxide gas sensors can be improved through the use of composite metal oxides (Chen *et al.*, 2008; Choi *et al.*, 2013; Kim *et al.*, 2007a; Zhu *et al.*, 2009). Nano-heterostructure is one of the ways to improve the sensitivity of composite metal oxides. A heterojunction is often referred to as the physical interface between two different materials, and the material including these two constituents is known as a heterostructure. The Fermi levels across the interface can equilibrate to the same energy by creating electrical contact at the interface between two different semiconducting materials (Chen *et al.*, 2011). Charge transfer at the interface between two dissimilar materials results in the formation of a charge depletion layer. This is the basis for unique effects that can lead to increased sensor performance (Miller *et al.*, 2014). Further, variation can happen by having two different materials in close vicinity when exposed to the gas due to synergistic reaction. Synergistic reaction is referred to as when the gas may react with one material most freely, and this reaction by-product may react with the second material in order to complete the reaction (Wang *et al.*, 2010). Nano-heterostructures are often used in gas sensors because their small dimensions and high surface-to-volume ratios increase the sensing performance (Choi *et al.*, 2013). Some other factors also attributed to the improvements in sensing performance of these metal oxide composites. It includes band bending due to Fermi level equilibration (Kusior *et al.*, 2012), depletion layer manipulation (Wang *et al.*, 2012), increased interfacial potential barrier energy (Wang *et al.*, 2010), decrease in activation energy (Gu *et al.*, 2012), charge carrier separation (Yu *et al.*, 2012), targeted catalytic activity (Rumyantseva *et al.*, 2006) and synergistic surface reactions (de Lacy Costello *et al.*, 2003) and geometrical effects such as grain refinement (Chen *et al.*, 2006) and surface area enhancement (Liangyuan *et al.*, 2008). The control the sensing behaviour of these heterostructures is essential in this field for understanding the mechanism.

Among the metal oxide used, ZnO and SnO<sub>2</sub> are wide band gap n-type semiconductor materials. According to the literature, ZnO/SnO<sub>2</sub> based nanostructures have been mostly synthesized by two-step fabrication process (Cheng *et al.*, 2009; Pan *et al.*, 2012; Park *et al.*, 2013a), and extensively used in various applications such as, transparent electrode, photovoltaic, light emitting diodes, field emission transistor and energy harvesting due to their great potential properties (Özgür *et al.*, 2005). Stoichiometric nature of each varies significantly. Generally SnO<sub>2</sub> is highly stoichiometric, while ZnO has defects in structure (Demir-Cakan *et al.*, 2008). Due to this behaviour, chemisorption of oxygen is high on ZnO than on SnO<sub>2</sub>, and SnO<sub>2</sub> enhances the desorption process in gas sensing performance by transferring electron from SnO<sub>2</sub> to ZnO (Lu *et al.*, 2012; Park *et al.*, 2013a).

Monitoring volatile organic compounds is a growing need in many industries due to possible health and safety concerns (Wang *et al.*, 2007). In numerous applications, ethanol sensors are being used to monitor chemical reactions, biomedical productions, quality control of foods, and breath analysis (Andrei Kolmakov *et al.*, 2003; Timmer *et al.*, 2005). Increased usage of ethanol raises concerns over groundwater pollution (Freitas *et al.*, 2010) and explosion hazards (Powers *et al.*, 2001). Thermodynamic analysis shows that ethanol reforms to methane at moderate temperatures, while hydrogen and carbon monoxide rich gases are formed at high temperatures (400-700 °C) (Fishtik *et al.*, 2000; Galvita *et al.*, 2001; Vasudeva *et al.*, 1996). For this reason, the need for selective sensing of ethanol at high temperatures in presence of hydrogen, carbonmonoxide and methane is important. Thus, this thesis contributes the single-step process of ZnO and SnO<sub>2</sub> based nanostructures for gas sensing applications.

## 1.2 Research Objectives

The objectives of this research are listed as below:

- (1) To study the growth of zinc oxide (ZnO) and tin oxide (SnO<sub>2</sub>) based nanostructures via a single-step carbon assisted thermal evaporation process.
- (2) To investigate the structural, optical and gas sensing properties of the zinc oxide and tin oxide based nanostructures.
- (3) To fabricate gas sensors based on zinc oxide and tin oxide nanostructures.
- (4) To evaluate the performance of nanostructures based gas sensors for several target gases.

## 1.3 Scope of Research

The overall scope of this research is to prepare ZnO and SnO<sub>2</sub> based nanostructures by a single-step process and fabricate gas sensors with high sensitivity and selectivity towards ethanol. Mechanism for nanostructures growth and sensing mechanism for gas sensors based on nanostructures are proposed.

Numerous analytical techniques were used to characterize the nanostructures. The data obtained from this research work were also analysed and compared with other published work. The phase, microstructure and elemental composition of nanostructures were investigated by X-ray diffractometer, field emission scanning electron microscopy and transmission electron microscopy equipped with energy dispersive X-ray spectroscopy. The crystalline quality of the nanostructures was analysed by photoluminescence spectroscopy. The fabricated Zn<sub>2</sub>SnO<sub>4</sub> nanowire and SnO<sub>2</sub>-core/ZnO-shell nanostructure-based gas sensors were tested for various reducing gas environment.

## 1.4 Organization of Thesis

This thesis is arranged in the following order. In Chapter 1, a brief introduction to this research work is provided. This chapter states the background of the metal oxide nanostructures and their synthesis, gas sensing properties of metal oxide nanostructures, the current technical problems in this field, research objectives and the scope of this research.

In Chapter 2, a comprehensive overview of the existing literature on various topics related to this research is provided. The topics discussed include the properties of ZnO, SnO<sub>2</sub> and Zn<sub>2</sub>SnO<sub>4</sub>, chemical gas sensing, sensing parameters, sensor designs, limitations of pristine metal oxide sensors, mixed metal oxide sensing materials and fabrication methods, thermodynamics and phase equilibriums of ZnO, SnO<sub>2</sub> systems.

In Chapter 3, the synthesis process of ZnO-SnO<sub>2</sub> based nanostructures by using single-step carbon-assisted thermal evaporation process is described. It includes the preparation of raw materials, procedures for substrate preparations, characterization techniques, process of sensor fabrication, and procedure for sensor measurements used in this research.

In Chapter 4, the results obtained from the experimental work by varying growth time, mass ratio of source mixture, temperature and deposition position are discussed. Gas sensing properties of volatile organic compound (ethanol), hazardous gas (CO) and other environment gases (H<sub>2</sub>, CH<sub>4</sub>) are also described. The obtained results are analysed and compared with the other published literature. The growth mechanism of nanostructures as well as suggested sensing mechanism is also proposed.

In Chapter 5, the summary of the research findings are given through the synthesis process and gas sensing properties. The recommendation of the future works is also outlined.

## **CHAPTER 2**

### **LITERATURE REVIEW**

This chapter explains the properties of zinc oxide and tin oxide based nanostructures, type of gas sensors and principle of operation of gas sensor. This chapter also reviews previous work in gas sensors based on ZnO-SnO<sub>2</sub> and Zn<sub>2</sub>SnO<sub>4</sub> nanostructures in particular.

#### **2.1 Metal Oxide Nanostructures and Their Applications**

With the continuous advancement of metal oxide and semiconductor nanostructures, a series of techniques have been developed to fabricate various functional oxides (ZnO, SnO<sub>2</sub>, In<sub>2</sub>O<sub>3</sub>, CuO and TiO<sub>2</sub>) based nanostructures. These techniques range from solution phase approach to vapour phase approach. These methods lead to design of various nanostructures from thin film, thick film, nanoparticles and one dimensional nanostructures followed by hierarchical nanostructures. Recently, one dimensional nanostructures and hierarchical nanostructures have attracted considerable interests than thick and thin film due to their potential applications in various fields and increased surface area of nanostructures. These nanostructures have been used in energy, environmental and sensing sectors in advanced nanodevices and nanosystems. This section mainly focuses on past literature related to SnO<sub>2</sub> and ZnO based nanostructures for gas sensing.

#### **2.2 Nanostructures Based on Zinc Oxide and Tin Oxide**

Both binary and ternary semiconductive metal oxides have been extensively researched for various application purposes. The most extensively studied photovoltaic and gas sensing materials are ZnO, SnO<sub>2</sub> and Zn<sub>2</sub>SnO<sub>4</sub>. These three metal oxides are under the



categories of transparent semiconducting materials (Wang *et al.*, 2004). Therefore, ZnO, SnO<sub>2</sub>, and Zn<sub>2</sub>SnO<sub>4</sub> exhibit similar semiconductor properties against various scenarios. The overview of the physical properties of the zinc and tin based oxide is illustrated in Table 2.1.

Table 2.1: Overview of the physical properties of the zinc and tin based oxides (Batzill & Diebold, 2005; Ellmer, 2001)

Property	ZnO	SnO <sub>2</sub>	Zn <sub>2</sub> SnO <sub>4</sub>
Mineral name	Zincite	Cassiterite	-
Crystal structure	Hexagonal, wurtzite	Tetragonal, rutile	Face centered cubic, inverse spinel
Space group	P6 <sub>3</sub> mc	P4 <sub>2</sub> mm	Fd3m
Lattice constants [nm]	a=0.325 c=0.5207	a=0.474 c=0.319	a=0.866
Density (gcm <sup>-3</sup> )	5.67	6.99	6.42
Melting point [°C]	2240	>1900	1550
Band gap (300 K) [eV]	3.37	3.6	3.6

### 2.2.1 Zinc Oxide (ZnO)

Zinc oxide is one of the important semiconductive metal oxide materials in the field of nanotechnology. It belongs to the class of transparent conductive oxide (TCO), similar to semiconductive compounds like In<sub>2</sub>O<sub>3</sub> and SnO<sub>2</sub> (Ellmer, 2001). It possesses a direct wide-bandgap of about 3.37 eV at room temperature (300 K) and a large exciton binding energy (60 meV) (Chen *et al.*, 2009; Norton *et al.*, 2004). It falls under the group of n-type II-VI semiconductor. Besides, it has a hexagonal wurtzite crystal structure. ZnO is a promising material for photonic applications in the UV or blue spectral range due to high exciton binding energy, which allows the emission of exciton at room temperature (Djurišić & Leung, 2006). ZnO displays multiple functions in electrical, piezoelectric and optical properties (Zhang *et al.*, 2005). One dimensional

ZnO nanostructures with a large surface area and quantum confinement effect has stimulated much attention (Chen *et al.*, 2009; Zhang *et al.*, 2009) owing to its potential applications in light emitting diodes (Guo *et al.*, 2008), solar cells (Zhang *et al.*, 2009), chemical sensors (Hsueh *et al.*, 2007a), catalysts (Bae *et al.*, 2009) and field effect transistors (Fan *et al.*, 2004).

It has also been suggested that ZnO exhibits sensitivity to various gas species, namely ethanol, acetylene, and carbon monoxide, which makes it suitable for sensing applications (Djurišić & Leung, 2006). Deep levels (DLs) affect the electrical and optical properties of ZnO, like other semiconductors. For example, resident and metallization-induced native defects were reported to severely degrade the potential barrier height of ZnO Schottky diodes. For optical applications of ZnO, DLs are responsible for the green luminescence (GL) of the obstacles for realizing ZnO light emitters (Ahn *et al.*, 2008). Moreover, its piezoelectric property makes it suitable for electromechanical sensor or actuator applications. It is also biocompatible which makes it suitable for biomedical applications.

ZnO have been so far extensively patterned through engineering designs into aligned arrays on various substrates in various forms and shapes (Qin *et al.*, 2008) such as thick films (Wagh *et al.*, 2006), thin films (Wöllenstein *et al.*, 2003), heterojunctions (Mridha & Basak, 2006), nanoparticles (Huang *et al.*, 2006) and nanowires (Wan *et al.*, 2004). A few decades ago, one dimensional ZnO nanostructures have become the focus point in nanoscience and nanotechnology. The attention is mainly attributed to the capability of ZnO nanotubes in UV radiation absorption due to transitions between conduction and valence bands (Bae *et al.*, 2009). Thus, ZnO is expected to perform as an excellent transparent conducting electrode in solar cells, flat panel displays, and as a window

material in antireflection coatings and optical filters. Recently, a variety of ZnO novel morphologies such as hierarchical nanostructures, bridge or nail-like nanostructures, tubular nanostructures, nanosheets, nanopropeller arrays, nanohelices, and nanorings have also been reported (Djurišić & Leung, 2006).

### **2.2.2 Tin Oxide (SnO<sub>2</sub>)**

Tin oxide is also one of the frequently used materials in the group of oxide material. It is an n-type semiconductor with a wide bandgap of 3.6 eV at 300 K (He Jr *et al.*, 2006). The typical crystal structure of SnO<sub>2</sub> is tetragonal rutile with stoichiometric form. It has low electrical resistance and high optical transparency in the visible region range of the electromagnetic spectrum (Batzill & Diebold, 2005). These properties are explored in a numerous applications; notably as transparent conductor, electrode materials in solar cell, oxidation catalyst, light emitting diodes, solid state gas sensor material and flat panel displays. Transparent in visible and highly reflective the infrared light properties of SnO<sub>2</sub> are used for the energy conserving. Therefore, SnO<sub>2</sub> is also focused as a main material (Batzill & Diebold, 2005).

Another important property of SnO<sub>2</sub> is high conductivity. Commonly binary TCO materials possess high conductivity due to its intrinsic defects including oxygen deficiencies. But, SnO<sub>2</sub> has stoichiometric structure, where stoichiometric forms a good insulator; while non-stoichiometry, in particularly oxygen deficiency, makes it a conductor. Conversely, Kılıç and Zunger (2002) reported that the formation energy of oxygen vacancies and tin interstitials in SnO<sub>2</sub> is very low. These defects form freely which explains the often observed high conductivity of pure SnO<sub>2</sub>. A charge carrier concentration and the conductivity of SnO<sub>2</sub> are further increased by using extrinsic dopants. Nowadays, numerous SnO<sub>2</sub> nanostructures including nanofibers (Viter *et al.*,

2014), nanowires (Zhou *et al.*, 2014), nanorods (Hu *et al.*, 2014), fishbone-like (Kim *et al.*, 2005), nanobox beam-like (Liu *et al.*, 2004), flower-like (Wang *et al.*, 2011) and hierarchical (Wang & Rogach, 2013) nanostructures have been developed in major applications of catalyst, gas sensors and TCO .

### **2.2.3 Zinc Stannate ( $\text{Zn}_2\text{SnO}_4$ )**

The zinc stannate compound,  $\text{Zn}_2\text{SnO}_4$  is categorized under ternary transparent semiconductive oxides. It exhibits versatile properties in a number of applications including humidity sensors, transparent electrode, flammable and toxic gas sensors, Li-ion batteries, and thin-film photovoltaic devices due to its large electron mobility ( $10 - 15 \text{ cm}^2 \text{ V}^{-1} \text{ s}^{-1}$ ), high electrical conductivity, high chemical sensitivity, low visible absorptions and excellent optical electronic properties (Rong *et al.*, 2006; Wang *et al.*, 2007). It possesses large band gap of 3.6 eV at 300 K with an inverse spinel structure (Tan *et al.*, 2007).  $\text{Zn}_2\text{SnO}_4$  is commonly referred to as ZTO or zinc orthostannate. It is the semiconductor group of II-IV-VI oxides. The ZTO composition is off stoichiometric with an element ratio of  $\text{Zn} : \text{Sn} : \text{O} = 1.75 : 1 : (2.6-3.5)$ , indicating a deficiency of zinc and oxygen (Fan *et al.*, 2009).

Recently, the studies on ZTO nanowires, nanodendrites raise even more interests on their predictable new electronic, optoelectronic, and sensing properties (Tan *et al.*, 2007). So far, ZTO quasi-1-D nanostructures including smooth belts, rings, chainlike single-crystal wires, twinned wires, and short rod are also demonstrated (Fan *et al.*, 2009). The twinned ZTO nanowires showed unique periodical morphologies with twins alternating along the axial direction of the nanowires, which are different from normal nanowires. These nanostructures are potentially useful in fabrication of nanodevices due

to the periodical axial arrangement of nanocrystals in one-dimension (Wang *et al.*, 2007).

### **2.3 Overview of Gas Sensors**

A gas sensor is defined as a device, which one or more of its physical properties such as resistance, capacitance, and electrical conductivity, changes upon its exposure towards gas species (Göpel *et al.*, 2008). A change of these properties can be measured and quantified directly or indirectly. A typical gas sensor consists of a sensing layer integrated with a transducing platform, which is in direct contact with the gas environment. Sensing layer should be thick/thin film or aligned one dimensional nanostructures of metal oxides. Gas molecules in a test gas environment interact chemically with the sensing layer, which result in a variation of the sensor's chemical or physical properties. Then, the transducer measures the changes and produces an electrical output signal (Stetter & Penrose, 2002). There are many different types of sensors using various technologies and principles, which can analyse the gas species qualitatively and quantitatively. These sensors should be able to offer accurate, high resolution, low cost sensing and stable. Several environmental factors including humidity, temperature, shock and vibrations can influence the performance of sensor. Therefore, it is crucial to account for these parameters when selecting a method.

#### **2.3.1 Solid State Gas Sensors**

Solid state gas sensors are based on a wide variety of technologies such as resistive-type metal-oxide, pyroelectric, piezoelectric, fibre optic, calorimetric and surface acoustic (Christofides & Mandelis, 1990). They have ability to sense both low ppm levels of toxic gases and high explosive limits. It can be classified into three categories depending on the sensing principles and sensor configuration. These categories are solid

electrolyte-based gas sensors, catalytic combustion, and resistive gas sensors based on semiconducting metal oxide (Azad *et al.*, 1992; Liu *et al.*, 2014).

#### **2.3.1.1 Solid Electrolyte Gas Sensors**

Potentiometric and amperometric gas sensors belong to the solid electrolyte-based sensor type. Such sensors generally function in the temperature range of 500-1300 °C (Azad *et al.*, 1992). For potentiometric sensor, solid electrolytes exhibit high ionic conductivity resulting from the migration of ions through the point defect sites in their lattices. Electronic conduction by electrons or holes only makes a small contribution (typically less than 1%) to the total conductivity in these sensors. The ionic transport number of a solid electrolyte is defined as the ratio between ionic conductivity and the total conductivity, which is normally greater than 0.99 (Park *et al.*, 2003). A potentiometric sensor operates under open-circuit conditions, in which no electrical current flows through the external electrical circuit, hence preventing ionic current from flowing through the electrolyte. Potentiometric sensors show logarithmic behaviour with the concentration of gas and low sensitivity at high concentrations (Liu *et al.*, 2014).

On the other hand, amperometric sensors can be operated under an externally applied voltage, which drives certain electrode reactions electrochemically. The sensor signal is usually a diffusion limited current with a diffusion barrier. Each analyte molecule passing the diffusion barrier reacts immediately at the electrode. But, the reaction rate reflected by the current at the sensing electrode occurs at a thermodynamically determined potential for any given reaction. When operated under appropriate diffusion-limited conditions, the sensor current is simply proportional to the concentration of the analyte. The linear relationship between current and concentration typically spans over

3 orders of magnitude. Measurements with high sensitivity to ppm or ppb level are achievable with excellent measurement accuracy under constant potential conditions. Amperometric sensors are more suitable for the detection of high gas concentrations (Liu *et al.*, 2014; Stetter & Li, 2008).

### **2.3.1.2 Catalytic Combustion Gas Sensors**

Catalytic combustion sensor is a single-port device, where the sensing material also acts as a heater. The sensor is fabricated by sintering porous, active alumina beads with certain amount of highly dispersed catalyst including Pt, Pd and Rh. Each bead is mounted on a platinum coil. When a combustible gas is admitted, it reacts with the catalyst and burns on the platinum coil, heated to about 400-450 °C by passing a current through it. The evolved heat of combustion of the gas results in further increase of temperature of the sensing element. Therefore, resistance of the sensing element is increased. The resistance increase is then correlated to the concentration of the inflammable gas (Arakawa *et al.*, 1979). The selection of platinum is due to excellent durability against high specific resistance with temperature increase. Thus, larger changes in resistance results than some other high melting metals such as Pd and Rh. These catalyst supported sensors are more sensitive to C<sub>4</sub>H<sub>10</sub> (butane) than to CH<sub>4</sub>, C<sub>2</sub>H<sub>5</sub>OH, CO and H<sub>2</sub>. Therefore this type of gas sensors are mostly used for the leak detection of LPG gas (Azad *et al.*, 1992).

### **2.3.1.3 Semiconductor Gas Sensors**

Among these three solid state gas sensors, semiconducting metal-oxide sensors have shown the most promising results especially in harsh and high temperature environments. They have shown extensive commercial applications and recent advances in nanotechnology has resulted in novel classes of materials with enhanced gas sensing

performance (Eranna *et al.*, 2004). These have provided the opportunity to dramatically increase the performances of semiconducting metal-oxide gas sensors. Resistor-type sensors are commonly used in semiconducting metal oxides based gas sensor. It possesses advantages such as simple configuration, easy fabrication, cost effectiveness and also offer advances in miniaturization and micro-electronic mechanical system (MEMS) (Ramamoorthy *et al.*, 2003). Resistor-type sensors measure electrical resistance changes in the semiconducting oxide caused by the interaction of the sensing material and test gas, which typically involves electron transfers. It has been long known that adsorption of a foreign species on a semiconducting surface provides surface states, and the electrical properties of these surfaces change as a result of adsorption and/or reaction. Significant progress has been made to utilize this change in the semiconductor property to quantify the presence of a specific reactive gas in a gaseous mixture. As compared to the organic and elemental or compound semiconductors, the metal oxide counterparts have been more successfully employed as sensing devices for the detection and monitoring of a host of gases such as CO, CO<sub>2</sub>, H<sub>2</sub>, H<sub>2</sub>O, NH<sub>3</sub>, SO<sub>x</sub> with varying degree of commercial success (Park & Akbar, 2003).

Semiconducting metal oxide-based sensors can be divided into three groups based on the interactions that occur between the sensing element and test gas. They are bulk conduction-based sensors, surface conduction-based sensors and metal/oxide junction based sensors. Bulk conduction-based sensors are used to detect oxygen at high temperatures (above 500 °C). But, surface conduction-based sensors are reported to show good sensitivity towards reducing gases including CO, H<sub>2</sub> and hydrocarbons, which is commonly detect at low and medium temperatures (200 - 500 °C). Metal/oxide junction based sensors work based on relative changes of work function. It includes



Schottky diodes, metal oxide-semiconductor capacitors and metal oxide-semiconductor field effect transistors (MOSFET) (Park & Akbar, 2003).

### **2.3.2 Gas Sensor Performance Characteristics**

In order to characterize the quality of the output signal produced by a sensor, some specific parameters are generally used. The most important parameters are sensitivity, selectivity, response time and recover time (Bochenkov & Sergeev, 2010). Enhanced sensitivity and selectivity together with reduced response and recover times are the main challenges to the developers of metal oxide gas sensors. These concepts will be elaborated further in this section.

#### **2.3.2.1 Sensitivity**

Sensitivity ( $S$ ) of a gas sensor towards a target gas is expressed as the ratio of the value of the measuring parameter at an ambient gas environment to that at the test gas environment. All over the literature, a sensor sensitivity is defined in several forms including  $S = R_a/R_g$ ,  $S = R_g/R_a$ ,  $S = \Delta R/R_a$  and  $S = \Delta R/R_g$ ; where  $R_a$  is the resistance in ambient air or nitrogen environment,  $R_g$  is the resistance in test gas environment and  $\Delta R = |R_a - R_g|$ . In the following, researchers use the terms “response” and “sensitivity” synonymously.

#### **2.3.2.2 Selectivity**

One of the main challenges to the developers of metal-oxide gas sensors is high selectivity. It is the ability of a sensor to respond to a certain gas in presence of other gases. Selectivity coefficient ( $K$ ) of a sensor is usually defined as by the ratio of the highest sensitivity related to the gas to be monitored and to the other testing gases at the same condition (Zhang *et al.*, 2011). Mathematically it can be expressed as follows:

$$K = \frac{S_{(highest\ sensitivity\ test\ gas)}}{S_{(test\ gas)}} \quad (2.1)$$

Currently, two general approaches exist for enhancing the selective properties of sensors. The first one is aimed at preparing a material that is specifically sensitive to one compound and has low or zero cross-sensitivity to other compounds that may be present in the working atmosphere (Bochenkov & Sergeev, 2010). To do this, the optimal temperature, doping elements, and their concentrations are investigated. However, it is usually very difficult to achieve an absolutely selective metal oxide gas sensor in practice, and most of the materials possess cross-sensitivity at least to humidity and other vapours or gases. Another approach is based on the preparation of materials for discrimination between several gases in a mixture. It is impossible to do this by using one sensor signal; therefore, it is usually done either by modulation of sensor temperature (Chakraborty *et al.*, 2006; Huang *et al.*, 2006; Nakata *et al.*, 2006; Parret *et al.*, 2006) or by using sensor arrays (Baschiroto *et al.*, 2008).

#### **2.3.2.3 Optimum Working Temperature**

Optimum working temperature is usually the temperature, where sensitivity of a gas sensor reaches a maximum value (Ahlers *et al.*, 2005). It depends on type of material and morphologies of nanostructures obtained by various processing routes.

#### **2.3.2.4 Response and Recovery Times**

It takes time for any sensor to produce its full response upon the exposure to a gas (Horn, 1995). There are several causes for that, the most important of which is the diffusion time of the gas inside the active material (Worsfold *et al.*, 2002). In order to establish the response speed of a sensor, which represents a primary topic in gas sensing field, response times are generally used. Response time is defined as the time to achieve a certain percentage of the final change in the sensor signal upon exposure to the test

gas. The most used parameter is  $t_{90}$ , defined as the time to achieve the 90% of the final change in the sensor signal. Similarly recovery time is the time to recover a certain percentage of the signal change after removal of test gas, where the most used parameter is  $t_{10}$ . These concepts are explained in the picture below.

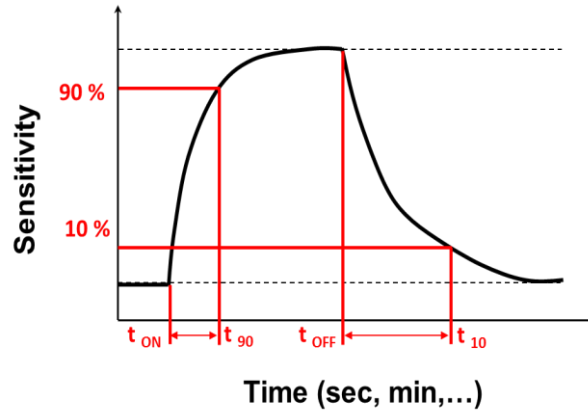


Figure 2.1: Explanation of the response time and recovery time in sensors.

#### 2.3.2.5 Lower Limit of Detection

It is the lowest concentration of the gas that can be detected by the sensor under given conditions, particularly at a given temperature. This can be referred to as detection limit or lower limit of detection (Bochenkov & Sergeev, 2010).

#### 2.3.3. Fabrication of Gas Sensor

In addition to the intrinsic characteristics of sensing material, the sensing properties also relies on morphology which is turn depend on sensor fabrication method. The sensor fabrication can be classified into four categories. They are bulk sensors, interdigitated substrate based sensors, tube-type sensors, and field effect transistor (FET) type sensors. In bulk sensor, powder materials are pressed into pellet form by die-pressing. Then, the flat surface of the pellet is painted by Pt or Au paste for the electrodes to measure the electrical variations. This type of sensor has the thickness of around 1-3 mm (Yu & Choi, 2001), which is shown in Figure 2.2(a). The second and most widely used sensors

are interdigitated substrate based sensors. It consists of embedded Au or Pt interdigitated in an alumina substrate. Pt or Au wires are attached to electrodes for making electrical contacts and monitor the variation of resistance. Sometimes, this sensor has embedded Pt heater on its back side (Wan *et al.*, 2004). This type of sensor can be designed by thin film or thick film. 1-D nanostructures typically make a paste or ink using organic binder to form thick or thin film on interdigitated substrate using screen-printing technique. In some cases, nanowire growth is integrated into device fabrication (Choi *et al.*, 2008; Hsueh *et al.*, 2007a). This type of sensor is shown in Figure 2.2(b).

Third type of sensor is tube sensors which are just one variation from interdigitated substrate based sensors. The shape of the sensor surface is tube instead of flat surface, which is shown in Figure 2.2(c). It has a ceramic tube which acts as a substrate and is made by  $\text{Al}_2\text{O}_3$  material. The surface of the tube is coated by the one dimensional gas sensor materials with different morphologies and form thick film with the thickness around  $150\text{ }\mu\text{m}$  (Lu *et al.*, 2012). It is typically coated between pair of gold electrodes printed on the surface of the ceramic tube. A Ni-Cr alloy is commonly used as a heating coil which is inserted into the tube to tune the operating temperature (Song *et al.*, 2009). The last category is the FET type sensor. A single nanowire is connected between the two metal electrodes in this type of sensor. These metal electrodes arrange on a heavily doped silicon substrate covered with  $\text{SiO}_2$  acting as insulating layer. The electrical changes measure between two electrodes which act as source and drain of FET type sensor (Huang & Wan, 2009). This kind of sensor is illustrated in Figure 2.2(d). Among them, interdigitated substrate based sensors and tube-type sensors were extensively studied in the literatures.

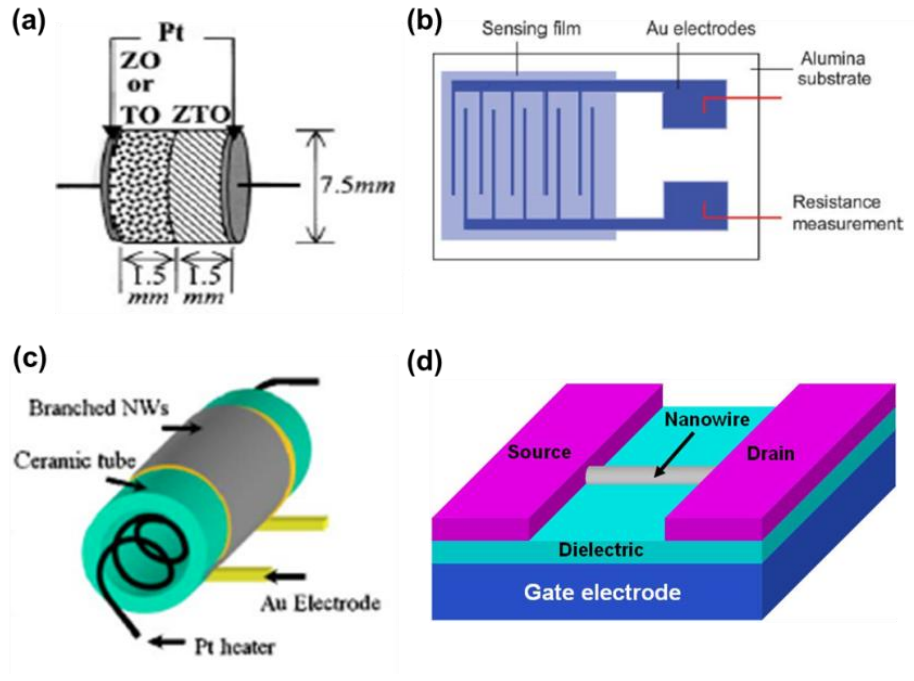


Figure 2.2: Schematic illustration of fabricated sensor device: (a) bulk sensor (Yu & Choi, 2001), (b) interdigitated substrate based sensor (Jiménez-Cadena *et al.*, 2007), (c) tube-type sensor (Wan *et al.*, 2008b), and (d) FET type sensor (Huang & Wan, 2009).

## 2.4 Metal Oxide Semiconductor Material for Gas Sensing

Metal oxides semiconductors are utilized for recent developments in gas sensing materials. It is known that the electrical conductivity of such materials varies with the composition of the surrounding gas atmosphere (Elisabetta Comini, 2006). At the beginning of the sensor technology, semiconductor metal oxides have been studied in the form of thick film. First generation devices were developed using powders as starting material and formed thick films. In 1991, Yamazoe (1991) reported that the improvement in sensor performance of metal oxide semiconductor film was due to the reduction of grain size. The main challenge lies on the preparation of materials with stable and smaller crystalline size for long time when the sensor operated at high temperature. Thus, the materials syntheses have been improved towards thin film technology to overcome the challenge. In thin film technology, higher reproducibility and compatibility with Si technology was obtained by fabrication of materials via chemical and physical vapour deposition. But, the technological enhancement went

along with a reduction of sensing performances due to a lower porosity of the fabricated devices. The electrical properties of both thick and thin films drift due to porosity modification, grain coalescence and grain boundary alteration. These effects are more critical because the metal oxide layers must be kept at a fairly high temperature in order to guarantee the reversibility of chemical reactions at surface (Eranna *et al.*, 2004). Hence, one of the solutions has been identified to stabilize the nanostructure, which is a one-dimensional (1D) nanostructure (nanowires, nanotubes, nanobelts, nanorods and so on). Therefore, thin film technology was turned towards 1D nanostructures. A wide number of metal oxide semiconductors such as  $\text{MoO}_3$ ,  $\text{ZnO}$ ,  $\text{CuO}$ ,  $\text{TiO}_2$ ,  $\text{SnO}_2$ ,  $\text{In}_2\text{O}_3$ ,  $\text{CdO}$ ,  $\text{AgVO}_3$ ,  $\text{WO}_x$ ,  $\text{TeO}_2$  and  $\text{Fe}_2\text{O}_3$  have been studied for chemical gas sensing applications (Arafat *et al.*, 2012). However, one dimensional metal oxide nanostructures have high aspect ratio, thus sensing surface area is increased. As a result, today most sensing research works mainly focus towards 1-D nanostructures. Numerous reports reveal pristine 1D nanostructures exhibit better results in terms of high sensitivity to detect certain gases (Cao *et al.*, 2009; Rout *et al.*, 2006; Wan *et al.*, 2004) which is shown in Figure 2.3.

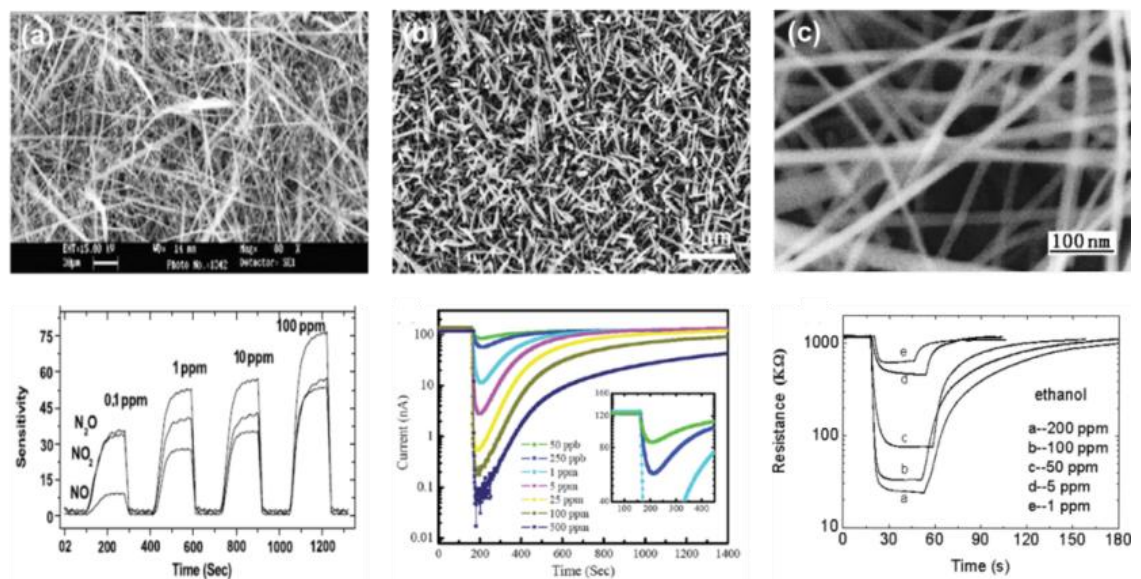


Figure 2.3: Pristine nanostructures for gas sensing: (a)  $\text{In}_2\text{O}_3$  nanowires for  $\text{N}_2\text{O}$  detection (Rout *et al.*, 2006), (b)  $\text{WO}_3$  nanowires for  $\text{NO}_2$  detection (Cao *et al.*, 2009), and (c)  $\text{ZnO}$  nanowires for ethanol sensing (Wan *et al.*, 2004).

### 2.4.1 Gas Sensing Mechanism

The sensing mechanism of metal oxide gas sensor is essential to reveal the influence factors on gas sensing properties of metal oxides. The exact fundamental mechanisms that cause a gas response are still controversial (Wang *et al.*, 2010). But, the general mechanism of gas sensing is based on the change in conductance upon chemisorption of gas molecules. The electric response by chemicals adsorbed on metal oxide is strongly dependent on the reaction of molecules on the surface. Depending on the reducing or oxidizing properties of the molecules, conductance through nanowires can decrease or increase upon molecular adsorption. Thus, it is important to investigate surface reactions between metal oxide and target molecules for better understanding of the sensing mechanism and for finding optimum sensing conditions such as temperature.

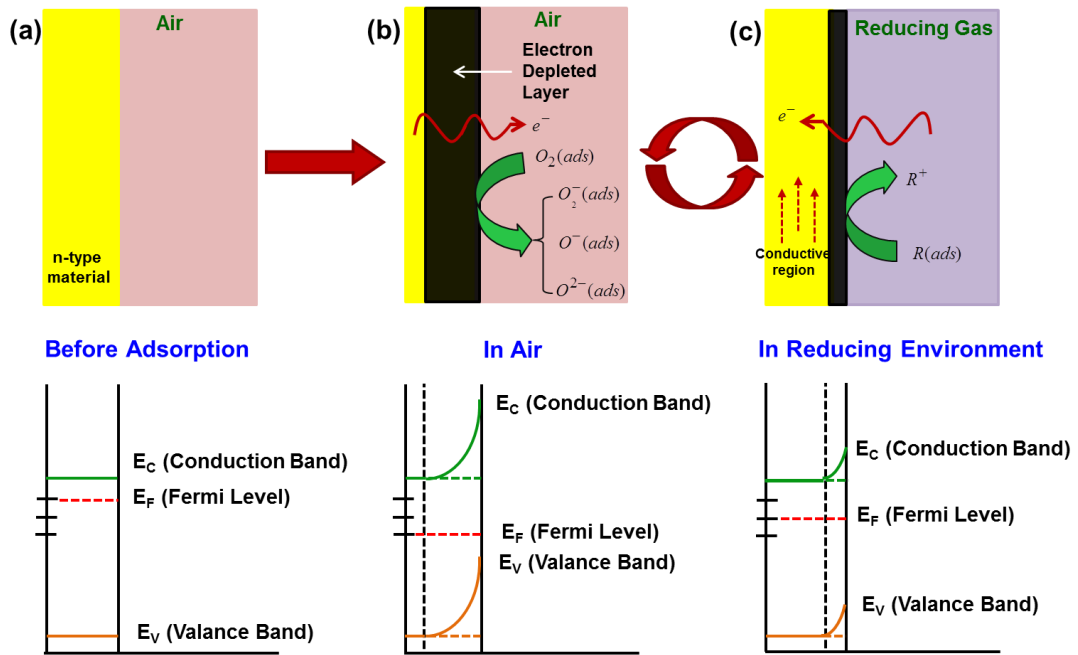


Figure 2.4: Sensing mechanism of reducing gas towards n-type sensing materials: (a) before adsorption of oxygen, (b) adsorption of oxygen in air environment and (c) adsorption of oxygen in reducing gas environment (Arafat *et al.*, 2014).

The basic sensing mechanism of semiconductor gas sensor is based on changes in conductivity or resistivity when the sensing materials interact with target test gases.

Oxygen molecules in ambient air are adsorbed on the sensing surface when the semiconducting metal oxides are exposed to air environment (Figure 2.4(a) and (b)). As a result, various kinds of oxygen ion species ( $O^-$ ,  $O_2^-$ ,  $O^{2-}$ ) are formed on the sensing surface by trapping free electrons from the conduction of the sensing material. Therefore, electron depleted layer is formed at the surface of the material. Due to the formation of electron depleted region leads to the band bending (Figure 2.4(b)). When the reducing gas is exposed, it reacts with surface adsorbed oxygen species and released the captured electrons in the materials. Therefore, resistance of the material reduces and decreases the band bending due to increased free electrons on the material (Figure 2.4(c)). This kind of electrical changes is used for gas sensing applications (Wang *et al.*, 2010).

The band bending theory is unfortunately not a universal mechanism that applies to all metal oxide solid materials. Many transparent conductive oxide materials like  $In_2O_3$ , ZnO and  $SnO_2$  are excellent gas sensing materials. The adsorbate induced band bending has the potential to result in strong conductivity changes in the material and thus trigger a gas response signal. In polycrystalline gas sensing materials, band bending related effect at the surface often contributes and amplifies the gas sensing response. This effect is due to the formation of Schottky barriers at grain boundaries. Upward band bending induced by surface charges result in a barrier that conduction electrons have to overcome to carry the current across the grain boundary (Batzill & Diebold, 2005).

#### **2.4.2 Factors Influencing the Enhanced Sensitivity and Selectivity**

As mentioned earlier, those pristine nanostructures sensors exhibit low sensitivity with less selectivity. As a result, research activities in these directions develop a great enhancement of performance of semiconducting materials in gas-sensing applications



by using various techniques. They are development of nanostructures with different morphologies, doping metal oxide catalyst, loading noble metal nanoparticles and mixed metal oxide nanostructures (Arafat *et al.*, 2012).

#### **2.4.2.1 Development of Nanostructures with Different Morphologies**

Processing of various kinds of nanostructure is one of the ways to enhance sensitivity in gas sensor application. A lot of research on nanomaterials has been carried out in recent years. However, there is still a lack of nanostructures that have a combination of superior properties such as efficient electron transport and high surface area (Agarwala *et al.*, 2012). Therefore, the focus in this field is on the development of nanostructures with different morphology. Such nanostructures are expected to exhibit both superior electron transport and high surface area, which leads to an increase in sensitivity of chemical gas sensors. Several unique morphologies of pristine metal oxide structures and their gas sensing properties have been reported as shown in Figure 2.5. With an ammonia ( $\text{NH}_3$ ) concentration of 5 ppm, the sensor constructed with rhombohedral corundum-type  $\text{In}_2\text{O}_3$  hierarchical nanostructures showed 10-folds enhanced sensitivity with a working temperature of 300 °C, compared to the sensors prepared from cubic  $\text{In}_2\text{O}_3$  nanoparticle (Jiang *et al.*, 2013) (Figure 2.5 (a)). Zhang *et al.* (2008) developed high performance gas sensors based on ZnO dendrites with excellent sensitivity and selectivity to  $\text{H}_2\text{S}$  gas at room temperature (Figure 2.5 (b)). The origin of the greater sensitivity was demonstrated that the macroscopical appearance and properties of ZnO dendrites. Additionally, the large modulation of the energy barrier of contact between nanorods in ZnO dendrites is also another reason for increased sensitivity. Figure 2.5(c) shows a unique 3D architecture with a relatively high surface area of  $\alpha\text{-Fe}_2\text{O}_3$  nanoflower provides excellent hydrogen gas sensing behaviour (7.1 at 50 ppm) at room temperature due to increased active sites for interaction of hydrogen gas (Agarwala *et*

*al.*, 2012). Hence, development of nanostructures with increased surface area is one of the techniques to get excellent sensitivity in chemical gas sensors.

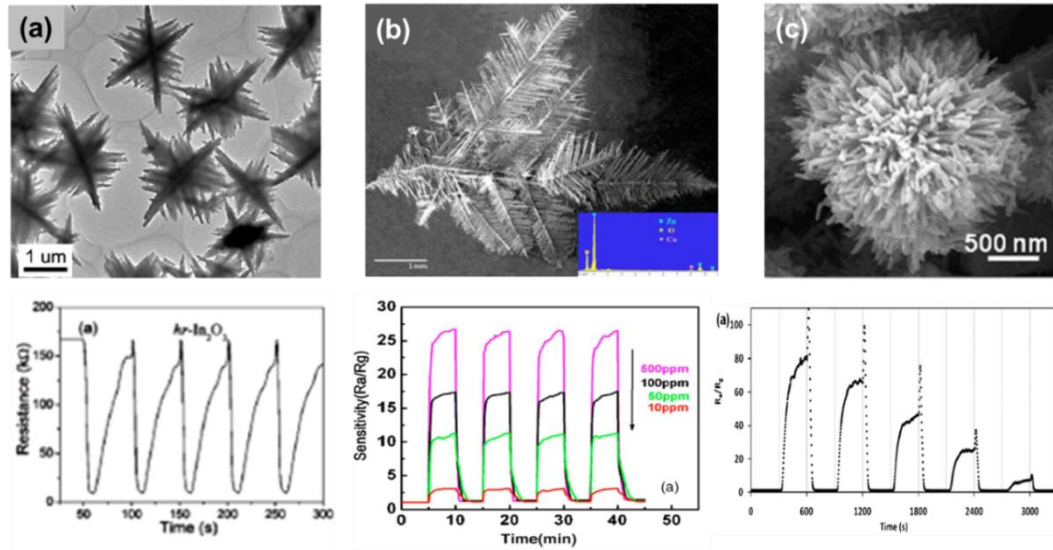


Figure 2.5: Various morphologies nanostructures for gas sensing: (a) hierarchical  $\text{In}_2\text{O}_3$  nanostructure (Jiang *et al.*, 2013), (b) ZnO dendrite nanostructure (Zhang *et al.*, 2008), and (c)  $\alpha\text{-Fe}_2\text{O}_3$  flower-like nanostructure (Agarwala *et al.*, 2012).

#### 2.4.2.2 Doping of Metal Oxide Catalyst

Another way to improve sensitivity is through doping of metal oxide nanoparticles, where a host material is loaded with certain amount of metal oxide particles such as (PdO,  $\text{Cr}_2\text{O}_3$ , NiO,  $\text{Co}_3\text{O}_4$  and CuO). These doped metal oxide particles often act as catalyst to enhance performance. However, the doped metal oxide particles are not suitable to be present as the host nanostructure due to instability, synthesis route or conductivity issues (Miller *et al.*, 2014). Therefore, low or discrete amounts ( $< 2\text{wt}\%$ ) of doped particles must be applied in order to achieve desired results (Kim *et al.*, 2011). It has been proved by authors with great success, which is revealed in Figure 2.6. Lou *et al.* (2013) reported PdO-decorated ZnO flower-like nanostructures sensor showed improved sensitivity to ethanol and toluene which could be selected by the operating temperature (Figure 2.6(a)). Na *et al.* (2011) demonstrated that the lenticular p-type  $\text{Co}_3\text{O}_4$  nanoislands decorated on ZnO nanowire showed enhanced sensitivity toward

ethanol (Figure 2.6(b)). Woo *et al.* (2012) found that the addition of semielliptical  $\text{Cr}_2\text{O}_3$  nanoparticles on ZnO nanowires sensor exhibited enhanced sensitivity toward trimethylamine (TMA) (Figure 2.6(c)). The increased sensitivity of sensor decorated by  $\text{Co}_3\text{O}_4$  and  $\text{Cr}_2\text{O}_3$  than pristine nanostructure sensor was explained by catalytic effect of addition of nanoparticles and extension of electron depletion layer via the formation of p-n junction.

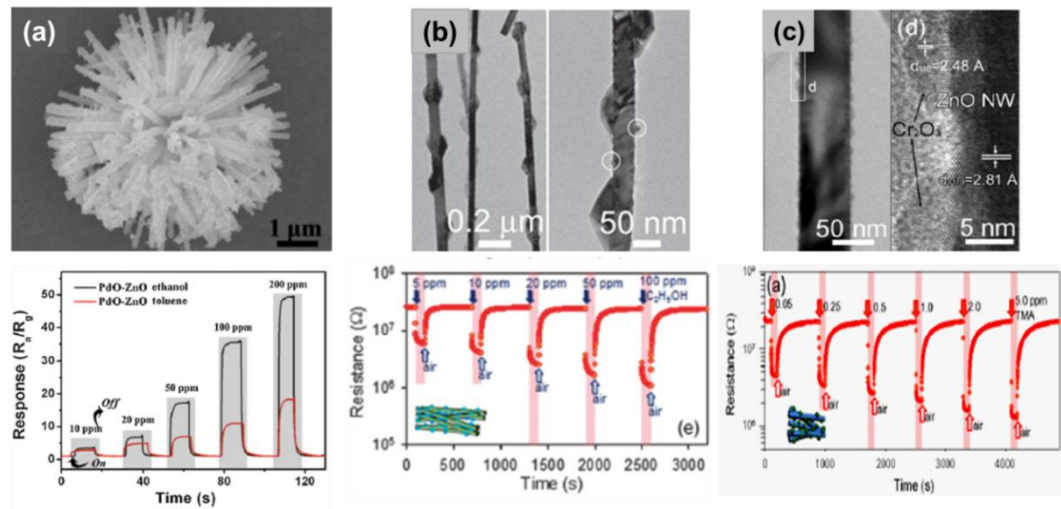


Figure 2.6: Doping of metal oxide catalyst for gas sensing: (a) PbO nanoparticle decorated on ZnO flower-like nanostructure (Lou *et al.*, 2013), (b)  $\text{Co}_3\text{O}_4$  nanoisland decorated on ZnO nanowires (Na *et al.*, 2011), and (c)  $\text{Cr}_2\text{O}_3$  nanoparticle decorated on ZnO nanowire (Woo *et al.*, 2012).

#### 2.4.2.3 Surface Modification by Noble Metal Particles

Noble metal nanoparticles such as Pt, Pd, Au, Rh, Ag can be decorated onto the surface of nanostructures to enhance the sensitivity of the sensor (Ippolito *et al.*, 2005). The sensitivity can be improved significantly in surface modified noble metal particles by means of spill-over effect or catalytic effect (Franke *et al.*, 2006). The metal catalysts create enhanced sites for gas molecular adsorption on the surface of sensing medium. Therefore, the presence of catalyst lowers the activation energy required for the sensing reaction to take place and improve the sensor performance (Lee *et al.*, 2009). Another way is the spill-over of gaseous species induced by metallic clusters at the surface of the

metal oxide or a Fermi energy controlled induced by metal dopants (Kappler *et al.*, 1998). These two effects are commonly proposed by authors to improve the sensing by adding noble metal particles.

Generally, the addition of noble metals results in a shift of the volcano-shaped correlation between gas sensitivity and temperature toward the lower temperature side, accompanied by an increase in the height of volcano top. These metal additive affect the sensor properties in a quite complex manner (Yamazoe *et al.*, 2003). As an example, noble metals such as Au, Pt and Pd were found to be efficient for increasing the sensitivity to NO<sub>2</sub> gas using ZnO nanowires (Rai *et al.*, 2012), to H<sub>2</sub> gas using WO<sub>3</sub> nanowires (Zhu *et al.*, 2010), and SnO<sub>2</sub> nanowires (Kolmakov *et al.*, 2005), respectively, which is illustrated in Figure 2.7. However, in real-life applications, such noble materials require very high cost to synthesis so that, the sensor price can be high. Another drawback of this method is the instability issues, including catalyst poisoning due to activity reduction from certain vapours and tendencies to roughen and cluster at elevated operating temperature (Miller *et al.*, 2014).

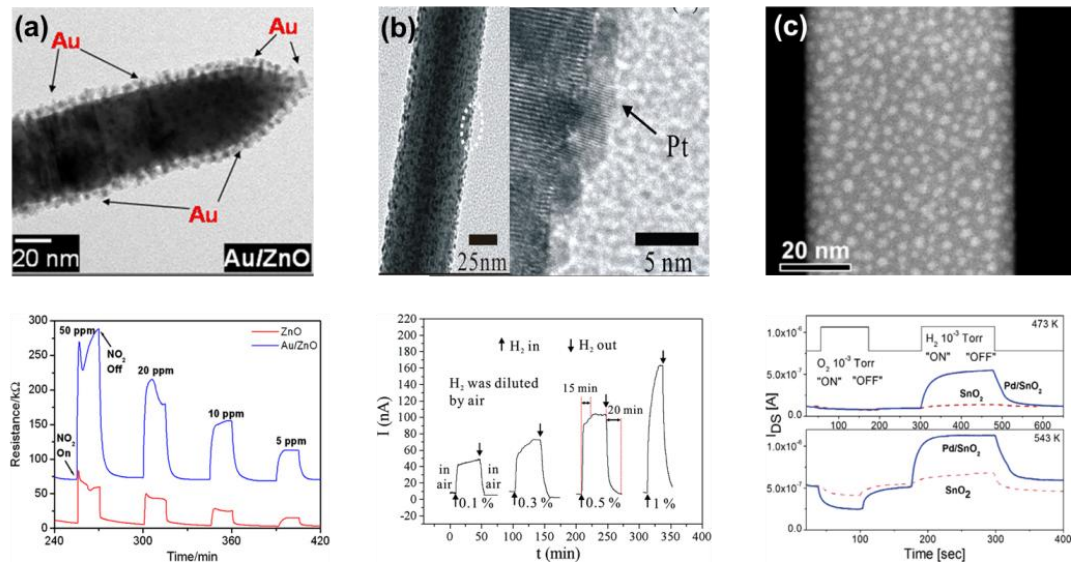


Figure 2.7: Surface modification using noble metal nanoparticles for gas sensing: (a) Au nanoparticle decorated on ZnO nanowires (Rai *et al.*, 2012), (b) Pt nanoparticle decorated on WO<sub>3</sub> nanowires (Zhu *et al.*, 2010), and (c) Pd nanoparticle decorated on SnO<sub>2</sub> nanowires (Kolmakov *et al.*, 2005).

#### 2.4.2.4 Mixed Metal Oxide Nanostructures

In recent years, mixed metal oxide nanostructures as gas sensors have become popular research topics. As an alternative to the noble metal oxide coating, mixed metal oxide nanostructures can provide good sensing performance with lower price compared with noble materials. Generally, hybrid nanostructure based gas sensors can be made by using nanowires or nanoribbons as base material and coating distributed nanoparticles or smaller nanostructures on the base materials, creating core-shell or branch-like structures. This hybrid nanostructure with different morphologies is another potential way to improve the sensitivity by increasing surface area of the nanostructures and band gap offset between different metal oxides. As further expectation, the hybrid nanostructures can be listed as a new class of nanomaterials with different properties. To date,  $\text{SnO}_2/\text{In}_2\text{O}_3$  (Her *et al.*, 2012),  $\alpha\text{-Fe}_2\text{O}_3/\text{SnO}_2$  (Wang *et al.*, 2014; Yu-Jin *et al.*, 2009; Zhang *et al.*, 2013),  $\text{TiO}_2/\text{ZnO}$  (Park *et al.*, 2009; Park *et al.*, 2013) (Deng *et al.*, 2013), multi-walled CNT/ $\text{SnO}_2$  (Chen, *et al.*, 2006),  $\text{ZnO}/\text{SnO}_2$  (Choi *et al.*, 2009; Hwang *et al.*, 2010a; Park *et al.*, 2013b),  $\text{CeO}_2/\text{TiO}_2$  (Chen *et al.*, 2011a),  $\text{W}_{18}\text{O}_{49}/\text{SnO}_2$  (Sen *et al.*, 2010),  $\text{Fe}_2\text{O}_3/\text{ZnO}$  (Jun *et al.*, 2011; Si *et al.*, 2006),  $\text{MoO}_3/\text{TiO}_2$  (Chen *et al.*, 2011b), and  $\text{Fe}_2\text{O}_3/\text{TiO}_2$  (Zhu *et al.*, 2012) hybrid nanostructures have been investigated for gas sensing.

Figure 2.8 shows the  $\text{ZnO}/\text{TiO}_2$  (Deng *et al.*, 2013),  $\text{W}_{18}\text{O}_{49}/\text{SnO}_2$  (Sen *et al.*, 2010) and  $\text{SnO}_2/\text{In}_2\text{O}_3$  hierarchical nanostructures (Her *et al.*, 2012) for gas sensing. Researches, as displayed in Figure 2.8, explained that sensitivity and/or selectivity of sensor was enhanced by combining two different oxide semiconductors which was due to modulation of energy band bending and built-in potential. (Deng *et al.*, 2013; Her *et al.*, 2012; Sen *et al.*, 2010). Because of two oxide semiconductors have different band gaps, electron affinities and work functions.

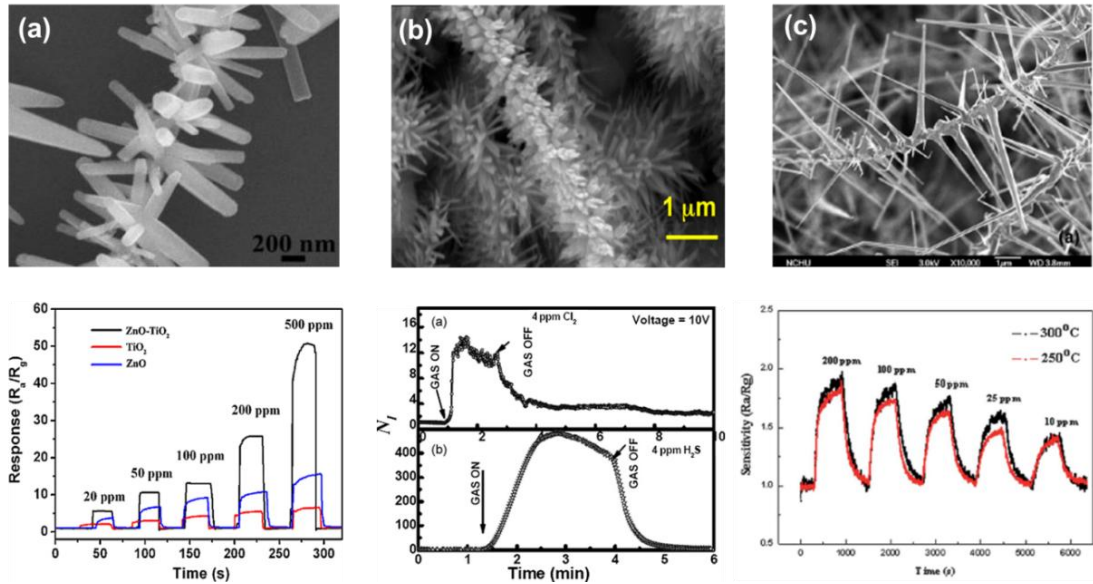


Figure 2.8: Mixed nanostructures for gas sensing application: (a) ZnO/TiO<sub>2</sub> hierarchical nanostructure (Deng *et al.*, 2013), (b) W<sub>18</sub>O<sub>49</sub>/SnO<sub>2</sub> nanowires (Sen *et al.*, 2010), and (c) SnO<sub>2</sub>/In<sub>2</sub>O<sub>3</sub> hierarchical nanostructure (Her *et al.*, 2012).

## 2.5 Gas Sensors based on ZnO/SnO<sub>2</sub> Nanostructures

### 2.5.1 Growth and Characterization

In this section, different types of ZnO/SnO<sub>2</sub> nanostructures are discussed in terms of their growth and characterization. Available reports in the literature show that ZnO and SnO<sub>2</sub> mixed nanostructures were grown via various synthesis techniques. It can be categorized into two groups according to their processing routes. They are single-step process and two-step process. A single-step process is ZnO and SnO<sub>2</sub> blended nanostructures grown via a particular single synthesis route. While two-step process is ZnO or SnO<sub>2</sub> nanostructures can be initially grown via one of the processes followed by SnO<sub>2</sub> or ZnO nanostructures synthesized on top of the ZnO or SnO<sub>2</sub> nanostructures via another processing route. Generally, a two-step method is a common approach to fabricate core-shell and hierarchical nanostructures. Core or trunk nanowires are fabricated in the first step. Shell or branch is grown on top of the core or trunk with either the same or a different material. To date, numerous heterogeneous core-shell and

hierarchical nanostructures have been synthesized by two-step methods which had ultra-low yield and very complicated procedures (Yu *et al.*, 2005).

#### **2.5.1.1 Nanostructures by Single-Step Process**

Electrospinning, thermal evaporation and hydrothermal processes are commonly used method for the production of one dimensional ZnO/SnO<sub>2</sub> nanostructures in a single-step process. Among the methods used, electrospinning technique is the most widely employed for the production of hybrid ZnO/SnO<sub>2</sub> nanofibers due to its simplicity, inexpensive, straight forward, and versatile method (Moon *et al.*, 2009b; Song & Liu, 2009). The nanostructures obtained by this process are mostly nanofibers with different configurations such as mesoporous (Song *et al.*, 2009), hollow (Tang *et al.*, 2014; Wei *et al.*, 2011) and core-shell nanofibers (Lee *et al.*, 2012b). The as-spun fibers were calcined at various temperatures between 500 °C and 650 °C for 3 h to 6 h interval to convert into nanofibers. Few reports of the production of ZnO/SnO<sub>2</sub> hybrid nanostructures from metal chloride as starting material by this method have been stated that the calcination temperature was used to convert the metal chlorides to metal oxides and the removal of PVP in as-spun fibers (Song & Liu, 2009; Song *et al.*, 2009; Wei *et al.*, 2011).

Mesoporous ZnO-SnO<sub>2</sub> nanofibers were deposited by Song *et al.* (2009) by electrospinning process. For this preparation, SnCl<sub>2</sub>.2H<sub>2</sub>O were mixed with *N,N* dimethylformamide (DMF) and ethanol in a glove box under stirring for 6 h. Subsequently ZnCl<sub>2</sub> and PVP were also added into the solution. The mixture was then loaded into a glass syringe with a voltage supply of 10 kV at an electrode distance of 20 cm. The as-prepared fibers were collected on an aluminium frame and calcined at 600 °C for 4 h. A TEM micrograph of SnO<sub>2</sub>-ZnO nanofiber exhibits nanofiber with

diameter size between 100 and 150 nm (Figure 2.9(a)). These nanofibers exhibited a highly mesoporous structure with some disordered wormhole-like pores. These porous structures have been destroyed during the calcination due to the collapse of meso-structured wall and the aggregation of nanofibers. Wei *et al.* (2011) and Tang *et al.* (2014) used the similar method for the production of SnO<sub>2</sub>-ZnO hollow nanofibers with different Zn precursors, which is presented in Table 2.2. A higher magnification SEM image of ruptured section in Figure 2.9(b) clearly shows both the hollow structure and the rough porous surface of SnO<sub>2</sub>-ZnO nanofibers were obtained by Wei *et al.* (2011). The diameters of the nanofibers were in the range of 80-160 nm. Here, the nanofiber was linked by the non-uniform ZnO and SnO<sub>2</sub> nanoparticles with the size of 15-30 nm. The inset in Figure 2.9(b) further proved the porous structure and the wall thickness of the fiber is about 39 nm. The possible formation mechanism of the hollow nanofibers was described on the basis of the evaporation effect induced phase separation during electrospinning. In this process, DMF and ethanol were served to dissolve PVP, Zn(Ac)<sub>2</sub> and SnCl<sub>2</sub> while ethyl acetate was used as the promoter of phase separation. Ethyl acetate evaporated rapidly during the electrospinning process. So concentration gradient of ethyl acetate was observed along the diameter of the fiber which was high in the center and low at the edge of the fiber. Therefore, ethyl acetate concentrated on the center line but PVP and enwrapped SnCl<sub>2</sub>-Zn(Ac)<sub>2</sub> was moved to the edge of the fiber due to the incompatibility with ethyl acetate. Since the molecules of SnCl<sub>2</sub> and Zn(Ac)<sub>2</sub> are much smaller than those of the PVP polymer, they may reach the outer boundary layer of the fiber easily. Thus, with the evaporation effect, phase separation occurs. After calcination, PVP was decomposed and formed hollow porous nanofibers. But, Tang *et al.* (2014) prepared hollow nanofibers using ZnNO<sub>3</sub> solution instead of Zn(Ac)<sub>2</sub> with different weight ratio of Zn and Sn. The formation mechanism of their hollow nanofibers (Zn/Sn=1:1) was slightly different from Wei *et al.* (2011). They explained



as, the spinning mixture contained  $\text{Sn}^{2+}$ ,  $\text{Zn}^{2+}$ ,  $\text{Cl}^-$ ,  $\text{NO}_3^-$  ions and the macromolecules of PVP in the solvent of ethanol and DMF. During heat treatment, the inorganic ions moved to the surface of the nanofibers because of heating. Therefore, all solvents were evaporated and leaving inorganic ions only. The PVP,  $\text{Cl}^-$  and  $\text{NO}_3^-$  were oxidized and decomposed with prolong heating time and the increase temperature. At the same time, the metal cations of  $\text{Sn}^{2+}$  and  $\text{Zn}^{2+}$  were oxidized into the grains of  $\text{SnO}_2$  and  $\text{ZnO}$ . These grains gradually grew and agglomerated into big particles, and eventually connected together in form of hollow nanofibers. Lee *et al.* (2012a) developed hybrid  $\text{SnO}_2$  nanofibers with N-doped  $\text{ZnO}$  nanonodules using similar technique. The core-shell nanofibers were obtained depending on the weight ratio between  $\text{ZnO}$  and  $\text{SnO}_2$  in the solution. N-doped  $\text{ZnO}$  nanonodule on  $\text{SnO}_2$  nanofiber was observed when the weight ratio between  $\text{ZnO}$  and  $\text{SnO}_2$  was 25/100 and 50/100, while core-shell like structure were obtained at weight ratio of 100/100. This process contained two different polymer solutions: PAN (contain PAN,  $\text{SnCl}_4 \cdot 5\text{H}_2\text{O}$  and DMF) and PVP (contain PVP, DMF, and various amounts of  $\text{ZnAc}_2$  and triethylamine). Both solutions were mixed at 80-90 °C for 3 h and injected into a syringe by applying voltage of 15 kV. The electrospun core-shell nanofibers were calcined at 600 °C for 1h. During the heat treatment,  $\text{Sn}^{4+}$  ions bound to the polymer chains were converted to  $\text{SnO}_2$  nanofibers, and  $\text{Zn}^{2+}$  ions were converted to  $\text{ZnO}$  nanonodules on the  $\text{SnO}_2$  nanofiber surface via decomposition of the PVP and PAN polymers. Furthermore, the oxygen atom of  $\text{ZnO}$  was replaced with a nitrogen atom from triethylamine to form N-doped  $\text{ZnO}$  nanonodules (Figure 2.9(c)). The  $\text{SnO}_2$  nanofiber had diameter of ~100 nm and N-doped  $\text{ZnO}$  nanonodule was 50 nm in diameter.

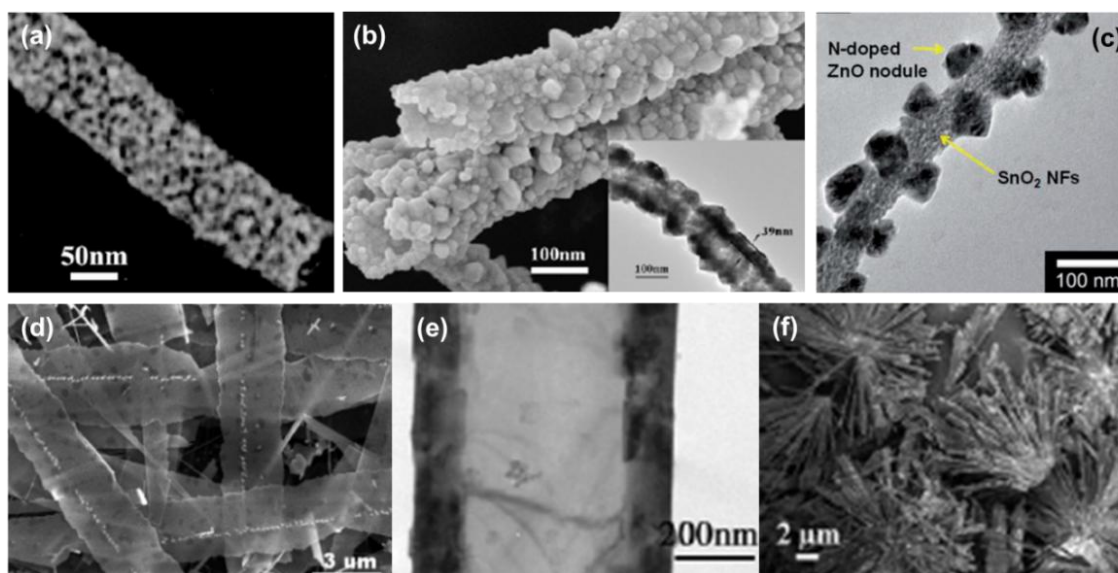


Figure 2.9. Different morphologies of ZnO/SnO<sub>2</sub> nanostructures obtained by single-step process: (a) mesoporous nanofibers (Song *et al.*, 2009), (b) hollow nanofibers (Wei *et al.*, 2011), (c) ZnO nanonodules on the SnO<sub>2</sub> nanofiber (Lee *et al.*, 2012b), (d) triangular SnO<sub>2</sub> nanoparticles on ZnO nanobelts (Wang *et al.*, 2007), (e) SnO<sub>2</sub>/ZnO/SnO<sub>2</sub> triaxial nanobelt (Zhao *et al.*, 2006), and (f) flower-like nanostructure (Li *et al.*, 2011).

Thermal evaporation has also been used to produce hybrid ZnO-SnO<sub>2</sub> nanobelts and SnO<sub>2</sub> nanowires coated quantum sized ZnO nanocrystals. For example, Sinha *et al.* (2012) grew hybrid ZnO-SnO<sub>2</sub> nanobelts by thermal evaporation together with O<sub>2</sub>/Ar flux from Zn and Sn powder placed separately. The mixture was evaporated at 850 °C in a quartz tube. The evaporated metal powders interacted with O<sub>2</sub> and deposited on a Si substrate located above the boat. The resulting nanobelts had a diameter of 100-250 nm with several micron lengths. Similarly, Yu *et al.* (2005) grew SnO<sub>2</sub> nanowire coated quantum sized ZnO nanocrystals by thermal evaporation process by supplying Ar at 900 °C from SnO, ZnCO<sub>3</sub> and graphite powder. The mixture of ZnCO<sub>3</sub> and graphite powder (weight: 3:2) was put bottom of the quartz boat and SnO powder was covered as layer on top of the mixture. The stainless steel mesh substrate with the pore of 150 μm diameter was placed on top of the boat. The diameters of resulting SnO<sub>2</sub> nanowires were 50-150 nm with a layer of ZnO nanoparticles (d< 5 nm) coated on the nanowire. The exact reason for the formation of ZnO nanocrystals was not clear.

Additionally, Wang *et al.* (2007) fabricated triangular SnO<sub>2</sub> nanoparticles on ZnO nanobelts (Figure 2.9(d)) by a vapour-phase transport method at 900 °C from SnO power in the presence of graphite and ZnO mixed powder placed separately. The widths of the nanobelts ranged from several hundred nanometers to several micrometers, and the lengths were about several tens of micrometers. Pyramid-like or triangular particles with sizes of about 100-200 nm were grown in the center of the nanobelts and aligned in a line through the whole length of the nanobelts. Further side-to-side SnO<sub>2</sub>/ZnO/SnO<sub>2</sub> triaxial nanobelts (Figure 2.9(e)) were fabricated by Zhao *et al.* (2006) via chemical vapour deposition from Zn and Sn powders placed separately at furnace temperature of 1000 °C for 80 min under constant Ar flow of 40 sccm. In this process, Zn powder was placed center of inner alumina tube with covered by quartz plate to maintain high vapour pressure, while Sn powder was located downstream of outer alumina tube covered by Si substrate to deposit nanostructures. The width of side layer of the belt was equal and about 30-100 nm. Pure ZnO nanobelts and SnO<sub>2</sub>/ZnO/SnO<sub>2</sub> triaxial nanobelts were observed at growth time of 10 min and 80 min, respectively. Growth of symmetric SnO<sub>2</sub> nanobelts was explained due to polar surface of ZnO nanobelts (Zhao *et al.*, 2006).

Among the single-step processing routes discussed, hydrothermal method requires the lowest average temperature compared to thermal evaporation and vapour-phase processing. Other advantages of hydrothermal processing include ease of transfer of end product to other substrates and high yield. Li *et al.* (2011) produced different morphologies of ZnO/SnO<sub>2</sub> nanostructures (flower-like, column-like and octahedral-crystal like) by hydrothermal route. Various morphologies were obtained by changing molar ratios between Zn<sup>2+</sup> and Sn<sup>4+</sup>, different concentrations of glucose and NaOH. The variation of NaOH concentration led to different formation rates and concentrations of

nuclei for the formation of various morphologies. Figure 2.9(f) shows the flower-like nanostructure obtained when the ratio of  $\text{Zn}^{2+}/\text{Sn}^{4+}$  equals to 8:1.

### 2.5.1.2 Nanostructures by Two-Step Process

Generally, core-shell and hierarchical nanostructures were mostly obtained in the reported literature in two-steps synthesis process. The core of the nanowires were synthesised by thermal evaporation, hydrothermal and electrospinning processes, while shell was deposited by atomic layer deposition (ALD), thermal evaporation, hydrothermal and pulsed laser deposition (PLD). Among the methods used, uniform shell was observed by ALD and PLD processes and thickness of shell was easily controlled by number of cycles.  $\text{SnO}_2$ -core nanowires by the thermal evaporation of Sn powders followed by the ALD of ZnO-shell nanowires were developed by Park *et al.* (2011) , Kim *et al.* (2012) and Pan *et al.* (2012). They used Au catalyst to grow  $\text{SnO}_2$  nanowire by vapour-liquid-solid mechanism. The diameter of core  $\text{SnO}_2$  nanowires of 80 nm and the thickness of ZnO shell layer of 10 nm were obtained by Park *et al.* (2013a) (Figure 2.10(a)). But, Sun *et al.* (2007) fabricated ZnO- $\text{SnO}_2$  hierarchical nanostructures by thermal evaporation of Zn and Sn powder at 800 °C. The secondary grown ZnO nanobelts on primary  $\text{SnO}_2$  nanobelts were achieved by a vapour-solid (VS) process, where the first step growth of  $\text{SnO}_2$  nanobelts served as substrates for the secondary growth of ZnO nanobelts. At lower growth temperature of 450 °C, ZnO nanowires was obtained with a sharp edge at the tip, while at 600 °C, ZnO nanorods with hexagonal cross sections were formed on the  $\text{SnO}_2$  nanobelt (Figure 2.10(b)). Shapes and sizes of ZnO nanostructures were tuned by varying the growth temperatures. Diameter and length of ZnO nanostructures increase from 30 to 300 nm, and 400 nm to several micrometers, respectively.

Additionally, Cheng *et al.* (2009) and Dai *et al.* (2013) synthesized ZnO branch nanorods on SnO<sub>2</sub> backbone nanowires by vapour transport and hydrothermal methods. SnO<sub>2</sub> powder and graphite powder were used to grow SnO<sub>2</sub> nanowires at 1000 °C with the help of Au catalyst. For the growth of ZnO nanorods, ZnO seed layer was subsequently formed by dip-coating (Cheng *et al.*, 2009) or RF sputtering (Dai *et al.*, 2013) followed by ZnO nanorods were grown by hydrothermal method using different zinc precursors. Leaves of pine tree-like structure was observed by using zinc nitrate hexahydrate precursor (Figure 2.10(c)), while brush-like structure was obtained by using zinc acetate dehydrate (Figure 2.10(d)). Figure 2.10(c) shows the nanorod branches stand perpendicular to the side surfaces of the SnO<sub>2</sub> nanowires as multiple rows in a parallel manner with the range of length from 100 to 200 nm and diameter of 30 nm. The most of the branches have four-fold symmetry. But, the SnO<sub>2</sub> nanowire backbones were as long as tens of micrometers. The number density and morphology of secondary ZnO nanostructure was tuned by adjusting the salt concentration of precursor and reaction time. SEM image in Figure 2.10(d) exhibits the brush-like SnO<sub>2</sub>/ZnO hierarchical nanostructure with a high surface-to-volume ratio. The branch-out ZnO nanorods on the SnO<sub>2</sub> nanowire have uniform diameter of about 50 nm and length of about 400 nm. The ZnO nanorods were grown randomly on the SnO<sub>2</sub> nanowire and present high surface-volume ratio due to the mismatch of SnO<sub>2</sub> and ZnO.

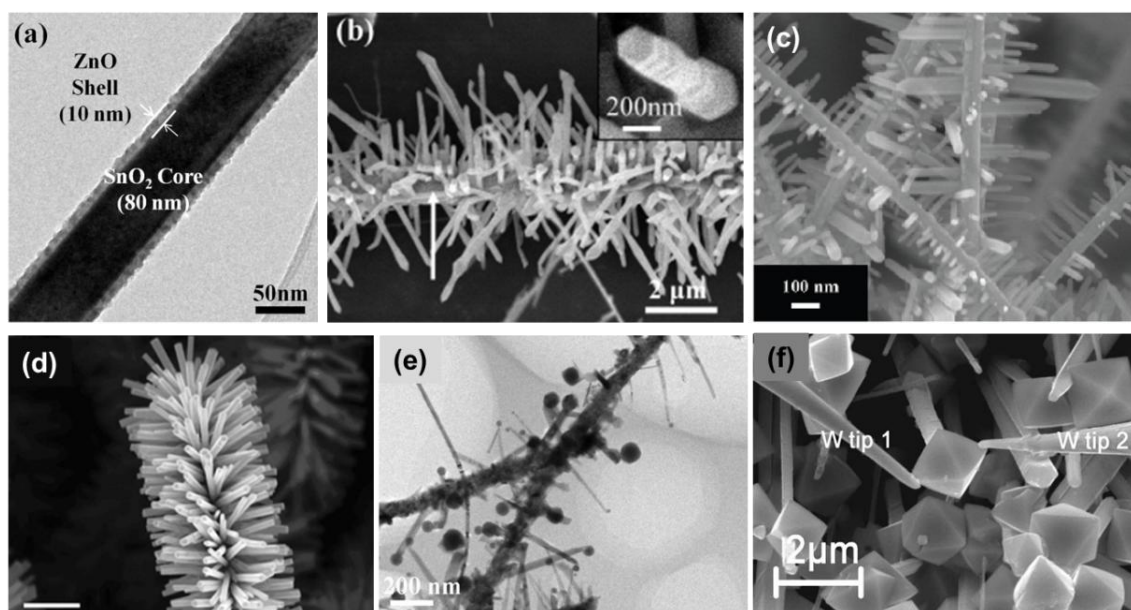
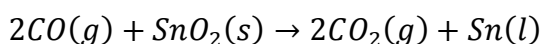
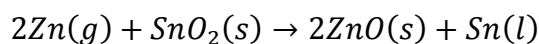


Figure 2.10. Different morphologies of ZnO/SnO<sub>2</sub> nanostructures obtained by two-step process: (a) SnO<sub>2</sub>-core/ZnO-shell nanowires (Park *et al.*, 2013a), (b, c, d and e) SnO<sub>2</sub>-ZnO hierarchical nanostructures (Sun *et al.*, 2007; Cheng *et al.*, 2009; Dai *et al.*, 2013; Lan *et al.*, 2012), and (f) SnO<sub>2</sub> capped ZnO nanowire (Liu *et al.*, 2008b).

Lan *et al.* (2012) deposited SnO<sub>2</sub>/ZnO hierarchical nanostructures by a two-step carbon assisted thermal evaporation method. SnO<sub>2</sub> nanowires were synthesized first followed by the synthesis of ZnO nanowires (Figure 2.10(e)). An equal molar ratio between SnO<sub>2</sub> and C powder was placed in a ceramic boat. A gold coated (10 nm) Si substrate was placed at 4 mm from the ceramic boat to collect SnO<sub>2</sub> nanowires. The pressure inside the system was at 1 Pa and Ar and O<sub>2</sub> (Ar:O<sub>2</sub>=100:1 by volume) was passed through the furnace at a flow rate of 20 sccm. White wool-like SnO<sub>2</sub> nanowires was formed at 800 °C of furnace temperature after cooled down. The same process was repeated for ZnO nanowire with furnace temperature of 850 °C. A black wool-like ZnO nanowire was deposited on white wool-like SnO<sub>2</sub> nanowire. The diameters of the newly formed ZnO nanowires range from 15 to 50 nm. The lengths of the ZnO nanowires were in the range of several tens nanometers to several micrometers. Sn particle was observed at the tip of each branch ZnO nanowire which is shown in Figure 2.10(e). The formation of hierarchical nanostructures was proposed by Lan *et al.* (2012) according to the

observation, which is shown in Figure 2.11. SnO<sub>2</sub> nanowires were formed at first step. In the second step, ZnO reacted with C to generate Zn and CO vapours. These vapours was reacted with surface of SnO<sub>2</sub> nanowires and form Sn droplets by following reactions.



The produced Zn vapour from source mixture transported to SnO<sub>2</sub> would be absorbed by Sn droplets. ZnO nanowires would be formed when the droplets became supersaturated.

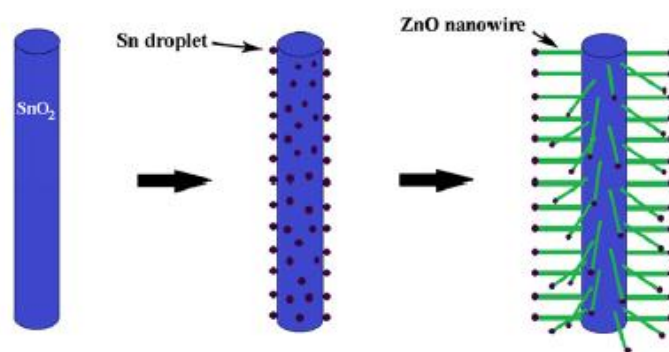


Figure 2.11. Schematic diagram showing the formation of the SnO<sub>2</sub>/ZnO hierarchical nanostructures (Lan *et al.*, 2012)

Hydrothermal method is a low cost method to fabricate various morphologies of nanostructure. Liu *et al.* (2008b) and Shi *et al.* (2007) grew SnO<sub>2</sub>-capped ZnO nanowire array on Zn substrate by two-step hydrothermal method. Initially, the ZnO nanowire arrays were grown on the Zn foil via 10 mL 2M NaOH and 5 mL 30% H<sub>2</sub>O<sub>2</sub>. The mixed solution and Zn substrate were transferred into the autoclave and temperature was maintained at 190 °C for 8 h. After that, another mixed solution with pH>12 was prepared using SnCl<sub>4</sub>.5H<sub>2</sub>O and NaOH. Tin solution was transferred into autoclave with ZnO nanowire formed on Zn foil. The temperature was maintained at 160 °C for 30 h. SEM image in Figure 2.10(f) shows the ZnO nanowires and SnO<sub>2</sub> caps observed after

end of the process. In this process,  $\text{H}_2\text{O}_2$  was served as strong oxidant for the Zn foil in alkaline solution of NaOH. Therefore, ZnO nanocrystals formed on Zn foil which become as nuclei for further growth of ZnO nanocrystals during the oxidation. The produced strong oxidizing environment assists as a kinetic driving force and promotes the anisotropic development and thus the growth of elongated nanocrystals. Due to this, ZnO nanowire arrays on the Zn foil were formed as nanowires. This nanowire arrays on the Zn substrate served as a template for the growth of  $\text{SnO}_2$  cap. Furthermore, Choi *et al.* (2013) fabricated ZnO- $\text{SnO}_2$  nanofiber-nanowire heterostructure (NNH) in the form of stem-branch structure. In the NNH, the  $\text{SnO}_2$  nanowire branches were grown through vapour-liquid-solid (VLS) growth on ZnO nanofiber stems synthesized by electrospinning.

Among all the processing, the obtained nanostructures in a single-step processing consist of hybrid nanofibers, nanobelts, core-shell nanostructures and hierarchical nanostructures with varying dimensions. Two-step synthesis processing yields a variety of nanostructures including core-shell nanostructures and hierarchical nanostructures, though the yield is poor in some cases. Hydrothermally grown nanostructures had limited length, while vapour transport and electrospinning methods provide long nanowires with fast growth rate. A summary of these processing details for the growth of ZnO/ $\text{SnO}_2$  nanostructures is presented in Table 2.2.



Table 2.2. Summary of various processing routes for the production of ZnO/SnO<sub>2</sub> nanostructures

Type of synthesis process	Synthesis Method	Morphology	Starting materials	Synthesis temperature	Reference
Single-step	Electrospinning	ZnO-SnO <sub>2</sub> nanofiber	SnCl <sub>2</sub> ·2H <sub>2</sub> O, N,N-dimethylformamide (DMF), Polyvinylpyrrolidone(PVP), ZnCl <sub>2</sub>	600 °C	Song & Liu, 2009; Song <i>et al.</i> , 2009; Zhang <i>et al.</i> , 2010
	Electrospinning	ZnO-SnO <sub>2</sub> nanofiber	Polyvinyl alcohol (PVA), Zn(CH <sub>3</sub> CO <sub>2</sub> ) <sub>2</sub> , SnCl <sub>2</sub> ·2H <sub>2</sub> O	600 °C	Asokan <i>et al.</i> , 2010
	Electrospinning	Mesoporous ZnO-SnO <sub>2</sub> nanofibers	SnCl <sub>2</sub> ·2H <sub>2</sub> O, (DMF), ethanol, ZnCl <sub>2</sub> , PVP	600 °C	Song <i>et al.</i> , 2009
	Electrospinning	SnO <sub>2</sub> -ZnO hollow nanofibers	DMF, ethanol, ethyl acetate, PVP, Zn(CH <sub>3</sub> CO <sub>2</sub> ) <sub>2</sub> ·2H <sub>2</sub> O, SnCl <sub>2</sub> ·2H <sub>2</sub> O	500 °C	Wei <i>et al.</i> , 2011
	Electrospinning	Hollow hierarchical SnO <sub>2</sub> -ZnO composite nanofibers	SnCl <sub>2</sub> ·2H <sub>2</sub> O, Zn(NO <sub>3</sub> ) <sub>2</sub> ·6H <sub>2</sub> O, PVP, DMF, ethanol	600 °C	Tang <i>et al.</i> , 2014 Tian <i>et al.</i> , 2013
	Electrospinning	SnO <sub>2</sub> nanofibers-ZnO nanonodules (core-shell nanofiber)	Poly(acrylonitrile) (PAN), PVP, zinc acetate, SnCl <sub>4</sub> ·5H <sub>2</sub> O, DMF	600 °C	Lee <i>et al.</i> , 2012a
	Thermal evaporation	SnO <sub>2</sub> nanowires coated quantum sized ZnO nanocrystals	SnO powder, ZnCO <sub>3</sub> , graphite powder, mesh substrate, Ar	900 °C	Yu <i>et al.</i> , 2005
	Thermal evaporation	hybrid ZnO-SnO <sub>2</sub> nanobelt	Zn powder, Sn powder, Si substrate, Ar, O <sub>2</sub>	850 °C	Sinha <i>et al.</i> , 2012
	Vapor-phase transport	SnO <sub>2</sub> triangular nanoparticles on ZnO nanobelt	SnO powder and ZnO/C mixed powder placed separately, Si substrate, N <sub>2</sub>	900 °C	Wang <i>et al.</i> , 2007
	Chemical vapour deposition	side-to-side SnO <sub>2</sub> /ZnO/SnO <sub>2</sub> triaxial nanobelt	Sn powder, Zn powder, Si substrate	1000 °C	Zhao <i>et al.</i> , 2006
	Hydrothermal	ZnO-SnO <sub>2</sub> hierarchical nanostructures	Zinc acetate, tin tetrachloride, NaOH, glucose	180 °C	Li <i>et al.</i> , 2011
Two-step	Thermal evaporation	SnO <sub>2</sub> -core/ZnO-shell nanowires	Sn powder, Au catalyst, Si substrate, N <sub>2</sub> , O <sub>2</sub>	900 °C	Park <i>et al.</i> , 2013a Kim <i>et al.</i> , 2012
	ALD		Diethylzinc (DEZn), H <sub>2</sub> O	150 °C	
	Thermal evaporation	SnO <sub>2</sub> -core/ZnO-shell nanowires	Sn powder, Au catalyst, alumina substrate, Ar, O <sub>2</sub>	950 °C	Pan <i>et al.</i> , 2012
	ALD		DEZn, H <sub>2</sub> O, N <sub>2</sub>	-	

	Thermal evaporation	ZnO-SnO <sub>2</sub> hierarchical nanostructures	Sn powder, Ar flow	800 °C	Sun <i>et al.</i> , 2007
	Thermal evaporation		Zn powder, Ar flow	800 °C	
	Vapour transport	ZnO nanorod arrays on SnO <sub>2</sub> nanowire backbones	SnO <sub>2</sub> powder, graphite powder, Au catalyst, Si substrate	1050 °C	Cheng <i>et al.</i> , 2009
	hydrothermal		Zinc nitrate hexahydrate, hexamethylenetetramine	95 °C	
	Vapour transport	Brush-like SnO <sub>2</sub> /ZnO hierarchical nanostructure	SnO <sub>2</sub> powder, graphite powder, Au catalyst, Sapphire substrate	1000 °C	Dai <i>et al.</i> , 2013
	hydrothermal		Zinc acetate dehydrate (Zn(CH <sub>3</sub> COO) <sub>2</sub> · 2H <sub>2</sub> O), hexamethylenetetramine (HMT)	90 °C	
	Carbon assisted thermal evaporation	SnO <sub>2</sub> /ZnO hierarchical nanostructures	SnO <sub>2</sub> /C powder, Ar, O <sub>2</sub> , Au catalyst, Si substrate	800 °C	Lan <i>et al.</i> , 2012
	Carbon assisted thermal evaporation		ZnO/C powder, Ar	850 °C	
	Carbothermal reduction	ZnO-core/SnO <sub>2</sub> -shell nanowires	ZnO powder, graphite powder, Au catalyst, Si substrate, Ar, O <sub>2</sub>	900 °C	Hwang <i>et al.</i> , 2010b
	Vapour transport		Tetramethyltin (CH <sub>3</sub> ) <sub>4</sub> Sn, Ar, O <sub>2</sub>	700 °C	
	Electrodeposition	ZnO/SnO <sub>2</sub> hierarchical and flower-like nanostructures	Zn(NO <sub>3</sub> ) <sub>2</sub> , NH <sub>4</sub> Ac, HMT	-	Liu <i>et al.</i> , 2012
	hydrothermal		SnCl <sub>2</sub> , sodium citrate, NaOH	120 °C	
	Hydrothermal	SnO <sub>2</sub> /ZnO core-shell nanorods and nanoflowers	SnCl <sub>4</sub> ·5H <sub>2</sub> O, NaOH, ethanol	210 °C	Jiang <i>et al.</i> , 2013
	Hydrothermal		Zinc acetate dihydrate, C <sub>6</sub> H <sub>12</sub> N <sub>4</sub> , ethanol	85 °C	
	Hydrothermal	SnO <sub>2</sub> capped ZnO nanowires	NaOH, H <sub>2</sub> O <sub>2</sub> , Zn substrate	190 °C	Liu <i>et al.</i> , 2008a; Shi <i>et al.</i> , 2007
	Hydrothermal		SnCl <sub>4</sub> ·5H <sub>2</sub> O, ethanol, distilled water	160 °C	
	Electrospinning	ZnO-SnO <sub>2</sub> nanofiber–nanowire heterostructure	Zinc acetate ((CH <sub>3</sub> CO <sub>2</sub> ) <sub>2</sub> Zn), Polyvinyl acetate (PVA)	600 °C	Choi <i>et al.</i> , 2013
	VLS growth method		Sn powder, N <sub>2</sub> , O <sub>2</sub>	900 °C	

### 2.5.2 Sensing Performance of ZnO/SnO<sub>2</sub> Nanostructures

The sensor performance of ZnO/SnO<sub>2</sub> nanostructures depends greatly on the processing techniques, surface morphology, arrangement of sensor fabrication and operating temperature. Various target gases such as, CO, methanol (CH<sub>3</sub>OH), H<sub>2</sub>S, ethanol (C<sub>2</sub>H<sub>5</sub>OH), acetone (C<sub>3</sub>H<sub>6</sub>O), H<sub>2</sub>, trimethylamine (C<sub>3</sub>H<sub>9</sub>N), NO<sub>2</sub> and toluene have been tested to evaluate the performance of ZnO/SnO<sub>2</sub> nanostructured sensors. Main performance parameters for gas sensors are sensitivity, response time, recovery time, detection range, and optimum working temperature. Reported gas sensing properties for a variety of ZnO/SnO<sub>2</sub> nanostructures for different gas species is summarized in Table 2.3.

In general, the sensitivity of ZnO/SnO<sub>2</sub> nanostructures increases with increasing target gas concentration, owing to the fact that both ZnO and SnO<sub>2</sub> are n-type semiconductors. Depending on the processing route, ZnO/SnO<sub>2</sub> nanostructures can be obtained in different surface states, size and morphology. Changes in these parameters can result in variations in gas sensing properties. For example, the surface morphology of ZnO/SnO<sub>2</sub> hierarchical nanostructures greatly affects the performance of the sensor. Li *et al.* (2011) showed that the flower-like nanostructure improves the sensitivity of ethanol (C<sub>2</sub>H<sub>5</sub>OH) than column-like or microcrystal nanostructure. A rougher surface exhibits higher sensitivity because it provides more active sites for oxygen and reducing gases on the surface of the sensor material. Also, nanostructures having smaller size have higher surface area resulting in higher gas sensitivity.

The sensitivity of ZnO/SnO<sub>2</sub> nanostructures towards ethanol is high compared with other target gases which are shown in Table 2.3. The resistivity of an n-type ZnO/SnO<sub>2</sub> sensor is decreased when exposed to reducing C<sub>2</sub>H<sub>5</sub>OH environment. Thus far, different

types of nanostructures including core-shell nanowires, hybrid nanofibers and hierarchical nanostructures were examined to evaluate their performance towards  $\text{C}_2\text{H}_5\text{OH}$  gas. It was seen that flower-like hierarchical  $\text{ZnO}/\text{SnO}_2$  nanostructures had higher sensitivity than thin film and hybrid nanofibers (Kim *et al.*, 2007a; Li *et al.*, 2011; Song & Liu, 2009). Among all described nanostructure assemblies, hierarchical nanostructures showed the highest sensitivity (209.8) towards ethanol gas at a temperature of  $300\text{ }^\circ\text{C}$  and a concentration of 1000 ppm (Li *et al.*, 2011). It was claimed that flower-like nanostructure with small diameters provide high surface area for sensor performance, thus sensitivity was augmented. Based on the literature, the response and recovery times of  $\text{ZnO}/\text{SnO}_2$  nanostructures were few tenths of seconds which are very less compare to ZTO nanostructures in an ethanol environment (Khorami *et al.*, 2011). Another important parameter is the optimum operating temperature for which data shows within the range of  $300\text{--}450\text{ }^\circ\text{C}$ . Khong *et al.* (2012b) reported that the enhanced ethanol sensing was due to dehydrogenation process of ethanol with basic oxides. At elevated temperature, ethanol ( $\text{C}_2\text{H}_5\text{OH}$ ) molecules can be decomposed and formed into  $\text{CH}_3\text{CHO}$  and  $\text{H}_2$  molecules. This  $\text{CH}_3\text{CHO}$  molecule can react with adsorbed oxygen species and released the trapped electron back to the surface of the structure. Thus, the sensitivity was improved in  $\text{ZnO}/\text{SnO}_2$  nanostructures.  $\text{SnO}_2$ -core/  $\text{ZnO}$ -shell nanowires showed the response of 14.1 for 100 ppm ethanol at  $400\text{ }^\circ\text{C}$  (Thanh Le *et al.*, 2013). They explained that the greater sensitivity was due to combination of  $\text{ZnO}$ - $\text{SnO}_2$  heterointerfaces at the grain-grain junction in the  $\text{ZnO}$  shell by lowering the potential barrier height via ethanol sensing.

Many reports in the literature agree that  $\text{ZnO}/\text{SnO}_2$  nanostructures have poor sensitivity towards  $\text{H}_2$  gas compared with ethanol (Huang *et al.*, 2011; Mondal *et al.*, 2014). However, it is also observed that  $\text{ZnO}$ -modified  $\text{SnO}_2$  nanorod array sensor showed n-p-

n transition in its sensing response to  $H_2$  in a wide working temperature between 150 °C and 450 °C, while the sensor exhibited n-type response to other test gases  $CO$ ,  $NH_3$  and  $CH_4$  gas (Huang *et al.*, 2011). They found that the type of sensing response depends on the concentration of the  $H_2$  gas. The ZnO-modified  $SnO_2$  nanorod sensors showed a normal n-type sensing response from 10 to 20 ppm and above the  $H_2$  concentration of 2000 ppm, while p-type sensing response was switched to between 20 ppm and 1000 ppm  $H_2$  concentration. The time-dependent n-p-n transition response was reported due to modification of ZnO. The dominant carriers at the interface of ZnO and  $SnO_2$  were inverted from electrons to holes because of electron depletion by surface adsorption and increasing holes by substitution of  $Sn^{4+}$  ions by  $Zn^{2+}$  cations. Therefore, formation of n-ZnO/ p-Zn-O-Sn/ n- $SnO_2$  heterojunction structures explained the n-p-n transitions of the ZnO-modified  $SnO_2$  nanorod sensor. Mondal *et al.* (2014) developed ZnO/ $SnO_2$  nanocomposites sensor, which showed very less response of 0.9 to 10 000 ppm  $H_2$  at 150 °C.

ZnO/ $SnO_2$  nanostructures also displayed a good response towards oxidizing  $NO_2$  gas detection. The resistance of the sensor increased when exposed to  $NO_2$  environment (Park *et al.*, 2013a). ZnO/ $SnO_2$  stem-branch heterostructure floated on Au interdigitated mask substrate was able to detect  $NO_2$  gas down to 0.1 ppm level at 350 °C (Choi *et al.*, 2013). Additionally, ceramic tube type sensor containing composite of ZnO nanorods and  $SnO_2$  nanoparticles detected  $NO_2$  gas at the 0.5 ppm level at room temperature (Lu *et al.*, 2012). The sensitivity of this ZnO/ $SnO_2$  composite was reported to be more than 1000 towards 0.5 ppm of  $NO_2$  at room temperature under UV illumination. In this case, the photo-generated carriers were produced after the semiconductor absorbs UV light. Therefore, carriers moved to the surface of the semiconductor and participated in the reaction with  $NO_2$  gas, thus the sensitivity is enhanced. The hybrid fibre-mats structure

(Park *et al.*, 2010) had higher response by an order of magnitude compared with the SnO<sub>2</sub>-core/ZnO-shell nanowires (Park *et al.*, 2013a). The difference between the sensing properties of these two structures can be ascribed to the differences in their morphologies. The more porous structure of ZnO/SnO<sub>2</sub> resulted in higher surface area available for reaction in hybrid fibre-mats, compared to the SnO<sub>2</sub>-core/ZnO-shell nanowire having a lower effective surface area. Even though, the response and recovery times were short to ZnO-core/SnO<sub>2</sub>-shell nanowires (Hwang *et al.*, 2010b) compared to hybrid nanofibers. It was varied from few tenths of seconds to few minutes.

ZnO-SnO<sub>2</sub> nanofiber-nanowire stem-branch heterostructure have been reported to have a good response to CO at low concentration (Choi *et al.*, 2013). They measured the sensitivity of hierarchical nanostructure at 300 °C, which exhibited the sensor response of 27 at 10 ppm of CO. In this case four components of resistance involved the sensing. They are modulation of the depletion width along the branch nanowires, potential barriers at nanograins in the stem nanofibers, both ZnO and SnO<sub>2</sub> networked homojunctions and heterojunctions between the stems and branches. Due to the variation of four components with target gas were likely to be the reason for the good sensing ability. But, the sensitivity of SnO<sub>2</sub> triangular nanoparticles on ZnO nanobelt (Wang *et al.*, 2007) exhibited low sensitivity compared to hierarchical nanostructures reported by Choi *et al.* (2013). It was seen that sensitivity of 300 ppm CO gas was 4.6 at 350 °C. But the response time (52 s) and recovery time (550 s) were too high.

Sensitivities of ZnO/SnO<sub>2</sub> hollow nanofiber and nanofiber web towards toluene was investigated by Wei *et al.* (2011) and Song *et al.* (2009). Hollow nanofibers exhibited good sensitivity of 25 at concentration of 100 ppm at low working temperature of 190 °C. But, nanofiber web sensor showed less sensitivity (9.8 for 100 ppm) and increased

optimum temperature of 360 °C than hollow nanofibers. It was claimed that the higher sensitivity in the hollow nanofibers was due to the increased porous structure and thus target gas react with all over the surface. On the other hand, the prolong response and recovery times were observed for hollow nanofibers than nanofiber mats due to slow down of adsorption and desorption reaction on the nanofiber's surface at low operating temperature.

In summary, it is observed that ZnO/SnO<sub>2</sub> nanostructures can detect ethanol gas most efficiently. But, ZnO-nanorod/SnO<sub>2</sub>-nanoparticle composite exhibited higher sensitivity for NO<sub>2</sub> gas under UV light radiation. The sensitivity of one dimensional ZnO/SnO<sub>2</sub> nanostructures and thin films towards other gases such as CO, methanol, H<sub>2</sub>S, acetone and toluene is relatively low compared with hierarchical nanostructures. The response and recovery times show a direct dependence on the target gas. The performance of the sensors depends greatly on the morphology of ZnO/SnO<sub>2</sub> nanostructures and the working temperature used.

Table 2.3. Summary of gas sensing properties of ZnO/SnO<sub>2</sub> nanostructures

Test gases	Morphology	Detection temperature (°C)	Detection range (ppm)	Optimum Temp (°C)	Gas response			Response time	Recovery time	Reference
					Sensitivity	Concentration (ppm)	Temperature (°C)			
CO	SnO <sub>2</sub> triangular nanoparticles on ZnO nanobelt	-	-	-	4.6 <sup>A</sup>	300	350	52 s	550 s	Wang <i>et al.</i> , 2007
	ZnO/SnO <sub>2</sub> heterocontact	-	-	380	7 <sup>A</sup>	200	380	-	-	Yu & Choi, 1999
	ZnO-SnO <sub>2</sub> composite	-	-	360	12 <sup>A</sup>	200	360	-	-	Yu & Choi, 1998b
	ZnO-SnO <sub>2</sub> nanofiber-nanowire heterostructure	300	1-90	-	27 <sup>A</sup>	10	300	-	-	Choi <i>et al.</i> , 2013
Methanol	Hollow hierarchical SnO <sub>2</sub> -ZnO composite nanofibers	350	1-500	350	~5.5 <sup>A</sup>	10	350	20 s	40 s	Tang <i>et al.</i> , 2014
H <sub>2</sub> S	SnO <sub>2</sub> -core/ZnO-shell nanorods	RT	20-100	-	3.3 <sup>A</sup>	100	RT	900 s	800 s	Kim <i>et al.</i> , 2012
Ethanol	SnO <sub>2</sub> /ZnO hierarchical nanostructures	400	25-500	-	3 <sup>A</sup>	25	400	-	-	Khoang <i>et al.</i> , 2012b
	ZnO-SnO <sub>2</sub> nanofiber	300	1-10000	-	18 <sup>A</sup>	100	300	5 s	6 s	Song & Liu, 2009
	ZnO-SnO <sub>2</sub> hierarchical nanostructures	300	10-1000	-	209.8 <sup>A</sup>	1000	300	-	-	Li <i>et al.</i> , 2011
	Mesoporous ZnO-SnO <sub>2</sub> nanofibers	300	5-10000	-	12.8 <sup>A</sup>	50	300	3 s	8 s	Song <i>et al.</i> , 2009
	SnO <sub>2</sub> -ZnO thin film	-	-	300	4.69 <sup>A</sup>	200	300	72 s	164 s	Kim <i>et al.</i> , 2007a
	flower-like ZnO-SnO <sub>2</sub> composite	400	5-100	-	1.52 <sup>A</sup>	5	400	10 s	10 s	Cui <i>et al.</i> , 2012
	SnO <sub>2</sub> /ZnO composite nanofibers	360	27.7-5000	360	3 <sup>A</sup>	27.7	360	14 s	2 s	Khorami <i>et al.</i> , 2011
	SnO <sub>2</sub> -core/ZnO-shell nanowires	400	25-500	400	14.1 <sup>A</sup>	100	400	-	-	Thanh Le <i>et al.</i> , 2013
	ZnO-doped porous SnO <sub>2</sub> hollow nanospheres	150	10-500	150	14.7 <sup>A</sup>	100	150	10 s	23 s	Ma <i>et al.</i> , 2013
	SnO <sub>2</sub> doped ZnO thin film	450	1-200	450	40 <sup>A</sup>	200	450	-	-	Nanto <i>et al.</i> , 1996



Acetone	ZnO doped SnO <sub>2</sub> nanocrystals	320	10-350	320	48 <sup>A</sup>	100	320	-	-	Tian <i>et al.</i> , 2012
H <sub>2</sub>	ZnO-modified SnO <sub>2</sub> Nanorod	350	10-3000	350	18.4 <sup>C</sup>	100	350	-	-	Huang <i>et al.</i> , 2011
	ZnO-SnO <sub>2</sub> micro/nanocomposite	150	1000-10000	150	0.9 <sup>D</sup>	10000	150	60 s	75 s	Mondal <i>et al.</i> , 2014
Trimethylamine	SnO <sub>2</sub> -ZnO nanocomposite	330	1-500	240	125 <sup>A</sup>	50	330	2 s	5 s	Zhang & Zhang, 2008b
NO <sub>2</sub>	ZnO nanorod/SnO <sub>2</sub> nanoparticles	RT	0.1-2	-	1266 <sup>B</sup>	0.5	20	420 s	480 s	Lu <i>et al.</i> , 2012
	SnO <sub>2</sub> -core/ZnO-shell nanowires	RT	1-5	-	6.19 <sup>C</sup>	5	RT	100 s	220 s	Park <i>et al.</i> , 2013a
	SnO <sub>2</sub> -coated ZnO nanofiber	200	0.4-5.5	-	100 <sup>C</sup>	5.5	200	-	-	Moon <i>et al.</i> , 2009a
	ZnO-core/SnO <sub>2</sub> -shell nanowires	200	0.5-10	-	66.3 <sup>C</sup>	10	200	~53 s	~62 s	Hwang <i>et al.</i> , 2010b
	SnO <sub>2</sub> -ZnO hybrid nanofibers	200	0.4-4	180	105 <sup>C</sup>	4	200	-	-	Park <i>et al.</i> , 2010
	ZnO-SnO <sub>2</sub> nanocomposite	-	-	250	34.5 <sup>C</sup>	500	250	-	-	Liangyuan <i>et al.</i> , 2008
	ZnO-SnO <sub>2</sub> nanofiber-nanowire heterostructure	350	0.1-70	-	35 <sup>C</sup>	0.1	350	~250 s	~250 s	Choi <i>et al.</i> , 2013
Oxygen	SnO <sub>2</sub> -core/ZnO-shell nanofibers	300	70-2000	-	0.2 <sup>B</sup>	70	300	-	-	Choi <i>et al.</i> , 2009
Toluene	ZnO-SnO <sub>2</sub> nanofibers	360	1-25000	360	9.8 <sup>A</sup>	100	360	5 s	6 s	Song <i>et al.</i> , 2009
	SnO <sub>2</sub> -ZnO hollow nanofibers	190	1-300	190	50.2 <sup>A</sup>	300	190	11 s	23 s	Wei <i>et al.</i> , 2011

$$A = (R_a/R_g), B = (R_g - R_a)/R_a, C = (R_g/R_a), D = (R_a - R_g)/R_a$$

where,  $R_a$ - Resistance in ambient environment,  $R_g$ - Resistance in test gas environment, and RT- room temperature.

## 2.6 Gas Sensors based on $\text{Zn}_2\text{SnO}_4$ Nanostructures

### 2.6.1 Growth and Characterization

The processing routes developed for the growth of  $\text{Zn}_2\text{SnO}_4$  nanostructures can be divided into two categories. They are wet processing route and vapour-phase processing route. The wet processing routes include hydrothermal, electrospinning, sol-gel, solvothermal and chemical-solution method. But, vapour-transport and thermal evaporation methods represent vapour phase processing routes.

Limited reports of the production of ZTO nanostructures by hydrothermal methods have been reported as compared to  $\text{ZnO}/\text{SnO}_2$ . There are a number of morphologies, such as hierarchical nanostructures, nanoflowers and nanoparticles were produced by this method, while nanowires are seldom generated by this process. However, Chen *et al.* (2011) reported an inexpensive fabrication technique for spinel ZTO flower-like hierarchical nanostructures at a low temperature compared to Mary Jaculin *et al.* (2013). A solution containing  $\text{Zn}(\text{CH}_3\text{COO})_2 \cdot 2\text{H}_2\text{O}$ ,  $\text{Na}_2\text{SnO}_3 \cdot 4\text{H}_2\text{O}$ , Cetyltrimethylammonium bromide (CTAB) and ethylenediamine (EDA) was employed for the growth of ZTO flower-like hierarchical nanostructures at 180 °C. Precipitate was transferred to substrate for fabricating tube-like ultrasensitive sensors (Chen *et al.*, 2011). The resulting flower-like hierarchical nanostructures are self-assembled from uniform nanorods with diameters of approximately 100 nm and they have good mechanical stability even at ultrasonic conditions (Figure 2.12(a)). The morphology and dimension of flower-like hierarchical nanostructures were function of growth times, amount of CTAB surfactant and EDA ligand in solution. Irregular cubes were produced by decreasing the concentration of CTAB and reaction time, and increasing the concentration of EDA in solution. Experimental results showed cooperation of self-assembly and Oswald ripening processes assist the formation of flower-like hierarchical

structure. Similarly, Mary Jaculin *et al.* (2013) demonstrated ZTO nanoflower by the same method without the use of seeds or templates or surfactants. The morphology with dense bouquet of flowers was obtained at a higher temperature growth due to enhance the atomic mobility and caused the better grain growth. These nanoflowers have multilayered petals, which are uniform in size like a cluster of nanosheets of 90 nm thickness (Figure 2.12(b)). In this case, the morphology of ZTO was strongly influenced by the reaction temperature and the reaction time. In contrary, Jiang *et al.* (2011), Annamalai *et al.* (2011) and Kim *et al.* (2011) were synthesized ZTO nanoparticles using the same method.

A solvothermal process was also used to produce ZTO nanostructures (Jiang *et al.*, 2012; Sun *et al.*, 2014; Li *et al.*, 2012). The morphology of nanoparticles and nanowires were obtained in this method. Jiang *et al.* (2012) synthesized cube-like hierarchical ZTO particles. The mixed solution of  $\text{ZnCl}_2$  and  $\text{SnCl}_4 \cdot 5\text{H}_2\text{O}$  was stirring vigorously until uniform suspension was formed. The suspension was then transferred to a autoclave and maintained at 220 °C for 6 h. After the autoclave was cooled to room temperature, the white precipitates were collected by centrifugation, washed to remove ions in the final product. Finally, the precipitates were dried at 60 °C in air. A SEM image shows that the as-prepared ZTO product is composed of a large number of uniform cube-like particles ranging from 1.5  $\mu\text{m}$  to 2.5  $\mu\text{m}$  in size (Figure 2.12(c)). Similarly, crystalline ZTO nanoparticles were synthesized via a simple solvothermal route by Sun *et al.* (2014). The nanoparticles were prepared using  $\text{Zn}(\text{CH}_3\text{COO})_2 \cdot 2\text{H}_2\text{O}$  and  $\text{SnCl}_4 \cdot 5\text{H}_2\text{O}$  as source materials, NaOH as mineralizing agent, and water and ethanol as mixed solvents. The size of these nanoparticles is measured to be about 5-8nm and 12-15 nm for molar ratio of  $\text{OH}^- : \text{Zn}^{2+} : \text{Sn}^{4+}$  of 4 : 2 : 1 and 8 : 2 : 1, respectively. These nanoparticles exhibit superior photocatalytic properties due to their small crystal size and high surface

area. In contrast, Li *et al.* (2012) demonstrated ZTO nanowire arrays for the first time grown onto a stainless steel mesh in a binary ethylenediamine/water solvent system using the similar method. The nanowires have needle-like sharp tips, diameters in the range 20-50 nm and lengths up to several  $\mu\text{m}$ , which are parallel to one another and perpendicular to the substrate. These nanowires exhibit great bendability and flexibility proving a potential advantage over other metal oxide nanowires such as  $\text{TiO}_2$ ,  $\text{ZnO}$  and  $\text{SnO}_2$  as photoanodes for flexible solar cells.

Choi *et al.* (2011) grew ZTO nanofibers by the electrospinning technique. In this process, the precursor solution containing zinc acetate, tin(IV) acetate and two different kinds of polymers (PVA and PVP). As-spun Zn-Sn composite fibers exhibited randomly oriented fibers in the form of nonwoven mats with diameters ranging from 380 to 718 nm and lengths of several hundred micrometres. The formation of polycrystalline ZTO fibers was observed after calcination of the composite fibers at 700 °C. Therefore, crystallization of Zn-Sn precursors formed into inverse spinel ZTO. Diameters of the ZTO fibers ranged from 352 to 705 nm, which are smaller than those of as-spun fibers (Figure 2.12(d)). This calcined ZTO fibers exhibited a porous surface and lotus-root-like morphologies due to decomposition of PVAs.

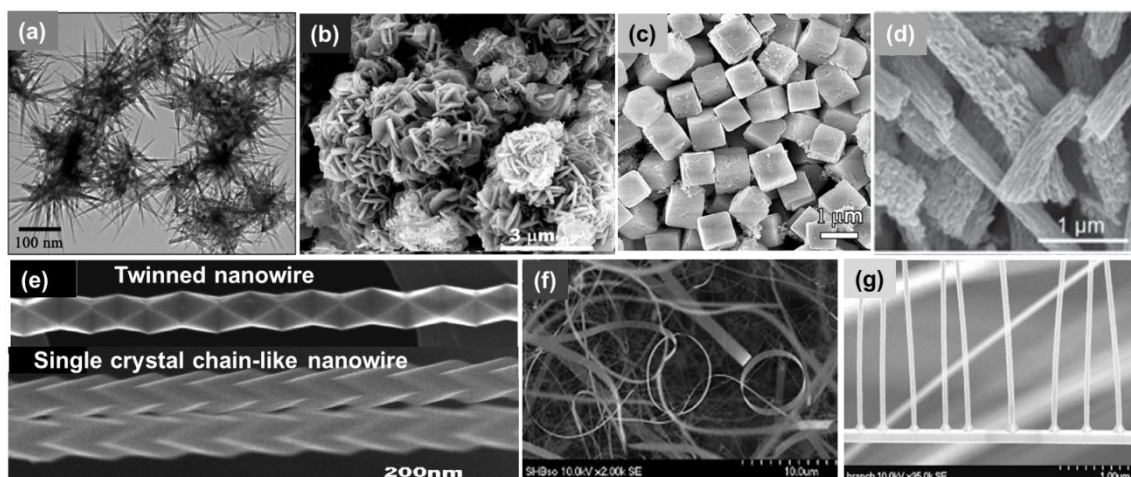


Figure 2.12. Various morphologies of  $\text{Zn}_2\text{SnO}_4$  nanostructures: (a) hierarchical nanostructure (Chen *et al.*, 2011), (b) nanoflower (Mary Jaculine *et al.*, 2013), (c) cube-like nanoparticles (Jiang *et al.*, 2012), (d) nanofibers (Choi *et al.*, 2011), (e) zig-zag nanowire (Wang *et al.*, 2007), (f) nanobelts and nanoring (Wang *et al.*, 2004), and (g) dendritic structure (Jun *et al.*, 2008).

Two different vapour phase routes were developed in reported literature according to their growth mechanism of ZTO nanowires. They are vapour-liquid-solid (VLS) and vapour-solid (VS) mechanism processes. In VLS mechanism growth process, two kinds of catalysts including Au and Sn were used for the growth of ternary ZTO nanowire, where Sn is act as self-catalytic (Su *et al.*, 2007). In the VLS growth process,  $\text{Zn}_2\text{SnO}_4$  nanostructures are fabricated mainly by thermal evaporation of a powder mixture of  $\text{ZnO} + \text{SnO}$  (Chen *et al.*, 2005) or  $\text{Zn} + \text{SnO}$  (Chen *et al.*, 2012) or  $\text{ZnO} + \text{SnO}_2$  (Jie *et al.*, 2004) or  $\text{ZnO} + \text{SnO} + \text{C}$  (Jun *et al.*, 2008; Pang *et al.*, 2010) or  $\text{ZnO} + \text{SnO}$  (Su *et al.*, 2007) on Au coated substrate. In contrast,  $\text{Zn} + \text{SnO}$  (Chen *et al.*, 2011; Wang *et al.*, 2007; Wang *et al.*, 2004; Wang *et al.*, 2004) or  $\text{Zn} + \text{Sn}$  (Liang *et al.*, 2012; Wang, *et al.*, 2005) powder mixtures were used for the VS growth of ZTO nanowires.

Reports on a series of ZTO nanostructures with very different morphologies have been published by the Xie group, who conducted similar evaporation experiments. They so-far demonstrated ZTO quasi-1-D nanostructures, including smooth nanobelts, nanorings

(Wang *et al.*, 2004), chainlike single-crystal wires (Wang *et al.*, 2004) and twinned wires (Wang *et al.*, 2007). In the following, the two types of extraordinary nanostructures are selectively discussed. The first is the twinned nanowire. Wang *et al.* (2007) reported VLS grown twinned ZTO nanowires by evaporating powder mixtures at 1000 °C with two types of weight ratios. In one case a ratio of Zn : SnO= 1:3 gave twinned nanowires (Figure 2.12(e)), whereas in the other case, a ratio of Zn : SnO= 2:1 was needed for the production of nanobelts and ring (Figure 2.12(f)). All these ZTO wires have a  $[1\bar{1}1]$  growth direction, with the twin planes being  $(1\bar{1}1)$  and the twinning direction perpendicular to the wire axes. The second is the single-crystal chainlike nanowire (Figure 2.12(e)). Structurally this type of wire was formed by a sequential stacking of rhombohedral nanocrystals along the  $[1\bar{1}1]$  direction. But according to the careful electron tomography study by Kim *et al.* (2008), who also obtained both types of chainlike ZTO nanowires and the above structure of the twinned nanowires were actually the same.

Jie *et al.* (2004) observed diameter modulated ZTO nanowires composed of linked ellipses using thermal evaporation of equal molar powder of ZnO and SnO<sub>2</sub> powder at 1400 °C under low pressure of 150 torr. In this process, diameter modulated ZTO nanowires were obtained due to variation of concentration of vapours. The high-temperature evaporation and deposition method involves a complicated thermodynamic and kinetic process. Therefore partial pressures of oxygen and ZnO/SnO vapour are very inhomogeneous which causes disturbances of the Au–Zn–Sn ternary droplet size in the VLS growth and hence diameter oscillations. Moreover, such an evaporation method usually ends up with a mixture of different phases and structures in the growth set. For example, ZnO and ZTO nanowires were identified in the XRD analysis (Jie *et al.*, 2004).

In the work of Jun *et al.* (2008), thermal evaporation and condensation process is utilized for the production of periodic ZTO dendritic nanostructures. In this procedure, ZnO powder was mixed with SnO and activated carbon powder with weight ratio of 6:4:1. The Au coated (~1 nm thick) Si substrate was used as a substrate to grow nanostructure under 2 Pa pressure at the temperature of 900 °C. The flow rate of 300 sccm Ar with 1 sccm O<sub>2</sub> was purged. The resulting nanodendritic had several hundreds of micrometers in length. The branch arrays are distributed only on one side of a rough trunk to form a dendritic structure as shown in Figure 2.15 (g). Moreover, branches reveals that it has own periodic structure formed by a row of overlaid rhombohedra of nanocrystals along the axis of the branch. At each junction between the trunk and the branch has pyramid structure. Besides the ZTO dendrites, there are some axially periodic ZTO nanowires. The growth mechanism of nanodendritic is mainly governed by VLS growth and surface diffusion of Au to form branches. Both Zn and Sn vapours react with Au and form Au-Zn-Sn alloy. Then this alloy further reacts with oxygen and form ZTO nanowires. After, the nanowires grown at first stage serve as substrate for the secondary deposition of the Au catalyst to grow branches. The detailed mechanism of the growth is not unclear.

Among the synthesis methods, thermal evaporation and hydrothermal are the most commonly employed methods for the production of ZTO nanostructures. The nanostructures obtained by hydrothermal and electrospinning processes are nanoparticles (cube, hierarchical) and nanofibers, respectively. However, presence of Au or Sn catalyst is essential during VLS mechanism assisted growth process for the production of ZTO nanowires. In the thermal evaporation process, temperature (900-1000 °C) and low pressure are involved and a variety of nanostructures could be obtained including nanowires (normal, zigzag), nanobelts, nanoring and nanodendritics.

In this synthesis method, ZTO nanostructures grow not only in the presence of Au/Sn catalyst but also in the absence of catalyst.

### 2.6.2 Sensing Performance of $\text{Zn}_2\text{SnO}_4$ Nanostructures

In the reported literatures, the sensitivity of ZTO nanostructures was evaluated for different target gases such as liquefied petroleum gas (LPG), ethanol, n-butylamine ( $\text{C}_4\text{H}_9\text{NH}_2$ ),  $\text{H}_2\text{S}$ , CO,  $\text{NO}_2$  and NO. The morphology of the nanostructures employed for sensing included nanowires, nanorods, hierarchical nanostructures, nanofibers, nanoparticles and thin films. Sensitivity, optimum detection temperature, response time and recovery time were considered to evaluate the sensing performance.

Chen *et al.* (2011) synthesized zigzag ZTO nanowires by thermal evaporation method for ethanol sensing. The sensitivity of zigzag ZTO nanowires was 12 upon exposure to 50 ppm ethanol. The detection or working temperature is not reported in this work. The response and recovery time were about 7 s and 8 s, respectively. Nanorods with a flowerlike morphology developed by Chen *et al.* (2011) had a response of 5 at 128 °C for 20 ppm ethanol concentration. The response was further increased by annealed of nanorods with a flowerlike morphology. It was seen that the sensitivity of annealed sensor had a response of 8 at 128 °C for 20 ppm, which was superior to that of the un-annealed sensor. The increased sensitivity with annealed sensor on ZTO flower like hierarchical structure was explained by the basic nature of formation of defects during annealing. Chen *et al.* (2015) showed flower-like ZTO structure had significance difference response towards  $\text{C}_2\text{H}_5\text{OH}$  with compact structure, which were prepared by similar synthesis procedure. Flower-like structure (30.4 for 50 ppm) exhibited ~3 times enhanced sensitivity than compact structure (12.8 for 50 ppm). The improvement of sensing performance was explained by increased effective surface area of the



hierarchical nanostructure. The compact structure showed greater response and recovery times for ethanol (13 s and 15 s) than the flower-like structure (9 s and 7 s). For the compact structure, the ethanol is difficult to diffuse into the interior structure, thus sensing reactions can only happen at the outer surface. As a result response shows low value and retard the fast response and recovery times. Choi *et al.* (2011) developed dense and porous ZTO nanofibers by electrospinning process. The gas response to 100 ppm of C<sub>2</sub>H<sub>5</sub>OH of porous ZTO nanofibers (300) was 3.75 times higher than that of dense ZTO nanofibers (80). The enhanced C<sub>2</sub>H<sub>5</sub>OH sensing of porous nanofibers was attributed to their highly porous structure with a higher surface area (29.02 m<sup>2</sup> g<sup>-1</sup>) and larger accessible pore volume than that of dense ZTO nanofibers. Therefore, porous structure facilitated fast gas transport and enhanced the sensitivity. The response to 100 ppm CO (~10) and H<sub>2</sub> (~10) was very negligible with C<sub>2</sub>H<sub>5</sub>OH (~300) at 450 °C. Thus, the selective detection of C<sub>2</sub>H<sub>5</sub>OH was observed with the minimum interference of CO and H<sub>2</sub>.

The performance of ZTO nanocomposites was evaluated for LPG gas and the response to 250 ppm concentration was found to be 2.5 at 375 °C (Singh *et al.*, 2010). It was also observed that the response tended to decrease from 2.5 to 1 with an increase in annealing temperature from 400 to 800 °C. They explained this behaviour was due to the annealing that had promoted the grain growth and led to decrease in the sensor sensitivity. The slow recovery was described by the sluggish surface reactions of adsorption, dissociation, and ionization of oxygen. It was found that with an increase in temperature the recovery time decreased. Sivapunniyam *et al.* (2011) attempted to improve the sensing performance of the sensor towards LPG by surface modification of ZnO nanorods using ZTO microcubes. They observed high response of 63% for 3000 ppm LPG at 250 °C when compared to sensor with pure ZnO nanorod (59%). The

enhancement in response was attributed to the chemical composition and crystal morphology of the ZTO that offers enhanced active sites for reaction of LPG molecules with adsorbed oxygen. The orientation and morphology of the crystals are the main factors influencing the adsorption and desorption processes. The ratio of edge and corner atoms increased as the size of the crystal domain become smaller, while the surface topology also became increasingly roughened. The crystal size distributions provide an opportunity to tailor the interaction and adsorption of gas molecules on the exposed surfaces of ZTO cubic structures on ZnO nanorods. Therefore, sensor performance was increased for LPG gas.

The multiple networked ZTO-core/ ZnO-shell nanorod sensors showed a response of 498 % to NO<sub>2</sub> concentrations of 5 ppm at 300 °C (Park *et al.*, 2013b). These response values are 4 times higher than those of the ZTO nanorod sensor (118 %) and 90 times greater than those of the ZnO nanorod sensor (5.56 %) over the same NO<sub>2</sub> concentration range. The substantial improvement in the response of the ZTO nanorods to NO<sub>2</sub> gas by the encapsulation of ZnO can be explained by the space-charge model. The calculated length of depleted layer was ~21.7 nm at 300 °C, whereas the observed thickness of ZnO shell was 20 nm. Therefore ZTO core also depleted during sensor response. Thus, effect of hetero-structure gave improved response towards NO<sub>2</sub> in core/shell structure. The response time of core/shell nanorods was also found to be faster (90 s) compared to undoped ZnO nanorod (370 s) or ZTO nanorod (100 s). Further, Ganbavle *et al.* (2014) developed ZTO thin film based sensor. It showed that highest response was achieved of 2.66 for NO<sub>2</sub> concentration of 200 ppm at 200 °C and selectively sensed against of NH<sub>3</sub>, CO, LPG, SO<sub>2</sub> and H<sub>2</sub>S. This greater sensitivity was attributed to the common sensing mechanism of adsorption-desorption process. The relatively long response time was believed to be caused by the low chemical reaction rate.

Cube-like hierarchical structure of ZTO was exposed to various n-butylamine concentrations by Jiang *et al.* (2012). It is reported that the gas response of the ZTO-based sensor increased far slowly with n-butylamine ( $C_4H_9NH_2$ ) concentration, and the value of sensitivity at 400 ppm n-butylamine was 102.2. The adsorption of gaseous n- $C_4H_9NH_2$  molecules from both Zn sites and Sn sites of ZTO could help to promote surface reaction efficiency. Thus, the better sensitivity was observed to n- $C_4H_9NH_2$ , rather than to other tested gases like HCHO,  $CH_3CN$  and  $CHCl_3$ . Ma *et al.* (2012) developed a hollow ZTO microcrystal-based sensor for  $H_2S$  detection. It was found that the sensitivity of hollow microcrystal at 260 °C was 45 for 100 ppm concentration. The improvement of sensitivity was ascribed to the higher surface area ( $43.768\text{ m}^2/\text{g}$ ) associated with the ZTO hollow structures.

From the review of reported literature, it can be surmised that  $Zn_2SnO_4$  nanostructure-based sensors were developed with reasonable success for detecting a range of gases including  $C_4H_9NH_2$ , LPG,  $C_2H_5OH$ ,  $H_2S$ ,  $NO_2$ , CO and NO. However, the sensitivity and selectivity was improved by morphological modifications. The hierarchical structures were enhanced sensitivity by increased surface area. Additionally, preparation of  $Zn_2SnO_4$  nanofiber also improves the sensitivity of the sensors by increased pores in its structure. The response times and recovery times were rarely reported in literature. A summary of  $Zn_2SnO_4$  nanostructured sensor performance is presented in Table 2.4.

Table 2.4. Summary of gas sensing properties of Zn<sub>2</sub>SnO<sub>4</sub> (ZTO) nanostructures

Tested gas	Morphology	Detection temperature (°C)	Detection range (ppm)	Type of sensor	Optimum temperature (°C)	Gas response			Response time	Recovery time	Reference
						Sensitivity	Concentrations (ppm)	Temperature (°C)			
n-butylamine	ZTO cube-like hierarchical structure	350	25-400	Tube	-	102.2 <sup>A</sup>	400	350	-	-	Jiang <i>et al.</i> , 2012
LPG	ZTO microcubes on ZnO nanorods	250	2250-3000	Film	-	0.63 <sup>D</sup>	3000	250	-	-	Sivapunniyam <i>et al.</i> , 2011
	ZTO Composite	375	-	Film	-	2.5 <sup>E</sup>	250	375	-	-	Singh <i>et al.</i> , 2010
	ZTO nanoparticles	400	50-500	-	-	0.65	100	400	-	-	Devi & Hamoon, 2012
Ethanol	Zigzag ZTO nanowires	-	1-200	Tube	-	12 <sup>A</sup>	50	-	7 s	8 s	Chen <i>et al.</i> , 2011
	flower like ZTO nanostructures	128	10-100	Tube	128	8 <sup>A</sup>	20	128	-	-	Chen <i>et al.</i> , 2011
	Quasi-cubic ZTO nanoparticles	325	30-600	Tube	325	94.3 <sup>A</sup>	600	325	-	-	Jiang <i>et al.</i> , 2011
	ZTO -SnO <sub>2</sub> nanocomposites	300	25-500	Tube	300	0.85 <sup>D</sup>	500	300	-	-	Lu & Tang, 2005
	ZTO nanofiber	450	1-100		-	300 <sup>A</sup>	100	450			Choi <i>et al.</i> , 2011
	3D hierarchical flower		5-100			30.8 <sup>A</sup>	50	380	9 s	7 s	Chen <i>et al.</i> , 2015
	polliwog-like Sn/ZTO structure	240	25-600	Tube	240	42 <sup>C</sup>	200	240	-	-	Han <i>et al.</i> , 2013
H <sub>2</sub> S	ZTO hollow microcrystal	260	1-100	Tube	-	45 <sup>A</sup>	100	260	10 s	25 s	Ma <i>et al.</i> , 2012
CO	SnO <sub>2</sub> -ZTO composite	-	-	pellet	350	12 <sup>A</sup>	200	350	-	-	Moon <i>et al.</i> , 2001
NO <sub>2</sub>	ZTO thin film	200	50-200	Film	200	2.66 <sup>D</sup>	200	200	43 s	326 s	Ganbavle <i>et al.</i> , 2014
	ZTO core/ZnO shell nanorod	300	1-5	Film	-	4.98 <sup>C</sup>	5	300	90 s	100 s	Park <i>et al.</i> , 2013b
NO	ZTO thin film	-	-	Film	420	5.6 <sup>A</sup>	120	420	-	90 s	Stambolova <i>et al.</i> , 1998

A= (R<sub>a</sub>/R<sub>g</sub>), B=(R<sub>g</sub>-R<sub>a</sub>)/R<sub>a</sub>, C=(R<sub>g</sub>/R<sub>a</sub>), D= (R<sub>a</sub>-R<sub>g</sub>)/R<sub>a</sub>, E=(G-G<sub>0</sub>)/G<sub>0</sub>, where, R<sub>a</sub>- resistance in ambient environment, R<sub>g</sub>- resistance in test gas environment, G- conductance of the sensor in the test gas, and G<sub>0</sub>- conductance of the sensor in the air.

## 2.7 Summary of Literature

Metal oxide semiconductors are promising candidate for gas sensing because of their unique electrical properties, moderate electron mobility, high performance, low cost and simple fabrication methods. Nanostructures provide very high effective surface to volume ratios which is essential for an efficient gas sensor. So, the direction of this research is moved towards one dimensional nanostructure from bulk sensing materials. Some factors which can influence the enhanced sensitivity and selectivity of sensor performance are related to the development of nanostructures with different morphologies, doping of metal oxide catalyst, mixed metal oxide nanostructures and surface modification by noble metal or metal oxide nanoparticles. In mixed metal oxide nanostructures, growth of  $\text{ZnO/SnO}_2$  and  $\text{Zn}_2\text{SnO}_4$  nanostructures for sensing application needs some extra care to conserve the required materials properties. The core-shell nanostructures provide greater sensing due to formation of a physical interface between two different materials. Usually, these nanostructures have been synthesized by a two-step process. But, this study focuses on the growth of  $\text{SnO}_2$ -core/ $\text{ZnO}$ -shell nanostructure by a single-step carbothermal reduction process. In literature, The sensing performance of  $\text{ZnO/SnO}_2$  and  $\text{Zn}_2\text{SnO}_4$  nanostructure based sensors was studied extensively for ethanol sensing. But, research to selectively sense ethanol in the present of other gases is not widely conducted. Thus, this study is motivated towards selectively sensing ethanol in the presence of other test gases using  $\text{ZnO/SnO}_2$  and  $\text{Zn}_2\text{SnO}_4$  nanostructures and finding the optimum conditions for sensing ethanol selectively.

## CHAPTER 3

### METHODOLOGY

This chapter describes the details of the raw materials and processing methods used for the synthesis of zinc oxide and tin oxide based nanostructures. Various characterization techniques including X-ray diffraction (XRD), field emission scanning electron microscopy (FESEM), transmission electron microscopy (TEM) and photoluminescence spectroscopy (PL) were used to investigate the properties of the nanostructures. The fabrication process of gas sensors and details in sensing measurements are also described.

#### 3.1 Experimental Flow Chart

Figure 3.1 shows the flow chart of the detailed experimental procedure.

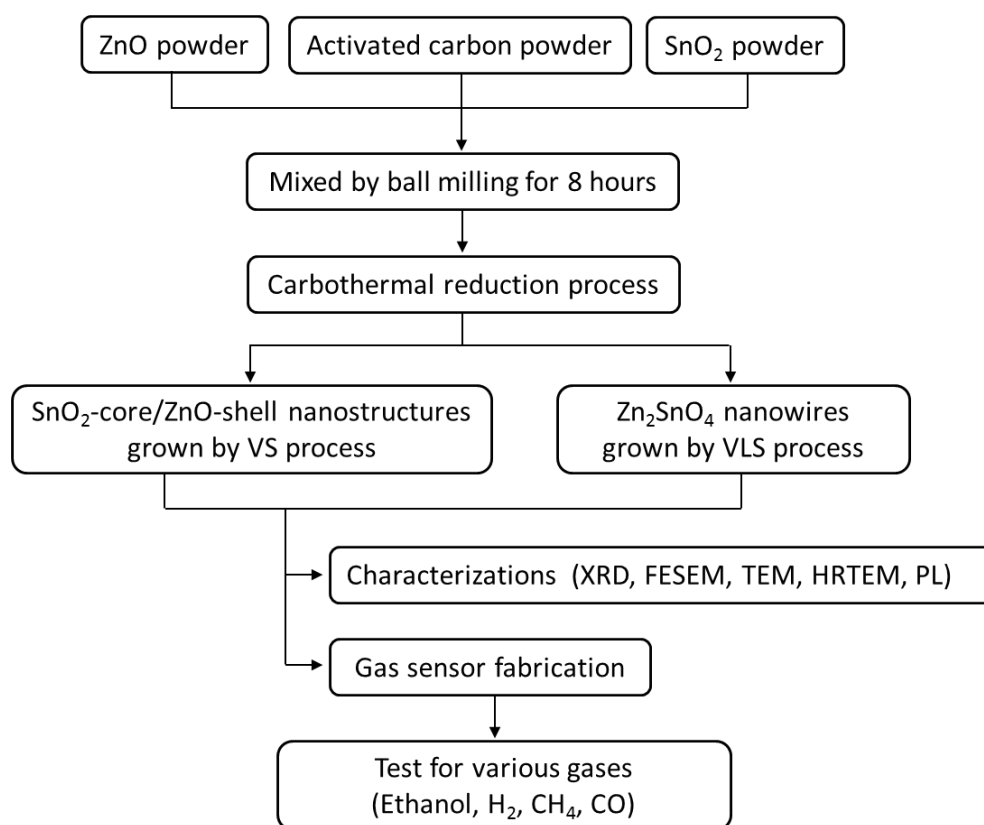


Figure 3.1: Flow chart of the experimental procedure adopted in this work.

### 3.2 Materials and Chemicals

In this research work, analytical grade commercial zinc oxide (ZnO) powder of 99 % purity with an average particle size of 350 nm (Sigma-Aldrich, USA), tin oxide (SnO<sub>2</sub>) powder of 99.9% trace metals basis with an average particle size of 44 μm (~325 mesh, Sigma-Aldrich, USA), and activated carbon (R&M Chemicals, UK) powder were used to prepare the precursor mixture to synthesis zinc oxide and tin oxide based nanostructures. α-terpineol (Sigma-Aldrich, USA), diethylene glycol dibutyl ether (DGDE, Sigma-Aldrich, Switzerland) and ethyl cellulose (Sigma-Aldrich, USA) were used as the binding materials to prepare the ink in sensor fabrication.

### 3.3 Preparation of Precursor Mixture

Planetary ball mill is typically used to enhance homogeneous mixing and to obtain fine mixture. A mixture of ZnO, SnO<sub>2</sub>, and activated carbon powders with the molar ratio of 9:1:10 was prepared. (Weight ratio;  $W_{ZnO} : W_{SnO_2} : W_C = 2.93 \text{ g} : 0.603 \text{ g} : 0.48 \text{ g}$ ). The powder mixture was then transferred into a ceramic grinding jar of diameter 4.5 cm, along with 25 hardened zirconia balls (diameter and weight of each ball is around 10 mm and 3 g, respectively) to perform dry grinding using Retsch-Planetary Ball Mill PM 100. The ball to particle weight ratio was 10:1. Milling was carried out for 8 hours continuously with a rotational speed of 250 rpm to obtain a homogeneous mixture of particles. The milling process was performed with an automatic reversal for every minute to avoid agglomeration and to enhance homogenization. After milling was completed, the mixture was separated from the milling balls. Finally, the milled powder was characterized by FESEM and XRD to evaluate the particle size and the phase content in the mixture after milling, respectively. Similarly, various mixtures with different molar ratio of ZnO to SnO<sub>2</sub> powder (ZnO: SnO<sub>2</sub> = 8:2, 7:3, 6:4, 5:5, 4:6, 3:7, 2:8 and 1:9) were prepared and characterized the nanostructures obtained.

### 3.4 Substrate Preparation

There are many techniques used in micro-fabrication such as sputtering and evaporation to deposit precious metals including gold and palladium on the substrate. In the present work, sputtering was used to deposit gold on the alumina ( $\text{Al}_2\text{O}_3$ ) substrate. Research grade Au sputtering target was used for deposition. Gold atoms were released from the sputtering target using  $\text{Ar}^+$  ion and deposited onto a substrate to form a thin film or a coating layer. In this process, the substrate was placed inside the sputtering chamber. The sputtering chamber was evacuated via standard rotary vacuum pump. The standard gas of argon was provided inside the chamber to bombard the Au sputtering target.

The thickness of the gold coating ( $d$ ) in angstroms ( $\text{\AA}$ ), can be expressed from the following equation (Mirchin *et al.*, 2013):

$$d = K I V t \quad (3.1)$$

where,  $K$  is a constant which depends on the deposition of metal used in sputtering,  $I$  is the plasma current (mA),  $V$  is the voltage applied (kV) and  $t$  is the sputtering time (s). Constant  $K$  for gold metal is about 0.07. For typical sputtering, plasma current applied for gold metal is 18 mA. In the present work, a thin gold layer of around 40  $\text{\AA}$  thickness was deposited to an alumina substrate by sputtering from a gold target at a rate of about 1.25  $\text{\AA}/\text{s}$  and the applied voltage was about 1 kV using SPI module sputter coater. The sputter time to produce 40  $\text{\AA}$  thickness of Au films and it was set to be 30 s based on the calculation given below:

$$\begin{aligned} t &= \frac{d}{KIV} \\ &= \frac{40 \text{ \AA}}{0.07 \times 18 \text{ mA} \times 1 \text{ kV}} = \sim 30 \text{ s} \end{aligned}$$



### 3.5 Synthesis of Zinc Oxide and Tin Oxide based Nanostructures

The synthesis of ZnO and SnO<sub>2</sub> based nanostructures in the present work involved a carbon-assisted thermal evaporation process under ambient pressure (1 atm). The schematic diagram of experimental setup is shown in Figure 3.2(a). Gold interdigitated alumina was used as the substrate (5 mm x 5 mm) and 99.99% purified Ar was used as a carrier gas to transfer Zn and Sn vapour from source to substrate. The grinded powder mixture was transferred into a quartz boat and then it was placed at the center of a horizontal tube furnace (Lindberg Blue M: TF55035COMA1), which is denoted as letter 'B'. Gold sputtered alumina substrates were placed towards the downstream of carrier gas which is represented by letter 'A'. These substrates were located at various distances (3 cm, 6 cm, 9 cm and 12 cm) from the center of the furnace to optimize the nanowire growth. Prior to the exposure of Ar gas with a constant flow rate, the quartz tube was first purged with Ar gas for 15 minutes to remove unwanted contaminations inside quartz tube including excess oxygen by using a digital mass flow controller (Sierra: C100L-CM-NR-2-0V1-SV1-PV2-V1). Then Ar gas was introduced with a constant flow rate of 25 sccm (standard cubic centimeters per minute) during the growth period. After that, the temperature of the furnace was increased from room temperature to various growth temperatures (800 °C, 850 °C, 900 °C and 950 °C) at a rate of 30 °C/min and maintained for various growth times (15 min, 30 min, 60 min, 90 min and 120 min). Subsequently, furnace temperature was cooled down to room temperature and the substrates were removed. A light grey layer was observed on the gold coated alumina substrate. Concurrently, a white wool-like mass was observed to form at the edges as well as on the top of the quartz boat. The white fluffy mass was also collected for characterizations. The temperature variation as a function of distance from the center of the furnace was measured using a ceramic bead thermocouple, which is presented in

Figure 3.2(b). This temperature profile helps to determine the optimum location of the substrate and growth temperature for the formation of nanowires.

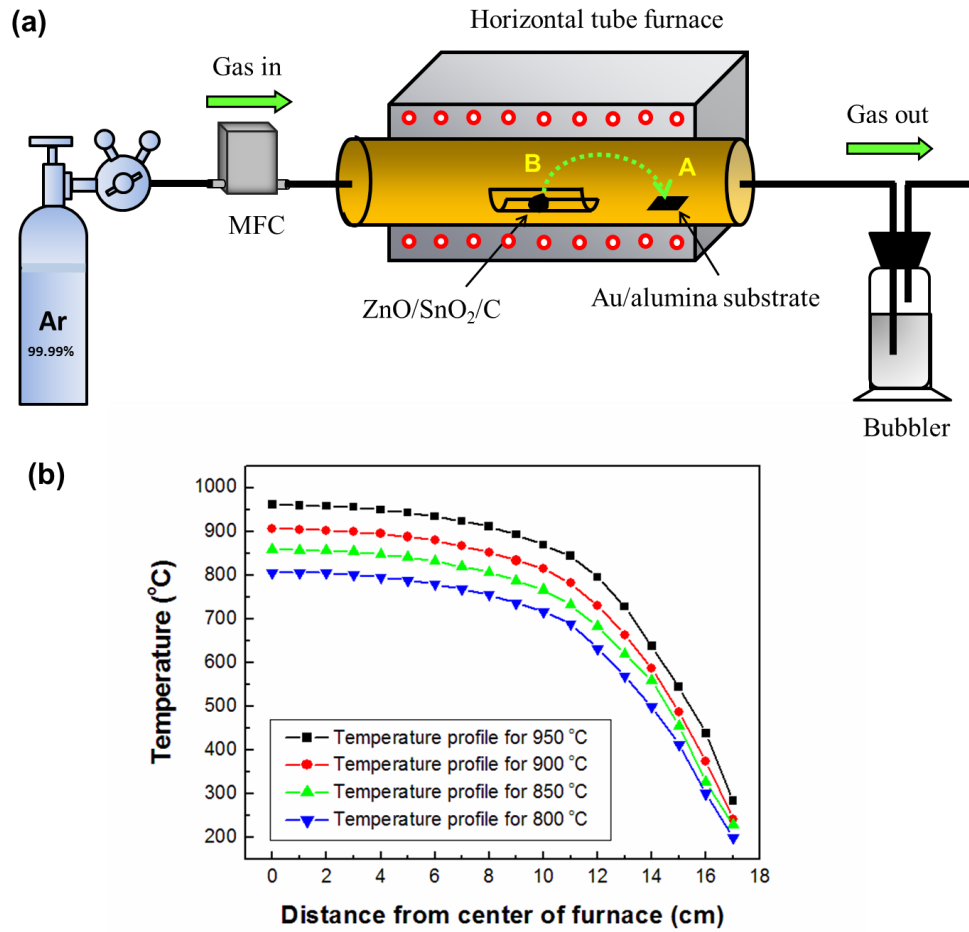


Figure 3.2: (a) Experimental setup for the growth of SnO<sub>2</sub>-core/ZnO-shell nanostructures (location B) and Zn<sub>2</sub>SnO<sub>4</sub> nanowires (location A); (b) measured temperature as a function of distance from the center of the furnace at 25 sccm Ar flow for various furnace center temperatures.

Two control experiments were conducted with two samples to find the effect of gold layer and activated carbon powder:

- (i) with activated carbon powder in the source mixture and no Au layer in alumina substrate, and
- (ii) with Au layer in alumina substrate and no activated carbon powder in the source mixture.

### 3.6 Sensor Fabrication

Gas sensor based on  $\text{SnO}_2$ -core/ $\text{ZnO}$ -shell nanostructures was fabricated as given below. Initially, 46 wt% of  $\alpha$ -terpineol, 8 wt% of ethyl cellulose, and 46 wt% of diethylene glycol dibutyl ether (DGDE) were weighted individually using digital balance (Pioneer, Ohaus). Then, the weighted  $\alpha$ -terpineol and DGDE were mixed at room temperature in a glass container. The ethyl cellulose was then added to the mixture and heated on a hotplate (Cole-parmer) around 200 °C until ethyl cellulose was completely dissolved. 1 mg of synthesized nanostructures was added to the ink of 50  $\mu\text{l}$  and ultrasonicated for 5 min. Finally, the ink was drop-coated via micropipette on an alumina substrate ( $\text{Al}_2\text{O}_3$ ) having a dimension of 5 mm x 5 mm with printed Au interdigitated electrode to form sensor (Case Western Reserve University, USA). After drying in air at room temperature, the sensor device was heat-treated at 700 °C for 1 hour in air atmosphere at which the phase contents were stabilized. The schematic illustration of sensor fabrication is presented in Figure 3.3. On the other hand, sensor based on  $\text{Zn}_2\text{SnO}_4$  nanowires was used directly for sensor measurements without further preparation.

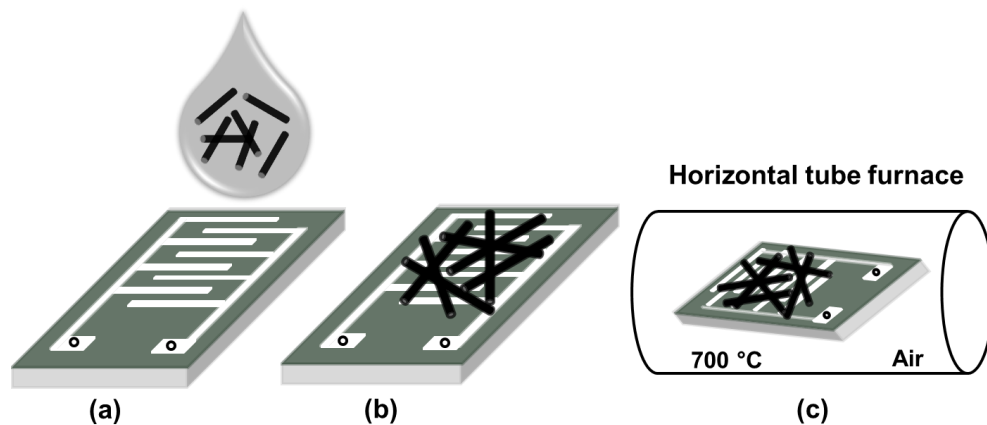


Figure 3.3: Schematic illustration for sensor fabrication process using  $\text{SnO}_2$ -core/ $\text{ZnO}$ -shell nanostructures: (a) drop coating  $\text{SnO}_2$ /ZnO nanostructure suspension on printed Au interdigitated electrode; (b) nanostructures arrangement on sensor device; (c) Heat treatment of sensor device.

### **3.7 Characterization Techniques**

#### **3.7.1 X-ray Diffraction (XRD)**

The phase of crystalline materials was examined by Siemens D-5000 model X-ray diffractometer with a monochromatic  $\text{CuK}_\alpha$  radiation ( $\lambda=1.5406 \text{ \AA}$ ) and Ni filter. The applied current and operating voltage were 40 mA and 40 kV, respectively. The scanning was performed between  $20^\circ$  and  $70^\circ$ , with a scanning rate of  $0.03^\circ/\text{sec}$ . The resulting diffraction peaks were compared with the standard reference pattern of Joint Committee on Powder Diffraction Standards (JCPDS) to identify the material. After the growth has been done, the collected samples were subjected to XRD to find the crystal structure of the composites. The white wool-like mass was collected from the quartz boat for various growth times and spread on a carbon tape for XRD characterization. A light grey layer observed on the alumina substrate was used directly for XRD characterization.

#### **3.7.2 Field Emission Scanning Electron Microscopy (FESEM)**

Morphological investigation of the fabricated nanostructures was carried out by two different models of FESEM instruments: Auriga Zeiss Ultra-60 and FEI Quanta FEG 450 field emission scanning electron microscopy. Elemental composition was obtained using field emission scanning electron microscopy coupled with energy dispersive X-ray spectroscopy (EDS) with applied beam voltage of 20 keV. Imaging was obtained by using Auriga Zeiss Ultra-60 FESEM. The white wool-like mass spread on a carbon tape was used for FESEM analysis. Light grey layer formed on alumina substrate was directly used to find the morphology of nanostructures.

#### **3.7.3 Transmission Electron Microscopy (TEM)**

Transmission electron microscopy was used to investigate the detailed morphology of  $\text{SnO}_2$ -core/ $\text{ZnO}$ -shell and  $\text{Zn}_2\text{SnO}_4$  nanostructures. A 200 KeV TEM (FEI Tecnai F-20

microscopy) was used to obtain the images. The elemental distribution of zinc oxide and tin oxide based nanostructures was obtained by TEM equipped with an energy dispersive X-ray spectroscopy (EDS). High-resolution transmission electron microscopy (HRTEM) was used to detect imaging of the atomic structure of the sample. The same microscopy was utilized to characterize the high resolution imaging (HRTEM) of the nanostructure and selected-area electron diffraction (SAED) pattern. Samples for TEM imaging were prepared as follows: zinc oxide and tin oxide based nanostructures scratched from the substrate were dispersed in deionized water. This was followed by ultra-sonication for 5 minutes, and then a tiny amount of suspension was drop-coated onto a carbon coated Cu grid (300 mesh) by using a micropipette. Finally the Cu grid was placed inside TEM for the high resolution observation of the oxide nanostructures.

#### **3.7.4 Photoluminescence Spectroscopy (PL)**

The crystalline quality and defect structure of the samples were studied by photoluminescence (PL) spectroscopy. PL spectra from SnO<sub>2</sub>-core/ZnO-shell nanostructures produced at various growth times and Zn<sub>2</sub>SnO<sub>4</sub> nanowires were recorded by Renishaw's inVia PL/Raman microscope, using He-Cd laser as an excitation source, with an operating wavelength of 325 nm. The scanning range for the samples was recorded within the wavelength range of 350-800 nm. Two different intensities of the source (2 mW and 10 mW) were used to characterize the nanostructures.

#### **3.7.5 Sensor Measurements**

The schematic representation of sensor measurement is shown in Figure 3.4. Ink made using SnO<sub>2</sub>-core/ZnO-shell nanostructures on printed Au interdigitated electrode, and Zn<sub>2</sub>SnO<sub>4</sub> nanowires grown on printed Au interdigitated electrode were used as gas sensors. Gold wire (99.9% metal basis, Alfa Aesar, USA) with the diameter of 0.2 mm

was connected to Au interdigitated electrode and small amount of Au conducting paste (Heraeus, Germany) was applied to make the effective electrical connection between electrode and gold wire junction. This was followed by curing at 700 °C for 1 h in an ambient environment to ensure the good conductivity of sensor.

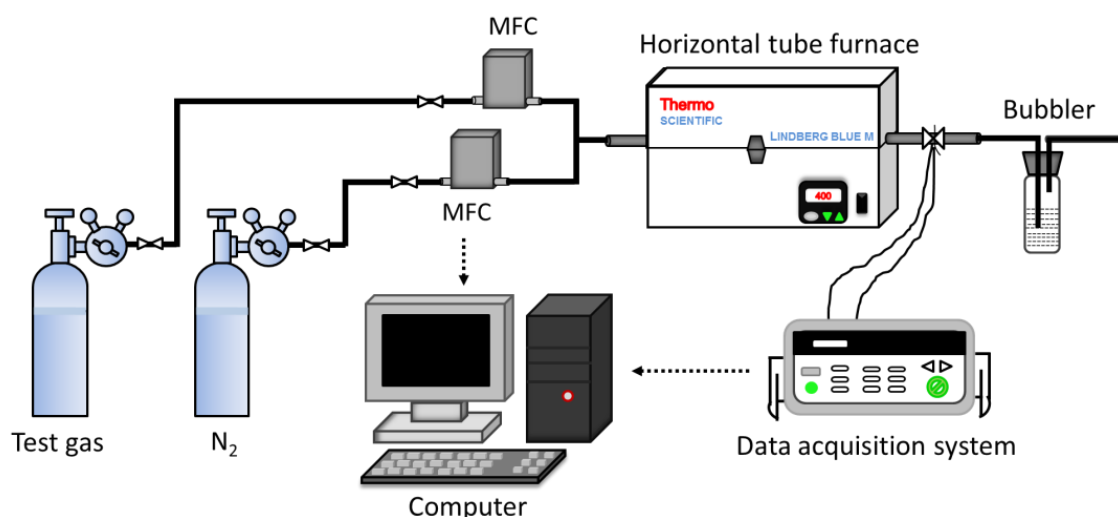


Figure 3.4: Schematic representation of setup for gas sensor characterization

For sensor measurement, the sensor was placed in a quartz tube inside a horizontal tube furnace and sensor electrical resistance measurements were carried out using a data acquisition system to find the optimum operating temperature for desired gases. The operating temperature was changed from 300 °C to 550 °C for Zn<sub>2</sub>SnO<sub>4</sub> nanowire-based sensor and SnO<sub>2</sub>-core/ZnO-shell nanostructures-based sensor at constant gas concentrations of 50 ppm and 20 ppm, respectively. After that, the sensor electrical resistance measurements were carried out in the desired test gas at various gas concentrations: 20, 50, 100, 250, and 400 ppm. The gas concentrations were controlled by changing the mixing ratio of the target gas to nitrogen gas using a computer controlled digital mass flow controller. The sensitivity of the sensor was defined as the ratio between ( $R_a - R_g$ ) and  $R_a$ , where  $R_a$  and  $R_g$  are the sensor resistances measured in

nitrogen, and target gases, respectively. The response and recovery times are defined as the time taken by the sensor to attain 90 % of the response and recovery signals, respectively (Yang *et al.*, 2006). The optimum operating temperature, sensitivity, response and recovery times were also determined for different target gases including carbon monoxide (CO), methane (CH<sub>4</sub>), hydrogen (H<sub>2</sub>) and ethanol (C<sub>2</sub>H<sub>5</sub>OH).

## CHAPTER 4

### RESULTS AND DISCUSSION

This chapter examines the effect of growth time, temperature and location of substrate on the development of  $\text{Zn}_2\text{SnO}_4$  and  $\text{SnO}_2/\text{ZnO}$  core-shell nanostructures, and study the microstructure, structural and optical properties of the fabricated nanostructures. Additionally, this chapter also explores the gas sensing properties of zinc and tin oxide based nanostructures with various morphologies.

#### 4.1 Microstructure of Mixed Powder after Ball Mill

The ball milling was used to mix the source materials of  $\text{ZnO}$ ,  $\text{SnO}_2$  and activated C powders well and also reduce the particle size of mixture. The small particle size mixture allows creating metal vapour easily. Figure 4.1(a) shows the morphology of the mixture of zinc oxide, tin oxide and activated carbon powders after ball milling for a grinding time of 8 hours. The particles in the mixture have irregular shape. The particle size varies in the range of 20 nm - 200 nm. The average size calculated from Figure 4.1(a) is around 150 nm. The XRD pattern of powder mixer after milling of 8 hours is shown in Figure 4.1(b). It exhibits the detection of single phase of  $\text{ZnO}$ ,  $\text{SnO}_2$  and C. This milled powder mixture was used as a source material to grow zinc oxide and tin oxide based nanostructures.

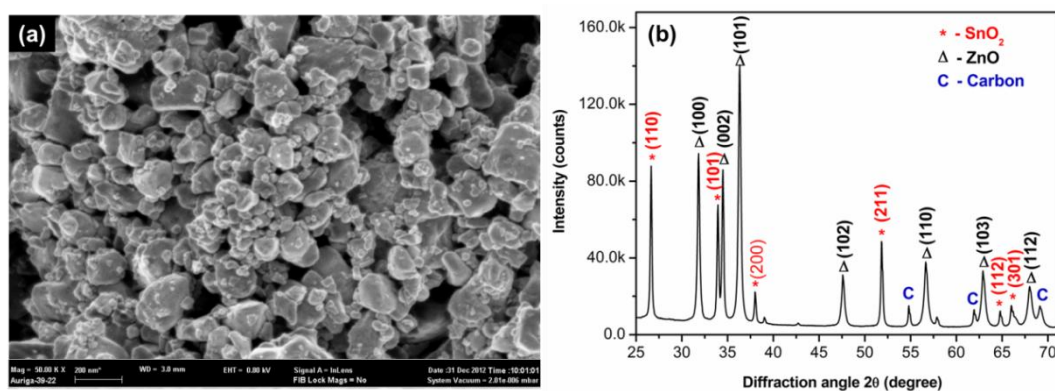


Figure 4.1: (a) Morphology and (b) XRD of source powder mixture after milling of 8 hours.



## 4.2 Growth of Nanostructures based on Zinc Oxide and Tin Oxide

This thesis work reports a novel single-step carbon assisted thermal evaporation (carbothermal reduction) approach for the synthesis of nanostructures based on zinc oxide and tin oxide. Zinc oxide, tin oxide and activated carbon were used as source material to form nanostructures. Initially, source material was loaded in the center of furnace and Au coated alumina substrate was placed at downstream of gas flow direction. Two different types of nanostructures were observed when the furnace center temperature was at 900 °C in two different places with a steady gas flow of purified argon at 25 sccm. Figure 4.2 shows the schematic representation of nanostructures formation at two different places.

- (i) on Au coated alumina substrate (denoted by letter 'A' in Figure 4.2) and
- (ii) on top of a quartz boat (denoted by letter 'B' in Figure 4.2).

These two different kinds of growth were observed concurrently in a single-step carbon assisted thermal evaporation process under ambient pressure. Single-crystalline  $\text{Zn}_2\text{SnO}_4$  nanowires were observed on gold (Au) coated alumina substrate (location A). On the other hand, a white fluffy mass was formed at the edge and on top of a quartz boat (location B) during the fabrication process. This white wool-like mass was identified as  $\text{SnO}_2$ -core/ $\text{ZnO}$ -shell nanowires and hierarchical nanostructures which depend on growth time. This process allows preparing and collecting various types of nanostructures by selecting the position of the substrate and deposition time.

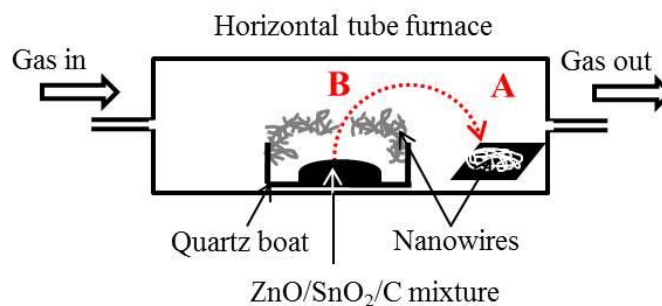


Figure 4.2: Schematic representation of formation of nanostructures at different places.

In this thesis, the characterizations of  $\text{Zn}_2\text{SnO}_4$  nanowires are firstly reported and later explained the characterization of  $\text{SnO}_2$ -core/ $\text{ZnO}$ -shell nanowires and hierarchical nanostructures. Finally gas sensing properties of both nanostructures based sensors towards various gases are described.

### **4.3 Characterization of $\text{Zn}_2\text{SnO}_4$ Nanowires**

#### **4.3.1 X-ray Diffraction Analysis (XRD)**

The phase structures of the as-synthesized products on Au coated alumina substrate (location A, Figure 4.2) were examined by X-ray diffraction. Figure 4.3 shows that the XRD pattern of  $\text{Zn}_2\text{SnO}_4$  nanowires obtained for samples prepared by carbothermal reduction process at 900 °C for a growth time of 120 min with molar ratio of  $\text{ZnO}$  to  $\text{SnO}_2$  in the source mixture of 9:1. Ternary compound of face-centered cubic spinel  $\text{Zn}_2\text{SnO}_4$  phase was detected in the XRD pattern which is denoted as ZTO in Figure 4.3. These peaks are consistent with the Joint Committee on Powder Diffraction Standard (JCPDS) card no of 24-1470. Au (111) and alumina peaks are also noticed which originated from the gold coated alumina substrate. A small peak of  $\text{ZnO}$  phase was also identified. Similar observation was previously made by Jie et al. (Jie *et al.*, 2004). The presence of sharp and strong X-ray diffraction peaks suggests that the  $\text{Zn}_2\text{SnO}_4$  nanowires have good crystallinity.

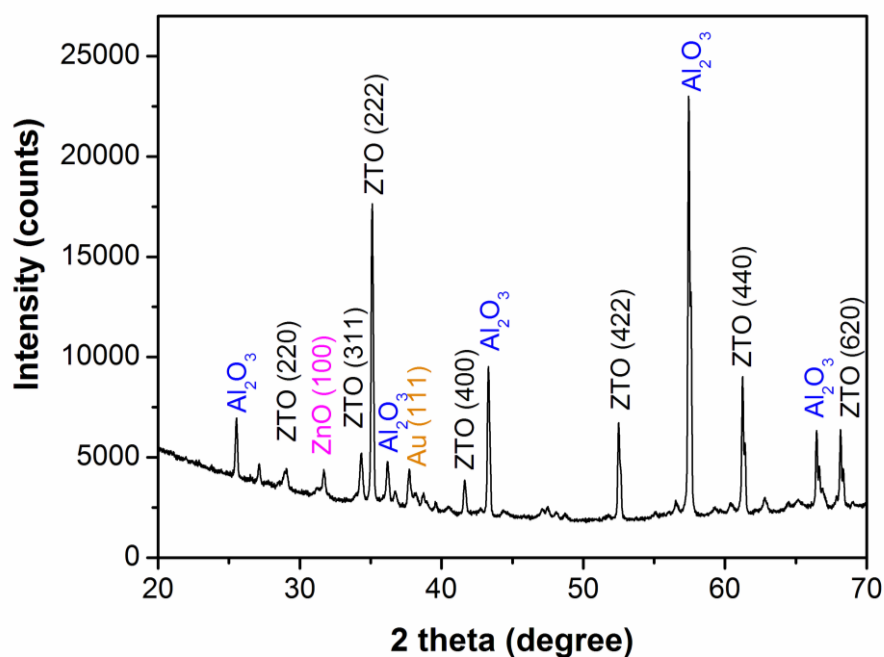


Figure 4.3: XRD patterns of nanowires obtained on Au coated alumina substrate at a furnace temperature of 900 °C with the deposition time of 120 min with molar ratio of ZnO to SnO<sub>2</sub> in the source mixture of 9:1 [ZTO represents Zn<sub>2</sub>SnO<sub>4</sub> phase].

#### 4.3.2 Effect of Au Catalyst and Activated Carbon

Two control experiments were performed to find the effect of Au layer and activated carbon on nanowire growth at a furnace temperature of 900 °C for 120 min with molar ratio of ZnO to SnO<sub>2</sub> in the source mixture of 9:1. One experiment involved the absence of Au layer on alumina substrate in the presence of activated carbon in the source mixture. Another involved the presence of Au layer on alumina substrate with the absence of activated carbon in the source mixture. Results of these two control experiments are illustrated in Figure 4.4. Figure 4.4(a) shows that no nanowires were formed in the absence of Au on alumina substrate in the presence of activated carbon. Similarly, no nanowires are present on Au/alumina substrate in the absence of activated carbon in the source mixture as it can be seen in Figure 4.4(b). High magnification image of the sample clearly shows spheroidal shaped particles on the substrate (Inset of Figure 4.4(b)). The EDS analysis of spheroidal shaped particles is illustrated in Figure

4.4(c). Higher intensity Au peak was detected on the particles. It confirmed that these are Au particles, which are formed by dewetting of the Au layer. Lower intensity peaks for elements such as Al, Cu, C, and O are also observed in the spectrum. These elements are believed to have originated from the substrate due to the use of high energy electron beam (20 keV). Therefore, the beam could have penetrated deeper than the diameter of Au nanoparticles.

In the presence of both carbon and Au, uniform and well distributed nanowires can be seen on Au/alumina substrate (Figure 4.4(d)). The diameter of the nanowires is in the range of 15-80 nm with a length of about 16-50  $\mu\text{m}$ . Figure 4.4(e) exhibits the enlarged image of the tip of a nanowire. The presence of a cap at the tip of the nanowire is observed. An EDS analysis was performed to find the composition of the tip of the nanowire which is shown in Figure 4.4(f). Peaks of Au, Zn, Sn and O were detected in the spectrum. The presence of high intensity Au peak at the tip of the nanowire strongly suggest that the growth of the nanowires was governed by the vapour-liquid-solid (VLS) assisted mechanism (Wang *et al.*, 2005) and gold acted as a catalyst for the growth of  $\text{Zn}_2\text{SnO}_4$  nanowires.

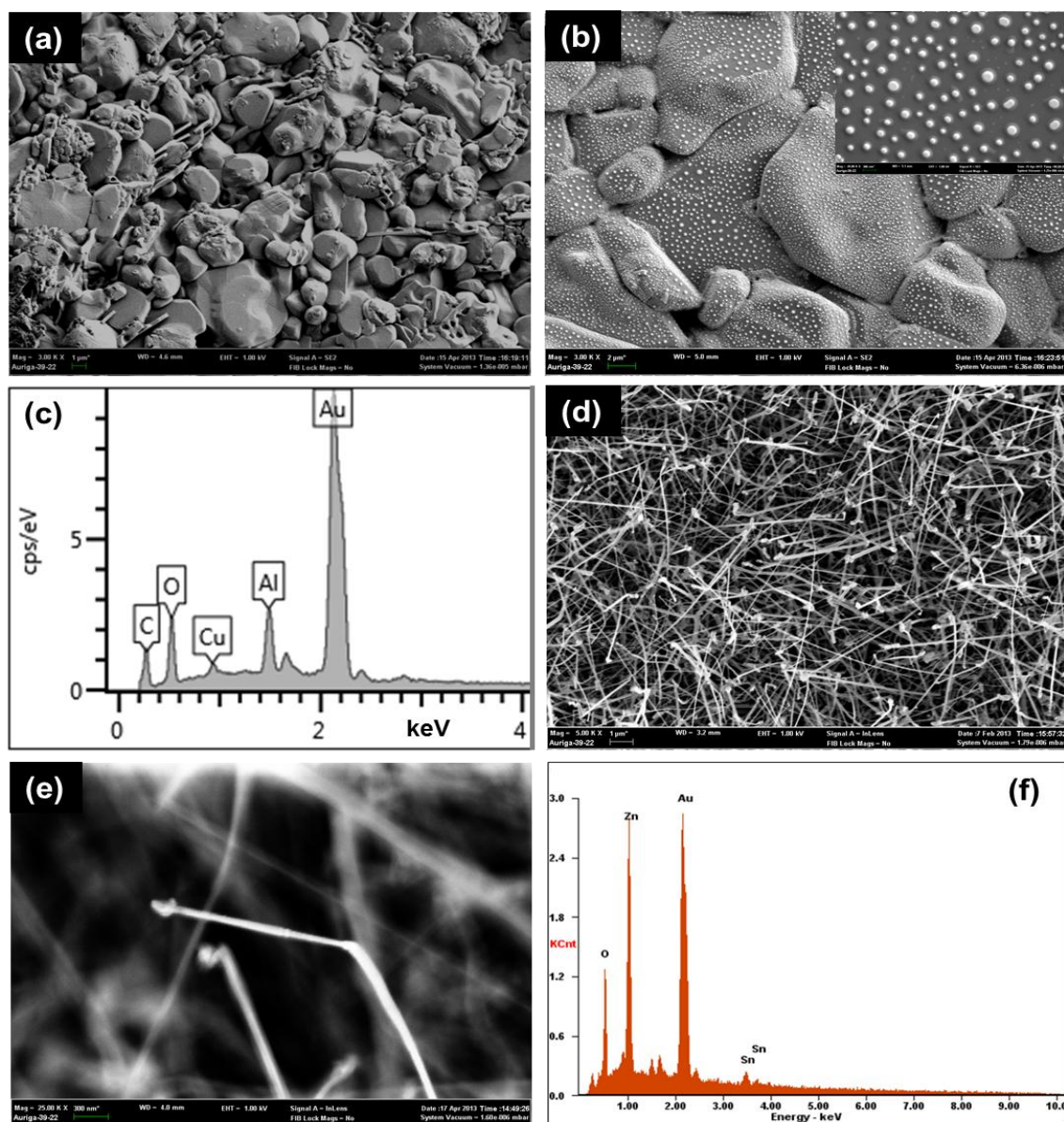


Figure 4.4: FESEM micrographs of the nanostructures prepared with molar ratio of ZnO to SnO<sub>2</sub> in the source mixture of 9:1 at a furnace temperature of 900 °C for 120 min grown on (a) alumina substrate in the presence of activated carbon, (b) Au/alumina substrate in the absence of activated carbon, (c) EDS analysis of spheroidal shaped particles on alumina substrate, (d) alumina substrate in the presence of both Au layer and activated carbon, (e) enlarged view of tip of the nanowire and (f) EDS analysis of tip of the nanowire.

It is believed that at a furnace temperature of 900 °C, the activated carbon dissociates ZnO and SnO<sub>2</sub> powders into Zn and Sn vapours, which condense on the Au/alumina substrate kept at a lower temperature region. The Sn and Zn metal vapours react with Au layer and form an alloy droplet on the alumina substrate. This alloy droplet becomes

super saturated after receiving more metal vapours that initiated the nanowire growth (Jun *et al.*, 2008). Therefore, the presence of activated carbon and Au are essential for the growth of nanowires, where the activated carbon acts as a reducing agent producing the metal vapours and the Au acts as a catalyst to grow the nanowires. In the literature, Jie *et al.* (2004) reported that the disturbance of the vapour concentration is a major factor that changes the diameter of the catalyst alloy droplets and the growth velocity of nanowires. A vapour disturbance induces a change in the zinc and/or tin concentration near the alloy droplet. Thus, the size of the droplet shrinks and the nanowire diameter decreases.

#### **4.3.3 Effect of Source Mixture**

Some experiments were carried out to find the effect of various parameters on the growth of  $\text{Zn}_2\text{SnO}_4$  nanowires by the carbothermal reduction method. The parameters including source mixture ratio, growth temperatures, growth times and substrate position from the center of the furnace were studied in this work. First, the effect of source mixture ratio between ZnO and  $\text{SnO}_2$  was studied. Figure 4.5 shows the micrographs of nanostructures obtained on Au/alumina substrate at a furnace temperature of 900 °C for 120 min with various ratios of source materials.

It shows the morphology changes from nanostructure to nanowire with increasing molar ratio of ZnO and decreasing amount of  $\text{SnO}_2$  in the source mixture. At the low molar ratio of ZnO in the mixture, no nanowires observed. At increasing molar ratio of ZnO to  $\text{SnO}_2$  from 2:8 to 7:3, nanowires start to initiate and observed nanowires rarely. At the ratio between ZnO and  $\text{SnO}_2$  of 8:2, the density of produced nanowires looks low and their length are relatively short (4  $\mu\text{m}$ ) compared to  $\text{ZnO}/\text{SnO}_2 = 9:1$ . A entangle and long nanowires was observed for the molar ratio of  $\text{ZnO}/\text{SnO}_2 = 9:1$ . The length of

produced nanowire is around 32  $\mu\text{m}$ . Therefore, the optimum growth of nanowires was observed when the source mixture contained ZnO to  $\text{SnO}_2$  of 9:1.

Several groups have reported various ZTO nanostructures produced by VLS mechanism with different ratio of source materials. ZTO dendritic nanostructures was observed by Jun et al. (Jun *et al.*, 2008) when the source materials contained ZnO to SnO weight ratio of 6:4. But, twinned ZTO nanowires was produced with ZnO/SnO mixed powders at weight ratio of 2:1 (Chen *et al.*, 2005). In contrast, normal ZTO nanowires was also developed with ZnO/SnO/C powder mixture with a weight ratio of 1:5:8 (Pang *et al.*, 2010). Thus, the ZTO ternary oxide nanowires in the final product depends on the ratio of source materials (Jie *et al.*, 2004).

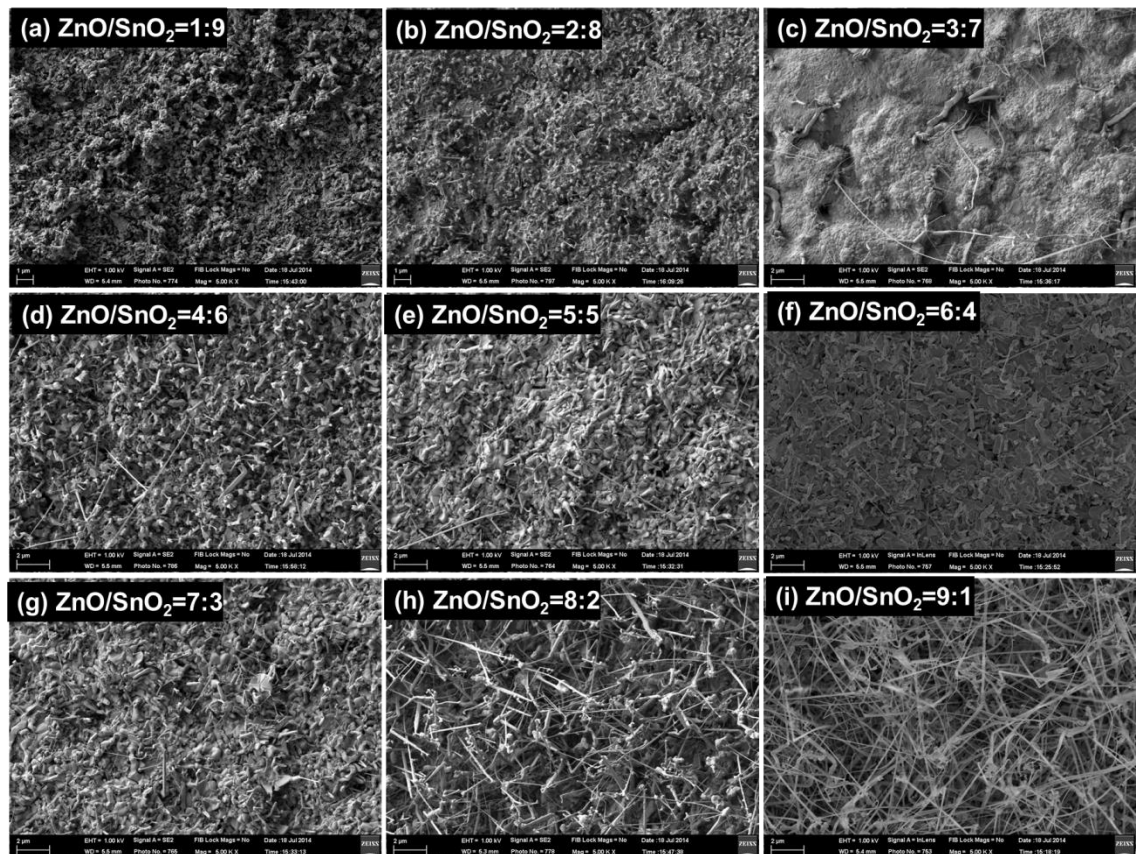


Figure 4.5: FESEM micrographs for nanostructures obtained at a furnace temperature of 900 °C with the deposition time of 120 min for different molar ratio of ZnO to  $\text{SnO}_2$  in the source mixture (a) 1:9, (b) 2:8, (c) 3:7, (d) 4:6, (e) 5:5, (f) 6:4, (g) 7:3, (h) 8:2 and (d) 9:1.

#### 4.3.4 Effect of Substrate Position and Various Growth Temperature

The effect of growth temperatures with various substrate positions was studied on the growth of ZTO nanowires. The temperature profile for the growth of nanostructures has 3 steps. In first step, furnace temperature was increased from room temperature to various growth temperatures (800 °C, 850 °C, 900 °C and 950 °C), and then hold the growth temperature for 2 hours followed by cooled down to room temperature. Figure 4.6 shows the FESEM micrographs of nanostructures grown at different furnace temperatures with various deposition positions. The growth temperatures of nanostructures at various deposition positions are illustrated in Table 4.1. At the low furnace center temperature of 800 °C, no nanowires were observed with different deposition positions (Figure 4.6(a)-(d)). The range of growth temperatures between 633 °C and 802 °C are not high enough to produce sufficient Zn and Sn vapour pressure to grow the nanowires (see Table 4.1). At these temperatures, a Au thin film does not break up into nanosized droplet (Wu *et al.*, 2002). Therefore no nanowires were observed. At a furnace center temperature of 850 °C, nanowires start to grow at the substrate position of 6 cm only (Figure 4.6(e)-(h)). Lengths of nanowires are very short and there are thicker in diameter which is shown at a high magnification in Figure 4.6(f). Therefore, the growth temperature of nanowires was found to be around 833 °C (Table 4.1). At moderate furnace center temperature of 900 °C, more heavily populated nanowires were observed at the deposition position of 9 cm in Figure 4.6(k). The length of nanowires was increased to several tens of micrometres with thinner diameter compared to furnace temperature of 850 °C, which is clearly shown in zoom in Figure 4.6(k). From this result, growth temperature of nanowires were observed at 834 °C (Table 4.1), which is consistent with the furnace center temperature of 850 °C at the deposition position of 6 cm. At high furnace temperature of 950 °C, a fewer nanowires were observed anywhere on the substrate (Figure 4.6(m)-(p)). This happens because the



growth temperatures for various deposition positions are too high for the condensation of metal vapours. Thus no nanowires were observed.

From these results, it is concluded that the optimum growth temperature for nanowire growth on Au coated alumina substrate is around 834 °C at a deposition position of 9 cm from the furnace center with a set furnace center temperature of 900 °C. Furnace temperatures of 800 °C and 850 °C are not high enough to produce sufficient vapour pressure to grow the nanowires. On the other hand, the furnace temperature of 950 °C is too high for the condensation of the metal vapours.

Table 4.1: Growth temperatures of nanostructures obtained at different furnace temperatures and various substrate positions.

Substrate position from center of furnace (cm)	Growth temperatures at different furnace center temperatures (°C)			
	800	850	900	950
3	802	854	900	956
6	780	833	880	935
9	737	788	834	893
12	633	684	730	796

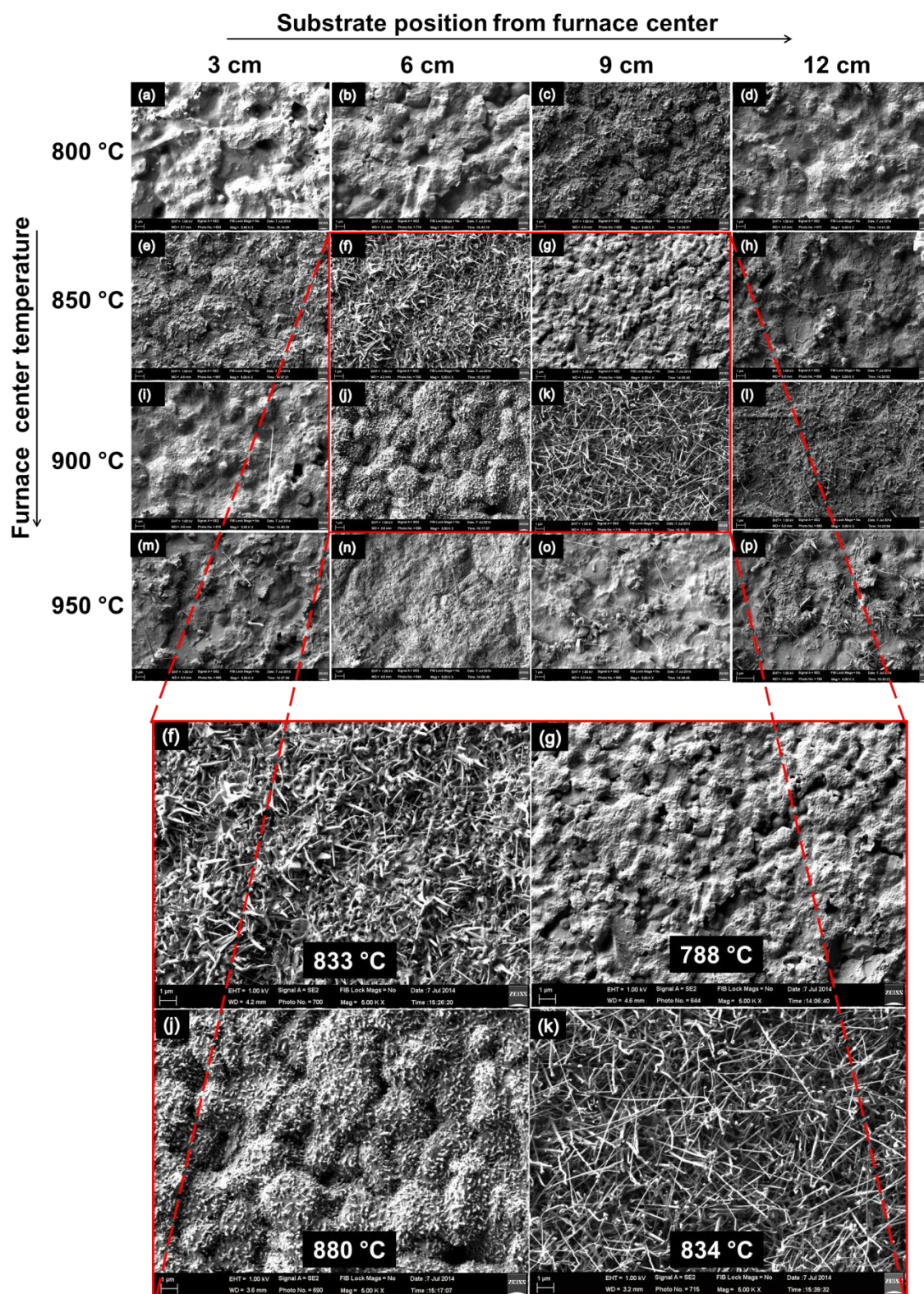


Figure 4.6: Top image: FESEM images of the nanostructures fabricated at different furnace temperature with various deposition positions of substrate from the center of the furnace. Bottom image: zoom in the FESEM images of nanostructures fabricated at 850 °C and 900 °C with the deposition positions of substrate at 6 cm and 9 cm.

#### 4.3.5 Effect of Growth Time

Figure 4.7 exhibits FESEM micrographs of  $\text{Zn}_2\text{SnO}_4$  nanowires grown on Au/alumina substrate at different growth times. The insets of figures show the single  $\text{Zn}_2\text{SnO}_4$  nanowire corresponding to the growth time. Growth time was varied from 15 min to 120 min, while the center position temperature of the tube furnace was kept at 900 °C and substrate was placed at 9 cm. As can be seen in Figures 4.7(a)-(c),  $\text{Zn}_2\text{SnO}_4$  nanowires grow sparsely on Au/Alumina substrate with 2-6 micrometer in length. But, Figures 4.7(d) and (e) exhibit that the  $\text{Zn}_2\text{SnO}_4$  nanowires grew homogeneously on the entire Au/Alumina substrate. For longer growth time of 120 min (Figure 4.7(e)), there was a dense growth of uniform and long nanowires. The lengths of the nanowires increased from 2 to 50 micrometer with increasing growth time from 15 min to 120 min. On the other hand, average diameter of the nanowire was observed as decreasing tendency with increasing growth time and which were measured around 80 nm, 72 nm, 68 nm, 63 nm and 58 nm for the growth time of 15 min, 30 min, 60 min, 90 min and 120 min, respectively. The decrease in diameter of nanowire may be attributed to the re-evaporation of materials during longer growth time. The smaller nanowire diameter can be explained by the Gibbs-Thomson effect (Fröberg *et al.*, 2007). It explains that an increasing reaction time and thereby decreasing supersaturating vapour lead to the diameter of the nanowire to become smaller (Wu *et al.*, 2002). From this analysis, it is concluded that the density and length of  $\text{Zn}_2\text{SnO}_4$  nanowires increased and diameter of nanowire decreased with increasing growth time.

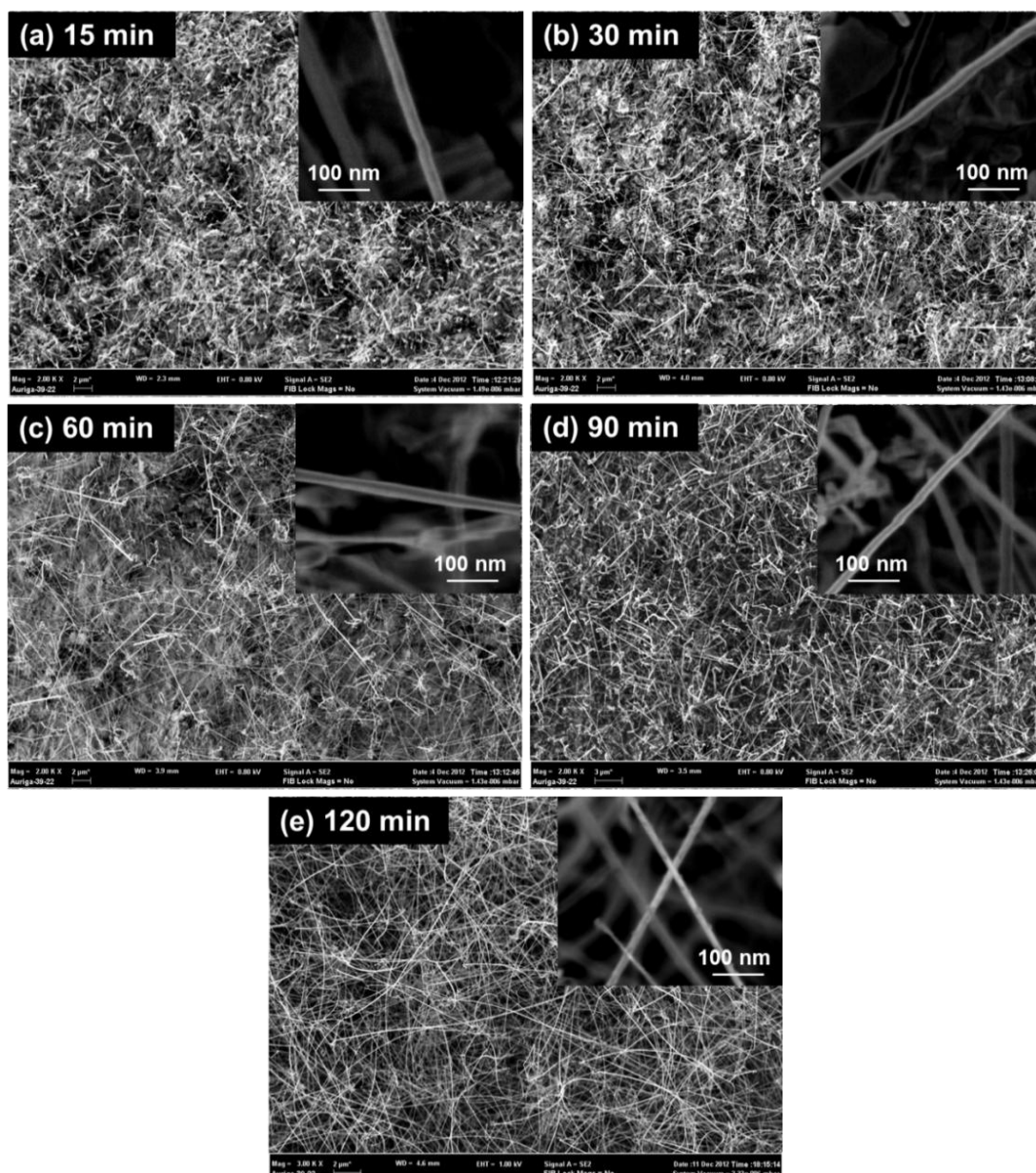


Figure 4.7: FESEM micrographs of the nanostructures synthesized at different growth time on Au/alumina substrate at a furnace center temperature of 900 °C: (a) 15 min, (b) 30 min, (c) 60 min, (d) 90 min and (e) 120 min. Inset are images of a single nanowire corresponding to the growth time.

#### 4.3.6 Transmission Electron Microscopy Analysis

To further analyse the crystal structure of  $\text{Zn}_2\text{SnO}_4$  nanowire, TEM characterization of the nanowires was conducted. A representative low magnification TEM image of a single  $\text{Zn}_2\text{SnO}_4$  nanowire detached from the substrate having a diameter of 25 nm is depicted in Figure 4.8(a). As we can see in Figure 4.8(b), a bright particle can be found at the tip of the nanowire, which presumably is the gold catalyst particle. The particle



size (10 nm) is smaller than the wire diameter (25 nm), which is unusual as most catalyst particles have similar or larger sizes than the diameters of the nanowires (Nguyen *et al.*, 2003; Wu *et al.*, 2004). Previously, FESEM-EDX analysis also confirmed that the tip of the catalyst particle was gold (Figure 4.4(f)). The presence of this gold cap at its tip indicating that the growth of nanowire was formed via the well-known vapour-liquid-solid (VLS) mechanism (Hu *et al.*, 2009; Morales & Lieber, 1998). The clear lattice fringes in Figure 4.8(c) of the HRTEM image show the single crystalline nature of the nanowire with an interplanar spacing of 0.26 nm, which is ascribed to the d-spacing of (311) plane of  $\text{Zn}_2\text{SnO}_4$  (Cherian *et al.*, 2013; Tan *et al.*, 2007). Thus the nanowire growth direction is believed to be [311] (Pang *et al.*, 2010). A selected area electron diffraction (SAED) pattern take over the nanowire is given in Figure 4.8(d). It also demonstrates the single-crystalline character of the nanowire.

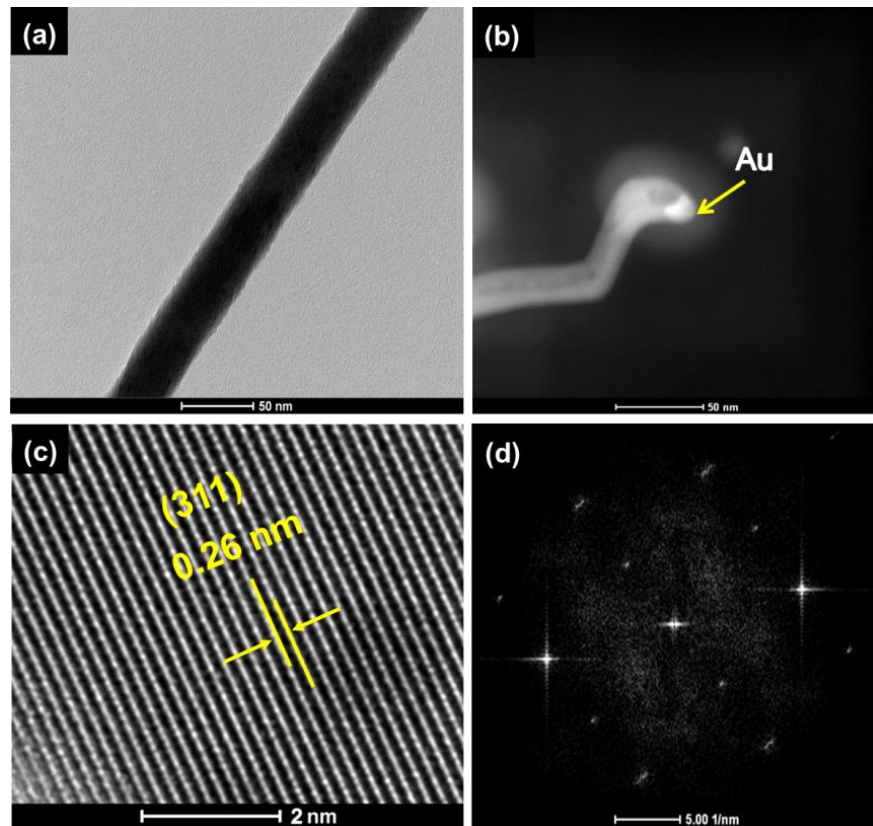


Figure 4.8: (a) Low magnification TEM images of a single  $\text{Zn}_2\text{SnO}_4$  nanowire deposited at 120 min, (b) nanowire with a gold catalyst at its tip, (c) High-resolution TEM image of the nanowire showing the lattice fringes and corresponding (d) SAED pattern over this single  $\text{Zn}_2\text{SnO}_4$  nanowire.

TEM elemental mapping and line scanning across the nanowire was performed to confirm the  $\text{Zn}_2\text{SnO}_4$  nanowires. A scanning TEM (STEM) mode was used to take an elemental image of the  $\text{Zn}_2\text{SnO}_4$  nanowire. Figure 4.9(a) exhibits the STEM image of an  $\text{Zn}_2\text{SnO}_4$  nanowire showing the elemental linescan trajectory across the nanowire diameter. The integrated EDX spectrum shows (Figure 4.9(b)) the presence of carbon and Cu, which originated from the carbon coated copper grid. The presence of peaks for Zn, Sn, and O are detected from the nanowire. Concentration line profiles of Zn, Sn, and O across the nanowire are presented in Figure 4.9(c). The profiles suggest that both Sn and Zn are homogeneously distributed within the nanowire and the nanowire is richer in Zn than Sn. This result is another evidence to prove that the nanowires are  $\text{Zn}_2\text{SnO}_4$  which were synthesized by the single-step carbothermal reduction method.

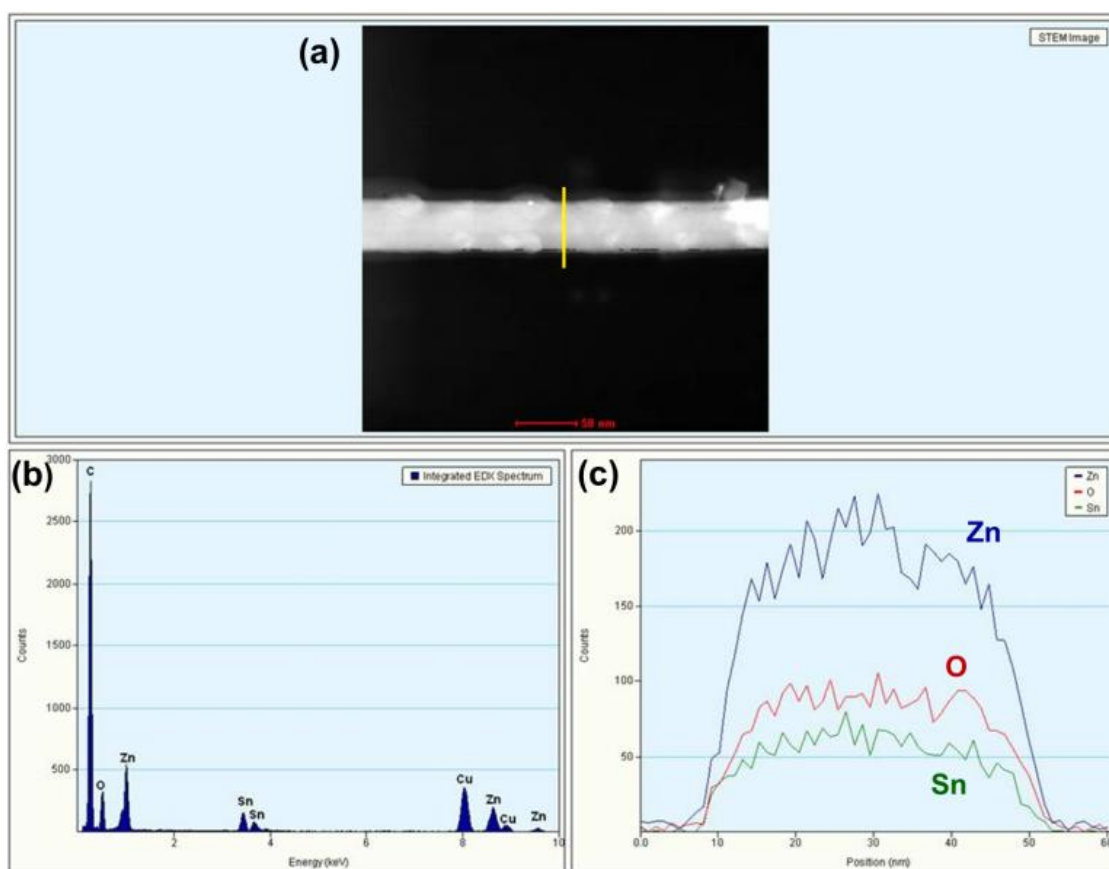


Figure 4.9: (a) STEM image of an  $\text{Zn}_2\text{SnO}_4$  nanowire showing the line scan trajectory, (b) Integrated EDX spectrum of the nanowire, and (c) Integrated peak counts as a function of spot position for Zn, Sn and O.

Additionally, the distribution of Zn, Sn and O in the nanowire was studied by TEM-EDX elemental mapping and is shown in Figure 4.10. Figure 4.10(a) presents a representative STEM image of the nanowire and the mapping area was denoted by yellow coloured box. The corresponding integrated EDX spectrum obtained from the nanowire is given in Figure 4.10(b). Counts of zinc were observed higher than that of tin. The enlarged image of mapping region (Figure 4.10(c)) and the corresponding Zn, Sn and O element maps illustrated in Figure 4.10(d)-(f). As shown in Figure 4.10(d)-(f), all elements in the  $\text{Zn}_2\text{SnO}_4$  nanowire are homogeneously distributed over the entire surface of the nanowire. From the distribution of elements, we further confirmed that all nanowires are  $\text{Zn}_2\text{SnO}_4$ . These observations are consistent with  $\text{Zn}_2\text{SnO}_4$  nanowires grown via catalyst free growth by Liang *et al.* (2012).

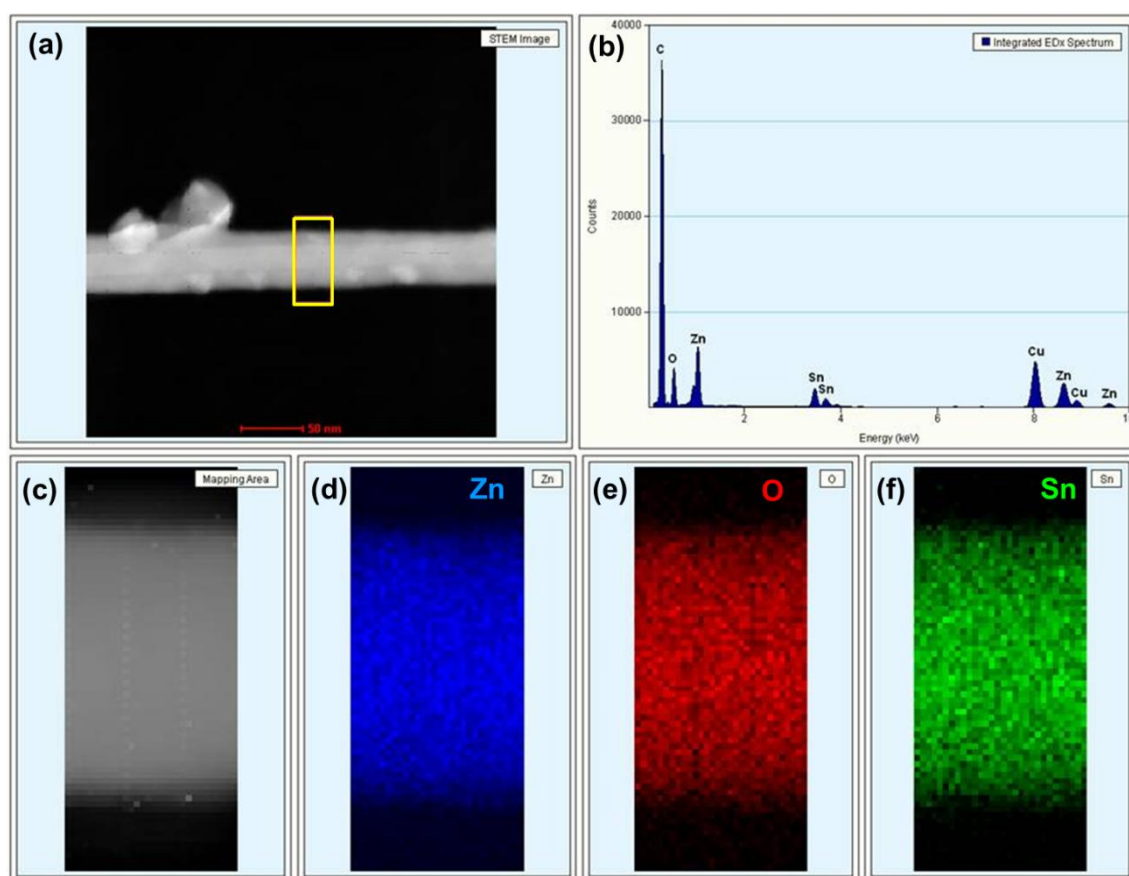


Figure 4.10: (a) STEM image of an  $\text{Zn}_2\text{SnO}_4$  nanowire, (b) Integrated EDX spectrum of the nanowire, (c) Magnified image of the mapping area indicated by box in (a), The colour maps demonstrating the spatial distribution of different elements, (d) Zn, (e) O, and (f) Sn, which are labelled in blue, red, green, respectively.

#### 4.3.7 Photoluminescence Studies

Optical properties of a semiconductor are related to both intrinsic and extrinsic effects (Sinha *et al.*, 2011). Photoluminescence (PL) is an appropriate technique to determine the crystalline quality and the existence of impurities in the nanostructures. Figure 4.11 shows the photoluminescence spectrum of  $\text{Zn}_2\text{SnO}_4$  nanowires measured at room temperature, with an output power of 2 mW. The inset of Figure 4.11 represents the intensity of source was increased to 10 mW and re-measured the PL spectrum within the wavelength range of 360 - 400 nm. Theoretically, the PL spectrum of nanostructures possesses two main features. One peak is at near band edge emission or band-to-band emission which originates from an exciton transition. Another one is the wide visible band emission due to the defects arising from impurities or vacancies in the nanostructures (Lee *et al.*, 2010).

As can be seen in Figure 4.11, high intensity peak for  $\text{Zn}_2\text{SnO}_4$  nanowires was detected in the visible emission band. It reveals that the nanowires have strong green emission band centered at a wavelength of 535 nm. In the previous investigations of the semiconducting nanowires, the PL mechanisms have been attributed to various luminescence centers, such as oxygen deficiency and residual strain during the growth process (Hu *et al.*, 2002; Wang *et al.*, 2007; Wang *et al.*, 2005). In this experiment, the carbothermal reduction process was employed to fabricate the  $\text{Zn}_2\text{SnO}_4$  nanowires, and thus as anticipated, will result in formation of oxygen vacancies due to insufficient oxygen during the growth process (Pang *et al.*, 2010). Also the one-dimensional nanostructures of the  $\text{Zn}_2\text{SnO}_4$  with high aspect ratio would favour the existence of large quantities of oxygen vacancies (Wang *et al.*, 2005). These oxygen vacancies induce new energy levels in the bandgap and lead the green emission (Wang *et al.*,



2004). Therefore, the green emission of  $\text{Zn}_2\text{SnO}_4$  nanowires in this study can be considered as mainly originating from the effect of the oxygen vacancies.

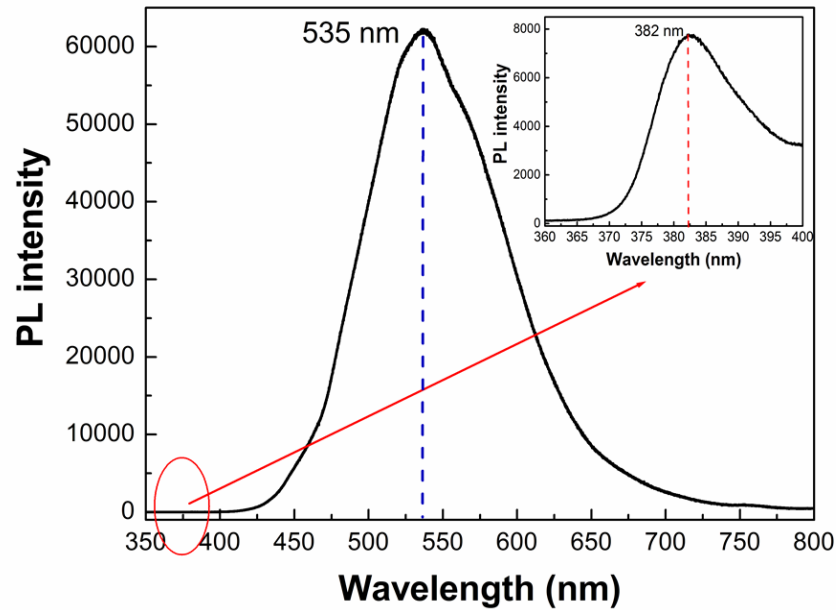


Figure 4.11: Photoluminescence spectrum of  $\text{Zn}_2\text{SnO}_4$  nanowires measured at room temperature with a power source of 2 mW, and inset shows the enlarged view of photoluminescence spectrum of  $\text{Zn}_2\text{SnO}_4$  nanowires recorded by increased power source of 10 mW within the wavelength range of 360-400 nm.

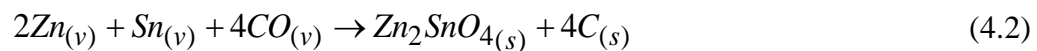
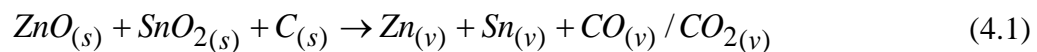
The PL spectrum (inset of Figure 4.11) was re-measured by increased power source of 10 mW within the wavelength range of 360 - 400 nm to find any observable peak. A weak peak was observed at 382 nm ( $\sim 3.3$  eV). Obviously, this emission peak is not the band-to-band emission of  $\text{Zn}_2\text{SnO}_4$ . Because of the limit of the PL detection range, the band-to-band emission peak ( $\sim 340$  nm) of the  $\text{Zn}_2\text{SnO}_4$  nanowires was not observed here. The energy gap of the bulk ZnO and  $\text{Zn}_2\text{SnO}_4$  are 3.3 eV (Chang *et al.*, 2006) and 3.6 eV (Coutts *et al.*, 2000), respectively. Hence, it is believed to be originated from the band edge emission of ZnO nanowires rather than  $\text{Zn}_2\text{SnO}_4$ . Therefore, it confirmed the presence of ZnO nanostructures in the sample and excitonic recombination corresponding to the band edge emission of ZnO material (Chen *et al.*, 1998). The

analysis result is further evidence of the existence of ZnO nanostructures in the sample which is consistent with our XRD result reported previously.

#### 4.3.8 Growth Mechanism of Zn<sub>2</sub>SnO<sub>4</sub> Nanowires

Reported literature reveals that the growth mechanism of ZTO dendritic nanostructures related to the growth on crystalline surfaces, nucleation and surface diffusion (Jun *et al.*, 2008). On the other hand, growth of ZTO diameter modulated nanowire via thermal evaporation depends on disturbance of vapour concentration of Zn and Sn and growth velocity of nanowires (Jie *et al.*, 2004). They reported that the Au nanoparticles absorb Zn and Sn atoms from the vapour and form alloy droplet, then the oxidation of the Zn and Sn atoms start to grow ZTO nanowires. A disturbance of vapour concentration induced decrease of the Zn and Sn concentration near the alloy droplet reduces the size of the droplet and results in a decrease of the nanowire diameter. A small size alloy droplet absorbs fewer atoms from the vapour, which induces the increase of the Zn and Sn concentration near the alloy droplet and finally results the increase of the droplet size and nanowire diameter. This sequential change of vapour concentration led to diameter modulated ZTO nanowire.

According to literature, a growth mechanism for the synthesized Zn<sub>2</sub>SnO<sub>4</sub> nanowires is proposed here. The schematic diagram for growth of Zn<sub>2</sub>SnO<sub>4</sub> nanowire using carbothermal reduction method is depicted in Figure 4.12. It is believed that the growth is governed by the following chemical reactions (Wang *et al.*, 2005):



In this experiment, Zn and Sn vaporize after reduction by activated carbon in the higher-temperature region (900 °C), which is the center of the furnace temperature. Then the vapours are transported to the substrate which is located downstream at a lower-temperature region (~830 °C). The vapour composed of Zn and Sn reacts with the gold nanoparticle on the substrate and form Au-Sn-Zn liquid alloy droplet (Jun *et al.*, 2008). This alloy further reacts with oxygen and nucleates  $\text{Zn}_2\text{SnO}_4$  nanowire. Although all experiments were done in purified Ar (99.99%) atmosphere, the oxygen could come from the small residual amount of oxygen in Ar (a few tens of ppm). When more Zn and Sn vapours are dissolved in the liquid droplet,  $\text{Zn}_2\text{SnO}_4$  would reach the supersaturated state. Subsequently, saturated solid  $\text{Zn}_2\text{SnO}_4$  precipitates from the droplets in the form of  $\text{Zn}_2\text{SnO}_4$  nanowires and continue to grow by absorbing more Zn and Sn vapours. As the furnace temperature decreases during cooling process, the Au metal droplets form the spherical caps in front of the  $\text{Zn}_2\text{SnO}_4$  nanowires. Further, carbon soot was observed on the wall of the quartz tube at 18 cm from the center of the furnace. This carbon soot form according to reaction (4.2). It is believed that re-oxidation was performed between Zn-Sn vapours and CO. Therefore, carbon soot was detected on the interior wall of quartz tube.

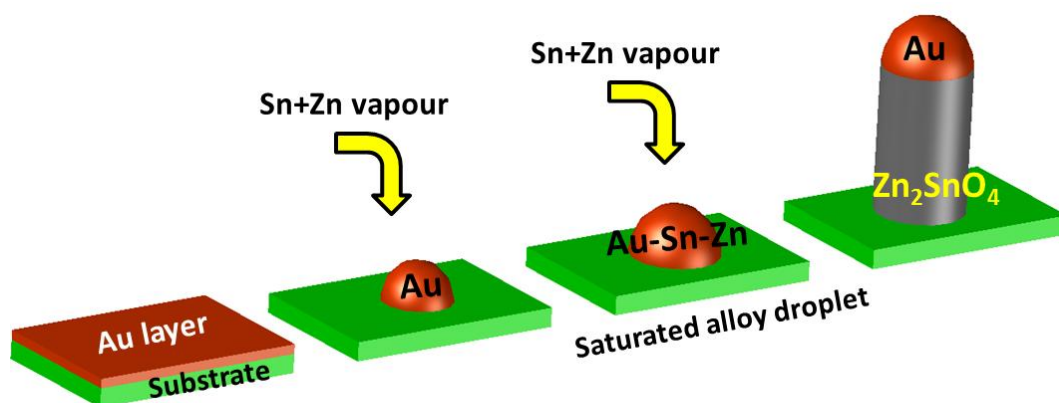


Figure 4.12: Schematic diagram of growth of  $\text{Zn}_2\text{SnO}_4$  nanowires on Au/alumina substrate [adapted from Jie *et al.*, 2004].

ZnO nanowires coexist with  $\text{Zn}_2\text{SnO}_4$  nanowires in our product which is evident from the XRD pattern (Figure 4.3). In the present work, more ZnO is used as compared to  $\text{SnO}_2$  (molar ratio between ZnO and  $\text{SnO}_2$  is 9:1). It is believed that, ZnO nanowires formed due to different speeds of vaporization of ZnO and  $\text{SnO}_2$ , and excess ZnO (Jie *et al.*, 2004). The control of the evaporation of source mixture is crucial for the synthesis of ternary oxide  $\text{Zn}_2\text{SnO}_4$  nanowires. Single phase  $\text{Zn}_2\text{SnO}_4$  ternary oxide nanowires might be acquired under optimum conditions of growth temperature, substrate position temperature and the ratio of source mixture. The phase diagram of  $\text{SnO}_2$ -ZnO system is not available in past literature. Therefore,  $\text{GaO}_{1.5}$ - $\text{SnO}_2$ -ZnO system was used to explain the ZnO nanostructures in  $\text{Zn}_2\text{SnO}_4$  nanowire system. The phase diagram of ZnO- $\text{SnO}_2$  system (Figure 4.13) clearly shows that the presence of ZnO phase is inevitable when the molar ratio between ZnO and  $\text{SnO}_2$  of 9:1 (Palmer & Poeppelmeier, 2002).

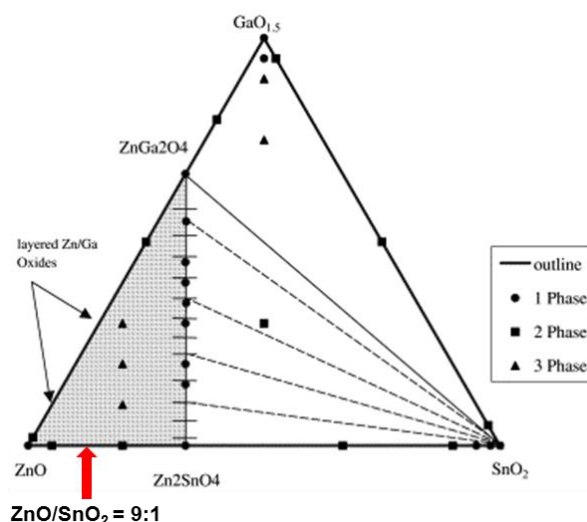


Figure 4.13: Phase diagram for the  $\text{GaO}_{1.5}$ - $\text{SnO}_2$ -ZnO system at 1250 °C (Palmer & Poeppelmeier, 2002).

#### 4.4 Characterization of $\text{SnO}_2$ -Core/ZnO-Shell Nanostructures

Two different kinds of growths (on Au/alumina substrate, on quartz boat) were observed concurrently in the carbothermal reduction process which is shown in Figure 4.2. The characterizations of one of the nanostructures obtained on Au/alumina

substrate were previously presented. Now, the other type of nanostructures observed on quartz boat is to be discussed in this section.

Figure 4.14 shows the white fluffy mass that was deposited at the edges and top of the quartz boat during the carbon assisted thermal evaporation process at a furnace temperature of 900 °C at various growth times. In carbon assisted thermal evaporation process, the reaction between carbon and metal oxide powder leads to the production of metal vapours. The condensation of these metal vapours forms the nanostructures at low temperature in controlled oxygen environment. In this process, the metal vapour is created by the reaction between zinc oxide, tin oxide and activated carbon. The vapour is transported by Ar carrier gas and condenses around the edges and the top of the boat. All white wool-like masses observed at various growth times were formed in opposite direction to the Ar gas flow, which are clearly shown in Figure 4.14. Further, it shows that these white masses nucleated from the edge of the quartz boat and spread towards center of the boat after prolong growth period (120 min). One control experiment was conducted to find the effect of shape of the boat using a flat alumina substrate instead of quartz boat. No white fluffy mass was observed on flat alumina substrate. Therefore, shape of the quartz boat induces the formation of mass. The formation of this white mass is suggested the variation of pressure and velocity at the end of the quartz boat due to its shape. The one end of quartz boat (point A) has high velocity of Ar compared to other end (Point B). Due to the shape of boat, pressure difference also formed at the end of quartz boat. Therefore, white wool-like mass was initiated to grow at point B that has low velocity and high pressure area.

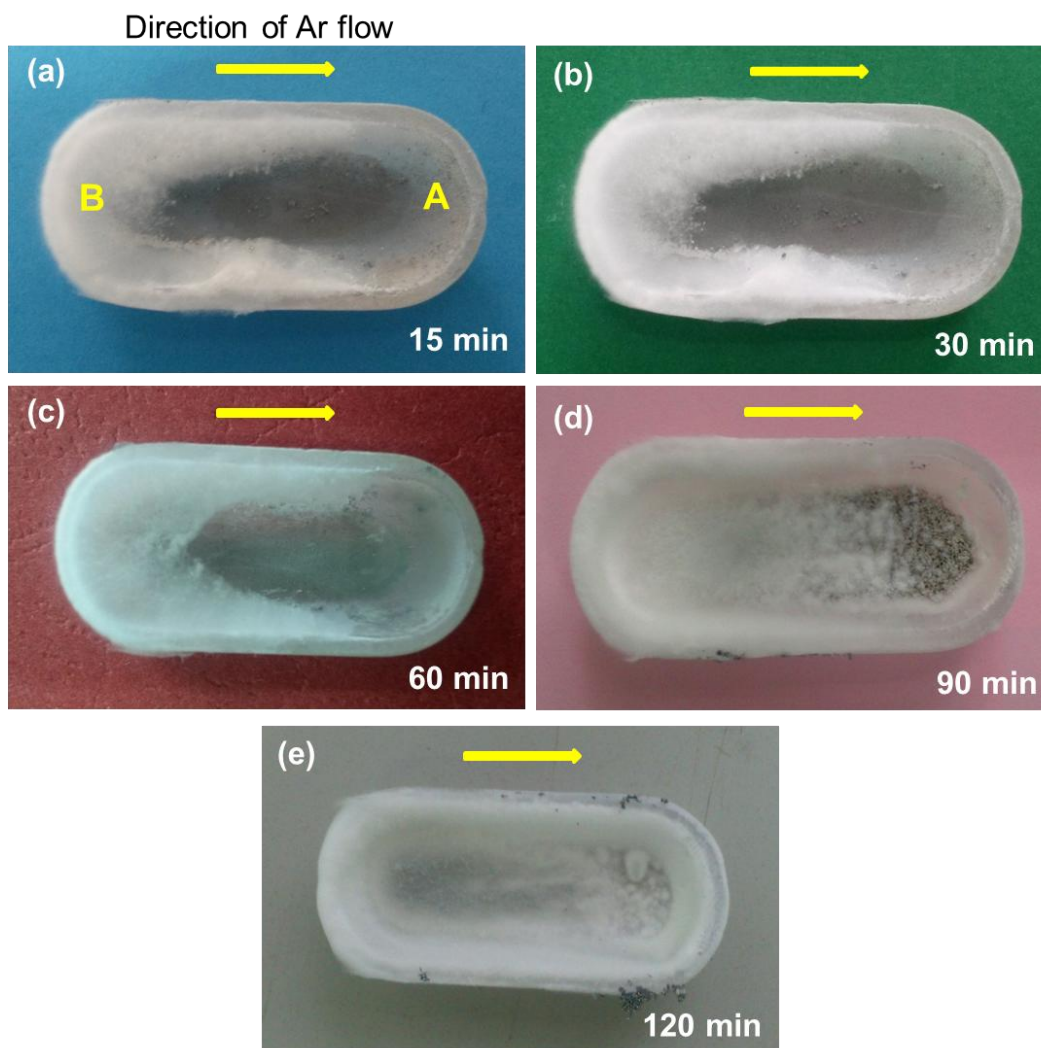


Figure 4.14: Photograph of nanostructures visible as white fluff mass with naked eyes formed at the edges and the top of the quartz boat at various growth times (a) 15 min, (b) 30 min, (c) 60 min, (d) 90 min and (e) 120 min. Arrow shows the direction of Ar flow.

#### 4.4.1 X-ray Diffraction Analysis

In order to characterize the white wool-like mass obtained at various growth times (15, 30, 60, 90 and 120 min) these were spread on carbon coated stub. The samples were then suggested to X-ray powder diffraction. Resulting patterns are shown in Figure 4.15. The XRD patterns indicate the coexistence of  $\text{SnO}_2$  and  $\text{ZnO}$  phases at growth time exceeding 30 min. No peaks associated with ternary  $\text{Zn}_2\text{SnO}_4$  or  $\text{ZnSnO}_3$  were observed. The diffraction patterns match well with those in the standard powder diffraction files for tetragonal rutile structure of  $\text{SnO}_2$  (JCPDS No. 88-0287), and

hexagonal wurtzite structure of ZnO (JCPDS No. 79-0208). Some peaks identified in the XRD patterns belong to carbon, which arises from the carbon tape used as a support for the nanostructures during XRD characterization. Pure SnO<sub>2</sub> nanowires were identified only at lower growth time of 15 min. With the increase of growth time from 30 min to 120 min, the intensity of ZnO peaks increased, and the presence of SnO<sub>2</sub> phase was also identified. The XRD peaks are seen to be quite sharp which indicates that the SnO<sub>2</sub>/ZnO nanostructures possess good crystallinity.

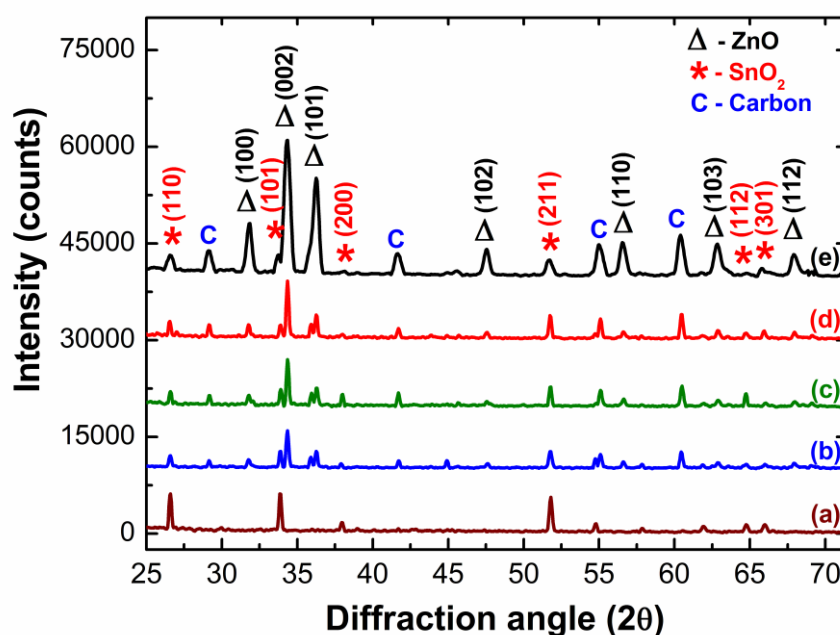


Figure 4.15: XRD patterns of SnO<sub>2</sub>/ZnO nanostructures obtained at different growth time at a furnace temperature of 900 °C: (a) 15 min, (b) 30 min, (c) 60 min, (d) 90 min, and (e) 120 min.

#### 4.4.2 Effect of Growth Time

Micrographs of SnO<sub>2</sub>-ZnO nanostructures synthesized at 900 °C for different growth time are shown in Figure 4.16. With increasing growth time from 15 min to 120 min, one can obviously notice that a change in morphology occurred with a transition from typical nanowires to hierarchical nanostructures. As can be seen in Figure 4.16(a), only rectangular cross-sectional nanowires are obtained at the growth time of 15 min.

Nanowires appear straight and flexible with smooth surfaces. The thickness of these nanowires varies in the range of 20 and 80 nm. As shown in Figure 4.16(b), the circular nanowires grown for 30 min have a several tens of micrometer in length and a diameter ranging from 50 to 100 nm.

Figure 4.16(c) exhibits two different types of nanostructures. One is observed as normal nanowire and other is branch-like structure. In this branch-like structure, the branches appear on backbone of normal nanowires and this special structure is later called as hierarchical structure. Figure 4.16(c)-(e) clearly shows the variation in the amount of hierarchical nanostructures with growth time. Most of the hierarchical nanostructures are very long, and can easily reach the lengths of 30  $\mu\text{m}$  or more. No catalyst tips appear at the end of the nanowires as shown in Figure 4.16(d). Therefore, growth of the nanostructures follows vapour-solid (VS) mechanism (Xue *et al.*, 2005). Eventually, all nanowires were completely changed to hierarchical nanostructures for a long growth time of 120 min, which is illustrated in Figure 4.16(e).



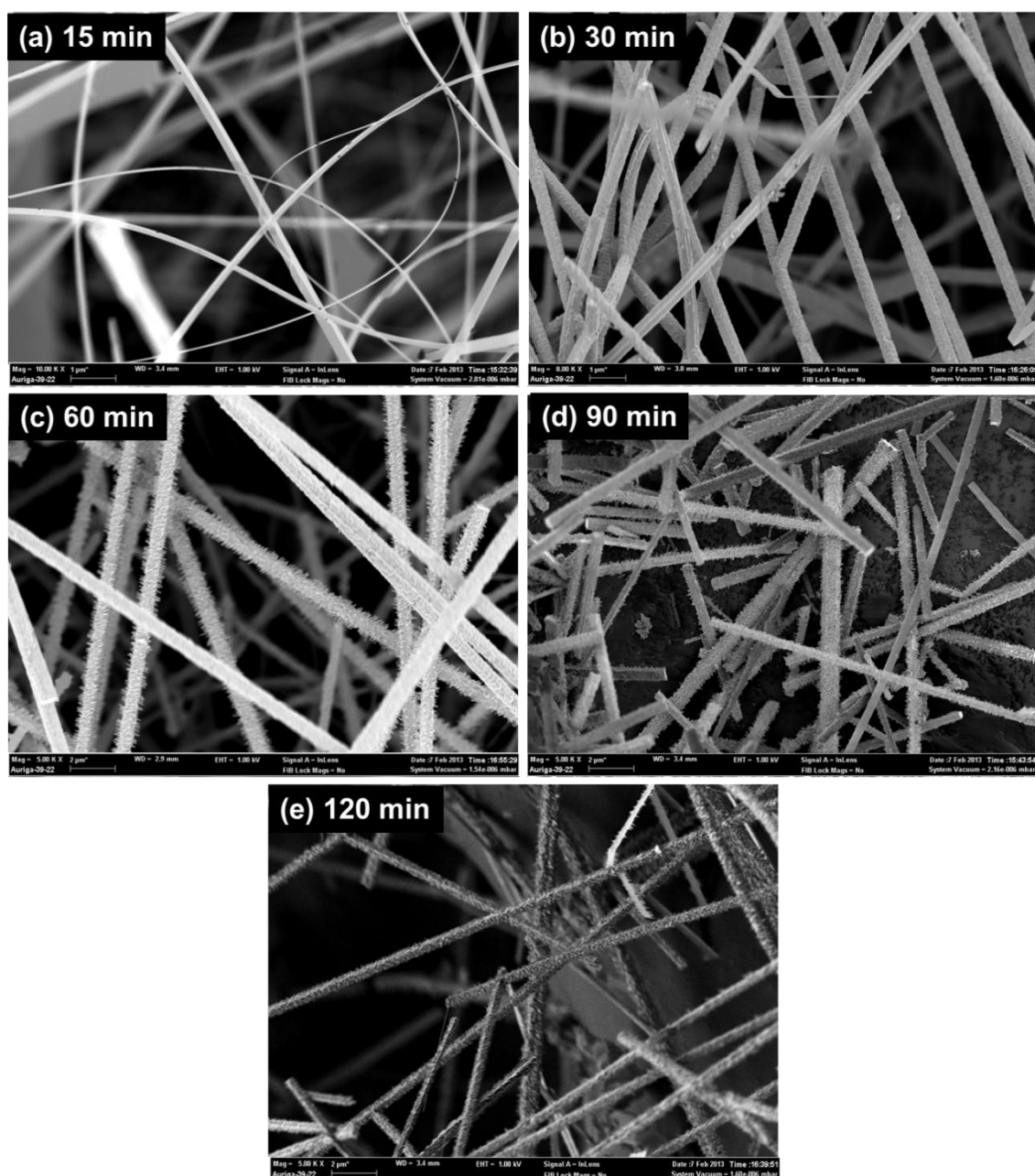


Figure 4.16: FESEM images of  $\text{SnO}_2\text{-ZnO}$  nanostructures obtained at different growth time at a furnace temperature of 900 °C: (a) 15 min, (b) 30 min, (c) 60 min, (d) 90 min, and (e) 120 min.

Figure 4.17 represents magnified FESEM micrographs of a single  $\text{SnO}_2\text{-ZnO}$  nanostructure developed at various growth times. A close examination of the samples under FESEM revealed that the  $\text{SnO}_2\text{-ZnO}$  nanostructures exhibited two types of structures depending on the deposition time. Only regular nanowires were observed at a shorter growth times (e.g., 15 and 30 min). When the growth time was increased, for example to 120 min, the nanowires exhibited mainly hierarchical nanostructures. Figure

4.17(a) reveals that the SnO<sub>2</sub> nanowires grown at 15 min exhibits rectangular shape with smooth surfaces. The width of the nanowires ranges from 20 to 50 nm with an average length of ~30 μm. Similar morphology of SnO<sub>2</sub> nanowires was previously reported by other authors (Leonardy *et al.*, 2009; Ma & Guo, 2009; Nguyen *et al.*, 2003; Wang *et al.*, 2004; Yu *et al.*, 2005). As shown in Figure 4.17(b), nanowires grown at 30 min tend to have more rounded shape with a diameter of approximately 70 nm. The surface morphology of the nanowires is not smooth. Generally nanowires obtained through vapour transport process exhibits perfectly smooth surface (Li *et al.*, 2004; Xiang *et al.*, 2007).

Figures 4.17(c) and (d) show a single hierarchical nanostructures obtained after 60 min and 90 min of deposition, respectively. All secondary branch nanowires grew perpendicular to the primary trunk nanowires. Two different hierarchical nanostructures obtained at longer growth time of 120 min is depicted in Figure 4.17(e) and (f). The individual branches of hierarchical nanostructures in Figure 4.17(e) seems to have merged into thicker branches, while randomly oriented branches on backbone nanowire with a hexagonal cross-section is shown in Figure 4.17(f). The lengths of the branches in hierarchical nanostructures increased from about 50 nm to 150 nm, and the diameter also increased with the increase of growth time from 60 min to 120 min. It may be attributed to condensation of higher amount of vapour due to increased deposition times. This single-step growth process demonstrates high yield formation of hierarchical structure depends on various deposition periods.

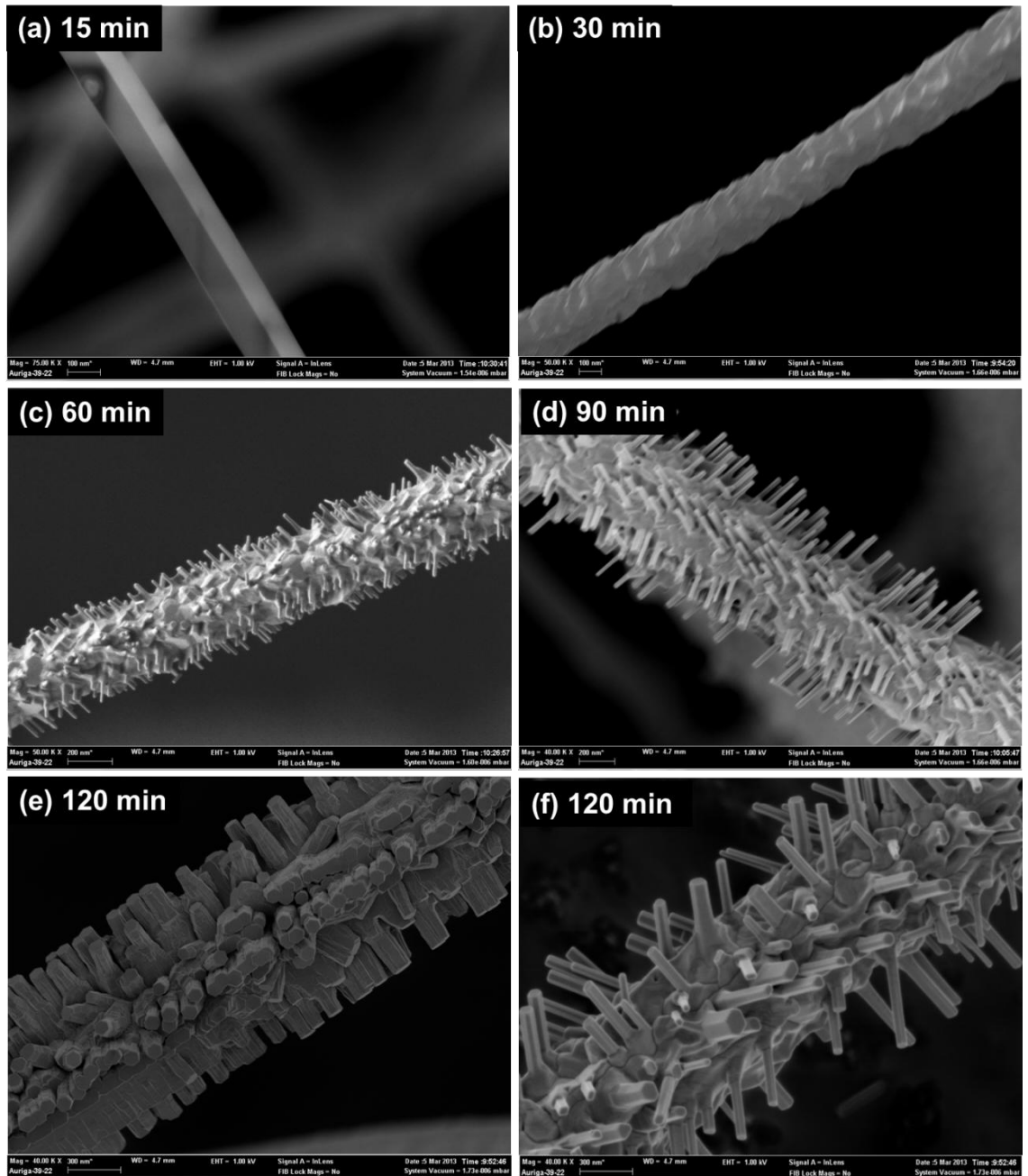


Figure 4.17: FESEM micrographs of a single SnO<sub>2</sub>/ZnO nanostructure obtained at different growth time at a furnace temperature of 900 °C: (a) 15 min, (b) 30 min, (c) 60 min, (d) 90 min, and (e and f) 120 min.

#### 4.4.3 Transmission Electron Microscopy Analysis

Detailed structures of nanostructures obtained at various growth times were analysed by transmission electron microscopy (TEM). EDX line scan and elemental mapping were conducted to determine the overall composition and spatial distribution of Zn, Sn and O in individual nanostructures.

#### 4.4.3.1 Nanowires obtained at 15 minutes

Integrated EDX spectrum collected along a line across the  $\text{SnO}_2/\text{ZnO}$  nanostructures obtained at 15 min under the scanning transmission electron microscopy (STEM) is shown in Figure 4.18. Figures 4.18(a) and (b) show the STEM image and corresponding integrated EDX spectrum obtained for the growth time of 15 min across the diameter. EDX microanalysis has detected only Sn and O within the detection limits. Signals for carbon and copper come from TEM grid (carbon coated copper grid). As shown in Figure 4.18(c), the elemental compositions along the line demonstrate that greater number of counts was obtained for Sn and O. A very low number of counts (less than 2) were identified for Zn. This is thought to be coming from background signal. The results there show that only pure  $\text{SnO}_2$  nanowires grow for time of up to 15 min.

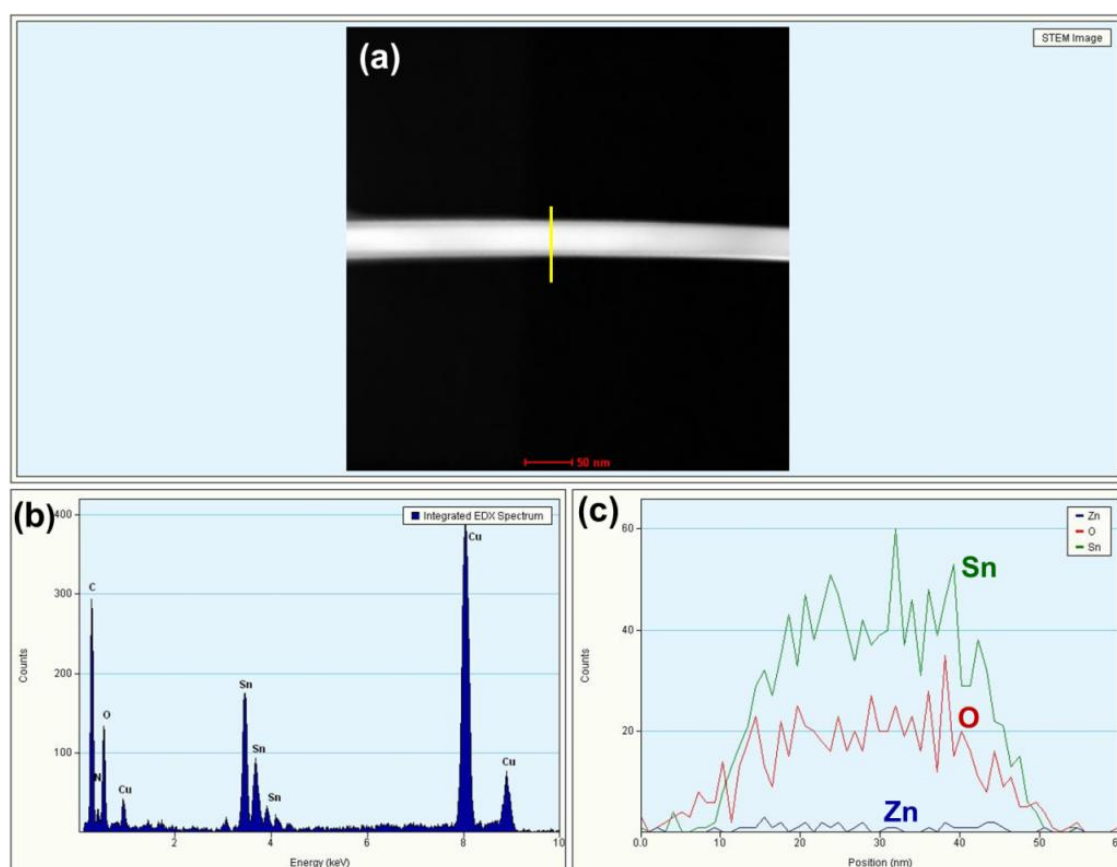


Figure 4.18: (a) STEM image of  $\text{SnO}_2/\text{ZnO}$  nanowire grown at 15 min showing the linescan trajectory, (b) Integrated EDX spectrum of the nanowire, and (c) Integrated peak intensities as a function of spot position for Zn, Sn and O peaks.

EDX elemental mapping was further carried out in order to confirm that the nanowire consists of only  $\text{SnO}_2$ , which is illustrated in Figure 4.19. EDX spectrum and spatial distribution of corresponding elemental maps on a representative nanowire were obtained in the box area shown in Figure 4.19(a). Figure 4.19(d) and (e) show that Sn (green) and O (red) exist in the nanowire. Sn and O are seen to be distributed uniformly over the area investigated. These results support the conclusion that the nanowires synthesized at 15 min has only  $\text{SnO}_2$  phase which is consistent with XRD patterns (Figure 4.15(a)).

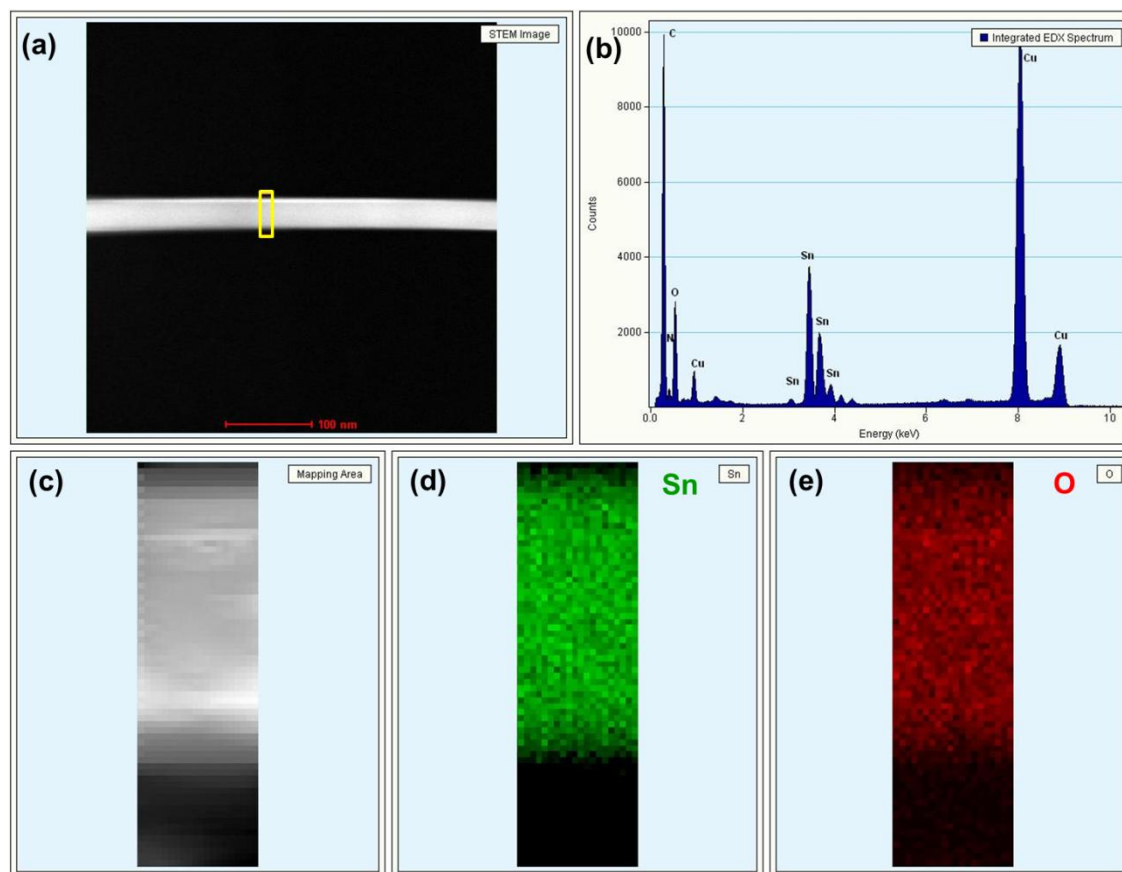


Figure 4.19: (a) STEM image of  $\text{SnO}_2/\text{ZnO}$  nanowire grown at 15 min, (b) Integrated EDX spectrum of the nanowire, (c) Magnified image of the mapping area indicated by box in (a), The colour maps demonstrating the spatial distribution of different elements, (d) Sn, and (e) O which are labelled in green, red, respectively.

Figure 4.20(a) illustrates a representative low magnification TEM image of a  $\text{SnO}_2$  nanowire. It shows that the nanowire has a smooth surface and it is very uniform in

diameter (about 52 nm) along its length. The clear lattice fringes in high resolution transmission electron microscopy (HRTEM) image of SnO<sub>2</sub> nanowire demonstrate that the SnO<sub>2</sub> nanowire is a single crystalline structure (Figure 4.20(b)). No defects such as dislocation are observed. The high resolution image exhibits the lattice fringes between adjacent planes of (110) which measures at 0.33 nm. It indicates that the possible growth direction of SnO<sub>2</sub> nanowire is [100] direction. However, Cui *et al.* (2012) reported that the [001] direction is a theoretically preferential growth direction of SnO<sub>2</sub> nanorods due to anisotropic growth.

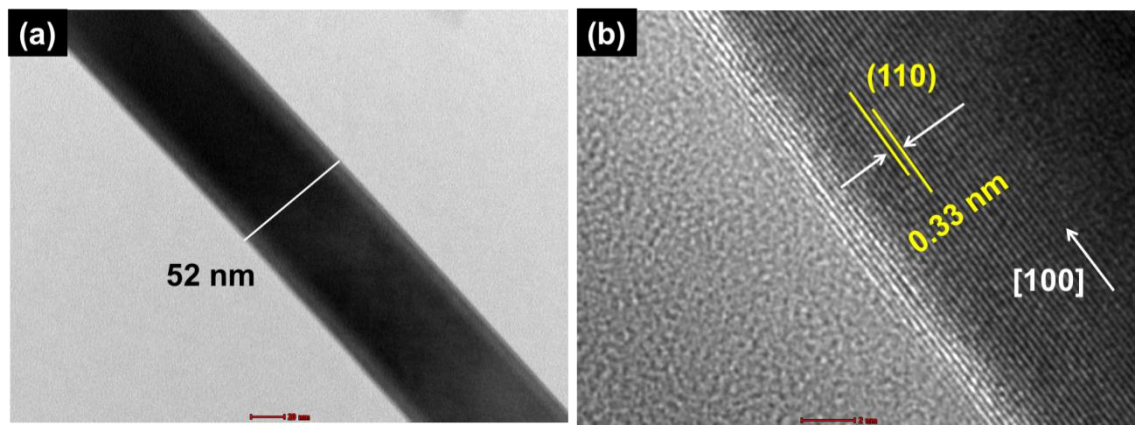


Figure 4.20: (a) Low magnification TEM images of a single SnO<sub>2</sub> nanowire deposited at 15 min, and (b) HRTEM image of SnO<sub>2</sub> nanowire.

#### 4.4.3.2 Nanowires synthesized at 30 minutes

Result of an EDX line scan along the radial direction of the nanowire synthesized at 30 min is shown in Figure 4.21. The integrated EDX spectrum shown in Figure 4.21(b) exhibits more intense Zn signal compared with those of Sn and O. The EDX-line analysis (Figure 4.21(c)) shows that maxima Zn signal occur at the edges of the nanowire, where the Sn intensity drops rapidly. The Zn signal exhibits a dip at the center of the nanowire, where the Sn signal shows a maximum. However, O is distributed homogenously through the nanowire. This suggests that the nanowire

consists of  $\text{SnO}_2$ -core/ $\text{ZnO}$ -shell nanostructure. It has shell thickness of approximately 15 nm and having core diameter of ~25 nm (Figure 4.21(c)). This structure of nanowire will further be confirmed by TEM-EDX elemental mapping.

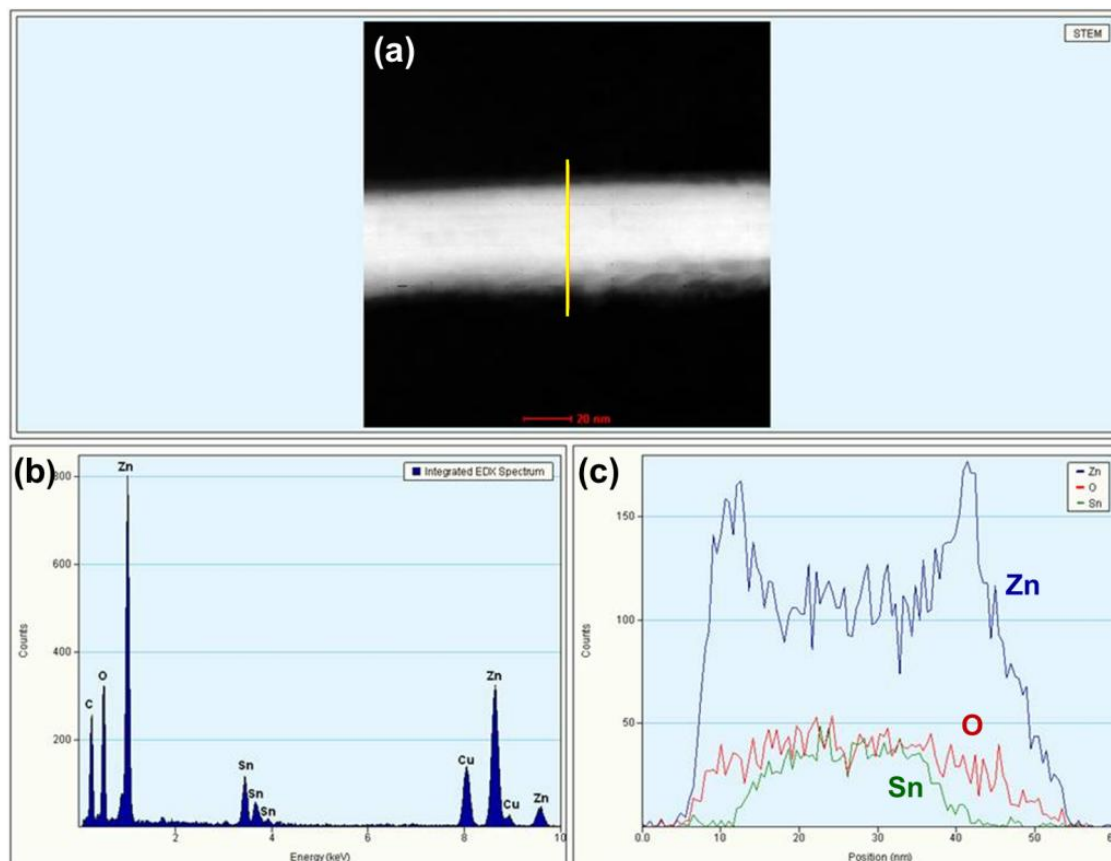


Figure 4.21: (a) STEM image of  $\text{SnO}_2/\text{ZnO}$  nanowire grown at 30 min showing the linescan trajectory, (b) Integrated EDX spectrum of the nanowire, and (c) Integrated peak intensities as a function of spot position for Zn, Sn and O peaks.

Figures 4.22(a)-(f) show a STEM image and EDX elemental maps for the  $\text{SnO}_2/\text{ZnO}$  core-shell nanowire. The elemental map for Zn shows occurrence of a higher concentration of Zn in the outer shell region of the nanowire (Figure 4.22(d)), while O is uniformly distributed in the nanowire (Figure 4.22(e)). By contrast, Sn is uniformly distributed in the core region of the nanowire, but is absent in the shell region (Figure 4.22(f)). On the basis of the TEM-elemental maps analysis, it further confirmed that the  $\text{SnO}_2/\text{ZnO}$  nanowires formed in the quartz boat at shorter deposition time of 30 min and have a core of  $\text{SnO}_2$  and a shell of  $\text{ZnO}$ .



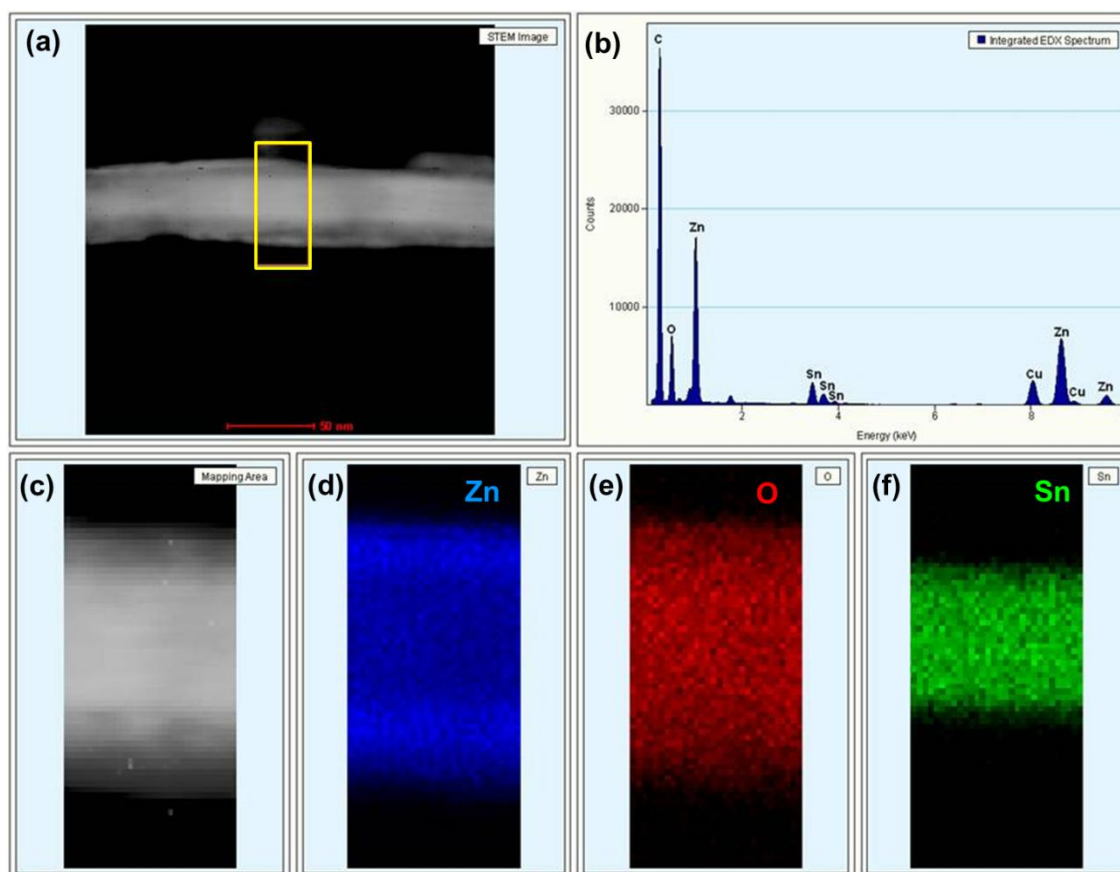


Figure 4.22: (a) STEM image of  $\text{SnO}_2/\text{ZnO}$  nanowire grown at 30 min, (b) Integrated EDX spectrum of the nanowire, (c) Magnified image of the mapping area indicated by box in (a), The colour maps demonstrating the spatial distribution of different elements, (d) Zn, (e) O, and (f) Sn which are labelled in blue, red, green, respectively.

TEM observations (Figure 4.23(a)) provide more detailed structural information on  $\text{SnO}_2$ -core/ $\text{ZnO}$ -shell nanowires obtained at 30 min. The image shows that the diameter of the core is about 50 nm and the thickness of the shell layer is about 17 nm. A HRTEM image taken from an individual core-shell indicates that it is a single crystal with well-defined fringes (Figure 4.23(b)). The lattice spacing in the core of the nanowire shown in HRTEM image is 0.33 nm, close to that of (110) plane of the  $\text{SnO}_2$  and growth direction is along [110]. The lattice spacing at the edge or shell of the nanowire is 0.26 nm, consistent with the (002) lattice spacing of hexagonal  $\text{ZnO}$ . The orientation of growth direction of  $\text{ZnO}$  shell is believed to be [001] c-axis direction (Ul Hasan *et al.*, 2011).



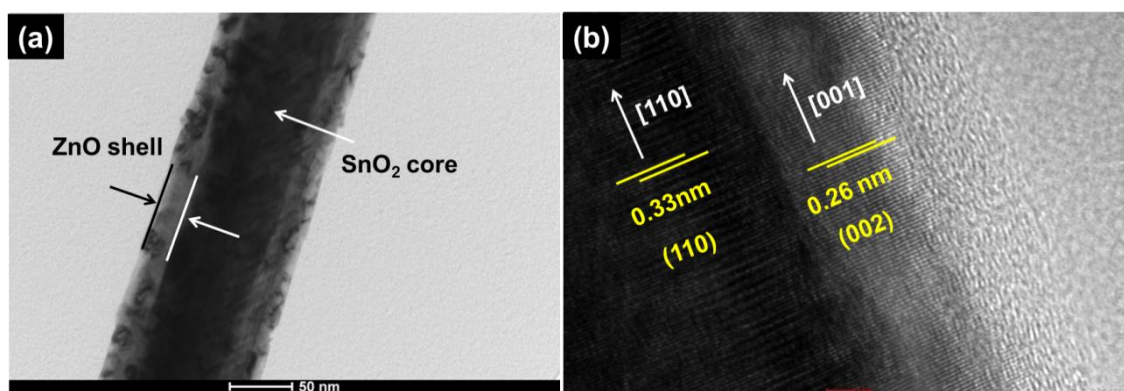


Figure 4.23: (a) Typical low magnification TEM images of a single SnO<sub>2</sub>-core/ZnO-shell nanowire deposited at 30 min, (b) HRTEM image of SnO<sub>2</sub>-core/ZnO-shell nanowire.

#### 4.4.3.3 Nanostructures obtained at 120 minutes

EDX elemental line scan recorded across a trunk or backbone of single SnO<sub>2</sub>/ZnO hierarchical nanostructure obtained at 120 min is shown in Figure 4.24. An inspection of the STEM image shows most part of the branches broke off presumably during TEM sample preparation by ultrasonication (Figure 4.24(a)). As shown in EDX spectrum (Figure 4.24(b)), Zn signal is prominent compared with that of Sn. An elemental line profile displayed in Figure 4.24(c) reveals the distribution of Zn, Sn and O in backbone nanowire. The elemental line scan for Zn on the backbone nanowire is non-uniform and exhibits peaks at the edges. The line scan for Sn reveals that this is present uniformly at the core and is absent at the edges. It demonstrates that Sn and Zn are distributed in the core and shell of the backbone nanowire, respectively, while oxygen is homogeneously distributed throughout the whole nanowire structure. The diameter of the SnO<sub>2</sub>-core and the thickness of the ZnO-shell are estimated to be 100 nm and 50 nm, respectively.

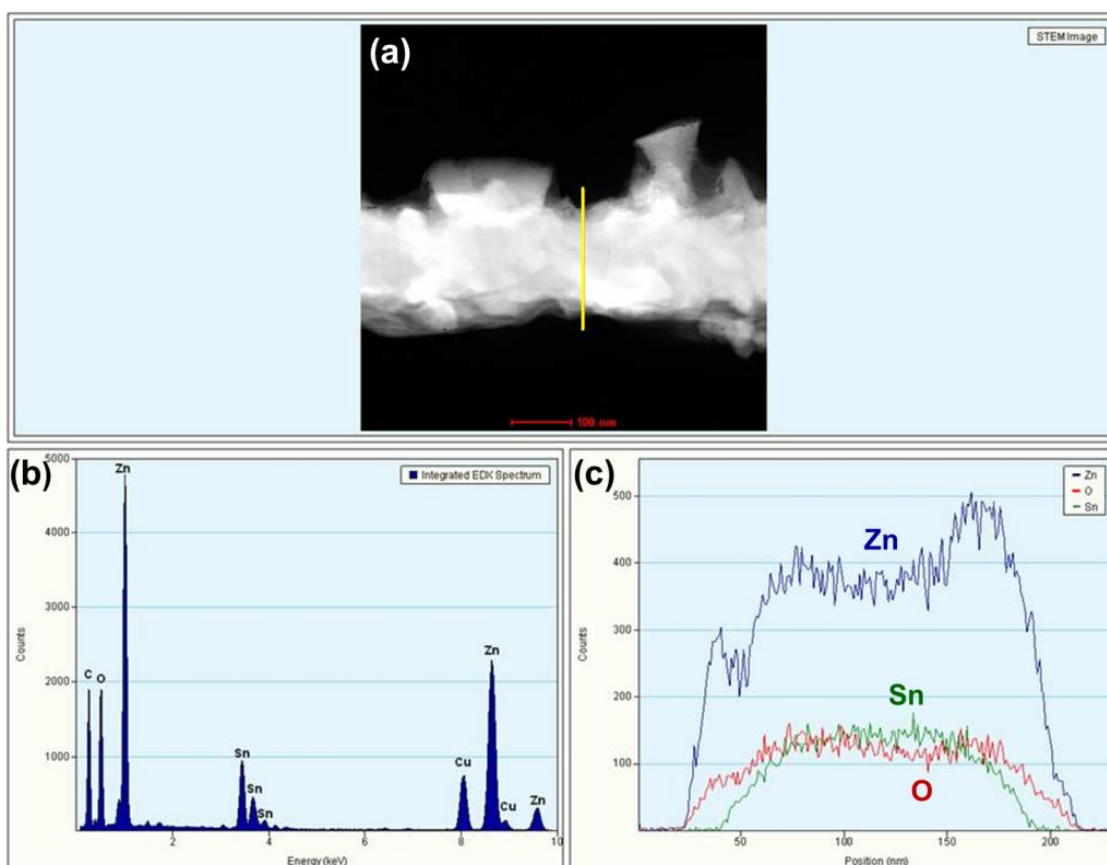


Figure 4.24: (a) STEM image of hierarchical SnO<sub>2</sub>/ZnO nanostructure grown at 120 min showing the linescan trajectory of backbone nanowire, (b) Integrated EDX spectrum of the backbone nanowire, and (c) Integrated peak intensities as a function of spot position for Zn, Sn and O peaks.

To achieve a better understanding about the distribution of Zn, Sn and O, the backbone nanowire of hierarchical nanostructures developed at 120 min was characterized by EDX-elemental mapping (Figure 4.25). Small portion of backbone nanowire was chosen to map the elements, which is shown in Figure 4.25(a). EDX spectrum presents stronger Zn signal than Sn and O (Figure 4.25(b)). The mapping area and corresponding elemental maps of Zn, Sn and O are revealed in Figure 4.25(c-f). As can be seen, the Sn is concentrated in the core region, whereas Zn and O signals are uniformly distributed shell and in the selected area, respectively. It confirms the formation of SnO<sub>2</sub>-core/ZnO-shell in backbone nanowire of the hierarchical nanostructure.

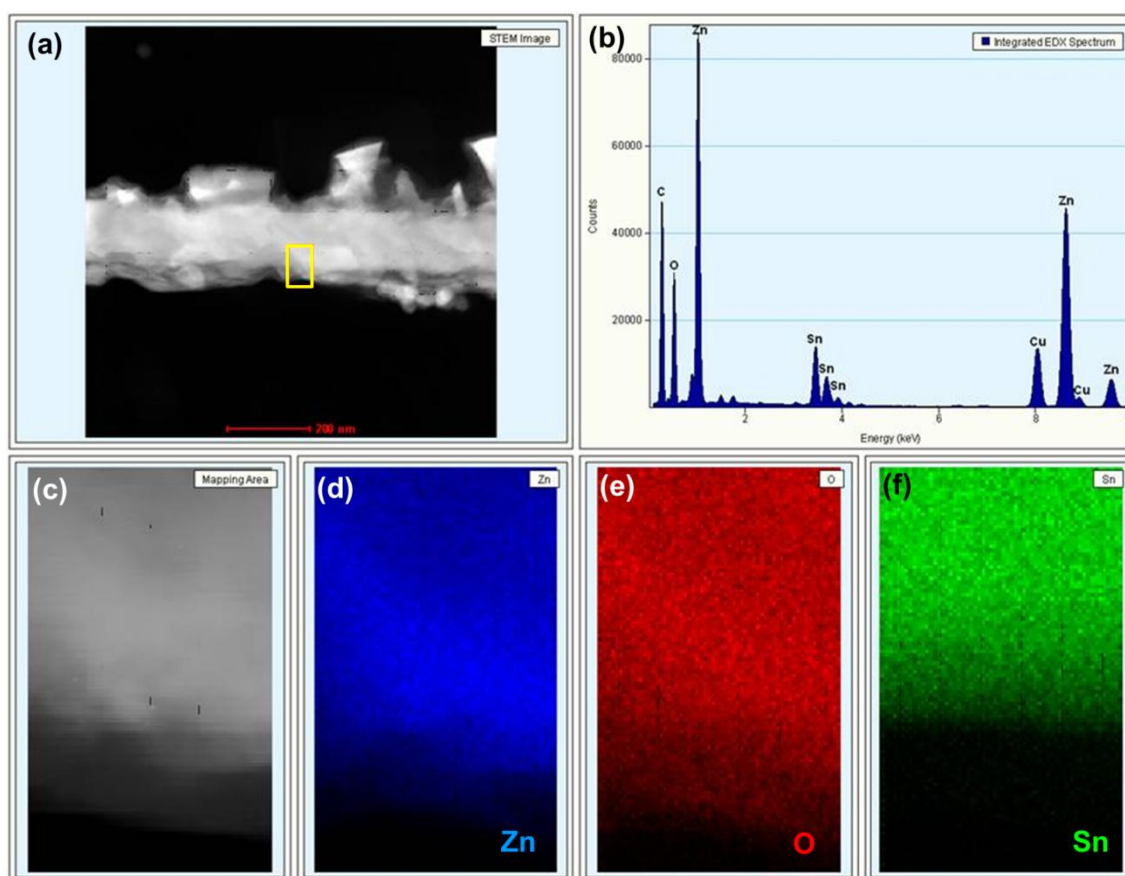


Figure 4.25: (a) STEM image of hierarchical  $\text{SnO}_2/\text{ZnO}$  nanostructure grown at 120 min, (b) Integrated EDX spectrum of the backbone nanowire, (c) Magnified image of the mapping area indicated by box in (a), The colour maps demonstrating the spatial distribution of different elements, (d) Zn, (e) O, and (f) Sn which are labelled in blue, red, green, respectively.

The distribution of the compositional elements within the branch of the hierarchical nanostructure was obtained by using TEM-EDX line scans along the branch's radial direction (marked by the yellow line in the Fig. 4.26(a)). As seen in Figure 4.26(b), only strong Zn and O signals were detected in the branch of the hierarchical nanostructure. In the intensity profile of the elements shown in Figure 4.26(c), only Zn and O signals are mainly observed in the branch. This result confirms that the secondary branch nanowire is composed of pure ZnO.

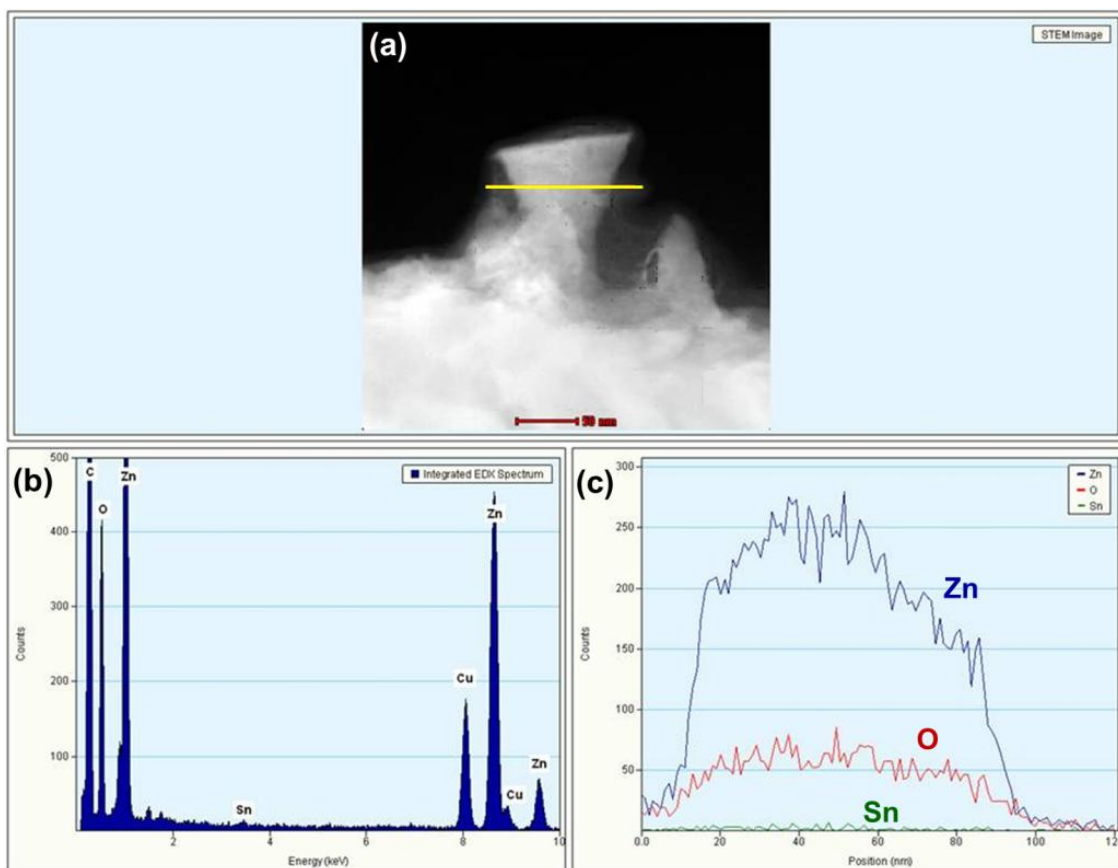


Figure 4.26: (a) STEM image of hierarchical  $\text{SnO}_2/\text{ZnO}$  nanostructure grown at 120 min showing the linescan trajectory of branch, (b) Integrated EDX spectrum of the branch, and (c) Integrated peak intensities as a function of spot position for Zn, Sn and O peaks.

To clarify the spatial distribution of the elements within the branch, EDX-elemental mapping was done. Figure 4.27(b) shows the TEM-EDX spectrum collected on the selected area of the branch in Figure 4.27(a). Two peaks of Zn and O are detected in the branch. The maps evidently show that the branches are enriched in Zn with a low level of Sn, suggesting that the Zn and O are concentrated on the branch. It is anticipated that the detection of very small amount of Sn is due to contamination during sonication used in the sample preparation. Sn signal could also come from background. Therefore, It is concluded that all branches are made up of pure  $\text{ZnO}$ , which are grown on top of  $\text{SnO}_2$ -core/ $\text{ZnO}$ -shell nanostructures.

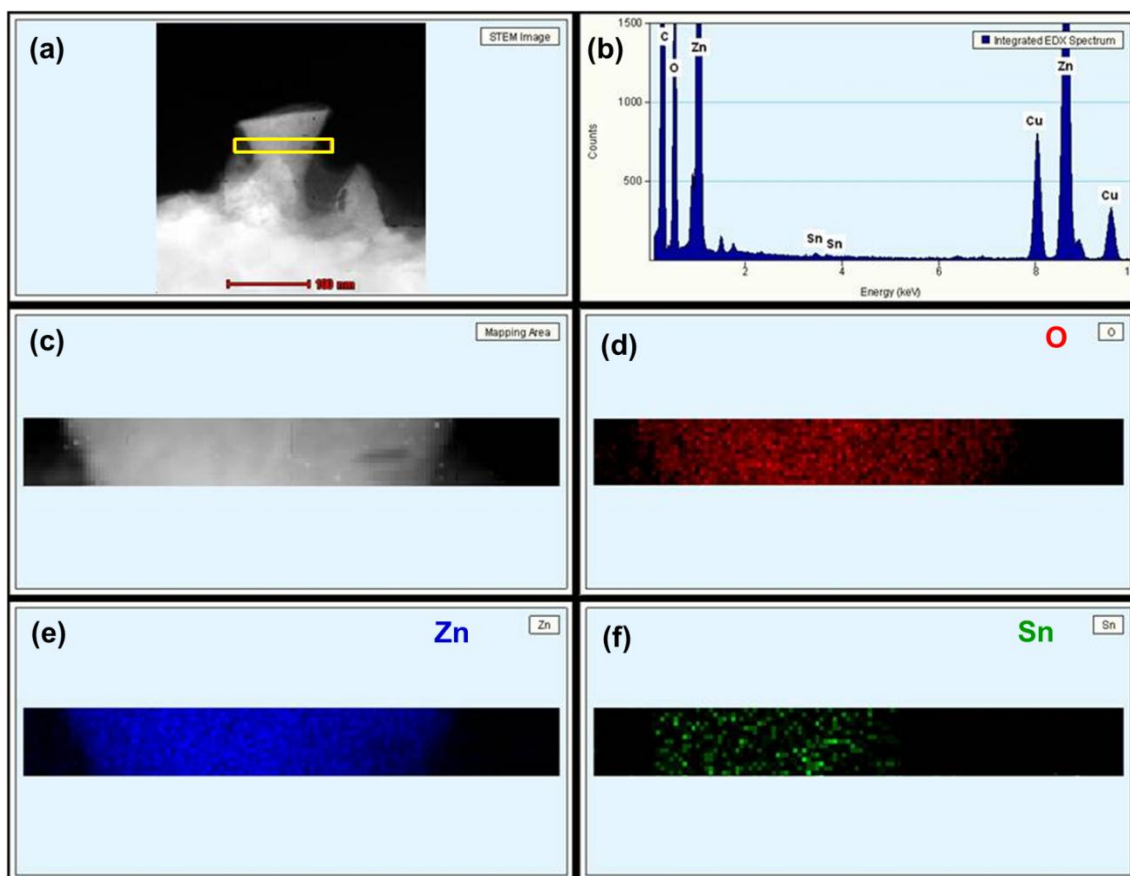


Figure 4.27: (a) STEM image of branch of hierarchical nanostructure grown at 120 min, (b) Integrated EDX spectrum of the branch nanowire, (c) Magnified image of the mapping area indicated by box in (a), The colour maps demonstrating the spatial distribution of different elements, (d) O, (e) Zn, and (f) Sn which are labelled in red, blue, green, respectively.

Another typical TEM image of a portion of a single  $\text{SnO}_2/\text{ZnO}$  hierarchical nanostructure obtained for a growth time of 120 min is shown in Figure 4.28(a). It is evident that the nanostructure is composed of a primary trunk nanowire and secondary branch nanowires as shown before. It is noted that some branches broke off from the primary trunk nanowires during sonication used for TEM sample preparation. The diameter of backbone nanowire approximates 200 nm. The result coincides with the FESEM observations. Figure 4.28(b) exhibits the HRTEM image of surface of backbone nanowire. The enlarged high resolution TEM image of backbone nanowire at the interface between core and shell was chosen to find the clear lattice fringes, which are illustrated in Figure 4.28(c). The interplanar spacing with 0.27 nm is observed on



core of the backbone nanowire. This fringes spacing is consistent with the  $d$ -spacing of the (101) plane of the tetragonal crystal structure of  $\text{SnO}_2$ . Another fringes spacing of 0.26 nm was determined at the shell of the nanostructures, which corresponding to the (002) lattice spacing of the hexagonal crystal structure of  $\text{ZnO}$ .

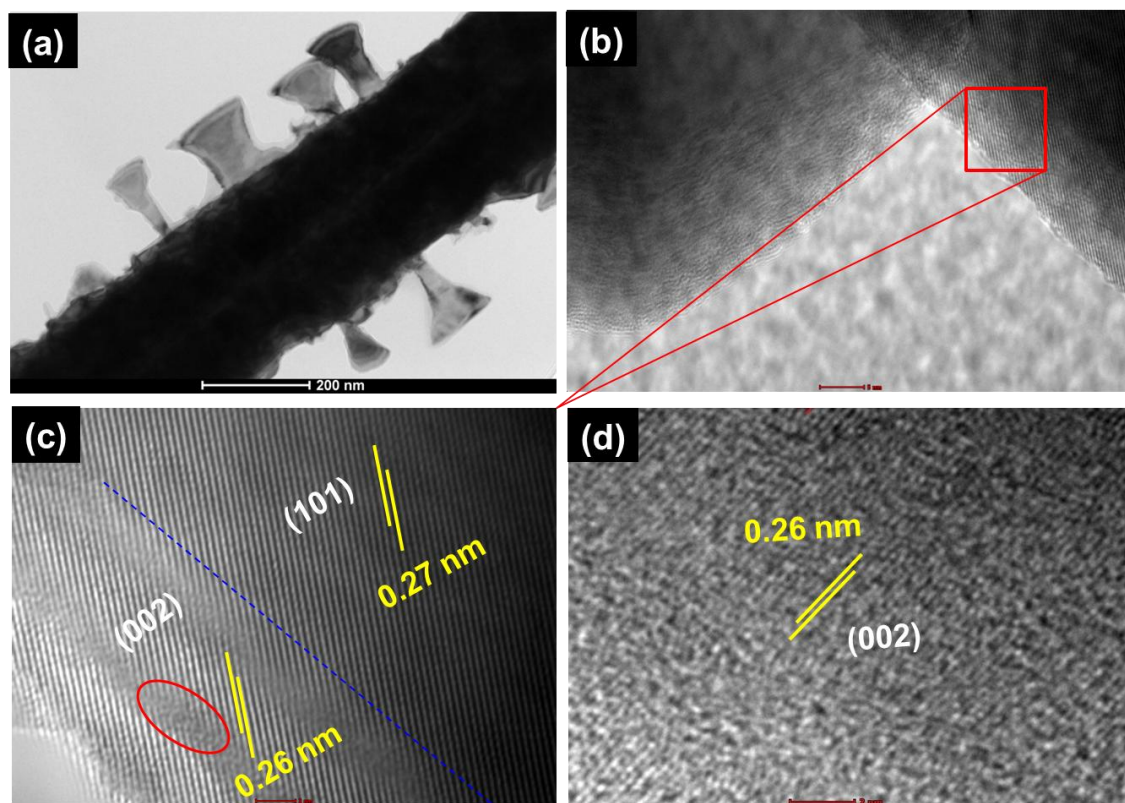


Figure 4.28: (a) Low magnification TEM images of hierarchical core-shell nanostructure deposited at 120 min, HRTEM images of (b) hierarchical nanostructure, (c) interface between core-shell structure of backbone nanowire and (d) branch nanostructure.

Further, the red circle noticed in HRTEM observation of  $\text{ZnO}$  shell area further reveals the distortion of atomic arrangement due to sonication in sample preparation. These above results confirmed that the primary nanowires in hierarchical nanostructures are composed of tetragonal crystal structure of  $\text{SnO}_2$  and the hexagonal crystal structure of  $\text{ZnO}$  which is consistent with XRD patterns obtained. Additionally, fringes spacing of secondary nanowire or branch of hierarchical nanostructure with 0.26 nm match well with the (002) lattice spacing of the similar phase of  $\text{ZnO}$  (Figure 4.28(d)). Moreover,

Zhao *et al.* (2006) reported that the mismatch at the interfacial region between SnO<sub>2</sub> (010), (001) planes and ZnO (002) plane could result in many defects and stacking faults. In contrast, this sample exhibits less defects and stacking faults due to not much varying lattice spacing observed (ZnO:  $d=0.26$  nm and SnO<sub>2</sub>:  $d=0.27$  nm). It can be clearly seen that the SnO<sub>2</sub> (101) plane has good structural compatibility with that of the ZnO (002) plane.

From the TEM studies of the SnO<sub>2</sub>/ZnO nanostructures grown for different time periods it is concluded that SnO<sub>2</sub> nanowires and SnO<sub>2</sub>-core/ZnO-shell nanowires are obtained at 15 min and 30 min, respectively, while SnO<sub>2</sub>-core/ZnO-shell hierarchical nanostructures are observed at growth time exceeding 60 min. All branches in the hierarchical nanostructures grown for 120 min were made up of pure ZnO, which grew on top of SnO<sub>2</sub>-core/ZnO-shell nanostructures. Moreover, EDX spectrum of various growth periods of nanostructures revealed that the intensity of Zn content increased with increasing growth times (Amount of Zn intensity is 0, 20000 and 80000 for nanostructures grown at 15 min, 30 min and 120 min, respectively). Further, it can be seen that the diameter of nanostructures increased with increasing deposition time.

#### **4.4.4 Photoluminescence Studies**

The optical properties of the SnO<sub>2</sub>/ZnO nanostructures were characterized by photoluminescence spectroscopy. Photoluminescence (PL) spectra of SnO<sub>2</sub>/ZnO nanostructures synthesized at various deposition time excited with a 325 nm He-Cd laser source at room temperature are presented in Figure 4.29(a). There are three dominant peaks observed within the broad spectral range of 300-800 nm. The first and prominent emission peaks were detected within a visible emission (450-650 nm), which originated from defects or impurities of the SnO<sub>2</sub>/ZnO nanostructures (Fonoberov *et al.*,

2006). The second stronger peaks were achieved within the wavelength of 730 nm and 800 nm, indicating the second order feature of UV band-edge emission (Lan *et al.*, 2013; Mahalingam *et al.*, 2007). The third and weakest peaks illustrate first order of UV band-edge emission with low PL intensity within the wavelength range of 380 and 410 nm (enlarged view is in Figure 4.29(b)).

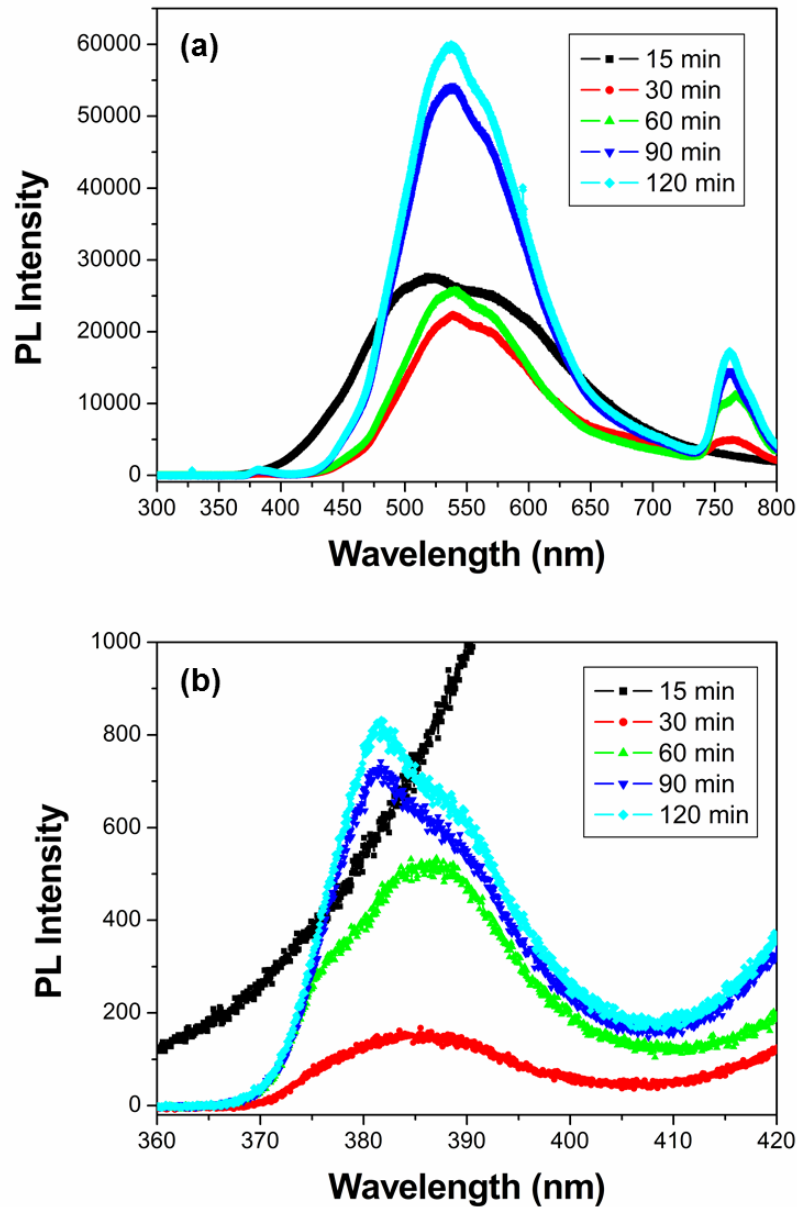


Figure 4.29: (a) Photoluminescence (PL) spectra of SnO<sub>2</sub>/ZnO nanostructures obtained at different growth times, and (b) enlarged view of PL spectra of SnO<sub>2</sub>/ZnO nanostructures within a wavelength of 360-420 nm.



As shown in Figure 4.29(a), all samples have a broad visible emission centered at around 540 nm, indicating a green light emission. The weak and broad peak was achieved for pure SnO<sub>2</sub> nanowires synthesized at 15 min. The broad peak is the result of the convolution of at least two emission lines: one dominating green emission with maximum at 520 nm and a shoulder on the long wave side of about 570 nm with a yellow emission. As for SnO<sub>2</sub>, the trapped emission is complicated. For example, SnO<sub>2</sub> nanopowder has shown two distinct PL emissions at 400 and 430 nm (Gu *et al.*, 2003). Three emission peaks at 439, 486 and 496 nm were observed from the as-synthesized SnO<sub>2</sub> nanoribbons (Hu *et al.*, 2002). The beak-like nanorods exhibited a strong emission peak at 602 nm and the field-emission properties (He Jr *et al.*, 2006). A broad yellow emission at a wavelength of around 597 nm as well as a small orange emission shoulder at 640 nm were reported in the nanostructured fishbone-like SnO<sub>2</sub> (Kim *et al.*, 2005). Up to now, the mechanisms of observed emissions are not yet clear. However, they should be associated with defect energy levels within the band gap of SnO<sub>2</sub>. Oxygen vacancies are well known to be the most common defects in oxides and usually act as radiative centres in luminescence processes. Thus, the nature of the transition is tentatively ascribed to oxygen vacancies, Sn vacancies or Sn interstitials, which form a considerable number of trapped states within the band gap (Calestani *et al.*, 2005; Gu *et al.*, 2003; He Jr *et al.*, 2006; Hu *et al.*, 2002; Kim *et al.*, 2005). These trapped states contribute to the visible emission bands.

The luminescence of the SnO<sub>2</sub>-core/ZnO-shell nanostructures obtained at 30 min and 60 min are less strong and broader centred at 540 nm, with an extra shoulder peak of 570 nm compared with that of nanostructures synthesized at 90 min and 120 min. An emission peak at 540 nm is implying that emission centers are associated to green emission of ZnO. The important effect on the green luminescence of ZnO nanostructure originate from the recombination of the holes with electrons occupying the singly

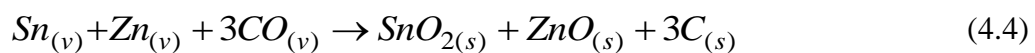
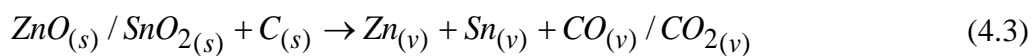
ionized O vacancy, and other structural defects or impurities (Hu *et al.*, 2003; Vanheusden *et al.*, 1996). The additional peak observed at 570 nm (yellow emission) in both nanostructures (SnO<sub>2</sub>-core/ZnO-shell nanostructures obtained at 30 min and 60 min) is attributed to influence of SnO<sub>2</sub> in the structure. The detailed origin of yellow emission from SnO<sub>2</sub> was discussed above. The stronger and narrow emissions centered at 538 nm were observed in SnO<sub>2</sub>-core/ZnO-shell hierarchical nanostructures obtained at 90 min and 120 min. Both emissions are responsible for the typical green luminescence center of ZnO nanomaterials, which are originated from oxygen vacancy. The relatively high PL intensity was observed at longer growth time (90 min and 120 min) of nanostructures compared with that of shorter growth time nanostructures. It means that longer growth time hierarchical nanostructures have more oxygen vacancy than shorter growth time nanostructures. Several research groups tried to determine the quantity of defects estimated from PL spectra in binary oxide such as ZnO (Ahn *et al.*, 2008; Phan & Chung, 2013). They reported that it was calculated from PL intensity ratio of visible luminescence to UV luminescence. However, ZnO/SnO<sub>2</sub> nanostructure samples show mixed or composite structure of ZnO and SnO<sub>2</sub>. Thus, the defect concentration could not be quantified from PL spectra.

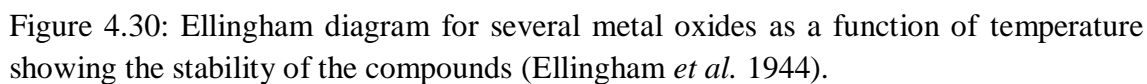
The peaks between 750 nm and 800 nm are believed to be the second-order peaks of the excitonic emission (Lan *et al.*, 2013; Mahalingam *et al.*, 2007). This excitonic emission is significantly quenched at shorter growth time of nanostructures and completely disappears at growth time of 15 min (SnO<sub>2</sub> nanowires). This further suggests that second-order peak originates from the effect of increasing amount of ZnO. As observed from TEM-EDS analysis, the amount of ZnO in the samples rises with increased growth time of nanostructures. Therefore, the second order UV peak was only observed with greater intensity of SnO<sub>2</sub>-core/ZnO-shell nanostructures obtained for longer growth time.

Figure 4.29(b) presents the first order UV emission detected within the wavelength of 370 and 410 nm. It should correspond to the near band-edge emission of ZnO. Because of the band gap of ZnO is and 3.3 eV (~377 nm). In this work, the SnO<sub>2</sub> nanowires do not show any pronounced peak that means it does not show band-to-band transition. Brovelli et al (Brovelli *et al.*, 2006) reported that the 318 nm (3.9 eV) emission was evidence of free-exciton decay in SnO<sub>2</sub>, with an energy shift of 0.3 eV with respect to the bulk gap energy (3.6 eV). This emission is not observed in this work due to the limit of the PL detection range with a He-Cd 325 nm excitation source. A similar phenomenon was observed in other one-dimensional SnO<sub>2</sub> nanostructures (Faglia *et al.*, 2005; He Jr *et al.*, 2006; Kim *et al.*, 2005). By contrast, SnO<sub>2</sub>-core/ZnO-shell nanostructures exhibit much stronger band-to-band transition together with luminescence. The UV peak centered blue shifted from 387 nm to 382 nm with increased growth time of nanostructures obtained from 30 min to 120 min. The blue shift of UV emission could be attributed to influence of increasing amount of ZnO in the nanostructures. In literatures, the band-edge recombination of free electrons of pure ZnO was reported as 382 nm (Cao *et al.*, 2006; Guo *et al.*, 2008; Li *et al.*, 2005; Li *et al.*, 2004). Hence, it is concluded that the nanostructures grown at 120 min act as pure ZnO due to more ZnO materials consumed in longer growth time.

#### 4.4.5 Growth Mechanism of SnO<sub>2</sub>-Core/ZnO-Shell Nanostructures

According to Ellingham diagram (Ellingham, 1944) shown in Figure 4.30, the possible reactions involved in the growth process of nanostructures at the deposition temperature used in the present study are:





114

compared with ZnO ( $10^{-10.7}$  bar) at the deposition temperature of 900 °C (Lamoreaux *et al.*, 1987a), which is shown in Figure 4.31. Due to the lower vapour pressure, SnO<sub>2</sub> starts to nucleate first and forms the core of the nanowires at a shorter growth time of 15 min. If the growth time is further increased to 30 min, the partial pressure of SnO<sub>2</sub> goes down, as the source (ZnO: SnO<sub>2</sub> = 9:1) contains more ZnO than SnO<sub>2</sub>. This makes the vapour saturated in ZnO<sub>(v)</sub> and creates a condition for ZnO to condense on top of the SnO<sub>2</sub> nanowires in the form of a shell. Therefore, SnO<sub>2</sub>-core/ZnO-shell nanowires are observed at a deposition time of 30 min (Figure 4.23(a)). Furthermore, hierarchical nanostructures are observed when the growth time further increases from 60 min to 120 min.

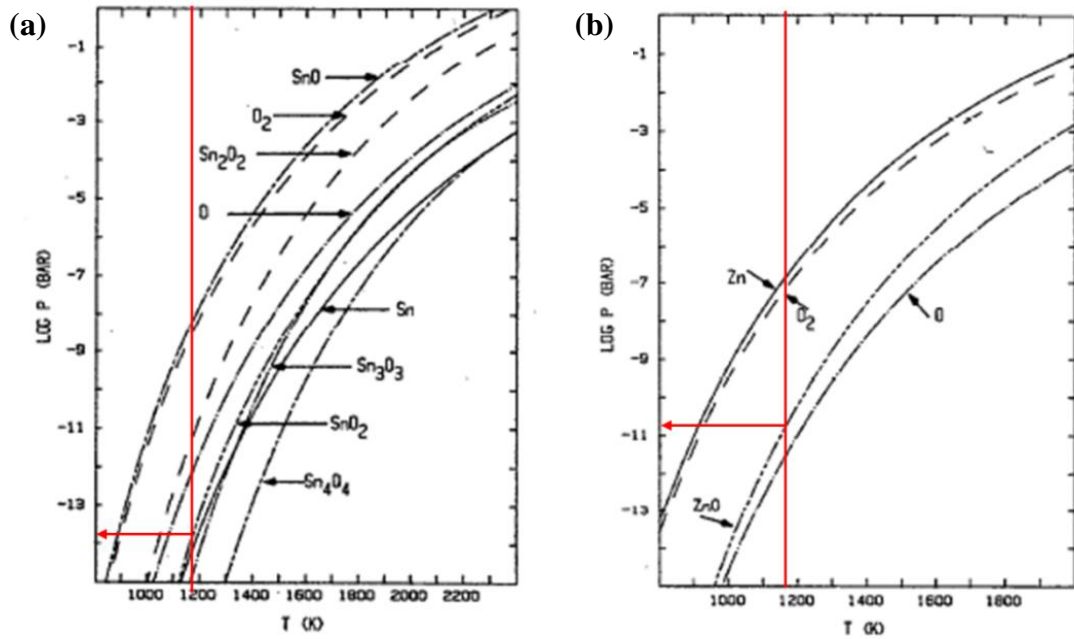


Figure 4.31: Vapour pressure detail of (a) SnO<sub>2</sub> and (b) ZnO nanostructure as a function of temperature (Lamoreaux *et al.*, 1987b).

It is suggested that the growth of hierarchical nanostructures can be divided into two steps. In the first step, the SnO<sub>2</sub> trunk nanowires grow, while the second step involves the growth of the ZnO shell layer on top of the SnO<sub>2</sub> core. The thickness of the ZnO shell increases as more Zn vapour condenses with increased growth time. When the

thickness of the ZnO shell layer reaches a critical value, then it acts as the seed layer for the growth of ZnO branches on top of the ZnO shell layer (Liu *et al.*, 2008). There is another possible reason to form 1-D branches. In XRD analysis, the (002) predominant peak was observed in ZnO phase (Figure 4.15), revealing the [001] oriented growth of the ZnO nanorods (Zhang *et al.*, 2004). Thus, (002) plane has rapid growth rate compared to other planes. Therefore, the growth rate along the [001] direction is much faster than that of radius direction which results in the crystal with 1-D structured morphology (Wu & Liu, 2002). When the growth time increases to 60 min,  $\text{SnO}_{2(v)}$  is mostly consumed, as source mixture contains more  $\text{ZnO}_{(s)}$  than  $\text{SnO}_{2(s)}$ . Therefore, ZnO hierarchical nanostructures can grow with a further increase of growth time; whereas for longer growth time of 120 min, nanorods branches tend to merge into wider structures (Figure 4.17(e)). All branches exhibit a hexagonal cross-section, which consist of ZnO only (Figure 4.17(f)). These branches come out perpendicular to the trunk of nanowires.

The morphology of the nanostructures depends on the growth parameters, including growth temperature, and the amount of starting materials (Zhang *et al.*, 2009). Zhang *et al.* (2009) found that a starting mixture of aluminum and alumina powder around 200 mg in weight favored the growth of regular  $\text{Al}_2\text{O}_3$  nanowires, while a larger amount of starting material around 500 mg induced the hierarchical nanostructures. In the present case, the amount of ZnO and  $\text{SnO}_2$  powder in the starting material is around 732 mg and 151 mg, respectively. A larger amount of ZnO in the starting mixture is another reason for the growth of ZnO nanorod branches at a longer deposition time (120 min).

#### **4.5 Gas Sensing Properties of $\text{Zn}_2\text{SnO}_4$ Nanowires**

The gas sensing properties of  $\text{Zn}_2\text{SnO}_4$  nanowires were measured at different operating temperatures and gas concentrations for various test gases (ethanol, hydrogen, carbon monoxide and methane). The concentration of target gas was varied from 20 ppm to 400

ppm. The gas concentration was increased from 20 ppm because of the sensor system can measure the minimum value of 20 ppm.

#### **4.5.1 Variation of Operating Temperature**

The gas sensing experiments were conducted for various reducing gases to examine the sensor performance of the  $\text{Zn}_2\text{SnO}_4$  nanowires. The sensitivity of a gas sensor is usually dependent on sensing temperature (Cao & Stetter, 1991). The sensitivity of the sensor to 50 ppm of ethanol, hydrogen, carbon monoxide and methane were tested to determine an optimum temperature, and the results are shown in Figure 4.32. It can be observed that the sensitivity of the sensor varies with the working temperature. From the results of ethanol, we can see that the sensitivity increases with temperature for up to 500 °C and then decreases. Similar trend is also obtained for hydrogen, carbon monoxide and methane with much less sensitivity compared to ethanol, shown in Figure 4.32(b)-(d). Thus, 500 °C was determined to be the optimum temperature for ethanol detection. Very similar values of optimum operating temperature are observed for all gases in the present case, though literature indicates varying optimum temperatures for different gases (Wen & Tian-Mo, 2010). The variations in the optimum operating temperature for different gases suggest variation in the adsorption and desorption characteristics of the gases (Wen & Tian-Mo, 2010). This property is utilized to design selective sensors. However, all sensors are operated over a wide range of temperature (300-550 °C) leading to different thermal energies for the surface reactions (Sivapunniam *et al.*, 2011). The sensitivity is very low below the operating temperature of 300 °C. It may be attributed to adsorbed gas molecules not being sufficiently activated to react with the adsorbed oxygen ion species on the surface of the sensing medium (Sivapunniam *et al.*, 2011). As the temperature is further increased above 300 °C, the activation energy barrier is surmounted allowing gas molecules to react with surface adsorbed oxygen



leading to the change in resistance and hence enhanced sensitivity (Lee & Reedy, 1999). The sensitivity of the sensor is observed to decrease above the temperature of 500 °C. This is a commonly observed phenomenon in resistive sensors since at higher temperatures desorption becomes dominant that leads to a decrease in sensitivity (Lee & Reedy, 1999; Ngo *et al.*, 2007).

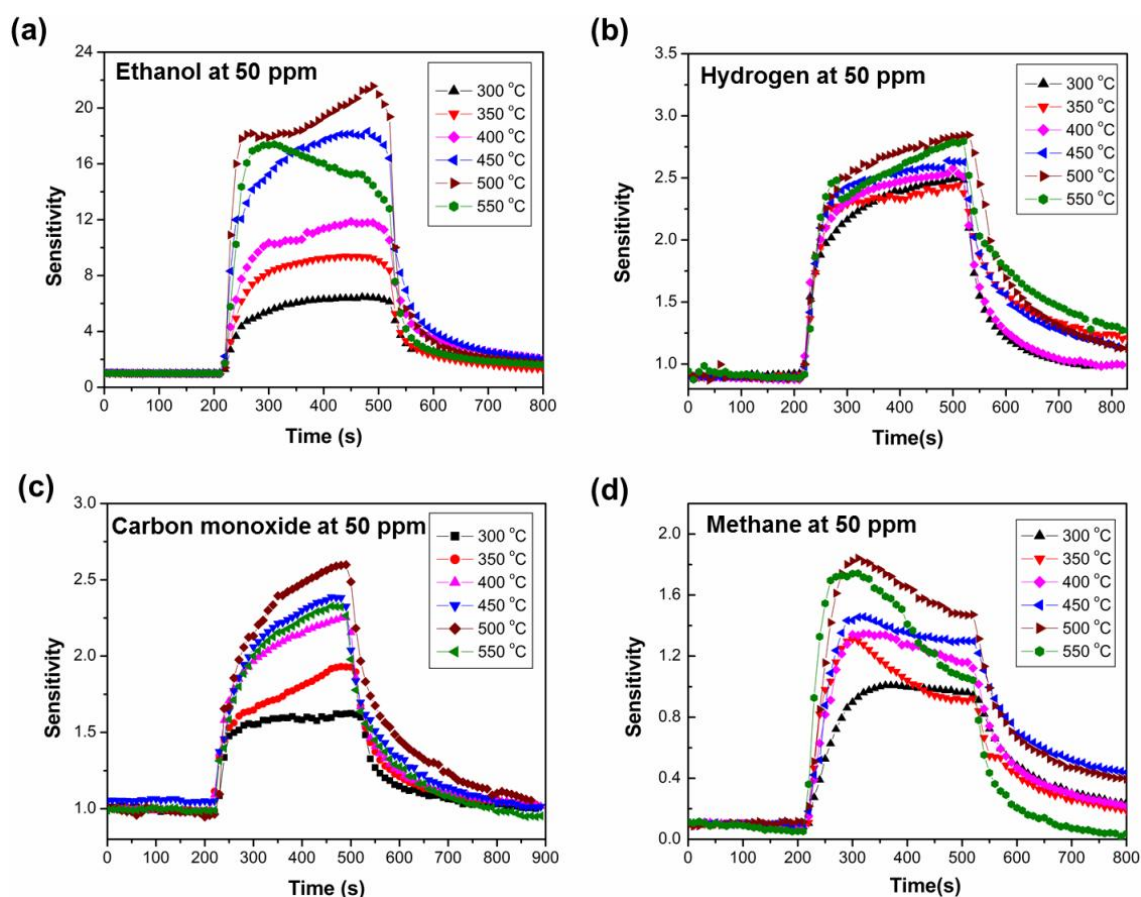


Figure 4.32: Sensitivity of  $\text{Zn}_2\text{SnO}_4$  sensor investigated at various operating temperatures for different gases at concentration of 50 ppm: (a) ethanol, (b) hydrogen, (c) carbon monoxide, and (d) methane.

#### 4.5.2 Dynamic Gas Response

Representative dynamic gas response of the  $\text{Zn}_2\text{SnO}_4$  sensor is measured upon exposure to ethanol, hydrogen, carbon monoxide and methane at an optimum operating temperature of 500 °C and the results are shown in Figure 4.33. These results imply that the sensor exhibits a strong response for ethanol and very little response for other three



gases at 500 °C. As seen in Figure 4.33, the fabricated sensors demonstrate fast response and recovery as well as reproducible sensitivity to ambient with different concentration of gases upon periodic switching from air ambient to reducing gas atmosphere. One of the key performance indicators for a gas sensor is to have good selectivity. Zn<sub>2</sub>SnO<sub>4</sub> nanowire-based sensor exhibits high selectivity toward ethanol compared to the other gases (Figure 4.33(a)). The response increases rapidly with increasing concentration of ethanol from 20 ppm to 400 ppm. This response curve reveals that the sensor could detect ethanol in a wide range. Five cycles were recorded with the concentrations of 20, 50, 100, 250 and 400 ppm. Sensitivities of ethanol corresponding to the above concentrations are 4.9, 21.6, 60.8, 254, and 468, respectively. The sensitivities of hydrogen, carbon monoxide and methane to 400 ppm are 4.75, 4.55 and 2.73, respectively, which is around 100 times lower than those for ethanol at the same concentration (Figure 4.33(b)-(d)). The response and recovery times for ethanol are 120 s and 200 s, respectively for the concentration of 20 ppm. Response time was decreased from 120 s to 100 s with increasing concentration from 20 ppm to 400 ppm. Similar observation was obtained for recovery time. Recovery time was reduced from 200 s to 60 s with increasing concentration from 20 ppm to 400 ppm

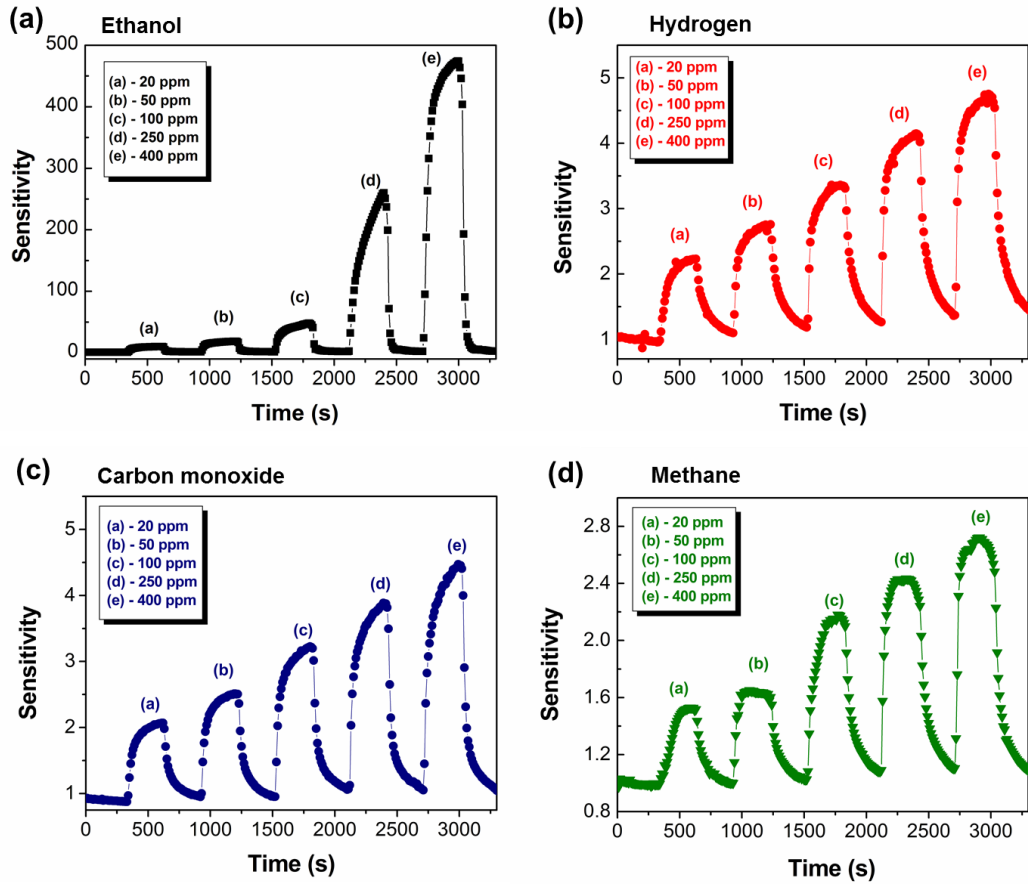


Figure 4.33: Five cycles of response-recovery characteristics of  $\text{Zn}_2\text{SnO}_4$  nanowires sensor exposed to different gas concentrations at an optimum operating temperature of 500 °C: (a) ethanol, (b) hydrogen, (c) carbon monoxide, and (d) methane.

#### 4.5.3 Variation of Gas Sensitivity with Concentration

Sensitivity as a function of concentration for various gases is shown in Figure 4.34. The ethanol sensing reveals that sensitivity increased linearly with increasing gas concentration from 20 ppm to 400 ppm (Figure 4.34(a)). However, in cases of hydrogen, carbon monoxide and methane the sensitivity increased non-linearly with gas concentration. The sensitivity towards these gases increases linearly up to 100 ppm concentration. Beyond 100 ppm concentration, the sensitivity tends to reach saturation gradually after climbing over the point of 400 ppm concentration. Further, this sensor exhibits the lowest detection limit for all gases is 20 ppm. As can be seen the sensitivity of  $\text{Zn}_2\text{SnO}_4$  nanowire-based sensors for ethanol is almost hundreds times higher than

the other gases at 500 °C for 400 ppm of gas concentration. Therefore  $\text{Zn}_2\text{SnO}_4$  nanowire-based sensors can be used to detect ethanol in practical application in the environmental field.

Carbon monoxide (CO) is a one of the hazardous gas among the gases tested which produced by the combustion of carbon-containing fuels or the insufficient ventilation of natural gas (Roth *et al.*, 2014). It is undetectable by humans. Once it enters inside the bloodstream of human body, CO prevents oxygen to reach living tissues. Therefore, CO leads the cause of death by poisoning blood in industrialized countries. The maximum time weighted average exposure value ascribed by the United States National Institute of Occupational Safety and Health is 35 ppm over an 8 h period (Goldstein, 2008; Health, 1992). But, Yu *et al.* (1998a) reported minimum detection limit for CO gas in  $\text{ZnO-SnO}_2$  nanocomposite-based sensor was about 200 ppm. There is no safety concern for under 50 ppm CO exposure for a short period of time. On the other hand, our  $\text{Zn}_2\text{SnO}_4$  nanowire-based sensor for CO exhibits that it can be detected even at 20 ppm of CO with a sensitivity of  $\sim 2.25$  (Figure 4.34(c)). Thus, this sensor is also suitable for monitoring CO.

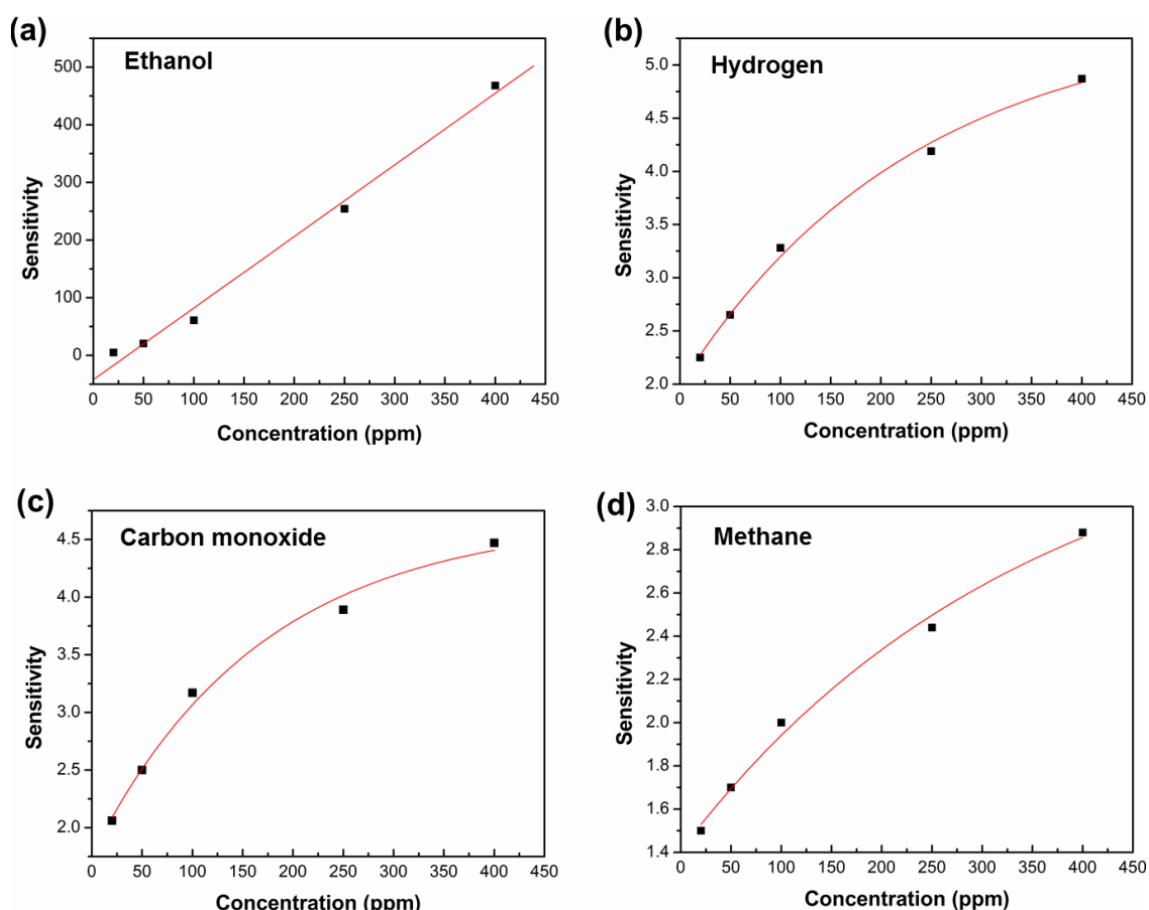


Figure 4.34: Sensitivity of  $\text{Zn}_2\text{SnO}_4$  nanowires sensor as a function of various gas concentrations: (a) ethanol, (b) hydrogen, (c) carbon monoxide, and (d) methane.

#### 4.5.4 Selectivity of $\text{Zn}_2\text{SnO}_4$ Nanowires based Sensor

The selectivity is one of the important properties of gas sensors for practical applications. Theoretically, the sensors should have high response to some gases and little or no response to other gases in the same surroundings (Patil *et al.*, 2010). To check the selectivity properties, different gases were exposed at 50 ppm to measure the sensitivity values as a function of operating temperatures. Figure 4.35 shows the comparison of sensitivity of  $\text{Zn}_2\text{SnO}_4$  nanowire-based sensor at different operating temperatures to 50 ppm of  $\text{CH}_4$ ,  $\text{H}_2$ ,  $\text{C}_2\text{H}_5\text{OH}$  and  $\text{CO}$  gases. With increasing working temperature, the sensitivity value of  $\text{Zn}_2\text{SnO}_4$  nanowire-based sensor increases gradually, undergoes a maximum and then decreases again. A good selectivity and high sensitivity of sensor was obtained for ethanol at 500 °C, while it exhibits leading sensitivity and

wide range of detection over various working temperature. Since the optimal operating temperature is high, the response and selectivity are inadequate, further research is required to decrease the optimal operating temperature by introducing some metal element (Au or Pt) or oxides (CuO or NiO).

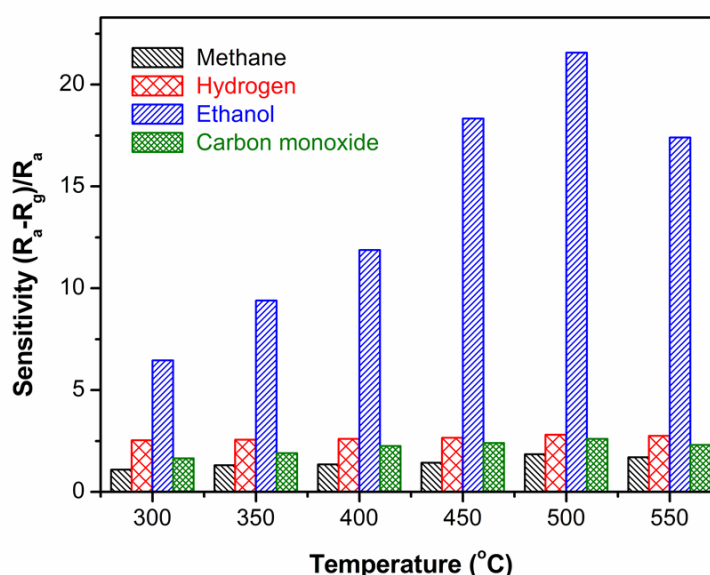


Figure 4.35: Variation of sensitivity as a function of operating temperature of  $\text{Zn}_2\text{SnO}_4$  nanowires gas sensors to 50 ppm of methane, hydrogen, ethanol, and carbon monoxide.

Several groups have investigated  $\text{Zn}_2\text{SnO}_4$  based nanowire sensor for ethanol detection. Detailed results obtained from various researchers are illustrated in Table 4.2. The present work of  $\text{Zn}_2\text{SnO}_4$  based nanowire sensor achieved better sensitivity compared with that, of previously reported results. Thus, for having high sensitivity and selectivity,  $\text{Zn}_2\text{SnO}_4$  based nanowire sensor is a suitable candidate for monitoring ethanol.

Table 4.2: Brief summary of  $\text{Zn}_2\text{SnO}_4$  gas sensor upon exposure to 100 ppm ethanol

$\text{Zn}_2\text{SnO}_4$ (ZTO) nanostructures	Detection range (ppm)	Sensitivity	Working temperature ( $^{\circ}\text{C}$ )	References
Zigzag nanowires	1-200	17	-	Chen <i>et al.</i> , 2011
Hierarchical nanostructures	10-100	34	128	Chen <i>et al.</i> , 2011
Quasi-cuboctahedra	30-600	34	325	Jiang <i>et al.</i> , 2011
ZTO- $\text{SnO}_2$ nanocomposites	25-500	0.73	300	Lu & Tang, 2005
3D-hierarchical flower	5-100	30.8	380	Chen <i>et al.</i> , 2015
Sn/ZTO nanocrystal	25-600	23	240	Han <i>et al.</i> , 2013
Nanowires	20-400	60.8	500	This work

#### 4.5.5 Sensing Mechanism for $\text{Zn}_2\text{SnO}_4$ Nanowires

Gas adsorption and desorption is a common mechanism for gas sensing (Wang *et al.*, 2010). Metal oxide based sensor is exposed to air, which results in the adsorption of  $\text{O}_2$  on the surface of the material [ $\text{O}_{2(\text{gas})} \leftrightarrow \text{O}_{2(\text{ads})}$ ]. Oxygen molecules trap electrons from the conduction band of the material because of their strong electronegativity hence induces oxygen adsorption (Geng *et al.*, 2008). The stable  $\text{O}_2^-$  ions are dominant when the temperature is below  $100\text{ }^{\circ}\text{C}$  [ $\text{O}_{2(\text{ads})} + e^- \leftrightarrow \text{O}_{2(\text{ads})}^-$ ]. At moderate temperature between  $100$  and  $300\text{ }^{\circ}\text{C}$ ,  $\text{O}^-$  ion species is more abundant than  $\text{O}_2^-$  [ $\text{O}_{2(\text{ads})}^- + e^- \leftrightarrow 2\text{O}_{(\text{ads})}^-$ ] and  $\text{O}^{2-}$  ion is stable above  $300\text{ }^{\circ}\text{C}$  [ $\text{O}_{(\text{ads})}^- + e^- \leftrightarrow \text{O}_{(\text{ads})}^{2-}$ ] (Oh *et al.*, 2009; Sadek *et al.*, 2007; Yao *et al.*, 2014). Due to oxygen adsorption, electron concentration in the conduction band drops, and the resistance of the material rises for an n-type oxide. When a reducing gas is introduced, a chemical reaction takes place between the reducing gas and the surface adsorbed oxygen, which results in electron injection to the surface of the material that results in the decrease of the resistance of the material.

A similar mechanism is at play in our  $\text{Zn}_2\text{SnO}_4$  based sensor. Optimum sensing was performed above 300 °C for all test gases. Therefore  $\text{O}^{2-}$  ion species interact with test gases. When hydrogen gas is introduced, it reacts with the chemisorbed oxygen and produces  $\text{H}_2\text{O}$ , which is expressed in equation (4.5) (Sadek *et al.*, 2007).



Kohl *et al.* (Kohl, 2001) reported the methane dissociation mechanism. They stated that methane dissociates to a methyl group and hydrogen. Subsequently, combination of adsorbed hydrogen atoms produces hydrogen molecule which is described by equations (4.6) and (4.7). Then the hydrogen molecule reacts with the adsorbed oxygen on the  $\text{Zn}_2\text{SnO}_4$  surface and creates  $\text{H}_2\text{O}$ , which is shown by equation (4.8).

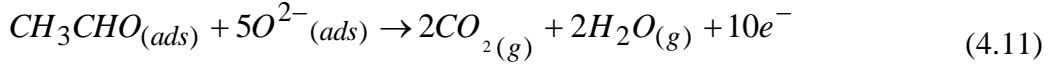
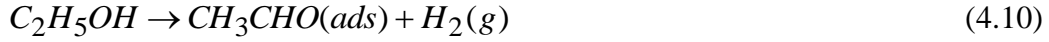


When the sensor of  $\text{Zn}_2\text{SnO}_4$  is exposed in carbon monoxide at 500 °C, the adsorbed CO gas then reacts with the chemisorbed oxygen anions of surface and formed  $\text{CO}_2$  gas, the reaction can be described as follows (equation 4.9) (Shi *et al.*, 2014):



Catalytic oxidation of ethanol gas is known to occur through two different routes depending on the acid or base properties of the catalyst surface. One is a dehydrogenation route through  $\text{CH}_3\text{CHO}$  intermediate (on the basic surface) and a dehydration route through a  $\text{C}_2\text{H}_4$  intermediate (on the acidic surface) (Kim *et al.*, 2007b). But,  $\text{Zn}_2\text{SnO}_4$  is an n-type semiconductor. Thus it acts as a basic oxide.

Therefore dehydrogenation is favoured, providing  $\text{CH}_3\text{CHO}$  as the main intermediate when  $\text{C}_2\text{H}_5\text{OH}$  is introduced. Then it undergoes consequent oxidation to form  $\text{CO}_2$  and  $\text{H}_2\text{O}$  which is shown in equations (4.10) and (4.11) (Kim *et al.*, 2007b).



When the gas sensor is exposed to the test gas, the resistance of the material decreases and the sensitivity increases due to the injection of electrons to the oxide as a result of the above reactions. According to these three test gas equations, the electron donating effect of ethanol ( $10e^-$ ) is stronger than that of the hydrogen, carbon monoxide and methane ( $2e^-$ ) gases. Hence, the sensitivity of ethanol is greater than that of the other gases for the same concentration.

The enhancement of ethanol sensing performance of  $\text{Zn}_2\text{SnO}_4$  nanowires can be easily attributed to more oxygen vacancy defects since the previous PL results showed high concentration of oxygen vacancy defects that exist in the as-deposited  $\text{Zn}_2\text{SnO}_4$  nanowires (Figure 4.11(a)). These oxygen vacancy defects, acting as active centers, can facilitate the adsorption of oxygen and enhance the chance of interaction with testing gases. Therefore, existence of oxygen vacancy is also another reason to enhance the gas sensitivity due to increase active centers.

#### 4.6 Sensing Performance of $\text{SnO}_2$ -Core/ $\text{ZnO}$ -Shell Nanostructures

The sensing properties of  $\text{SnO}_2$ -core/ $\text{ZnO}$ -shell nanostructures grown for different times were compared with various test gases (ethanol, hydrogen, carbon monoxide and methane) in order to demonstrate their gas sensing properties.



#### 4.6.1 Variation of Operating Temperature

Temperature is an important factor to affect the performance of gas sensors as discussed in the previous section 4.5.1. The gas sensing experiments were performed for SnO<sub>2</sub>-core/ZnO-shell nanostructure grown for 90 min gas sensor at different temperatures in order to find out the optimum operating temperature for different gas detection. The effect of sensing temperature on the response of the synthesized SnO<sub>2</sub>-core/ZnO-shell nanostructure to 20 ppm ethanol, hydrogen, carbon monoxide and methane gases is shown in Figure 4.36. The relationship between the gas response and the operating temperature exhibits a trend of “increase-maximum-decay” behaviour to 20 ppm of all test gases. Ethanol sensor shown in Figure 4.36(a) reveals sensitivity increase with increasing working temperature and reached maximum sensing value of 25.2 at 400 °C and thereafter the sensitivity decreases with temperature exceeding 400 °C. The sensor show high sensitivity and good response characteristic to ethanol at 400 °C. It indicates that the optimum working temperature of SnO<sub>2</sub>-core/ZnO-shell nanostructure is 400 °C. This working temperature is the modest from the viewpoint of other semiconducting oxide gas sensors such as TiO<sub>2</sub> (Arafat *et al.*, 2014). Similar trend was observed by other such gases: H<sub>2</sub>, CO and CH<sub>4</sub> which exhibit the same optimum sensing temperature of 400 °C (Figure 4.34(b)-(d)). Especially, the ethanol sensor shows ~10 times enhanced sensitivity than that of other test gas sensors at an optimum operating temperature of 400 °C.

Furthermore, the stability of ethanol sensor is easily attained upon exposure of ethanol gas. In contrast, other test gases take long time to achieve their stability, which is illustrated by shape of sensitivity graph. They exhibit saw-tooth shape in their time-dependent sensitivity graphs except ethanol sensor. Additionally, a remarkable

difference in the shape of the sensitivity curve also depends on the operating temperature (Choi *et al.*, 2013).

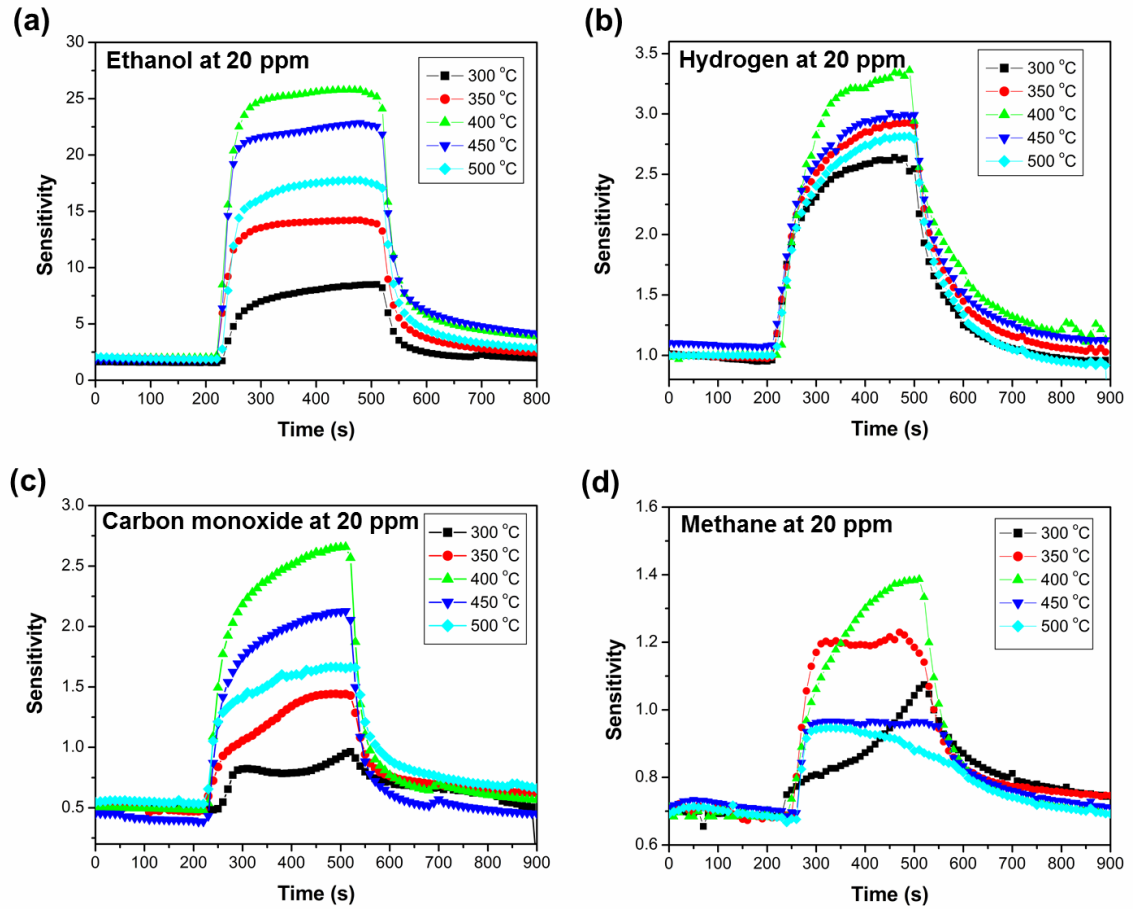


Figure 4.36: Sensitivity of SnO<sub>2</sub>-core/ZnO-shell nanostructure grown for 90 min sensor investigated at various operating temperatures for different gases: (a) ethanol, (b) hydrogen, (c) carbon monoxide, and (d) methane.

#### 4.6.2 Dynamic Gas Responses

Figure 4.37 shows the typical transient response of the SnO<sub>2</sub>-core/ZnO-shell nanostructures-based sensors upon exposure to 20, 50, 100, 250 and 400 ppm ethanol, hydrogen, carbon monoxide and methane at 400 °C. As clearly seen in Figure 4.37 (a), the SnO<sub>2</sub>-core/ZnO-shell nanostructures gas sensors shows not only high sensitivity but also fast response and recovery characteristics at the optimum operating temperature of 400 °C for all the detection range of ethanol gas. SnO<sub>2</sub>-core/ZnO-shell hierarchical nanostructures exhibit higher sensitivity to ethanol than just SnO<sub>2</sub> nanowires, which is

obtained for a deposition time of 15 min. The enhancement of the ethanol gas sensing performance of hierarchical SnO<sub>2</sub>-core/ZnO-shell nanostructures can be attributed to the greater sensing surface area due to the hierarchical structure. It can be seen from Figure 4.37(a) that when exposed to 20 ppm ethanol, the responses are about 6.1, 20.4, 22.5, 31.9 and 17.3 for SnO<sub>2</sub>/ZnO nanostructures grown for 15, 30, 60, 90 and 120 min, respectively. The results show that optimum sensing was observed for the nanostructures grown for 90 min. Due to the superstructure of SnO<sub>2</sub>-core/ZnO-shell hierarchical nanostructures, the nanostructures grown for 90 min should exhibit excellent sensing characteristics. As the ethanol concentration increased from 20 ppm to 400 ppm, the sensitivity increased from 31.9 to 128, which means that the reversibility and repeatability of the gas sensors are excellent (Huang *et al.*, 2005; Wan *et al.*, 2008a). Therefore, nanostructures grown for 90 min exhibit nearly a five-fold enhanced sensitivity compared to just SnO<sub>2</sub> nanowires (which was obtained for a growth time of 15 min). A sudden drop in the ethanol response was observed when the nanostructures were grown for 120 min. A possible explanation for this is given later in the discussion of the sensing mechanism. Good contact of SnO<sub>2</sub>-core/ZnO-shell nanostructures with Au contact could also be witnessed by good sensing behaviour to all test gases and quick recovery after the turn-off of sensing gases. However, the dynamic sensor response towards hydrogen and carbon monoxide are very poor compared to ethanol, and negligible response was obtained for methane (Figure 4.37(b)-(d)). The response and recovery time of sensor for SnO<sub>2</sub>-core/ZnO-shell nanostructures grown at 90 min was measured to be 20 s and 150 s for 20 ppm of ethanol concentration. Moreover, the response time shows the reducing tendency from 20 s to 10 s with an increasing ethanol concentration from 20 ppm to 400 ppm, while recovery time decreased from 320 s to 200 s.

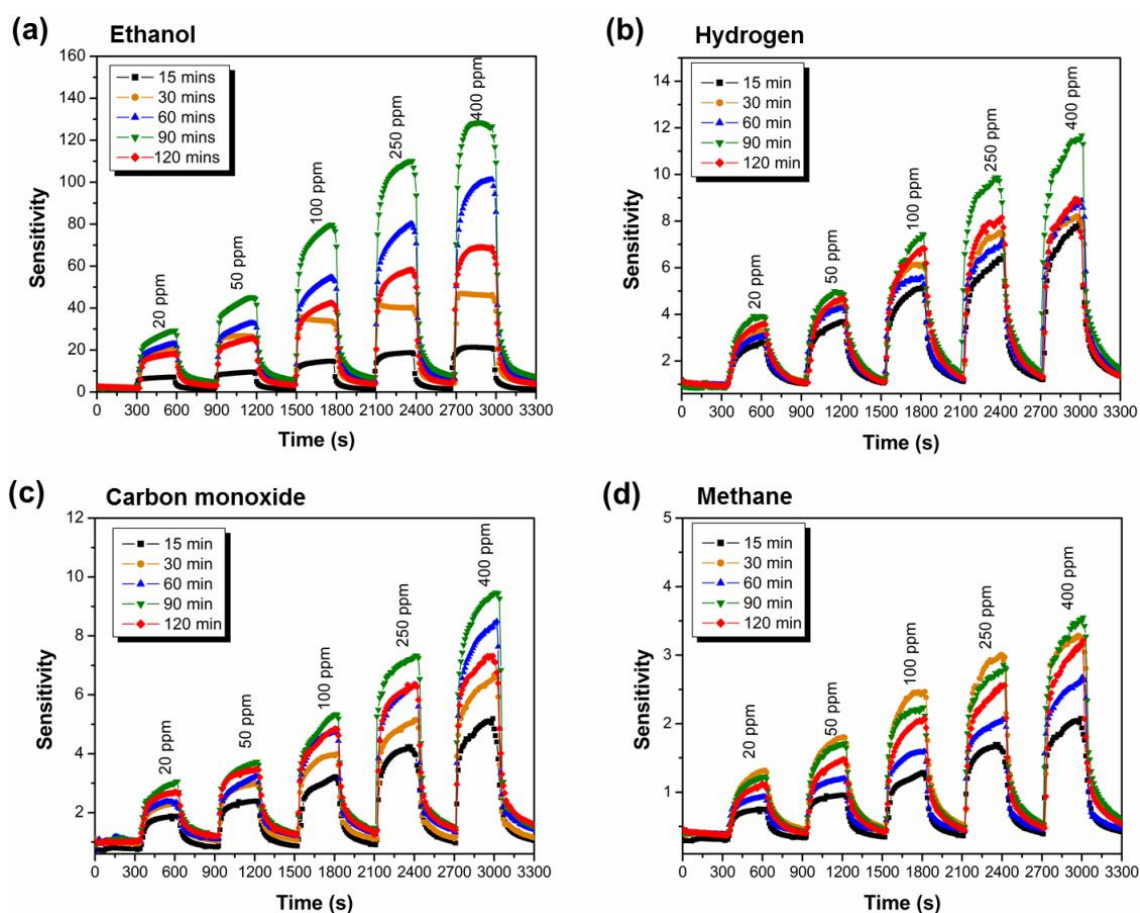


Figure 4.37: Time-dependent sensitivity of various growth times of SnO<sub>2</sub>-core/ZnO-shell nanostructure sensors with different gas concentrations at an optimum operating temperature of 400 °C: (a) ethanol, (b) hydrogen, (c) carbon monoxide, and (d) methane.

#### 4.6.3 Selectivity of SnO<sub>2</sub>-Core/ZnO-Shell Nanostructures Based Sensor

The bar chart of sensor responses of SnO<sub>2</sub>-core/ZnO-shell nanostructures in terms of sensitivity towards various gases at a fixed concentration of 20 ppm and a sensing temperature of 400 °C is illustrated in Figure 4.38. It shows that the ethanol is highly sensed by all sensors rather than that of other gases. It is noteworthy that SnO<sub>2</sub>-core/ZnO-shell nanostructures exhibit greater sensitivity towards ethanol than just SnO<sub>2</sub> nanowires (growth time of 15 min). As shown in Figure 4.38, SnO<sub>2</sub>-core/ZnO-shell nanostructures grown for 90 min have the highest response towards ethanol. It is also seen that the sensors exhibit a poor response to hydrogen and carbon monoxide, and are almost insensitive to methane. Selectivity coefficients are calculated between the

highest response of the test gas and the other test gases (Zhang *et al.*, 2011). The selectivity coefficients of  $K_{C_2H_5OH/H_2}$ ,  $K_{C_2H_5OH/CO}$  and  $K_{C_2H_5OH/CH_4}$  (where,  $K_{C_2H_5OH/H_2}$ ,  $K_{C_2H_5OH/CO}$  and  $K_{C_2H_5OH/CH_4}$  are the sensitivity ratio between ethanol and hydrogen; ethanol and carbon monoxide; and ethanol and methane, respectively) for SnO<sub>2</sub>-core/ZnO-shell nanostructures grown for 90 min were determined to be about 8, 10 and 32, respectively, to 20 ppm of test gases. The results indicate that the fabricated SnO<sub>2</sub>-core/ZnO-shell nanostructures grown for 90 min have a much higher selectivity toward ethanol.

Liu *et al.* (2011) reported that a sensor prepared using a 3D hierarchical porous ZnO structure functionalized by Au nanoparticles exhibited a sensitivity of 8.9 towards 50 ppm ethanol. Xue *et al.* (2010) demonstrated that a Pt-loaded SnO<sub>2</sub> nanorod sensor showed a sensitivity up to 9.5 towards 50 ppm of ethanol. Compared with the reported results, the present work shows that high sensitivity and selectivity towards ethanol sensors can be achieved without additives.

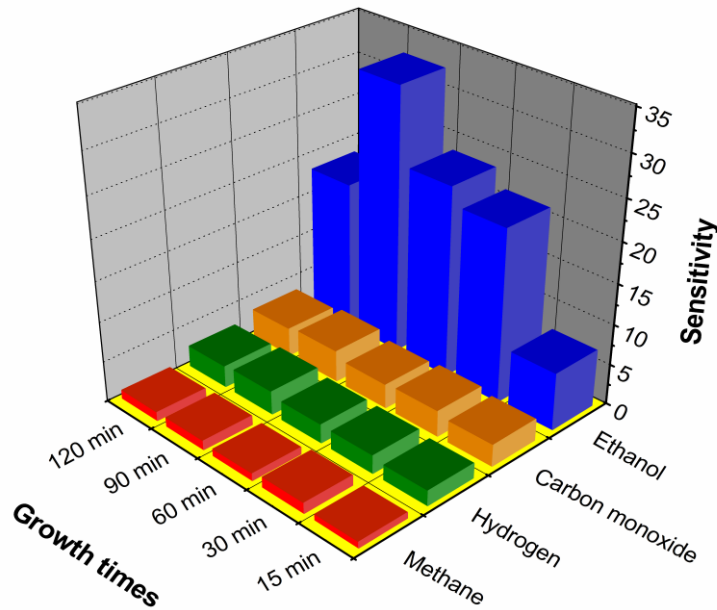


Figure 4.38: Sensitivity bar chart of sensors towards 20 ppm of methane, hydrogen, carbon monoxide and ethanol.

The brief summary of results reported on ZnO/SnO<sub>2</sub> gas sensor upon exposure of 100 ppm ethanol is illustrated in Table 4.3. It clearly shows that the SnO<sub>2</sub>-core/ZnO-shell hierarchical nanostructures obtained at growth time of 90 min exhibits greater sensitivity among previously reported results for 100 ppm of ethanol. Therefore, the present ethanol sensor can be used to detect ethanol in environmental monitoring. Even though, the present ternary Zn<sub>2</sub>SnO<sub>4</sub> nanowire sensor shows reduced ethanol gas response (60.8) compared to SnO<sub>2</sub>-core/ZnO-shell sensor (76) at same concentration of 100 ppm.

Table 4.3. Brief summary of ZnO/SnO<sub>2</sub> gas sensor upon exposure to 100 ppm ethanol

ZnO/SnO <sub>2</sub> nanostructures	Detection range (ppm)	Sensitivity	Working temperature (°C)	References
SnO <sub>2</sub> /ZnO hierarchical nanostructures	25-500	6	400	Khoang <i>et al.</i> , 2012b
ZnO-SnO <sub>2</sub> nanofiber	1-10000	18	300	Song & Liu, 2009
ZnO-SnO <sub>2</sub> hierarchical nanostructures	10-1000	30	300	Li <i>et al.</i> , 2011
Mesoporous ZnO-SnO <sub>2</sub> nanofibers	5-10000	21	300	Song <i>et al.</i> , 2009
flower-like ZnO-SnO <sub>2</sub> composite	5-100	3.4	400	Cui <i>et al.</i> , 2012
SnO <sub>2</sub> /ZnO composite nanofibers	27.7-5000	6	360	Khorami <i>et al.</i> , 2011
SnO <sub>2</sub> - core/ZnO-shell nanowires	25-500	14.05	400	Thanh Le <i>et al.</i> , 2013
ZnO-doped porous SnO <sub>2</sub> hollow nanospheres	10-500	14.7	150	X. Ma <i>et al.</i> , 2013
SnO <sub>2</sub> doped ZnO thin film	1-200	40	450	Nanto <i>et al.</i> , 1996
SnO <sub>2</sub> - core/ZnO-shell hierarchical nanostructures obtained at 90 min	20-400	76	400	This work

#### 4.6.4 Sensing Mechanism for SnO<sub>2</sub>-core/ZnO-shell Nanostructures

According to the above sensing results, SnO<sub>2</sub>-core/ZnO-shell nanostructure sensors exhibit significantly improved ethanol sensing properties compared with just SnO<sub>2</sub> nanowires grown for 15 min. The improvement in the sensing property is thought to be

related to the core/shell nanostructures. ZnO and SnO<sub>2</sub> are n-type semiconductors with different band gaps, electron affinities and work functions which is shown in Table 4.4.

Table 4.4. The value of electronic properties of ZnO and SnO<sub>2</sub> nanostructures (Robertson *et al.*, 2006; Zhang *et al.*, 2010; Zheng *et al.*, 2009).

Electronic properties	ZnO (eV)	SnO <sub>2</sub> (eV)
electron affinity ( $\chi$ )	4.3	4.5
work function ( $\phi$ )	5.2	4.9
band gap ( $E_g$ )	3.37	3.6

As seen in Figure 4.23(a), a heterojunction has formed at the interface between SnO<sub>2</sub>-core and ZnO-shell. Figure 4.39 shows the possible energy band diagram of the fabricated SnO<sub>2</sub>-core/ZnO-shell nanostructures. Figure 4.39 (a) shows that ZnO has a lower work function than SnO<sub>2</sub>. Therefore, electrons are transferred from SnO<sub>2</sub> to ZnO until both Fermi levels become equal (Zheng *et al.*, 2009), which is shown in Figure 4.39(b). An electron depletion layer is formed at the interface between SnO<sub>2</sub> and ZnO, leading to a heterojunction barrier due to band bending. The enhanced sensing properties is ascribed to the variation of the heterojunction barrier when exposed to various kinds of gases (Chen *et al.*, 2011a).

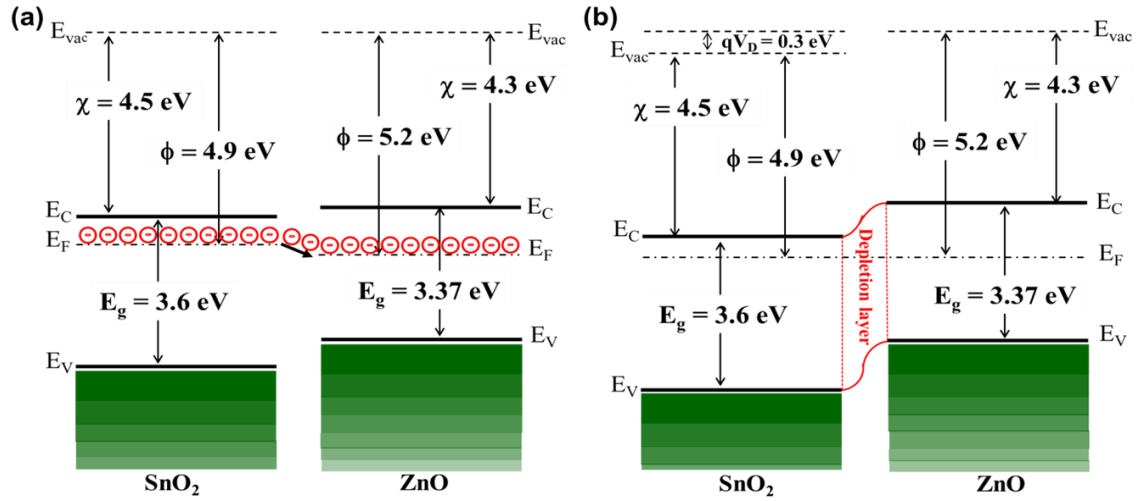


Figure 4.39: Energy band diagram of (a) SnO<sub>2</sub> and ZnO, and (b) SnO<sub>2</sub>-core/ZnO-shell nanostructures (adapted from Zhang *et al.*, 2011; Zhang *et al.*, 2010; Zheng *et al.*, 2009).

Electron depletion region theory is widely used in explaining sensing mechanism (Wang *et al.*, 2010). Electrons in the ZnO shell is depleted by adsorbing oxygen molecules from the air, leading to the formation of various ionized forms ( $O_2^-$ ,  $O^{2-}$ ,  $O^-$ ) (Hsueh *et al.*, 2007b) when the SnO<sub>2</sub>-core/ZnO-shell nanostructures are exposed to air. When the core/shell sensor is exposed to ethanol, it reacts with adsorbed oxygen and releases the trapped electrons back to the conduction band of the ZnO shell by the dehydrogenation process (Zhu *et al.*, 2012), because ZnO and SnO<sub>2</sub> are basic oxides. Thus, the resistance of the core/shell sensor is decreased, and the response is augmented. This fact is also supported by the fact that the resistance of just SnO<sub>2</sub> nanowires is  $\sim 7.5 \text{ M}\Omega$ , which is greater than that of the SnO<sub>2</sub>-core/ZnO-shell nanostructures ( $\sim 3.5 \text{ M}\Omega$ ). The thickness of the shell is also another important parameter in gas sensing (Chen *et al.*, 2011a). In gas sensors, the thickness of the shell material must be close to the Debye length of nanomaterials for the sensor to exhibit enhanced sensitivity (Park *et al.*, 2013b). This effect is called a synergistic effect. The value of the Debye length for metal oxides is in the range of 3–30 nm, which depends



on the sensing material, charge carrier concentration and ambient temperature (Barsan & Weimar, 2001; Ogawa *et al.*, 1982).

The width of the surface depletion layer is in the order of the Debye length  $\lambda_D$ , which can be expressed as follows (Park *et al.*, 2013a):

$$\lambda_D = \sqrt{\frac{\varepsilon k_B T}{n q^2}} \quad (4.5)$$

where  $\varepsilon$  is the static dielectric constant ( $=8.75 \times 8.85 \times 10^{-12}$  F/m in ZnO),  $k$  is the Boltzmann constant ( $=1.38 \times 10^{-23}$  J/K),  $T$  is the sensing temperature in K,  $q$  is the electrical charge of the carrier ( $=1.6 \times 10^{-19}$  C) and  $n$  is the carrier concentration.

Park *et al.* (2013a) calculated the carrier concentration ( $5.1 \times 10^{16}/\text{cm}^3$ ) and Debye length (21.7 nm) of ZnO shell on  $\text{Zn}_2\text{SnO}_4$ -core/ZnO-shell nanorods at a sensing temperature of 300 °C. But, since ZnO is a n-type non-degenerate semiconductor, therefore the carrier concentration of ZnO can be described as follows (Zeghbroeck, 2011):

$$n = N_c e^{\frac{(E_F - E_C)}{kT}} \quad (4.6)$$

Using the above two equations (4.5) and (4.6), the calculated value of carrier concentration and Debye length ( $\lambda_D$ ) at 400 °C are  $5.0 \times 10^{16}/\text{cm}^3$  and 23.8 nm, respectively. This means that gas molecules not only deplete the electrons in the ZnO shell layer, but also take electrons from the  $\text{SnO}_2$  core. The shell thickness of nanowire grown for 30 min is slightly small ( $\sim 20$  nm) (Figure 4.23(a)) compared to calculated value (23.8 nm). Therefore, in  $\text{SnO}_2$ -core/ZnO-shell nanowires, the heterojunction barrier at the interface of the core and shell should also be considered because electron transport is modulated by the heterojunction.

The calculated value of surface area of just  $\text{SnO}_2$  and  $\text{SnO}_2$ -core/ZnO-shell nanowires obtained for 15 min and 30 min samples are  $20.56 \text{ m}^2/\text{g}$  and  $19.23 \text{ m}^2/\text{g}$ , respectively.

Just SnO<sub>2</sub> nanowires grown for 15 min have high surface area than SnO<sub>2</sub>-core/ZnO-shell nanowires grown for 30 min. Because, lower growth time nanostructures have small diameter compared to longer growth time nanowire. As a result just SnO<sub>2</sub> nanowire has high surface area. But, SnO<sub>2</sub>-core/ZnO-shell nanowires grown for 30 min sensor exhibited enhanced ethanol sensing compared to just SnO<sub>2</sub> nanowire. Therefore, the dominant sensing mechanism is synergistic effect of encapsulation of SnO<sub>2</sub> by ZnO nanostructures (heterojunction) than surface area.

As described above, the proposed mechanism for the enhanced ethanol sensing of the SnO<sub>2</sub>-core/ZnO-shell hierarchical nanostructures grown for 60 min and 90 min is attributed to the synergistic effect of the encapsulation of SnO<sub>2</sub> by ZnO nanostructures and the increased surface sites in the hierarchical structure. On the other hand, if the thickness of the shell is larger than 45 nm, the core/shell nanostructures have weak sensing characteristics (Chen *et al.*, 2011a). The thickness of the ZnO shell determined was increased to ~50 nm when the core/shell nanostructures were grown for a longer time of 120 min (Figure 4.24(c)). Thus, this sensor could not meet the synergistic effect, due to the increased shell thickness of 50 nm. But, the sensor sensitivity towards ethanol is high for core/shell hierarchical nanostructures grown for 90 min compared with 60 min growth time nanostructures. It may be due to increased sensing sites owing to increased surface area. Because the calculated surface area of nanostructures grown for 60 min has lower surface area (11.62 m<sup>2</sup>/g) than that of nanostructures obtained for 90 min (16.17 m<sup>2</sup>/g).

Moreover, the thickness of the ZnO shell (~50 nm) is higher compared to core-shell nanostructures grown for 60 min and 90 min, due to the added amount of Zn condensed on the nanostructures with increased growth time (Figure 4.24(c)). Therefore, SnO<sub>2</sub>-core/ZnO-shell nanostructures grown for 120 min behave just ZnO nanowire sensors. For a longer growth time of 120 min, the branches of the SnO<sub>2</sub>-core/ZnO-shell hierarchical

nanostructures tend to merge into coarser structures (Figure 4.17(e)) and calculated surface area has also low value ( $6.49 \text{ m}^2/\text{g}$ ) compared to nanostructures obtained at 60 min ( $11.62 \text{ m}^2/\text{g}$ ) and 90 min ( $16.17 \text{ m}^2/\text{g}$ ). As a result, sensing surface areas are reduced compared to other hierarchical core/shell nanostructures. Therefore, the sensor fabricated using  $\text{SnO}_2$ -core/ $\text{ZnO}$ -shell hierarchical nanostructures deposited at 120 min exhibits lower sensing response than  $\text{SnO}_2$ -core/ $\text{ZnO}$ -shell hierarchical nanostructures deposited at 90 min, because of their reduced sensing surface and shell thickness being greater than the Debye length. From these results, it is concluded that the size and morphology of nanostructures have significant influence on their sensing response to ethanol gas.

## CHAPTER 5

### CONCLUSIONS AND RECOMMENDATIONS

#### 5.1 Conclusions

In this thesis, the simultaneous synthesis of  $\text{Zn}_2\text{SnO}_4$  nanowires and  $\text{SnO}_2$ -core/ $\text{ZnO}$ -shell nanostructures by a single-step carbon-assisted thermal evaporation technique is reported. A mixture of zinc oxide, tin oxide and carbon powder mixture was used as the source to grow these nanostructures. The mixture was loaded in a quartz boat inside tube furnace, and a Au coated alumina substrate was placed at near the quartz boat with opposite direction of gas flow. Purified Ar was purged in the furnace at elevated temperatures. Grey and white-wool like deposits formed on Au coated alumina substrate and at the side as well as on the top of the quartz boat, respectively. Sensors based on these two types of nanostructures were fabricated for various reducing gases. The results obtained from the present work have led to the following conclusions.

#### Nanostructures Growth on Au Coated Alumina Substrate:

- $\text{Zn}_2\text{SnO}_4$  nanowires grew on the Au coated alumina substrate following the vapour-liquid-solid (VLS) mechanism.
- Sputtered Au layer acted as a catalyst and the formation of the ternary  $\text{Zn}_2\text{SnO}_4$  nanowires was due to the intermediate liquid state during the growth.
- The length and diameter of  $\text{Zn}_2\text{SnO}_4$  nanowires depend on growth temperature, growth time, and the distance between the source and the substrate.
- The optimum growth condition for nanowires was achieved at 9 cm away from the center of furnace, at a growth temperature of 834 °C and a growth time of 2 hours.

### **Nanostructures Growth on Quartz Boat:**

- The white fluffy deposit found on the quartz boat was found to be SnO<sub>2</sub>-core/ZnO-shell type nanowires as well as hierarchical nanostructures.
- Both hierarchical and core-shell nanostructures formed in the quartz boat were suggested to grow by vapour-solid (VS) mechanism as there was no catalyst involved.
- At shorter growth duration of 15 min, only SnO<sub>2</sub> nanowires with a rectangular cross-section were found in the quartz boat, while the SnO<sub>2</sub>-core/ZnO-shell structure was observed when the growth time was increased to 30 min.
- Hierarchical core-shell nanostructures were obtained at growth time exceeded 60 min. Hexagonal cross-section ZnO branch nanowires in the hierarchical nanostructures were built up on top of ZnO shell when growth time was increased to 60 min.
- The growth of SnO<sub>2</sub>-core/ZnO-shell nanowires and hierarchical nanostructures are due to variation of vapour pressures between ZnO and SnO<sub>2</sub> at a growth temperature of 900 °C.

### **Gas Sensing Performance:**

- Sensing performance of Zn<sub>2</sub>SnO<sub>4</sub> nanowires and SnO<sub>2</sub>-core/ZnO-shell nanostructures based sensor was studied for various reducing test gases including ethanol, methane, carbon monoxide and hydrogen.
- Sensors based on Zn<sub>2</sub>SnO<sub>4</sub> nanowires exhibited greater sensitivity of 60.8 for 100 ppm at an operating temperature of 500 °C. Ethanol was selectively detected with quick response and recovery times.
- The enhanced sensitivity of Zn<sub>2</sub>SnO<sub>4</sub> nanowires based sensor was due to high aspect ratio of entangled nanowires with a greater electrons donating effect

during adsorption-desorption. This effect was observed to be stronger in ethanol compared to other gases.

- Sensors based on SnO<sub>2</sub>-core/ZnO-shell nanostructures obtained at a growth time of 90 min exhibited enhanced sensitivity to ethanol in the presence of methane, carbon monoxide and hydrogen.
- The sensitivity of SnO<sub>2</sub>-core/ZnO-shell nanostructures grown for 90 min sensor was about 5-times higher than that of pristine SnO<sub>2</sub> nanowires towards 20 ppm ethanol at an operating temperature of 400 °C.
- The improvement in ethanol gas response for SnO<sub>2</sub>-core/ZnO-shell hierarchical nanostructures grown for 90 min sensor was attributed to high active sensing sites and the synergistic effect of the encapsulation of SnO<sub>2</sub> by ZnO nanostructures.
- SnO<sub>2</sub>-core/ZnO-shell nanostructures based sensors exhibited excellent sensitivity towards ethanol compared with Zn<sub>2</sub>SnO<sub>4</sub> nanowires based sensors.

## 5.2 Recommendations for Future Work

The results obtained from this thesis point out to numerous interesting directions for future work:

- This work proved that the carbon-assisted thermal evaporation process is an efficient method to grow high-quality ternary and core-shell nanostructures at moderate-temperatures. However, the combination of ZnO-TiO<sub>2</sub> and SnO<sub>2</sub>-TiO<sub>2</sub> has relatively similar electronic properties. Therefore, this metal oxide composites can also be used to synthesis the similar process.
- This study mainly focused on simultaneous synthesis of SnO<sub>2</sub>-core/ZnO-shell nanostructures and Zn<sub>2</sub>SnO<sub>4</sub> nanowires by single-step process for gas sensing application. Numerous literatures stated that optimized gas sensing properties could

be obtained by varying the shell thickness of core-shell nanostructures. According to that, the effect of ZnO shell thickness from different growth time on gas sensing properties can be studied.

- The reducing gases  $C_2H_5OH$ , CO,  $H_2$  and  $CH_4$  were tested in this present work. The gas sensing properties of  $SnO_2$ -core/ZnO-shell nanostructures sensor can be extended to oxidizing gases ( $NO_2$ ,  $O_3$ ) and other reducing gases such as:  $H_2S$ ,  $CH_3OH$  (methanol), benzene, toluene, TMA (Trimethylamine) and ammonia to check the selectivity towards ethanol.
- The present work exhibits that gas sensing properties of  $SnO_2$ -core/ZnO-shell hierarchical structures are enhanced by increased active sensing surface area. This sensing properties of  $SnO_2$ -core/ZnO-shell nanostructures should be further improved by spill-over effect or n-p type heterojunction using decoration of functional metal oxides (NiO, CuO) or noble metal nanoparticles (Au, Ag, Pt, Pd).

## REFERENCES

- Agarwala, S, Lim, ZH, Nicholson, E, & Ho, GW. (2012). Probing the morphology-device relation of  $\text{Fe}_2\text{O}_3$  nanostructures towards photovoltaic and sensing applications. *Nanoscale*, 4(1), 194-205.
- Ahlers, S., Müller, G., & Doll, T. (2005). A rate equation approach to the gas sensitivity of thin film metal oxide materials. *Sensors and Actuators B: Chemical*, 107(2), 587-599.
- Ahn, M-W, Park, K-S, Heo, J-H, Park, J-G, Kim, D-W, Choi, KJ, Hong, S-H. (2008). Gas sensing properties of defect-controlled ZnO-nanowire gas sensor. *Applied Physics Letters*, 93(26), 263103.
- Annamalai, Alagappan, Eo, Yang Dam, Im, Chan, & Lee, Man-Jong. (2011). Surface properties and dye loading behavior of  $\text{Zn}_2\text{SnO}_4$  nanoparticles hydrothermally synthesized using different mineralizers. *Materials Characterization*, 62(10), 1007-1015.
- Arafat, M.M., Haseeb, A.S.M.A., & Akbar, S.A. (2014). Developments in semiconducting oxide-based gas sensing materials *Comprehensive Materials Processing* (first ed., Vol. 13, pp. 205-219): Elsevier.
- Arafat, MM, Dinan, B, Akbar, Sheikh A, & Haseeb, ASMA. (2012). Gas sensors based on one dimensional nanostructured metal-oxides: a review. *Sensors*, 12(6), 7207-7258.
- Arafat, MM, Haseeb, ASMA, & Akbar, Sheikh A. (2014). A Selective Ultrahigh Responding High Temperature Ethanol Sensor Using  $\text{TiO}_2$  Nanoparticles. *Sensors*, 14(8), 13613-13627.
- Arakawa, T, Takeda, S, Adachi, G, & Shiokawa, J. (1979). Catalytic properties of compounds between the rare earths and copper oxide. *Materials Research Bulletin*, 14(4), 507-511.
- Asokan, Kandasami, Park, Jae Young, Choi, Sun-Woo, & Kim, Sang Sub. (2010). Nanocomposite ZnO– $\text{SnO}_2$  nanofibers synthesized by electrospinning method. *Nanoscale research letters*, 5(4), 747-752.
- Azad, AM, Akbar, SA, Mhaisalkar, SG, Birkefeld, LD, & Goto, KS. (1992). Solid-state gas sensors: A review. *Journal of the Electrochemical Society*, 139(12), 3690-3704.
- Bae, Joonho, Han, Jing Bin, Zhang, Xiao-Mei, Wei, Min, Duan, Xue, Zhang, Yue, & Wang, Zhong Lin. (2009). ZnO nanotubes grown at low temperature using Ga as catalysts and their enhanced photocatalytic activities. *The Journal of Physical Chemistry C*, 113(24), 10379-10383.
- Barreca, Davide, Comini, Elisabetta, Ferrucci, Angelo P., Gasparotto, Alberto, Maccato, Chiara, Maragno, Cinzia, Tondello, Eugenio. (2007). First Example of ZnO– $\text{TiO}_2$  Nanocomposites by Chemical Vapor Deposition: Structure,



Morphology, Composition, and Gas Sensing Performances. *Chemistry of Materials*, 19(23), 5642-5649.

- Barsan, Nicolae, & Weimar, Udo. (2001). Conduction model of metal oxide gas sensors. *Journal of Electroceramics*, 7(3), 143-167.
- Baschiroto, A., Capone, S., D'Amico, A., Di Natale, C., Ferragina, V., Ferri, G., Siciliano, P. (2008). A portable integrated wide-range gas sensing system with smart A/D front-end. *Sensors and Actuators B: Chemical*, 130(1), 164-174.
- Batzill, Matthias, & Diebold, Ulrike. (2005). The surface and materials science of tin oxide. *Progress in surface science*, 79(2), 47-154.
- Bochenkov, VE, & Sergeev, GB. (2010). Sensitivity, selectivity, and stability of gas-sensitive metal-oxide nanostructures (Vol. 3, pp. 31-52): American Scientific Publishers: Valencia, CA.
- Brovelli, S, Chiodini, N, Meinardi, F, Lauria, A, & Paleari, A. (2006). Ultraviolet free-exciton light emission in Er-passivated SnO<sub>2</sub> nanocrystals in silica. *Applied physics letters*, 89(15), 153126-153126-153123.
- Calestani, D, Lazzarini, L, Salviati, G, & Zha, M. (2005). Morphological, structural and optical study of quasi-1D SnO<sub>2</sub> nanowires and nanobelts. *Crystal Research and Technology*, 40(10-11), 937-941.
- Cao, Baobao, Chen, Jiajun, Tang, Xiaojun, & Zhou, Weilie. (2009). Growth of monoclinic WO<sub>3</sub> nanowire array for highly sensitive NO<sub>2</sub> detection. *J. Mater. Chem.*, 19(16), 2323-2327.
- Cao, HL, Qian, XF, Gong, Q, Du, WM, Ma, XD, & Zhu, ZK. (2006). Shape-and size-controlled synthesis of nanometre ZnO from a simple solution route at room temperature. *Nanotechnology*, 17(15), 3632.
- Cao, Zhuang, & Stetter, Joseph R. (1991). A selective solid-state gas sensor for halogenated hydrocarbons. *Sensors and Actuators B: Chemical*, 5(1), 109-113.
- Chakraborty, S., Sen, A., & Maiti, H. S. (2006). Selective detection of methane and butane by temperature modulation in iron doped tin oxide sensors. *Sensors and Actuators B: Chemical*, 115(2), 610-613.
- Chang, Chih-Yang, Tsao, Fu-Chun, Pan, Ching-Jen, Chi, Gou-Chung, Wang, Hung-Ta, Chen, Jau-Juin, Chen, Kuei-Hsien. (2006). Electroluminescence from ZnO nanowire/polymer composite pn junction. *Applied physics letters*, 88(17), 173503-173503-173503.
- Chen, Aifan, Bai, Shouli, Shi, Bingjie, Liu, Zhiyong, Li, Dianqing, & Liu, Chung Chiun. (2008). Methane gas-sensing and catalytic oxidation activity of SnO<sub>2</sub>-In<sub>2</sub>O<sub>3</sub> nanocomposites incorporating TiO<sub>2</sub>. *Sensors and Actuators B: Chemical*, 135(1), 7-12.
- Chen, Aifan, Huang, Xiaodong, Tong, Zhangfa, Bai, Shouli, Luo, Ruixian, & Liu, Chung Chiun. (2006). Preparation, characterization and gas-sensing properties

- of  $\text{SnO}_2\text{--In}_2\text{O}_3$  nanocomposite oxides. *Sensors and Actuators B: Chemical*, 115(1), 316-321.
- Chen, Chao, Li, Guizhi, Li, Junhua, & Liu, Yanli. (2015). One-step synthesis of 3D flower-like  $\text{Zn}_2\text{SnO}_4$  hierarchical nanostructures and their gas sensing properties. *Ceramics International*, 41(1 Part B), 1857-1862.
- Chen, Di, Xu, Jing, Liang, Bo, Wang, Xianfu, Chen, Po-Chiang, Zhou, Chongwu, & Shen, Guozhen. (2011). Electric transport, reversible wettability and chemical sensing of single-crystalline zigzag  $\text{Zn}_2\text{SnO}_4$  nanowires. *Journal of Materials Chemistry*, 21(43), 17236-17241.
- Chen, Hanyuan, Wang, Jianxiong, Yu, Hongchun, Yang, Huaixin, Xie, Sishen, & Li, Jianqi. (2005). Transmission electron microscopy study of pseudoperiodically twinned  $\text{Zn}_2\text{SnO}_4$  nanowires. *The Journal of Physical Chemistry B*, 109(7), 2573-2577.
- Chen, J, Lei, W, Song, JL, Sun, XW, Zhang, XB, & Deng, WQ. (2009). Two-step growth of a hierarchical ZnO nanostructure by aqueous thermal decomposition in a neutral solution and its photovoltaic property. *Physica E: Low-dimensional Systems and Nanostructures*, 41(5), 822-827.
- Chen, Jiajun, Lu, Liyou, & Wang, Wenyong. (2012).  $\text{Zn}_2\text{SnO}_4$  nanowires as photoanode for dye-sensitized solar cells and the improvement on open-circuit voltage. *The Journal of Physical Chemistry C*, 116(20), 10841-10847.
- Chen, Y.J., Xiao, G., Wang, T.S., Zhang, F., Ma, Y., Gao, P., Li, Q. (2011a). Synthesis and enhanced gas sensing properties of crystalline  $\text{CeO}_2/\text{TiO}_2$  core/shell nanorods. *Sensors and Actuators B: Chemical* 156(2), 867-874.
- Chen, Y.J., Xiao, G., Wang, T.S., Zhang, F., Ma, Y., Gao, P., Li, Q. (2011b).  $\alpha\text{-MoO}_3/\text{TiO}_2$  core/shell nanorods: Controlled-synthesis and low-temperature gas sensing properties. *Sensors and Actuators B: Chemical*, 155(1), 270-277.
- Chen, Yujin, Zhu, Chunling, & Wang, Taihong. (2006). The enhanced ethanol sensing properties of multi-walled carbon nanotubes/ $\text{SnO}_2$  core/shell nanostructures. *Nanotechnology*, 17(12), 3012.
- Chen, Zhe, Cao, Minhua, & Hu, Changwen. (2011). Novel  $\text{Zn}_2\text{SnO}_4$  hierarchical nanostructures and their gas sensing properties toward ethanol. *The Journal of Physical Chemistry C*, 115(13), 5522-5529.
- Cheng, Chuanwei, Liu, Bo, Yang, Huiying, Zhou, Weiwei, Sun, Li, Chen, Rui, Sun, Handong. (2009). Hierarchical assembly of ZnO nanostructures on  $\text{SnO}_2$  backbone nanowires: Low-temperature hydrothermal preparation and optical properties. *Acs Nano*, 3(10), 3069-3076.
- Cherian, Christie T, Zheng, Minrui, Reddy, Mogalahalli Venkatasamy, Chowdari, BVR, & Sow, Chorng Haur. (2013).  $\text{Zn}_2\text{SnO}_4$  Nanowires versus Nanoplates: Electrochemical Performance and Morphological Evolution during Li-Cycling. *ACS applied materials & interfaces*, 5(13), 6054-6060.

- Choi, S. W., Park, J. Y., & Kim, S. S. (2009). Synthesis of SnO<sub>2</sub>-ZnO core-shell nanofibers via a novel two-step process and their gas sensing properties. *Nanotechnology*, 20(46), 465603.
- Choi, Seung-Hoon, Hwang, In-Sung, Lee, Jong-Heun, Oh, Seong-Geun, & Kim, Il-Doo. (2011). Microstructural control and selective C<sub>2</sub>H<sub>5</sub>OH sensing properties of Zn<sub>2</sub>SnO<sub>4</sub> nanofibers prepared by electrospinning. *Chemical Communications*, 47(33), 9315-9317.
- Choi, Sun-Woo, Katoch, Akash, Sun, Gun-Joo, & Kim, Sang Sub. (2013). Synthesis and gas sensing performance of ZnO-SnO<sub>2</sub> nanofiber-nanowire stem-branch heterostructure. *Sensors and Actuators B: Chemical*, 181, 787-794.
- Choi, Sun-Woo, Park, Jae Young, & Kim, Sang Sub. (2009). Synthesis of SnO<sub>2</sub>-ZnO core-shell nanofibers via a novel two-step process and their gas sensing properties. *Nanotechnology*, 20(46), 465603.
- Choi, Young-Jin, Hwang, In-Sung, Park, Jae-Gwan, Choi, Kyoung Jin, Park, Jae-Hwan, & Lee, Jong-Heun. (2008). Novel fabrication of an SnO<sub>2</sub> nanowire gas sensor with high sensitivity. *Nanotechnology*, 19(9), 095508.
- Christofides, Constantinos, & Mandelis, Andreas. (1990). Solid-state sensors for trace hydrogen gas detection. *Journal of Applied Physics*, 68(6), R1-R30.
- Comini, E., Ferroni, M., Guidi, V., Faglia, G., Martinelli, G., & Sberveglieri, G. (2002). Nanostructured mixed oxides compounds for gas sensing applications. *Sensors and Actuators B: Chemical*, 84(1), 26-32.
- Comini, E., Guidi, V., Frigeri, C., Riccò, I., & Sberveglieri, G. (2001). CO sensing properties of titanium and iron oxide nanosized thin films. *Sensors and Actuators B: Chemical*, 77(1-2), 16-21.
- Comini, Elisabetta. (2006). Metal oxide nano-crystals for gas sensing. *Analytica Chimica Acta*, 568(1-2), 28-40.
- Coutts, Timothy J, Young, David L, Li, Xiaonan, Mulligan, WP, & Wu, X. (2000). Search for improved transparent conducting oxides: A fundamental investigation of CdO, Cd<sub>2</sub>SnO<sub>4</sub>, and Zn<sub>2</sub>SnO<sub>4</sub>. *Journal of Vacuum Science & Technology A*, 18(6), 2646-2660.
- Cui, Yuming, Yu, Ang, Pan, Hao, Zhou, Xingfu, & Ding, Weiping. (2012). Catalytic outgrowth of SnO<sub>2</sub> nanorods from ZnO-SnO<sub>2</sub> nanoparticles microsphere core: combustion synthesis and gas-sensing properties. *CrystEngComm*, 14(21), 7355-7359.
- Dai, Jun, Xu, Chunxiang, Guo, Jiyan, Xu, Xiaoyong, Zhu, Gangyi, & Lin, Yi. (2013). Brush-like SnO<sub>2</sub>/ZnO hierarchical nanostructure: Synthesis, characterization and application in UV photoresponse. *AIP Advances*, 3(6), 062108.
- de Lacy Costello, BPJ, Ewen, Richard J, Ratcliffe, Norman M, & Sivanand, PS. (2003). Thick film organic vapour sensors based on binary mixtures of metal oxides. *Sensors and Actuators B: Chemical*, 92(1), 159-166.

- Demir-Cakan, Rezan, Hu, Yong-Sheng, Antonietti, Markus, Maier, Joachim, & Titirici, Maria-Magdalena. (2008). Facile one-pot synthesis of mesoporous SnO<sub>2</sub> microspheres via nanoparticles assembly and lithium storage properties. *Chemistry of Materials*, 20(4), 1227-1229.
- Deng, Jianan, Yu, Bo, Lou, Zheng, Wang, Lili, Wang, Rui, & Zhang, Tong. (2013). Facile synthesis and enhanced ethanol sensing properties of the brush-like ZnO–TiO<sub>2</sub> heterojunctions nanofibers. *Sensors and Actuators B: Chemical*, 184(0), 21-26.
- Devi, G Sarala, & Hamoon, HZR. (2012). Zn<sub>2</sub>SnO<sub>4</sub>: A Suitable Material for Liquid Petroleum Gas (LPG) Detection. *Tagungsband*, 772-773.
- Djurišić, Aleksandra B, & Leung, Yu Hang. (2006). Optical properties of ZnO nanostructures. *Small*, 2(8-9), 944-961.
- Ellingham, H.J.T. (1944). *J. Soc. Chem. Ind.*, 66, 125-133.
- Ellmer, K. (2001). Resistivity of polycrystalline zinc oxide films: current status and physical limit. *Journal of Physics D: Applied Physics*, 34(21), 3097.
- Eranna, G, Joshi, BC, Runthala, DP, & Gupta, RP. (2004). Oxide materials for development of integrated gas sensors-a comprehensive review. *Critical Reviews in Solid State and Materials Sciences*, 29(3-4), 111-188.
- Faglia, G, Baratto, C, Sberveglieri, G, Zha, M, & Zappettini, A. (2005). Adsorption effects of NO<sub>2</sub> at ppm level on visible photoluminescence response of SnO<sub>2</sub> nanobelts. *Applied Physics Letters*, 86(1), 011923.
- Fan, Hong Jin, Yang, Yang, & Zacharias, Margit. (2009). ZnO-based ternary compound nanotubes and nanowires. *Journal of Materials Chemistry*, 19(7), 885-900.
- Fan, Zhiyong, Wang, Dawei, Chang, Pai-Chun, Tseng, Wei-Yu, & Lu, Jia G. (2004). ZnO nanowire field-effect transistor and oxygen sensing property. *Applied Physics Letters*, 85(24), 5923-5925.
- Fishtik, I, Alexander, A, Datta, R, & Geana, D. (2000). A thermodynamic analysis of hydrogen production by steam reforming of ethanol via response reactions. *International Journal of Hydrogen Energy*, 25(1), 31-45.
- Fonoberov, Vladimir A, Alim, Khan A, Balandin, Alexander A, Xiu, Faxian, & Liu, Jianlin. (2006). Photoluminescence investigation of the carrier recombination processes in ZnO quantum dots and nanocrystals. *Physical review B*, 73(16), 165317.
- Franke, Marion E, Koplin, Tobias J, & Simon, Ulrich. (2006). Metal and metal oxide nanoparticles in chemiresistors: does the nanoscale matter? *Small*, 2(1), 36-50.
- Freitas, Juliana G, Fletcher, Barbara, Aravena, Ramon, & Barker, James F. (2010). Methane production and isotopic fingerprinting in ethanol fuel contaminated sites. *Groundwater*, 48(6), 844-857.

- Fröberg, LE, Seifert, Werner, & Johansson, Jonas. (2007). Diameter-dependent growth rate of InAs nanowires. *Physical Review B*, 76(15), 153401.
- Galvita, VV, Semin, GL, Belyaev, VD, Semikolenov, VA, Tsiakaras, P, & Sobyenin, VA. (2001). Synthesis gas production by steam reforming of ethanol. *Applied Catalysis A: General*, 220(1), 123-127.
- Ganbavle, V. V., Patil, M. A., Deshmukh, H. P., & Rajpure, K. Y. (2014). Development of Zn<sub>2</sub>SnO<sub>4</sub> thin films deposited by spray pyrolysis method and their utility for NO<sub>2</sub> gas sensors at moderate operating temperature. *Journal of Analytical and Applied Pyrolysis*, 107(0), 233-241.
- Geng, Baoyou, Fang, Caihong, Zhan, Fangming, & Yu, Nan. (2008). Synthesis of Polyhedral ZnSnO<sub>3</sub> Microcrystals with Controlled Exposed Facets and Their Selective Gas-Sensing Properties. *Small*, 4(9), 1337-1343.
- Goldstein, Mark. (2008). Carbon Monoxide Poisoning. *Journal of Emergency Nursing*, 34(6), 538-542.
- Göpel, Wolfgang, Jones, TA, Kleitz, Michel, Lundström, Ingemar, & Seiyama, Tetsuro. (2008). *Sensors, Chemical and Biochemical Sensors* (Vol. 2): John Wiley & Sons.
- Gu, Feng, Fen Wang, Shu, Feng Song, Chun, Kai Lü, Meng, Xin Qi, Yong, Jun Zhou, Guang, Rong Yuan, Duo. (2003). Synthesis and luminescence properties of SnO<sub>2</sub> nanoparticles. *Chemical physics letters*, 372(3), 451-454.
- Gu, Haoshuang, Wang, Zhao, & Hu, Yongming. (2012). Hydrogen gas sensors based on semiconductor oxide nanostructures. *Sensors*, 12(5), 5517-5550.
- Guo, Honghui, Zhou, Jianzhang, & Lin, Zhonghua. (2008). ZnO nanorod light-emitting diodes fabricated by electrochemical approaches. *Electrochemistry Communications*, 10(1), 146-150.
- Haeng Yu, Ji, & Man Choi, Gyeong. (1998a,b). Electrical and CO gas sensing properties of ZnO–SnO<sub>2</sub> composites. *Sensors and Actuators B: Chemical*, 52(3), 251-256.
- Han, Xi-Guang, Cao, Xiao-Wei, Li, Liang, & Wang, Chao. (2013). Fabrication and characterization of polliwog-like Sn/ Zn<sub>2</sub>SnO<sub>4</sub> heterostructure nanocrystal and their gas sensing properties. *Sensors and Actuators B: Chemical*, 185, 383-388.
- He Jr, H, Wu, Te H, Hsin, Cheng L, Li, Kun M, Chen, Lih J, Chueh, Yu L, Wang, Zhong L. (2006). Beaklike SnO<sub>2</sub> Nanorods with Strong Photoluminescent and Field-Emission Properties. *small*, 2(1), 116-120.
- Health, National Institute for Occupational safety and. (1992). Recommendations from Occupational safety and Health: Compendium of policy documents and statements. Cincinnati, OH, (USA).

- Her, Yung-Chiun, Chiang, Ching-Kuo, Jean, Sen-Tsun, & Huang, Sing-Lin. (2012). Self-catalytic growth of hierarchical  $\text{In}_2\text{O}_3$  nanostructures on  $\text{SnO}_2$  nanowires and their CO sensing properties. *CrystEngComm*, 14(4), 1296-1300.
- Horn, M. (1995). A new theory of adsorption for the quantitative description of gas sensors. *Sensors and Actuators B: Chemical*, 26(1-3), 217-219.
- Hsueh, Ting-Jen, Hsu, Cheng-Liang, Chang, Shou-Jinn, & Chen, I. (2007a, b). Laterally grown ZnO nanowire ethanol gas sensors. *Sensors and Actuators B: Chemical*, 126(2), 473-477.
- Hu, Dan, Han, Bingqian, Deng, Shaojuan, Feng, Zhipeng, Wang, Yan, Popovic, Jasminka, Djerdj, Igor. (2014). Novel Mixed Phase  $\text{SnO}_2$  Nanorods Assembled with  $\text{SnO}_2$  Nanocrystals for Enhancing Gas-Sensing Performance towards Isopropanol Gas. *The Journal of Physical Chemistry C*.
- Hu, JQ, Bando, Y, Zhan, JH, Li, YB, & Sekiguchi, T. (2003). Two-dimensional micrometer-sized single-crystalline ZnO thin nanosheets. *Applied physics letters*, 83(21), 4414-4416.
- Hu, JQ, Ma, XL, Shang, NG, Xie, ZY, Wong, NB, Lee, CS, & Lee, ST. (2002). Large-scale rapid oxidation synthesis of  $\text{SnO}_2$  nanoribbons. *The Journal of Physical Chemistry B*, 106(15), 3823-3826.
- Hu, QR, Jiang, P, Xu, H, Zhang, Y, Wang, SL, Jia, X, & Tang, WH. (2009). Synthesis and photoluminescence of  $\text{Zn}_2\text{SnO}_4$  nanowires. *Journal of Alloys and Compounds*, 484(1), 25-27.
- Huang, Genin Gary, Wang, Chien-Tsung, Tang, Hsin-Ta, Huang, Yih-Shiaw, & Yang, Jyisy. (2006). ZnO nanoparticle-modified infrared internal reflection elements for selective detection of volatile organic compounds. *Analytical chemistry*, 78(7), 2397-2404.
- Huang, Hui, Gong, Hua, Chow, Chee Lap, Guo, Jun, White, Timothy John, Tse, Man Siu, & Tan, Ooi Kiang. (2011). Low-Temperature Growth of  $\text{SnO}_2$  Nanorod Arrays and Tunable n-p-n Sensing Response of a ZnO/ $\text{SnO}_2$  Heterojunction for Exclusive Hydrogen Sensors. *Advanced Functional Materials*, 21(14), 2680-2686.
- Huang, Hui, Tan, OK, Lee, YC, Tran, TD, Tse, MS, & Yao, X. (2005). Semiconductor gas sensor based on tin oxide nanorods prepared by plasma-enhanced chemical vapor deposition with postplasma treatment. *Applied Physics Letters*, 87(16), 163123-163123-163123.
- Huang, J. R., Li, G. Y., Huang, Z. Y., Huang, X. J., & Liu, J. H. (2006). Temperature modulation and artificial neural network evaluation for improving the CO selectivity of  $\text{SnO}_2$  gas sensor. *Sensors and Actuators B: Chemical*, 114(2), 1059-1063.
- Huang, Jin, & Wan, Qing. (2009). Gas sensors based on semiconducting metal oxide one-dimensional nanostructures. *Sensors*, 9(12), 9903-9924.

- Hwang, In-Sung, Kim, Sun-Jung, Choi, Joong-Ki, Choi, Jaewan, Ji, Hyunjin, Kim, Gyu-Tae, Lee, Jong-Heun. (2010a). Synthesis and gas sensing characteristics of highly crystalline ZnO–SnO<sub>2</sub> core–shell nanowires. *Sensors and Actuators B: Chemical*, 148(2), 595-600.
- Ippolito, S. J., Kandasamy, S., Kalantar-zadeh, K., & Wlodarski, W. (2005). Hydrogen sensing characteristics of WO<sub>3</sub> thin film conductometric sensors activated by Pt and Au catalysts. *Sensors and Actuators B: Chemical*, 108(1–2), 154-158.
- Jiang, Haihui, Zhao, Lichun, Gai, Ligang, Ma, Li, Ma, Yun, & Li, Mei. (2013). Hierarchical rh-In<sub>2</sub>O<sub>3</sub> crystals derived from InOOH counterparts and their sensitivity to ammonia gas. *CrystEngComm*, 15(35), 7003-7009.
- Jiang, Ya-Qi, Chen, Xiao-Xia, Sun, Ran, Xiong, Zhao, & Zheng, Lan-Sun. (2011). Hydrothermal syntheses and gas sensing properties of cubic and quasi-cubic Zn<sub>2</sub>SnO<sub>4</sub>. *Materials Chemistry and Physics*, 129(1), 53-61.
- Jiang, Ya-Qi, He, Chun-Xiao, Sun, Ran, Xie, Zhao-Xiong, & Zheng, Lan-Sun. (2012). Synthesis of Zn<sub>2</sub>SnO<sub>4</sub> nanoplate-built hierarchical cube-like structures with enhanced gas-sensing property. *Materials Chemistry and Physics*, 136(2), 698-704.
- Jiang, Zhixing, Xue, Shaolin, Wu, Shuxian, Zou, Rujia, Zhang, Zhengyu, & Jang, Meng. (2013). Synthesis of unique SnO<sub>2</sub>/ZnO core–shell nanorods and nanoflowers and their field emission properties. *Materials Letters*, 105, 239-241.
- Jie, Jiansheng, Wang, Guanzhong, Wang, Guanzhong, Han, Xinhai, Fang, Jieping, Yu, Qingxuan, Hou, JG. (2004). Growth of ternary oxide nanowires by gold-catalyzed vapor-phase evaporation. *The Journal of Physical Chemistry B*, 108(24), 8249-8253.
- Jiménez-Cadena, Giselle, Riu, Jordi, & Rius, F Xavier. (2007). Gas sensors based on nanostructured materials. *Analyst*, 132(11), 1083-1099.
- Jun, Shen, Bing-Hui, Ge, Wei-Guo, Chu, Shu-Dong, Luo, Zeng-Xing, Zhang, Dong-Fang, Liu, Yan-Juan, Xiang. (2008). Synthesis and characterization of axially periodic Zn<sub>2</sub>SnO<sub>4</sub> dendritic nanostructures. *Chinese Physics B*, 17(6), 2184.
- Jun, Zhang, Xianghong, Liu, Liwei, Wang, Taili, Yang, Xianzhi, Guo, Shihua, Wu, . . . Shoumin, Zhang. (2011). Synthesis and gas sensing properties of  $\alpha$ -Fe<sub>2</sub>O<sub>3</sub>@ZnO core–shell nanospindles. *Nanotechnology*, 22(18), 185501.
- Kappler, J, Barsan, N, Weimar, U, Dieguez, A, Alay, JL, Romano-Rodriguez, A, Göpel, W. (1998). Correlation between XPS, Raman and TEM measurements and the gas sensitivity of Pt and Pd doped SnO<sub>2</sub> based gas sensors. *Fresenius' journal of analytical chemistry*, 361(2), 110-114.
- Khoang, Nguyen Duc, Trung, Do Dang, Van Duy, Nguyen, Hoa, Nguyen Duc, & Van Hieu, Nguyen. (2012a). Design of SnO<sub>2</sub>/ZnO hierarchical nanostructures for enhanced ethanol gas-sensing performance. *Sensors and Actuators B: Chemical*, 174(0), 594-601.

- Khoang, Nguyen Duc, Trung, Do Dang, Van Duy, Nguyen, Hoa, Nguyen Duc, & Van Hieu, Nguyen. (2012b). Design of SnO<sub>2</sub>/ZnO hierarchical nanostructures for enhanced ethanol gas-sensing performance. *Sensors and Actuators B: Chemical*, 174, 594-601.
- Khorami, Hamed Akbari, Keyanpour-Rad, Mansoor, & Vaezi, Mohammad Reza. (2011). Synthesis of SnO<sub>2</sub>/ZnO composite nanofibers by electrospinning method and study of its ethanol sensing properties. *Applied Surface Science*, 257(18), 7988-7992.
- Kılıç, Çetin, & Zunger, Alex. (2002). Origins of coexistence of conductivity and transparency in SnO<sub>2</sub>. *Physical Review Letters*, 88(9), 095501.
- Kim, Hae-Ryong, Haensch, Alexander, Kim, Il-Doo, Barsan, Nicolae, Weimar, Udo, & Lee, Jong-Heun. (2011). The Role of NiO Doping in Reducing the Impact of Humidity on the Performance of SnO<sub>2</sub>-Based Gas Sensors: Synthesis Strategies, and Phenomenological and Spectroscopic Studies. *Advanced Functional Materials*, 21(23), 4456-4463.
- Kim, Han Sung, Hwang, Seon Oh, Myung, Yoon, Park, Jeunghye, Bae, Seung Yong, & Ahn, Jae Pyoung. (2008). Three-dimensional structure of helical and zigzagged nanowires using electron tomography. *Nano letters*, 8(2), 551-557.
- Kim, Hyoun Woo, Kim, Nam Ho, Myung, Ju Hyun, & Shim, Seung Hyun. (2005). Characteristics of SnO<sub>2</sub> fishbone-like nanostructures prepared by the thermal evaporation. *physica status solidi (a)*, 202(9), 1758-1762.
- Kim, Hyunsu, Jin, Changhyun, Park, Sunghoon, & Lee, Chongmu. (2012). Enhanced H<sub>2</sub>S gas sensing properties of multiple-networked Pd-doped SnO<sub>2</sub>-core/ZnO-shell nanorod sensors. *Materials Research Bulletin*, 47(10), 2708-2712.
- Kim, Ki-Won, Cho, Pyeong-Seok, Kim, Sun-Jung, Lee, Jong-Heun, Kang, Chong-Yun, Kim, Jin-Sang, & Yoon, Seok-Jin. (2007a,b). The selective detection of C<sub>2</sub>H<sub>5</sub>OH using SnO<sub>2</sub>-ZnO thin film gas sensors prepared by combinatorial solution deposition. *Sensors & Actuators: B. Chemical*, 123(1), 318-324.
- Kim, Myung-Jin, Park, Seong-Hun, & Huh, Young-Duk. (2011). Photocatalytic activities of hydrothermally synthesized Zn<sub>2</sub>SnO<sub>4</sub>. *Bull. Korean Chem. Soc.*, 32(5), 1757-1760.
- Kim, Sun-Jung, Hwang, In-Sung, Na, Chan Woong, Kim, Il-Doo, Kang, Yun Chan, & Lee, Jong-Heun. (2011). Ultrasensitive and selective C<sub>2</sub>H<sub>5</sub>OH sensors using Rh-loaded In<sub>2</sub>O<sub>3</sub> hollow spheres. *Journal of Materials Chemistry*, 21(46), 18560-18567.
- Kohl, Dieter. (2001). Function and applications of gas sensors. *Journal of Physics D: Applied Physics*, 34(19), R125.
- Kolmakov, A, Klenov, DO, Lilach, Y, Stemmer, S, & Moskovits, M. (2005). Enhanced gas sensing by individual SnO<sub>2</sub> nanowires and nanobelts functionalized with Pd catalyst particles. *Nano Letters*, 5(4), 667-673.



- Kolmakov, Andrei, Zhang, Youxiang, Cheng, Guosheng, & Moskovits, Martin. (2003). Detection of CO and O<sub>2</sub> using tin oxide nanowire sensors. *Advanced Materials*, 15(12), 997-1000.
- Kusior, A, Radecka, M, Rekas, M, Lubecka, M, Zakrzewska, K, Reszka, A, & Kowalski, BJ. (2012). Sensitization of Gas Sensing Properties in TiO<sub>2</sub>/SnO<sub>2</sub> Nanocomposites. *Procedia Engineering*, 47, 1073-1076.
- Lamoreaux, RH, Hildenbrand, DL, & Brewer, L. (1987a,b). High-Temperature Vaporization Behavior of Oxides II. Oxides of Be, Mg, Ca, Sr, Ba, B, Al, Ga, In, Tl, Si, Ge, Sn, Pb, Zn, Cd, and Hg. *Journal of physical and chemical reference data*, 16(3), 419-443.
- Lan, Changyong, Gong, Jiangfeng, & Jiang, Yuwen. (2013). Synthesis and photoluminescence properties of string-like ZnO/SnO nanowire/nanosheet nano-heterostructures. *Journal of Alloys and Compounds*, 575(0), 24-28.
- Lan, Changyong, Gong, Jiangfeng, Su, Yun, Li, Kenan, & Yang, Shaoguang. (2012). Synthesis and photoluminescence properties of SnO<sub>2</sub>/ZnO hierarchical nanostructures. *Physica E: Low-dimensional Systems and Nanostructures*, 44(4), 791-796.
- Lee, Andrew P., & Reedy, Brian J. (1999). Temperature modulation in semiconductor gas sensing. *Sensors and Actuators B: Chemical*, 60(1), 35-42.
- Lee, Geon Joon, Lee, Youngpak, Lim, Hwan-Hong, Cha, Myoungsik, Kim, Sung Soo, Cheong, Hyeonsik, Han, Sung-Hwan. (2010). Photoluminescence and Lasing Properties of ZnO Nanorods. *Journal of the Korean Physical Society*, 57(6), 1624-1629.
- Lee, Jun Seop, Kwon, Oh Seok, & Jang, Jyongsik. (2012a). Facile synthesis of SnO<sub>2</sub> nanofibers decorated with N-doped ZnO nanonodules for visible light photocatalysts using single-nozzle co-electrospinning. *Journal of Materials Chemistry*, 22(29), 14565-14572.
- Lee, Young-In, Lee, Kun-Jae, Lee, Don-Hee, Jeong, Young-Keun, Lee, Hee Soo, & Choa, Yong-Ho. (2009). Preparation and gas sensitivity of SnO<sub>2</sub> nanopowder homogenously doped with Pt nanoparticles. *Current Applied Physics*, 9(1, Supplement), S79-S81.
- Leonardy, Adrianus, Hung, Wen-Zhong, Tsai, Dah-Shyang, Chou, Chen-Chia, & Huang, Ying-Sheng. (2009). Structural features of SnO<sub>2</sub> nanowires and Raman spectroscopy analysis. *Crystal Growth and Design*, 9(9), 3958-3963.
- Li, Cheng Chao, Yin, Xiao Ming, Li, Qiu Hong, & Wang, Tai Hong. (2011). Enhanced gas sensing properties of ZnO/SnO<sub>2</sub> hierarchical architectures by glucose-induced attachment. *CrystEngComm*, 13(5), 1557-1563.
- Li, QH, Gao, T, Wang, YG, & Wang, TH. (2005). Adsorption and desorption of oxygen probed from ZnO nanowire films by photocurrent measurements. *Applied Physics Letters*, 86(12), 123117.

- Li, QH, Wan, Q, Liang, YX, & Wang, TH. (2004). Electronic transport through individual ZnO nanowires. *Applied Physics Letters*, 84(22), 4556-4558.
- Li, Seu Yi, Lin, Pang, Lee, Chia Ying, & Tseng, Tseung Yuen. (2004). Field emission and photofluorescent characteristics of zinc oxide nanowires synthesized by a metal catalyzed vapor-liquid-solid process. *Journal of applied physics*, 95(7), 3711-3716.
- Li, Zhengdao, Zhou, Yong, Bao, Chunxiong, Xue, Guogang, Zhang, Jiyuan, Liu, Jianguo, Zou, Zhigang. (2012). Vertically building Zn<sub>2</sub>SnO<sub>4</sub> nanowire arrays on stainless steel mesh toward fabrication of large-area, flexible dye-sensitized solar cells. *Nanoscale*, 4(11), 3490-3494.
- Liang, Yuan-Chang, Huang, Chiem-Lum, Hu, Chia-Yen, Deng, Xian-Shi, & Zhong, Hua. (2012). Morphology and optical properties of ternary Zn-Sn-O semiconductor nanowires with catalyst-free growth. *Journal of Alloys and Compounds*, 537, 111-116.
- Liangyuan, Chen, Shouli, Bai, Guojun, Zhou, Dianqing, Li, Aifan, Chen, & Liu, Chung Chiun. (2008). Synthesis of ZnO-SnO<sub>2</sub> nanocomposites by microemulsion and sensing properties for NO<sub>2</sub>. *Sensors and Actuators B: Chemical*, 134(2), 360-366.
- Liu, Jun, She, Juncong, Deng, Shaozhi, Chen, Jun, & Xu, Ningsheng. (2008). Ultrathin seed-layer for tuning density of ZnO nanowire arrays and their field emission characteristics. *The Journal of Physical Chemistry C*, 112(31), 11685-11690.
- Liu, Xianghong, Zhang, Jun, Wang, Liwei, Yang, Taili, Guo, Xianzhi, Wu, Shihua, & Wang, Shurong. (2011). 3D hierarchically porous ZnO structures and their functionalization by Au nanoparticles for gas sensors. *Journal of Materials Chemistry*, 21(2), 349-356.
- Liu, Y, Wang, S, Zhang, ZY, Peng, L-M, Shi, L, & Li, Quan. (2008a,b). Measuring the electrical characteristics of individual junctions in the SnO<sub>2</sub> capped ZnO nanowire arrays on Zn substrate. *Applied Physics Letters*, 92(3), 033102.
- Liu, Ying, Dong, Jian, & Liu, Meilin. (2004). Well-Aligned “Nano-Box-Beams” of SnO<sub>2</sub>. *Advanced Materials*, 16(4), 353-356.
- Liu, Yixin, Parisi, Joseph, Sun, Xiangcheng, & Lei, Yu. (2014). Solid-state gas sensors for high temperature applications—a review. *Journal of Materials Chemistry A*.
- Liu, Yuanjun, Zhu, Guoxing, Chen, Junzhi, Xu, Huan, Shen, Xiaoping, & Yuan, Aihua. (2013). Co<sub>3</sub>O<sub>4</sub>/ZnO nanocomposites for gas-sensing applications. *Applied Surface Science*, 265, 379-384.
- Liu, Zhao-Qing, Ding, Liang-Xin, Wang, Zi-Long, Mao, Yan-Chao, Xie, Shi-Lei, Zhang, Yuan-Ming, Tong, Ye-Xiang. (2012). ZnO/SnO<sub>2</sub> hierarchical and flower-like nanostructures: facile synthesis, formation mechanism, and optical and magnetic properties. *CrystEngComm*, 14(6), 2289-2295.

- Lou, Zheng, Deng, Jianan, Wang, Lili, Wang, Lijie, Fei, Teng, & Zhang, Tong. (2013). Toluene and ethanol sensing performances of pristine and PdO-decorated flower-like ZnO structures. *Sensors and Actuators B: Chemical*, 176(0), 323-329.
- Lu, Geyu, Xu, Jing, Sun, Jianbo, Yu, Yingshuo, Zhang, Yiqun, & Liu, Fengmin. (2012). UV-enhanced room temperature NO<sub>2</sub> sensor using ZnO nanorods modified with SnO<sub>2</sub> nanoparticles. *Sensors and Actuators B: Chemical*, 162(1), 82-88.
- Lu, Zhouguang, & Tang, Yougen. (2005). Two-step synthesis and ethanol sensing properties of Zn<sub>2</sub>SnO<sub>4</sub>-SnO<sub>2</sub> nanocomposites. *Materials chemistry and physics*, 92(1), 5-9.
- Ma, Guanxiang, Zou, Rujia, Jiang, Lin, Zhang, Zhenyu, Xue, Yafang, Yu, Li, Hu, Junqing. (2012). Phase-controlled synthesis and gas-sensing properties of zinc stannate (ZnSnO<sub>3</sub> and Zn<sub>2</sub>SnO<sub>4</sub>) faceted solid and hollow microcrystals. *CrystEngComm*, 14(6), 2172-2179.
- Ma, LA, & Guo, TL. (2009). Synthesis and field emission properties of needle-shaped SnO<sub>2</sub> nanostructures with rectangular cross-section. *Materials Letters*, 63(2), 295-297.
- Ma, Xicheng, Song, Haiyan, & Guan, Congsheng. (2013). Enhanced ethanol sensing properties of ZnO-doped porous SnO<sub>2</sub> hollow nanospheres. *Sensors and Actuators B: Chemical*, 188, 193-199.
- Mahalingam, T, Lee, Kyung Moon, Park, Kyung Ho, Lee, Soonil, Ahn, Yeonghwan, Park, Ji-Yong, & Koh, Ken Ha. (2007). Low temperature wet chemical synthesis of good optical quality vertically aligned crystalline ZnO nanorods. *Nanotechnology*, 18(3), 035606.
- Mary Jaculine, M., Justin Raj, C., & Jerome Das, S. (2013). Hydrothermal synthesis of highly crystalline Zn<sub>2</sub>SnO<sub>4</sub> nanoflowers and their optical properties. *Journal of Alloys and Compounds*, 577(0), 131-137.
- Miller, Derek R, Akbar, Sheikh A, & Morris, Patricia A. (2014). Nanoscale metal oxide-based heterojunctions for gas sensing: A review. *Sensors and Actuators B: Chemical*, 204, 250-272.
- Mirchin, Nina, Lapsker, Igor, Tannous, Ewdard, & Peled, Aaron. (2013). Palladium Ultra Thin Layer Profiles Evaluation by Evanescent Light. *Materials Sciences & Applications*, 4(9).
- Mondal, Biplob, Basumatari, Borat, Das, Jayoti, Roychaudhury, Chirosree, Saha, Hiranmay, & Mukherjee, Nillohit. (2014). ZnO-SnO<sub>2</sub> based composite type gas sensor for selective hydrogen sensing. *Sensors and Actuators B: Chemical*, 194(0), 389-396.
- Moon, Jaehyun, Park, Jin-Ah, Lee, Su-Jae, & Zyung, Taehyoung. (2009a, b). Semiconducting ZnO Nanofibers as Gas Sensors and Gas Response Improvement by SnO<sub>2</sub> Coating. *ETRI journal*, 31(6), 636-641.

- Moon, Won Jae, Yu, Ji Haeng, & Choi, Gyeong Man. (2001). Selective CO gas detection of  $\text{SnO}_2\text{-Zn}_2\text{SnO}_4$  composite gas sensor. *Sensors and Actuators B: Chemical*, 80(1), 21-27.
- Morales, Alfredo M, & Lieber, Charles M. (1998). A laser ablation method for the synthesis of crystalline semiconductor nanowires. *Science*, 279(5348), 208-211.
- Mridha, S, & Basak, D. (2006). Investigation of a p-CuO/n-ZnO thin film heterojunction for  $\text{H}_2$  gas-sensor applications. *Semiconductor science and technology*, 21(7), 928.
- Na, Chan Woong, Woo, Hyung-Sik, Kim, Il-Doo, & Lee, Jong-Heun. (2011). Selective detection of  $\text{NO}_2$  and  $\text{C}_2\text{H}_5\text{OH}$  using a  $\text{Co}_3\text{O}_4$ -decorated ZnO nanowire network sensor. *Chemical Communications*, 47(18), 5148-5150.
- Nakata, Satoshi, Okunishi, Hirokazu, & Nakashima, Yusuke. (2006). Distinction of gases with a semiconductor sensor under a cyclic temperature modulation with second-harmonic heating. *Sensors and Actuators B: Chemical*, 119(2), 556-561.
- Nanto, H, Morita, T, Habara, H, Kondo, K, Douguchi, Y, & Minami, T. (1996). Doping effect of  $\text{SnO}_2$  on gas sensing characteristics of sputtered ZnO thin film chemical sensor. *Sensors and Actuators B: Chemical*, 36(1), 384-387.
- Ngo, Kieu An, Lauque, Pascal, & Aguir, Khalifa. (2007). High performance of a gas identification system using sensor array and temperature modulation. *Sensors and Actuators B: Chemical*, 124(1), 209-216.
- Nguyen, Pho, Ng, Hou T, Kong, Jing, Cassell, Alan M, Quinn, Richard, Li, Jun, Meyyappan, M. (2003). Epitaxial directional growth of indium-doped tin oxide nanowire arrays. *Nano letters*, 3(7), 925-928.
- Norton, David P, Heo, YW, Ivill, MP, Ip, K, Pearton, SJ, Chisholm, Matthew F, & Steiner, T. (2004). ZnO: growth, doping & processing. *Materials today*, 7(6), 34-40.
- Ogawa, Hisahito, Nishikawa, Masahiro, & Abe, Atsushi. (1982). Hall measurement studies and an electrical conduction model of tin oxide ultrafine particle films. *Journal of Applied Physics*, 53(6), 4448-4455.
- Oh, Eugene, Choi, Ho-Yun, Jung, Seung-Ho, Cho, Seungho, Kim, Jae Chang, Lee, Kun-Hong, Jeong, Soo-Hwan. (2009). High-performance  $\text{NO}_2$  gas sensor based on ZnO nanorod grown by ultrasonic irradiation. *Sensors and Actuators B: Chemical*, 141(1), 239-243.
- Özgür, Ü, Alivov, Ya I, Liu, C, Teke, A, Reshchikov, MA, Doğan, S, Morkoc, H. (2005). A comprehensive review of ZnO materials and devices. *Journal of applied physics*, 98(4), 041301.
- Palmer, GB, & Poepfelmeier, KR. (2002). Phase relations, transparency and conductivity in  $\text{Ga}_2\text{O}_3\text{-SnO}_2\text{-ZnO}$ . *Solid state sciences*, 4(3), 317-322.

- Pan, Ko-Ying, Lin, Yu-Hung, Lee, Po-Sheng, Wu, Jyh-Ming, & Shih, Han C. (2012). Synthesis of SnO<sub>2</sub>-ZnO core-shell nanowires and their optoelectronic properties. *Journal of Nanomaterials*, 2012, 6.
- Pang, Christina, Yan, Bin, Liao, Lei, Liu, Bo, Zheng, Zhe, Wu, Tom, Yu, Ting. (2010). Synthesis, characterization and opto-electrical properties of ternary Zn<sub>2</sub>SnO<sub>4</sub> nanowires. *Nanotechnology*, 21(46), 465706.
- Park, Chong O, & Akbar, SA. (2003). Ceramics for chemical sensing. *Journal of materials science*, 38(23), 4611-4637.
- Park, CO, Akbar, SA, & Weppner, W. (2003). Ceramic electrolytes and electrochemical sensors. *Journal of materials science*, 38(23), 4639-4660.
- Park, Jae Young, Choi, Sun-Woo, & Kim, Sang Sub. (2011). A model for the enhancement of gas sensing properties in SnO<sub>2</sub>-ZnO core-shell nanofibres. *Journal of Physics D: Applied Physics*, 44(20), 205403.
- Park, Jae Young, Choi, Sun-Woo, Lee, Jun-Won, Lee, Chongmu, & Kim, Sang Sub. (2009). Synthesis and Gas Sensing Properties of TiO<sub>2</sub>-ZnO Core-Shell Nanofibers. *Journal of the American Ceramic Society*, 92(11), 2551-2554.
- Park, Jin-Ah, Moon, Jaehyun, Lee, Su-Jae, Kim, Seong Hyun, Chu, Hye Yong, & Zyung, Taehyoung. (2010). SnO<sub>2</sub>-ZnO hybrid nanofibers-based highly sensitive nitrogen dioxides sensor. *Sensors and Actuators B: Chemical*, 145(1), 592-595.
- Park, Sunghoon, An, Soyeon, Ko, Hyunsung, Jin, Changhyun, & Lee, Chongmu. (2013a, b). Enhanced NO<sub>2</sub> sensing properties of Zn<sub>2</sub>SnO<sub>4</sub>-core/ZnO-shell nanorod sensors. *Ceramics International*, 39(4), 3539-3545.
- Park, Sunghoon, An, Soyeon, Ko, Hyunsung, Lee, Sangmin, Kim, HyounWoo, & Lee, Chongmu. (2013). Enhanced ethanol sensing properties of TiO<sub>2</sub>/ZnO core-shell nanorod sensors. *Applied Physics A*, 1-7.
- Park, Sunghoon, An, Soyeon, Mun, Youngho, & Lee, Chongmu. (2013a, b). UV-Enhanced NO<sub>2</sub> Gas Sensing Properties of SnO<sub>2</sub>-Core/ZnO-Shell Nanowires at Room Temperature. *ACS applied materials & interfaces*, 5(10), 4285-4292.
- Parret, F., Ménini, Ph, Martinez, A., Soulantica, K., Maisonnat, A., & Chaudret, B. (2006). Improvement of micromachined SnO<sub>2</sub> gas sensors selectivity by optimised dynamic temperature operating mode. *Sensors and Actuators B: Chemical*, 118(1-2), 276-282.
- Patil, Dewyani, Patil, Pradip, Subramanian, Vijayanand, Joy, Pattayil A, & Potdar, Hari S. (2010). Highly sensitive and fast responding CO sensor based on Co<sub>3</sub>O<sub>4</sub> nanorods. *Talanta*, 81(1), 37-43.
- Penza, M, Rossi, R, Alvisi, M, Cassano, G, & Serra, E. (2009). Functional characterization of carbon nanotube networked films functionalized with tuned loading of Au nanoclusters for gas sensing applications. *Sensors and Actuators B: Chemical*, 140(1), 176-184.

- Phan, Duy-Thach, & Chung, Gwi-Sang. (2013). Effects of defects in Ga-doped ZnO nanorods formed by a hydrothermal method on CO sensing properties. *Sensors and Actuators B: Chemical*, 187, 191-197.
- Powers, Susan E, Hunt, Craig S, Heermann, Stephen E, Corseuil, Henry X, Rice, David, & Alvarez, Pedro JJ. (2001). The transport and fate of ethanol and BTEX in groundwater contaminated by gasohol. *Critical Reviews in Environmental Science and Technology*, 31(1), 79-123.
- Qi, Qi, Zhang, Tong, Zheng, Xuejun, Fan, Huitao, Liu, Li, Wang, Rui, & Zeng, Yi. (2008). Electrical response of  $\text{Sm}_2\text{O}_3$ -doped  $\text{SnO}_2$  to  $\text{C}_2\text{H}_2$  and effect of humidity interference. *Sensors and Actuators B: Chemical*, 134(1), 36-42.
- Qin, Yong, Wang, Xudong, & Wang, Zhong Lin. (2008). Microfibre–nanowire hybrid structure for energy scavenging. *Nature*, 451(7180), 809-813.
- Rai, Prabhakar, Kim, Yun-Su, Song, Hyeon-Min, Song, Min-Kyung, & Yu, Yeon-Tae. (2012). The role of gold catalyst on the sensing behavior of ZnO nanorods for CO and  $\text{NO}_2$  gases. *Sensors and Actuators B: Chemical*, 165(1), 133-142.
- Ramamoorthy, R, Dutta, PK, & Akbar, SA. (2003). Oxygen sensors: materials, methods, designs and applications. *Journal of materials science*, 38(21), 4271-4282.
- Robertson, J., Xiong, K., & Clark, S. J. (2006). Band gaps and defect levels in functional oxides. *Thin Solid Films*, 496(1), 1-7.
- Rong, A, Gao, XP, Li, GR, Yan, TY, Zhu, HY, Qu, JQ, & Song, DY. (2006). Hydrothermal synthesis of  $\text{Zn}_2\text{SnO}_4$  as anode materials for Li-ion battery. *The Journal of Physical Chemistry B*, 110(30), 14754-14760.
- Roth, D, Schreiber, W, Herkner, H, & Havel, C. (2014). Prevalence of carbon monoxide poisoning in patients presenting to a large emergency department. *International journal of clinical practice*.
- Rout, Chandra Sekhar, Ganesh, K, Govindaraj, Achutharao, & Rao, CNR. (2006). Sensors for the nitrogen oxides,  $\text{NO}_2$ , NO and  $\text{N}_2\text{O}$ , based on  $\text{In}_2\text{O}_3$  and  $\text{WO}_3$  nanowires. *Applied Physics A*, 85(3), 241-246.
- Rumyantseva, M, Kovalenko, V, Gaskov, A, Makshina, E, Yuschenko, V, Ivanova, I, Comini, E. (2006). Nanocomposites  $\text{SnO}_2/\text{Fe}_2\text{O}_3$ : Sensor and catalytic properties. *Sensors and Actuators B: Chemical*, 118(1), 208-214.
- Sadek, Abu Z, Choopun, Supab, Wlodarski, Wojtek, Ippolito, Samuel J, & Kalantar-zadeh, Kourosh. (2007). Characterization of ZnO Nanobelt-Based Gas Sensor. *Sensors Journal, IEEE*, 7(6), 919-924.
- Sen, Shashwati, Kanitkar, Prajakta, Sharma, Ankit, Muthe, K. P., Rath, Ashutosh, Deshpande, S. K., Yakhmi, J. V. (2010). Growth of  $\text{SnO}_2/\text{W}_{18}\text{O}_{49}$  nanowire hierarchical heterostructure and their application as chemical sensor. *Sensors and Actuators B: Chemical*, 147(2), 453-460.

- Shen, Yanbai, Zhang, Baoqing, Cao, Xianmin, Wei, Dezhou, Ma, Jiawei, Jia, Lijun, Jin, Yongcheng. (2014). Microstructure and enhanced H<sub>2</sub>S sensing properties of Pt-loaded WO<sub>3</sub> thin films. *Sensors and Actuators B: Chemical*, 193, 273-279.
- Shi, Changmin, Qin, Hongwei, Zhao, Ming, Wang, Xiaofeng, Li, Ling, & Hu, Jifan. (2014). Investigation on electrical transport, CO sensing characteristics and mechanism for nanocrystalline La<sub>1-x</sub>Ca<sub>x</sub>FeO<sub>3</sub> sensors. *Sensors and Actuators B: Chemical*, 190, 25-31.
- Shi, Liang, Xu, Yeming, Hark, Suikong, Liu, Yang, Wang, Sheng, Peng, Lian-mao, Li, Quan. (2007). Optical and electrical performance of SnO<sub>2</sub> capped ZnO nanowire arrays. *Nano letters*, 7(12), 3559-3563.
- Si, Shufeng, Li, Chunhui, Wang, Xun, Peng, Qing, & Li, Yadong. (2006). Fe<sub>2</sub>O<sub>3</sub>/ZnO core-shell nanorods for gas sensors. *Sensors and Actuators B: Chemical*, 119(1), 52-56.
- Singh, Ravi Chand, Singh, Onkar, Singh, Manmeet Pal, Chandi, Paramdeep Singh, & Thangaraj, R. (2010). Sensing behaviour of nanosized zinc-tin composite oxide towards liquefied petroleum gas and ethanol. *Materials Research Bulletin*, 45(9), 1162-1164.
- Sinha, SK, Rakshit, T, Ray, SK, Bysakh, Sandip, & Manna, Indranil. (2012). Growth and low-temperature photoluminescence properties of hybrid ZnO-SnO<sub>2</sub> nanobelts. *Philosophical Magazine Letters*, 92(9), 469-477.
- Sinha, SK, Rakshit, T, Ray, SK, & Manna, Indranil. (2011). Characterization of ZnO-SnO<sub>2</sub> thin film composites prepared by pulsed laser deposition. *Applied Surface Science*, 257(24), 10551-10556.
- Sivapunniam, Aarthi, Wiromrat, Niti, Myint, Myo Tay Zar, & Dutta, Joydeep. (2011). High-performance liquefied petroleum gas sensing based on nanostructures of zinc oxide and zinc stannate. *Sensors and Actuators B: Chemical*, 157(1), 232-239.
- Song, X., Wang, Z., Liu, Y., Wang, C., & Li, L. (2009). A highly sensitive ethanol sensor based on mesoporous ZnO-SnO<sub>2</sub> nanofibers. *Nanotechnology*, 20.
- Song, Xiaofeng, & Liu, Li. (2009). Characterization of electrospun ZnO-SnO<sub>2</sub> nanofibers for ethanol sensor. *Sensors and Actuators A: Physical*, 154(1), 175-179.
- Song, Xiaofeng, Wang, Zhaojie, Liu, Yongben, Wang, Ce, & Li, Lijuan. (2009). A highly sensitive ethanol sensor based on mesoporous ZnO-SnO<sub>2</sub> nanofibers. *Nanotechnology*, 20(7), 075501.
- Song, Xiaofeng, Zhang, Dejiang, & Fan, Meng. (2009). A novel toluene sensor based on ZnO-SnO<sub>2</sub> nanofiber web. *Applied Surface Science*, 255(16), 7343-7347.
- Stambolova, I, Konstantinov, K, Khristova, M, & Peshev, P. (1998). NO sensitivity of spinel type Zn<sub>2</sub>SnO<sub>4</sub> spray deposited films. *physica status solidi (a)*, 167(2), R11-R12.

- Stetter, Joseph R, & Li, Jing. (2008). Amperometric gas sensors a review. *Chemical reviews*, 108(2), 352-366.
- Stetter, Joseph R, & Penrose, William R. (2002). Understanding Chemical Sensors and Chemical Sensor Arrays(Electronic Noses): Past, Present, and Future. *Sensors update*, 10(1), 189.
- Su, Yong, Zhu, Li-ang, Xu, Liang, Chen, Yiqing, Xiao, Haihua, Zhou, Qingtao, & Feng, Yi. (2007). Self-catalytic formation and characterization of  $\text{Zn}_2\text{SnO}_4$  nanowires. *Materials Letters*, 61(2), 351-354.
- Sun, Guang, Zhang, Saisai, & Li, Yanwei. (2014). Solvothermal Synthesis of  $\text{Zn}_2\text{SnO}_4$  Nanocrystals and Their Photocatalytic Properties. *International Journal of Photoenergy*, 2014.
- Sun, Shuhui, Meng, Guowen, Zhang, Gaixia, & Zhang, Lide. (2007). Controlled growth and optical properties of one-dimensional ZnO nanostructures on  $\text{SnO}_2$  nanobelts. *Crystal Growth & Design*, 7(10), 1988-1991.
- Tan, Bing, Toman, Elizabeth, Li, Yanguang, & Wu, Yiyang. (2007). Zinc stannate ( $\text{Zn}_2\text{SnO}_4$ ) dye-sensitized solar cells. *Journal of the American Chemical Society*, 129(14), 4162-4163.
- Tang, Huixiang, Yan, Mi, Zhang, Hui, Li, Shenzhong, Ma, Xingfa, Wang, Mang, & Yang, Deren. (2006a, b). A selective  $\text{NH}_3$  gas sensor based on  $\text{Fe}_2\text{O}_3$ -ZnO nanocomposites at room temperature. *Sensors and Actuators B: Chemical*, 114(2), 910-915.
- Tang, Wei, Wang, Jing, Yao, Pengjun, & Li, Xiaogan. (2014). Hollow hierarchical  $\text{SnO}_2$ -ZnO composite nanofibers with heterostructure based on electrospinning method for detecting methanol. *Sensors and Actuators B: Chemical*, 192(0), 543-549.
- Thanh Le, Dang Thi, Trung, Do Dang, Chinh, Nguyen Duc, Thanh Binh, Bui Thi, Hong, Hoang Si, Van Duy, Nguyen, Van Hieu, Nguyen. (2013). Facile synthesis of  $\text{SnO}_2$ -ZnO core-shell nanowires for enhanced ethanol-sensing performance. *Current Applied Physics*, 13(8), 1637-1642.
- Tian, Shouqin, Gao, Yingri, Zeng, Dawen, & Xie, Changsheng. (2012). Effect of Zinc Doping on Microstructures and Gas-Sensing Properties of  $\text{SnO}_2$  Nanocrystals. *Journal of the American Ceramic Society*, 95(1), 436-442.
- Tian, Wei, Zhai, Tianyou, Zhang, Chao, Li, Song-Lin, Wang, Xi, Liu, Fei, Golberg, Dmitri. (2013). Low-Cost Fully Transparent Ultraviolet Photodetectors Based on Electrospun ZnO- $\text{SnO}_2$  Heterojunction Nanofibers. *Advanced Materials*, 25(33), 4625-4630.
- Timmer, Björn, Olthuis, Wouter, & Berg, Albert van den. (2005). Ammonia sensors and their applications—a review. *Sensors and Actuators B: Chemical*, 107(2), 666-677.



- Ul Hasan, Kamran, Alvi, NH, Lu, Jun, Nur, Omer, & Willander, Magnus. (2011). Single nanowire-based UV photodetectors for fast switching. *Nanoscale research letters*, 6(1), 1-6.
- Vanheusden, K, Warren, WL, Seager, CH, Tallant, DR, Voigt, JA, & Gnade, BE. (1996). Mechanisms behind green photoluminescence in ZnO phosphor powders. *Journal of Applied Physics*, 79(10), 7983-7990.
- Vasudeva, K, Mitra, N, Umasankar, P, & Dhingra, SC. (1996). Steam reforming of ethanol for hydrogen production: thermodynamic analysis. *International Journal of Hydrogen Energy*, 21(1), 13-18.
- Viter, Roman, Katoch, Akash, & Kim, Sang Sub. (2014). Grain size dependent bandgap shift of SnO<sub>2</sub> nanofibers. *Metals and Materials International*, 20(1), 163-167.
- Wagh, M. S., Jain, G. H., Patil, D. R., Patil, S. A., & Patil, L. A. (2006). Modified zinc oxide thick film resistors as NH<sub>3</sub> gas sensor. *Sensors and Actuators B: Chemical*, 115(1), 128-133.
- Wan, Qing, Huang, Jin, Xie, Zhong, Wang, Taihong, Dattoli, Eric N, & Lu, Wei. (2008a, b). Branched SnO<sub>2</sub> nanowires on metallic nanowire backbones for ethanol sensors application. *Applied Physics Letters*, 92(10), 102101-102101-102103.
- Wan, Qing, Li, QH, Chen, YJ, Wang, Ta-Hung, He, XL, Li, JP, & Lin, CL. (2004). Fabrication and ethanol sensing characteristics of ZnO nanowire gas sensors. *Applied Physics Letters*, 84(18), 3654-3656.
- Wang, B, Yang, YH, Wang, CX, & Yang, GW. (2005). Growth and photoluminescence of SnO<sub>2</sub> nanostructures synthesized by Au–Ag alloying catalyst assisted carbothermal evaporation. *Chemical physics letters*, 407(4), 347-353.
- Wang, B. B., Fu, X. X., Liu, F., Shi, S. L., Cheng, J. P., & Zhang, X. B. (2014). Fabrication and gas sensing properties of hollow core–shell SnO<sub>2</sub>/α-Fe<sub>2</sub>O<sub>3</sub> heterogeneous structures. *Journal of Alloys and Compounds*, 587(0), 82-89.
- Wang, Chengxiang, Yin, Longwei, Zhang, Luyuan, Xiang, Dong, & Gao, Rui. (2010). Metal oxide gas sensors: sensitivity and influencing factors. *Sensors*, 10(3), 2088-2106.
- Wang, Chia-Chi, Weng, Yu-Ching, & Chou, Tse-Chuan. (2007). Acetone sensor using lead foil as working electrode. *Sensors and Actuators B: Chemical*, 122(2), 591-595.
- Wang, Hongkang, & Rogach, Andrey L. (2013). Hierarchical SnO<sub>2</sub> Nanostructures: Recent Advances in Design, Synthesis, and Applications. *Chemistry of Materials*.
- Wang, Hua, Liang, Qingqin, Wang, Weijie, An, Yiran, Li, Jinghong, & Guo, Lin. (2011). Preparation of flower-like SnO<sub>2</sub> nanostructures and their applications in gas-sensing and lithium storage. *Crystal Growth & Design*, 11(7), 2942-2947.

- Wang, J. X., Xie, S. S., Gao, Y., Yan, X. Q., Liu, D. F., Yuan, H. J., Wang, G. (2004). Growth and characterization of axially periodic  $\text{Zn}_2\text{SnO}_4$  (ZTO) nanostructures. *Journal of Crystal Growth*, 267(1–2), 177-183.
- Wang, J. X., Xie, S. S., Yuan, H. J., Yan, X. Q., Liu, D. F., Gao, Y., Wang, G. (2004). Synthesis, structure, and photoluminescence of  $\text{Zn}_2\text{SnO}_4$  single-crystal nanobelts and nanorings. *Solid State Communications*, 131(7), 435-440.
- Wang, Jianxiong, Sun, Xiao Wei, Xie, Shishen, Zhou, Weiya, & Yang, Yi. (2007). Single-crystal and twinned  $\text{Zn}_2\text{SnO}_4$  nanowires with axial periodical structures. *Crystal Growth and Design*, 8(2), 707-710.
- Wang, JX, Liu, DF, Yan, XQ, Yuan, HJ, Ci, LJ, Zhou, ZP, Zhou, WY. (2004). Growth of  $\text{SnO}_2$  nanowires with uniform branched structures. *Solid state communications*, 130(1), 89-94.
- Wang, JX, Sun, XW, Xie, SS, Yang, Y, Chen, HY, Lo, GQ, & Kwong, DL. (2007). Preferential growth of  $\text{SnO}_2$  triangular nanoparticles on ZnO nanobelts. *The Journal of Physical Chemistry C*, 111(21), 7671-7675.
- Wang, Lisheng, Zhang, Xiaozhong, Liao, Xing, & Yang, Weiguo. (2005). A simple method to synthesize single-crystalline  $\text{Zn}_2\text{SnO}_4$  (ZTO) nanowires and their photoluminescence properties. *Nanotechnology*, 16(12), 2928.
- Wang, Liwei, Kang, Yanfei, Wang, Yao, Zhu, Baolin, Zhang, Shoumin, Huang, Weiping, & Wang, Shurong. (2012). CuO nanoparticle decorated ZnO nanorod sensor for low-temperature  $\text{H}_2\text{S}$  detection. *Materials Science and Engineering: C*, 32(7), 2079-2085.
- Wang, Wei, Li, Zhenyu, Zheng, Wei, Huang, Huimin, Wang, Ce, & Sun, Jinghui. (2010).  $\text{Cr}_2\text{O}_3$ -sensitized ZnO electrospun nanofibers based ethanol detectors. *Sensors and Actuators B: Chemical*, 143(2), 754-758.
- Wei, Shaohong, Zhang, Yan, & Zhou, Meihua. (2011). Toluene sensing properties of  $\text{SnO}_2$ -ZnO hollow nanofibers fabricated from single capillary electrospinning. *Solid State Communications*, 151(12), 895-899.
- Wen, Zeng, & Tian-Mo, Liu. (2010). Gas-sensing properties of  $\text{SnO}_2$ - $\text{TiO}_2$ -based sensor for volatile organic compound gas and its sensing mechanism. *Physica B: Condensed Matter*, 405(5), 1345-1348.
- Wöllenstein, J, Plaza, JA, Cane, C, Min, Y, Böttner, H, & Tuller, HL. (2003). A novel single chip thin film metal oxide array. *Sensors and Actuators B: Chemical*, 93(1), 350-355.
- Woo, Hyung-Sik, Na, Chan Woong, Kim, Il-Doo, & Lee, Jong-Heun. (2012). Highly sensitive and selective trimethylamine sensor using one-dimensional ZnO- $\text{Cr}_2\text{O}_3$  hetero-nanostructures. *Nanotechnology*, 23(24), 245501.
- Worsfold, O, Dooling, CM, Richardson, TH, Vysotsky, MO, Tregonning, R, Hunter, CA, & Malins, C. (2002). Thermal characteristics of porphyrin entrapped sol-

gels during exposure to toxic gases. *Colloids and Surfaces A: Physicochemical and Engineering Aspects*, 198, 859-867.

- Wu, Jih-Jen, & Liu, Sai-Chang. (2002). Catalyst-free growth and characterization of ZnO nanorods. *The Journal of Physical Chemistry B*, 106(37), 9546-9551.
- Wu, Yiyi, Fan, Rong, & Yang, Peidong. (2002). Block-by-block growth of single-crystalline Si/SiGe superlattice nanowires. *Nano Letters*, 2(2), 83-86.
- Wu, Yue, Cui, Yi, Huynh, Lynn, Barrelet, Carl J, Bell, David C, & Lieber, Charles M. (2004). Controlled growth and structures of molecular-scale silicon nanowires. *Nano Letters*, 4(3), 433-436.
- Xiang, Bin, Wang, Pengwei, Zhang, Xingzheng, Dayeh, Shadi A, Aplin, David PR, Soci, Cesare, Wang, Deli. (2007). Rational synthesis of p-type zinc oxide nanowire arrays using simple chemical vapor deposition. *Nano Letters*, 7(2), 323-328.
- Xu, Xiumei, Zhao, Peilu, Wang, Dawei, Sun, Peng, You, Lu, Sun, Yanfeng, Lu, Geyu. (2013). Preparation and gas sensing properties of hierarchical flower-like  $\text{In}_2\text{O}_3$  microspheres. *Sensors and Actuators B: Chemical*, 176(0), 405-412.
- Xue, Xinyu, Chen, Zhaohui, Ma, Chunhua, Xing, Lili, Chen, Yujin, Wang, Yanguo, & Wang, Taihong. (2010). One-step synthesis and gas-sensing characteristics of uniformly loaded Pt@  $\text{SnO}_2$  nanorods. *The Journal of Physical Chemistry C*, 114(9), 3968-3972.
- Xue, XY, Chen, YJ, & Wang, YG. (2005). Synthesis and ethanol sensing properties of  $\text{ZnSnO}_3$  nanowires. *Applied Physics Letters*, 86(23), 233101-233101-233103.
- Y.F. Chen, D.M. Bagnall, H.J. Koh, K.T. Park, K. Hiraga, Z.Q. Zhu, & T. Yao. (1998). *J. Appl. Phys.*, 84, 3912.
- Yamazoe, Noboru. (1991). New approaches for improving semiconductor gas sensors. *Sensors and Actuators B: Chemical*, 5(1), 7-19.
- Yamazoe, Noboru. (2005). Toward innovations of gas sensor technology. *Sensors and Actuators B: Chemical*, 108(1-2), 2-14.
- Yamazoe, Noboru, Sakai, Go, & Shimano, Kengo. (2003). Oxide semiconductor gas sensors. *Catalysis Surveys from Asia*, 7(1), 63-75.
- Yang, Dae-Jin, Kamienchick, Itai, Youn, Doo Young, Rothschild, Avner, & Kim, Il-Doo. (2010). Ultrasensitive and highly selective gas sensors based on electrospun  $\text{SnO}_2$  nanofibers modified by Pd loading. *Advanced Functional Materials*, 20(24), 4258-4264.
- Yang, H., Zhang, X., & Tang, A. (2006). Mechanosynthesis and gas-sensing properties of  $\text{In}_2\text{O}_3/\text{SnO}_2$  nanocomposites. *Nanotechnology*, 17, 2860.
- Yao, Mingshui, Ding, Fei, Cao, Yuebin, Hu, Peng, Fan, Junmei, Lu, Chen, Chen, Yunfa. (2014). Sn doped ZnO layered porous nanocrystals with hierarchical

structures and modified surfaces for gas sensors. *Sensors and Actuators B: Chemical*, 201, 255-265.

- Yu-Jin, Chen, Chun-Ling, Zhu, Li-Jiao, Wang, Peng, Gao, Mao-Sheng, Cao, & Xiao-Ling, Shi. (2009). Synthesis and enhanced ethanol sensing characteristics of  $\alpha$ - $\text{Fe}_2\text{O}_3$  /  $\text{SnO}_2$  core-shell nanorods. *Nanotechnology*, 20(4), 045502.
- Yu, J. H., & Choi, G. M. (2001). Current-voltage characteristics and selective CO detection of  $\text{Zn}_2\text{SnO}_4$  and  $\text{ZnO}/\text{Zn}_2\text{SnO}_4$ ,  $\text{SnO}_2/\text{Zn}_2\text{SnO}_4$  layered-type sensors. *Sensors and Actuators B: Chemical*, 72(2), 141-148.
- Yu, Ji Haeng, & Choi, Gyeong Man. (1999). Electrical and CO gas-sensing properties of  $\text{ZnO}/\text{SnO}_2$  hetero-contact. *Sensors and Actuators B: Chemical*, 61(1-3), 59-67.
- Yu, WD, Li, XM, & Gao, XD. (2005). Microstructure and photoluminescence properties of bulk-quantity  $\text{SnO}_2$  nanowires coated with  $\text{ZnO}$  nanocrystals. *Nanotechnology*, 16(12), 2770.
- Yu, Weidong, Li, Xiaomin, Gao, Xiangdong, & Wu, Feng. (2005). Large-scale synthesis and microstructure of  $\text{SnO}_2$  nanowires coated with quantum-sized  $\text{ZnO}$  nanocrystals on a mesh substrate. *The Journal of Physical Chemistry B*, 109(36), 17078-17081.
- Yu, Xuelian, Zhang, Guangjin, Cao, Hongbin, An, Xiaoqiang, Wang, Yun, Shu, Zhongjun, Hua, Fei. (2012).  $\text{ZnO}@\text{ZnS}$  hollow dumbbells-graphene composites as high-performance photocatalysts and alcohol sensors. *New Journal of Chemistry*, 36(12), 2593-2598.
- Zampiceni, E., Comini, E., Faglia, G., Sberveglieri, G., Kaciulis, S., Pandolfi, L., & Viticoli, S. (2003). Composition influence on the properties of sputtered  $\text{Sn}_x\text{W}_y\text{O}$  films. *Sensors and Actuators B: Chemical*, 89(3), 225-231.
- Zeghbroeck, BV. (2011). Principles of Semiconductor Devices: June.
- Zhang, Haijiao, Wu, Ruofei, Chen, Zhiwen, Liu, Gang, Zhang, Zongnan, & Jiao, Zheng. (2012). Self-assembly fabrication of 3D flower-like  $\text{ZnO}$  hierarchical nanostructures and their gas sensing properties. *CrystEngComm*, 14(5), 1775-1782.
- Zhang, Hui, Yang, Deren, Ji, Yujie, Ma, Xiangyang, Xu, Jin, & Que, Duanlin. (2004). Low temperature synthesis of flowerlike  $\text{ZnO}$  nanostructures by cetyltrimethylammonium bromide-assisted hydrothermal process. *The Journal of Physical Chemistry B*, 108(13), 3955-3958.
- Zhang, Jun, Liu, Xianghong, Wang, Liwei, Yang, Taili, Guo, Xianzhi, Wu, Shihua, Zhang, Shoumin. (2011). Synthesis and gas sensing properties of  $\alpha$ - $\text{Fe}_2\text{O}_3$ @ $\text{ZnO}$  core-shell nanospindles. *Nanotechnology*, 22(18), 185501.
- Zhang, Jun, Yang, Yongdong, Jiang, Feihong, Xu, Baolong, & Li, Jianping. (2005). Controlled growth of semiconducting oxides hierarchical nanostructures. *Journal of Solid State Chemistry*, 178(9), 2804-2810.

- Zhang, N, Yu, Ke, Li, Q, Zhu, ZQ, & Wan, Q. (2008). Room-temperature high-sensitivity H<sub>2</sub>S gas sensor based on dendritic ZnO nanostructures with macroscale in appearance. *Journal of Applied Physics*, 103(10), 104305-104305-104306.
- Zhang, Qifeng, Dandeneau, Christopher S, Zhou, Xiaoyuan, & Cao, Guozhong. (2009). ZnO Nanostructures for Dye-Sensitized Solar Cells. *Advanced Materials*, 21(41), 4087-4108.
- Zhang, Shaofeng, Ren, Feng, Wu, Wei, Zhou, Juan, Xiao, Xiangheng, Lingling, Sun, Jiang, Changzhong. (2013). Controllable synthesis of recyclable core-shell  $\gamma$ -Fe<sub>2</sub>O<sub>3</sub>@ SnO<sub>2</sub> hollow nanoparticles with enhanced photocatalytic and gas sensing properties. *Physical Chemistry Chemical Physics*.
- Zhang, Wen-Hui, & Zhang, Wei-De. (2008a,b). Fabrication of SnO<sub>2</sub>-ZnO nanocomposite sensor for selective sensing of trimethylamine and the freshness of fishes. *Sensors and Actuators B: Chemical*, 134(2), 403-408.
- Zhang, Yong, Li, Ruying, Zhou, Xiaorong, Cai, Mei, & Sun, Xueliang. (2009). Hierarchical Al<sub>2</sub>O<sub>3</sub> nanobelts and nanowires: morphology control and growth mechanism. *Crystal Growth & Design*, 9(10), 4230-4234.
- Zhang, Yuan, Xu, Jiaqiang, Xiang, Qun, Li, Hui, Pan, Qingyi, & Xu, Pengcheng. (2009). Brush-Like Hierarchical ZnO Nanostructures: Synthesis, Photoluminescence and Gas Sensor Properties. *The Journal of Physical Chemistry C*, 113(9), 3430-3435.
- Zhang, Zhenyi, Shao, Changlu, Li, Xinghua, Zhang, Li, Xue, Hongmei, Wang, Changhua, & Liu, Yichun. (2010). Electrospun Nanofibers of ZnO-SnO<sub>2</sub> Heterojunction with High Photocatalytic Activity. *The Journal of Physical Chemistry C*, 114(17), 7920-7925.
- Zhao, Jianwei, Ye, Changhui, Fang, Xiaosheng, Qin, Lirong, & Zhang, Lide. (2006). Selective growth of crystalline SnO<sub>2</sub> on the polar surface of ZnO nanobelts. *Crystal growth & design*, 6(12), 2643-2647.
- Zheng, Lirong, Zheng, Yuanhui, Chen, Chongqi, Zhan, Yingying, Lin, Xingyi, Zheng, Qi, Zhu, Jiefang. (2009). Network structured SnO<sub>2</sub>/ZnO heterojunction nanocatalyst with high photocatalytic activity. *Inorganic chemistry*, 48(5), 1819-1825.
- Zhou, Chongwu, Wang, Xiaoli, Aroonyadet, Noppadol, Zhang, Yuzheng, Mecklenburg, Matthew, Fang, Xin, Chen, Haitian. (2014). Aligned Epitaxial SnO<sub>2</sub> Nanowires on Sapphire: Growth and Device Applications. *Nano letters*.
- Zhu, C. L., Chen, Y. J., Wang, R. X., Wang, L. J., Cao, M. S., & Shi, X. L. (2009). Synthesis and enhanced ethanol sensing properties of  $\alpha$ -Fe<sub>2</sub>O<sub>3</sub>/ZnO heteronanostructures. *Sensors and Actuators B: Chemical*, 140(1), 185-189.
- Zhu, Chun-Ling, Yu, Hai-Long, Zhang, Yue, Wang, Tie-Shi, Ouyang, Qiu-Yun, Qi, Li-Hong, Xue, Xin-Yu. (2012). Fe<sub>2</sub>O<sub>3</sub>/TiO<sub>2</sub> Tube-like nanostructures: Synthesis,

structural transformation and the enhanced sensing properties. *ACS applied materials & interfaces*, 4(2), 665-671.

Zhu, Jianzhong, Ren, Congxin, Chen, Guoliang, Yu, Chunying, Wu, Jiali, & Mu, Haicuan. (1996). A new automotive air/fuel sensor based on TiO<sub>2</sub>-doped Nb<sub>2</sub>O<sub>5</sub> thin film by ion-beam-enhanced deposition. *Sensors and Actuators B: Chemical*, 32(3), 209-213.

Zhu, Lian Feng, She, Jun Cong, Luo, Jian Yi, Deng, Shao Zhi, Chen, Jun, & Xu, Ning Sheng. (2010). Study of physical and chemical processes of H<sub>2</sub> sensing of Pt-coated WO<sub>3</sub> nanowire films. *The Journal of Physical Chemistry C*, 114(36), 15504-15509.

## LIST OF PUBLICATIONS AND PAPERS PRESENTED

### PUBLICATIONS

- Tharsika T, Haseeb A.S.M.A, Akbar S.A, Sabri M.F.M, “Catalyst free single-step fabrication of SnO<sub>2</sub>/ZnO core-shell nanostructures”, *Ceramics International*, 40(5), 7601-7605, (2014).
- Tharsika T, Haseeb A.S.M.A, Akbar S.A, Sabri M.F.M, Wong Y.H, “Enhanced ethanol gas sensing properties of SnO<sub>2</sub>-core/ZnO-shell nanostructures”, *Sensors*, 14(8), 14586-14600, (2014).
- Tharsika T, Haseeb A.S.M.A, Akbar S.A, Sabri M.F.M, Wong Y.H, “Gas sensing properties of zinc stannate (Zn<sub>2</sub>SnO<sub>4</sub>) nanowires prepared by carbon assisted thermal evaporation process”, *Journal of Alloys and Compounds*, 618, 455- 462, (2015).
- Tharsika T, Haseeb A.S.M.A, Akbar S.A, Sabri M.F.M, “Co-synthesis of ZnO/SnO<sub>2</sub> mixed nanowires via a single-step carbothermal reduction method”, *Ceramics International*, 40 (3), 5039-5042, (2014).
- Tharsika T, Haseeb A.S.M.A, Sabri M.F.M, “Structural and optical properties of ZnO-SnO<sub>2</sub> mixed thin films deposited by spray pyrolysis”, *Thin Solid Films*, 558, 283-288, (2014).
- Tharsika T, Haseeb A.S.M.A, Sabri M.F.M, “Photoluminescence studies on spray pyrolysis deposited ZnO-SnO<sub>2</sub> mixed thin films”, *Advanced Materials Research*, 925, 318-322, (2014).

### PATENT

- Haseeb A.S.M.A, Tharsika T, Sabri M.F.M, “Method of fabricating hybrid zinc oxide and tin oxide nanostructures”, (Patent: PI2014700833) 2014, (National).

## CONFERENCES

- Tharsika T, Haseeb A.S.M.A, Akbar S.A, Sabri M.F.M, Wong Y.H, “Carbon monoxide gas sensing properties of SnO<sub>2</sub>-ZnO core-shell nanostructures”, AUN/SEED-Net Regional Conference on Materials Engineering, Kuala Lumpur, Malaysia, 2014.
- Tharsika T, Haseeb A.S.M.A, Akbar S.A, Sabri M.F.M, “Controlled growth of ZnO/SnO<sub>2</sub> mixed nanowires by carbon assisted thermal evaporation process”, 1<sup>st</sup> Ruhuna International Science and Technology Conference, Matara, Sri Lanka, 2014.
- Tharsika T, Haseeb A.S.M.A, Sabri M.F.M, “Fabrication and characterization of ZnO-SnO<sub>2</sub> mixed nanostructures”, 1<sup>st</sup> International Conference on Science & Engineering of Materials, Kuala Lumpur, Malaysia, 2013.
- Tharsika T, Haseeb A.S.M.A, Sabri M.F.M, “Fabrication and characterization of ZnO-SnO<sub>2</sub> mixed thin films by spray pyrolysis”, Joint International Conference on Nanoscience, Engineering, and Management, Penang, Malaysia, 2013.